THÈSE

Pour obtenir le grade de

DOCTEUR DE L'UNIVERSITÉ GRENOBLE ALPES

École doctorale : PHYS - Physique
Spécialité : Nanophysique
Unité de recherche : CEA LETI - Laboratoire d'électronique et de technologie de l'information

Epitaxie sélective de nanostructures HgTe/CdTe et transport électronique cohérent à basse température

Selective area epitaxy of HgTe/CdTe nanostructures and coherent electronic transport at low temperature

Présentée par :

Nicolas CHAIZE

Direction de thèse :

Philippe BALLET INGENIEUR DE RECHERCHE HDR, CEA CENTRE DE GRENOBLE	Directeur de thèse
Hermann SELLIER PROFESSEUR DES UNIVERSITES, UNIVERSITE GRENOBLE ALPES	Co-directeur de thèse

Rapporteurs :

ERWANN BOCQUILLON
FULL PROFESSOR, UNIVERSITÄT ZU KÖLN
SEBASTIEN PLISSARD
CHARGE DE RECHERCHE HDR, CNRS DELEGATION OCCITANIE OUEST

Thèse soutenue publiquement le **11 décembre 2025**, devant le jury composé de :

KUNTHEAK KHENG, PROFESSEUR DES UNIVERSITES, UNIVERSITE GRENOBLE ALPES	Président
ERWANN BOCQUILLON, FULL PROFESSOR, UNIVERSITÄT ZU KÖLN	Rapporteur
SEBASTIEN PLISSARD, CHARGE DE RECHERCHE HDR, CNRS DELEGATION OCCITANIE OUEST	Rapporteur
GILLES PATRIARCHE, DIRECTEUR DE RECHERCHE, CNRS DELEGATION ILE-DE-FRANCE SUD	Examinateur
CECILE NAUD, CHARGEE DE RECHERCHE, CNRS DELEGATION ALPES	Examinatrice

Résumé

La cohérence quantique, c'est-à-dire la capacité à préserver la phase électronique pendant le transport, est essentielle aux technologies quantiques et se manifeste à travers des effets d'interférence tels que les oscillations Aharonov-Bohm. Dans cette perspective, les systèmes unidimensionnels à fort couplage spin-orbite sont une plateforme idéale grâce à leurs grandes longueurs de cohérence. Parmi les matériaux candidats, HgTe est particulièrement attractif; mais son intégration dans des dispositifs unidimensionnels reste limitée par des difficultés technologiques.

Dans cette thèse, nous démontrons la réalisation expérimentale de nanostructures HgTe obtenues par épitaxie sélective (Selective Area Growth, SAG) et l'exploration de leurs effets d'interférence quantique. La technique SAG permet de surmonter les limitations de nanofabrication associées au HgTe. Un travail approfondi a été mené pour clarifier le mode de croissance des nanostructures HgTe par épitaxie par jets moléculaires sélective. Nous avons étudié de manière systématique l'influence de paramètres tels que l'épaisseur déposée, la température de croissance, la géométrie du masque, l'orientation cristallographique dans le plan et l'épaisseur de la couche de recouvrement, afin d'optimiser la sélectivité, d'améliorer la qualité structurale et de faciliter la fabrication de dispositifs. Cette optimisation garantit un contrôle précis de la croissance mais aussi la structure de bandes inversée, à l'origine des états de surface topologiques du HgTe.

Des mesures de magnéto-transport à basse température ont été réalisées sur différents dispositifs de HgTe, notamment des barres de Hall, des nanofils et des anneaux. Les barres de Hall micrométriques ont révélé un effet Hall quantique robuste avec une résistance longitudinale nulle, confirmant le choix de la SAG pour la fabrication de dispositifs HgTe. Sur cette base, nous avons étudié les phénomènes d'interférence quantique dans des structures unidimensionnelles afin de caractériser le régime de transport cohérent. La longueur de cohérence de phase a été extraite à partir des fluctuations universelles de conductance et des signatures d'antilocalisation faible dans des nanofils, ainsi que des oscillations Aharonov-Bohm dans des dispositifs en anneaux.

Dans l'ensemble, ces résultats démontrent que la croissance sélective constitue une méthode fiable pour fabriquer des dispositifs unidimensionnels cohérents à base de HgTe, ouvrant la voie à de futures études sur le couplage spin-orbite et le transport quantique topologique.

Mots clefs: Epitaxie Sélective, HgTe, Nanostructures, Transport Electronique, Cohérence de Phase

Abstract

Quantum coherence, i.e. the ability to preserve the phase of electrons during transport, is essential for quantum technologies and manifests through interference effects such as Aharonov-Bohm oscillations. In this context, one-dimensional systems with strong spin-orbit coupling provide an ideal platform thanks to their large coherence lengths. Among candidate materials, HgTe is particularly attractive, but its integration in one-dimensional devices is hindered by fabrication challenges.

In this thesis, we demonstrate the experimental realization of in-plane HgTe-based nanodevices obtained by selective area growth (SAG) and investigate their quantum interference effects. The SAG technique overcomes the nanofabrication limitations usually associated with HgTe. Considerable effort has been devoted to understand the growth behavior of HgTe nanostructures by selective-area molecular beam epitaxy. We systematically studied the influence of parameters such as deposited thickness, growth temperature, mask design, in-plane orientation, and cap layer thickness in order to optimize selectivity, improve structural quality, and facilitate device fabrication. This optimization ensures not only controlled growth but also the preservation of the inverted band structure, which underpins the topological surface states of HgTe.

Low-temperature magneto-transport measurements were performed on a variety of HgTe devices, including Hall bars, nanowires and ring geometries. Micrometric Hall bars revealed a well-developed quantum Hall effect with vanishing longitudinal resistance, confirming the suitability of SAG-grown HgTe for device fabrication. Building on this result, we investigated quantum interference phenomena in one-dimensional structures to characterize the regime of coherent transport. The phase coherence length was extracted from universal conductance fluctuations and weak anti-localization signatures in nanowires, as well as from Aharonov-Bohm oscillations in ring devices.

Altogether, these results demonstrate that selective area growth is a reliable method to fabricate coherent one-dimensional HgTe-based devices, paving the way for future studies of spin-orbit coupling and topological quantum transport.

Keywords: Selective Epitaxy, HgTe, Nanostructures, Electronic Transport, Phase Coherence

Acknowledgement

This thesis was mainly carried out at CEA-Leti in Grenoble, with more and more back-and-forth trips to the Institut Néel next door as time flew by. I see PhD life as a roller coaster. During this parenthesis, I followed a gnarly and unexpected journey in which the enjoyment of an expected result is suddenly replaced by the despair of "nothing works"...and vice versa fortunately ! The past three years have been extremely rich. This work not only enhanced my skills but also helped me grow as a person, focusing on what truly matters and sharpening my perspective. I am sincerely grateful to the many people who supported me throughout this journey.

First and foremost, I would like to thank my supervisors, Philippe Ballet and Hermann Sellier, for giving me the opportunity to work on this ambitious subject. They always gave me the freedom and the right advice to explore new ideas and learn from various fields. Their feedback helped shape my thinking and focus on the key points. Their guidance, in their respective areas of expertise, was essential in overcoming the challenges encountered throughout these three years and is a major reason for this successful thesis. I also thank them for the time they never hesitated to devote to this project and for helping me always see things from the right perspective. It was a pleasure to work with them.

I would like to thank the reporters and members of my jury, Erwann Bocquillon and Sébastien Plissard, for accepting to devote their time to evaluating this thesis, as well as Kuntheak Kheng, Gilles Patriarche, and Cécile Naud for being members of my jury.

But sorry Philippe, the real master of epitaxy is definitely Xavier ! Without him, none of this would have been possible. I am deeply grateful for his work, which allowed me to carry out my research under the best possible conditions. It was always a pleasure to come and discuss with you in the MBE room.

I would also like to thank the people at IEMN, in particular Ludovic Desplanque and Bruno Grandidier, for their kind support and for the management of the masks. I also take the opportunity to thank Clément Barbot, who became a friend, it was a real pleasure to share conferences with you.

I thank as well the people from PFNC with whom I had the chance to work on material characterization. Their help was a real asset to my work. In particular, I thank Denis Mariolle, Pierre-Henri Jouneau, Eric Gautier, Jean-Luc Rouvière, and Nicolas Bernier.

I am also grateful to the LMP lab and in particular the II-VI team for the great chitchats and the funny breaks : Eric, Nicolas (the nicest moustache in the lab) and Timotée. A special mention goes to Axel for your support, your jokes, your cool stories

and the wise advice ! I would also like to thank all the service members with whom I had the chance to work or simply discuss : David, Alex, Alexandra, Antoine, Bérangère, Céline, Clément, Fred, Guillaume, Matthieu, Matt, Maxime, Sarah, Samira, Simona, Amélie, Solène, and Fabien. Going on mission would not have been easy without the help of Carmelo, always there when needed.

A big thank-you to my officemates, thanks to whom I shared many great moments at work and over beers in Grenoble. You were by my side during difficult times and brought so much positivity to the office that it was always a pleasure to come in. Thank you to Thomas (the memes are still on the wall, and still the best) and Vishwajit for welcoming me, as well as Alejandro, Julien, and Hassan. This international environment was truly appreciated, and I already miss our discussions at H1. I would also like to thank Guillaume, Matteo, Lucas, Virgile, and Angie, who supported me during my last year while I was writing this manuscript. We have beers to catch up !

I also thank all the people who made my time in Grenoble far funnier and exciting : Elena, Luc, Lilian, Léopold, Yanis, Federico, Adélie, Victor, Mathurin, Mimi, Martina, and Pablo for the mountains, skiing, climbing, beers, cycling, laughs, and all the good vibes. A special thanks to Clément, whom I am proud to call my friend. These years would not have been the same without you. I would also like to thank Rémi, Eliott, Julien, and Blaise for the holidays we shared. It was truly great to travel together. A special thank to Henri and the sunny week-ends in Nyons by the river. I am happy to count you as friend, we keep in touch !

Finally, I would like to sincerely thank my family. I am deeply grateful to my grand-parents, who took care of me in France after I left Tahiti, where my parents have always supported me from afar. I thank my brother, my sister, and my entire family for their constant support. Last but not least, a very special and sincere thank-you to Ana, who supported and helped me with all she got during this last year. Without your kindness and support, things would have been very different. I am very happy and proud to share these important moments with you. We are sharing something beautiful, and I hope it continues. Thank you for taking such good care of me, this thesis is also the result of your devotion.

Table of Contents

Résumé ii

Abstract iv

Acknowledgement v

List of figures x

List of tables xxi

Introduction Générale xxii

General Introduction xxvi

1 In-plane nanostructures for quantum physics 1
- 1 Introduction . . . 1
- 2 Physics of the HgTe/CdTe system . . . 4
  - 2.1 Band structure . . . 4
  - 2.2 Quantum well and band inversion . . . 5
  - 2.3 HgTe-based devices . . . 7
- 3 Epitaxy of low-dimensional structures . . . 9
  - 3.1 Vapor-Liquid-Solid technique . . . 11
  - 3.2 Selective Area Growth . . . 11

2 Selective area epitaxy of HgTe-based nanostructures 16
- 1 Introduction . . . 16
- 2 MBE growth of HgCdTe material . . . 18
- 3 Mask definition and characterization . . . 18
- 4 Selective epitaxy of HgTe-based nanostructures . . . 22
  - 4.1 Demonstration and morphological study . . . 22
  - 4.2 Crystal organization . . . 26
  - 4.3 Influence of the growth parameters and the pattern design . . . 31
    - 4.3.1 Change with the opening width . . . 31
    - 4.3.2 Growth temperature . . . 33
    - 4.3.3 Deposited thickness . . . 36
  - 4.4 Cap layer . . . 39
- 5 Investigation of alternative mask materials . . . 40
- 6 Conclusion . . . 42

3 Nanofabrication **44**
1 Introduction . . . 44
2 Definition of the design for the nanodevices . . . 45
3 Process of fabrication . . . 46
3.1 Gate dielectric . . . 46
3.2 Top gate electrode . . . 47
3.3 Ohmic contacts . . . 47
3.4 Bonding . . . 48
4 Gate efficiency . . . 48
4.1 Determination of the Cd concentration in the cap layer . . . 49
4.2 Calculating the depleting factor . . . 50

4 Hall bars measurements **52**
1 Introduction . . . 52
2 Experimental set up . . . 54
2.1 Electronics . . . 54
2.2 Magnetic field control . . . 54
2.3 Lowering the temperature . . . 56
3 Magneto-transport properties of HgTe . . . 57
3.1 Hall effect . . . 57
3.2 Quantum Hall effect . . . 58
4 Low magnetic field measurements . . . 63
4.1 Extraction of the density . . . 63
4.2 Extraction of the mobility . . . 69
4.3 Mean free path . . . 70
5 High magnetic field measurements . . . 70
5.1 Parity of dominant filling factors . . . 70
5.2 Fan diagram versus magnetic field and gate voltage . . . 72
6 Temperature dependence of resistance minima . . . 74
7 Conclusion . . . 76

5 1D nanostructures : nanowire & ring **78**
1 Introduction . . . 78
2 Quantum transport in nanostructures . . . 80
2.1 Scattering phenomena . . . 80
2.2 Coherent backscattering . . . 81
2.3 Dephasing by magnetic field . . . 82
2.4 Spin-orbit coupling at play . . . 84
2.5 Weak anti-localization . . . 85
2.6 Universal conductance fluctuations . . . 87
2.7 Correlation field of conductance fluctuations . . . 89
2.8 Summary . . . 90
3 Nanowire . . . 90
3.1 Density and mobility . . . 91
3.1.1 Measurements at low magnetic field . . . 91
3.1.2 Measurements at high magnetic field . . . 92
3.1.3 Electron side . . . 94
3.1.4 Mean free path . . . 96
3.2 Universal conductance fluctuations . . . 96

3.2.1 About measuring accurately . . . 97
3.2.2 Correlation energy from gate voltage sweeps . . . 98
3.2.3 Magnetic field sweeps . . . 100
3.2.4 Temperature dependence . . . 101
3.3 Phase coherence length . . . 104
3.3.1 Extraction from the standard deviation . . . 104
3.3.2 Extraction from the correlation field . . . 105
3.3.3 Influence of the bias voltage . . . 106
3.3.4 Discussion of the uncertainties . . . 107
3.4 Weak anti-localization . . . 109
3.4.1 Fitting method . . . 109
3.4.2 Temperature dependence . . . 113
3.5 Conclusion . . . 115
4 Nanoring . . . 116
4.1 Theoretical background . . . 116
4.1.1 Origin of the oscillations . . . 116
4.1.2 Temperature dependence . . . 118
4.1.3 Coherence length . . . 119
4.2 Experimental results . . . 121
4.2.1 Periodic oscillations . . . 121
4.2.2 Temperature dependence . . . 122
4.2.3 Determination of the phase coherence length . . . 124
4.3 Conclusion . . . 125
5 Conclusion . . . 126

Conclusions and Perspectives **127**

Conclusions et Perspectives **130**

A Material characterization techniques **133**
1 Atomic Force Microscopy . . . 133
2 X-ray . . . 134
2.1 Diffraction . . . 134
3 Transmission electron microscopy . . . 136
3.1 Nanobeam precession electron diffraction . . . 137

B Complementary works on selective growth **139**
1 Deformation maps of a 50 nm-wide nanowire . . . 139
2 Selective growth of HgTe on InSb(001) substrate . . . 141
3 Selective homoepitaxy of CdTe . . . 142
4 Selective area growth of HgTe/CdTe(111) . . . 143

C Magneto-transport measurements for a smaller Hall bar **144**
1 Low magnetic field measurements . . . 144
2 Shubnikov-de Haas oscillations . . . 146

List of publications **148**

Bibliography **150**

List of figures

1.1 Schematic representation of the HgTe and CdTe zinc-blende crystal structure. Taken from [Thomas, 2016]. 4
1.2 Schematic representation of the energy bands at the Γ point of (a) CdTe and (b) HgTe. The alteration of the energy bands from the unperturbed Hamiltonian (H_I) due to relativistic effects : the mass-velocity (H_{mv}) and spin-orbit (H_{SO}) corrections. Adapted from [Chu, 2008]. 6
1.3 Representation of the two main subbands in a CdTe/HgTe/CdTe QW. On the left hand side, $d < d_c$ so the well in the normal regime, $E_1 > H_1$. On the right hand side, we show the inverted regime, $E_1 < H_1$, reached when $d > d_c$. Adapted from [Bernevig, 2006] 7
1.4 Subband energies of HgTe/$Hg_{0.3}Cd_{0.7}$Te quantum wells as a function of the well thickness, d. Taken from [Büttner, 2011]. 7
1.5 Sketch of the CdTe and HgTe band structure in the vicinity of the Γ point. Adapted from [Bernevig, 2006]. When the HgTe layer is thick enough, above d_c, gapless surface state arise at the interface between CdTe and HgTe to ensure band continuity. These states are represented by the dashed lines. . 8
1.6 Examples of HgTe structures obtained by wet etching techniques or directly as 1D growth. (a) SEM image of a wet-etched mesa. The 7.5 nm HgTe QW is visible as a bright layer [Bendias, 2018]. (b) SEM micrograph of a representative HgTe nanowire. It has a length of 1.3 μm and a median width of 163 nm. (c) TEM image of a HgTe- and Te-based nanowire grown from a Au nucleation site [Haakenaasen, 2008a]. (d) SEM image showing high density of HgTe nanowires grown on Si substrate [Selvig, 2006]. 9
1.7 Simplified representation of the different behaviors of the adatoms at the substrate surface during epitaxial growth. 10
1.8 Examples of realization performed with the VLS technique. (a) SEM image of GaAs NWs grown on GaAs(110) substrate [Zhang, 2017]. (b) SEM image of a pair of connected InAs nanowires grown on InP ridges. Advanced VLS technique showing high precision control of the NW position to design structures which connect individual nanowires [Dalacu, 2013]. 11
1.9 Sketch of the SAG principle. The substrate is covered by a hard mask where the desired geometry is patterned. When perfect selectivity is achieved, the grown crystal follows the designed pattern. However, if the selectivity is compromised, parasitic growth may occur on the masked regions. 12

1.10 Examples of nanostructures obtained by SAE. (a) SEM image of $\langle 11\bar{2}\rangle$-oriented InAs NWs network morphology on InP(111)B substrates [Aseev, 2018] (b) PbTe SAG on InP(111)A substrate. Top left shows all in-plane $\langle 110\rangle$ crysyal directions, while the bottom left, all $\langle 112\rangle$ crystal directions. The pattern on the right hand sign is a combination of both crystal directions families [Jung, 2022]. (c) InAs NWs grown on an InP(001) substrate. Well-defined facets are formed in particular ridge directions : (b) $[1\bar{1}0]$, (c) [110], and (d) [100] [Lee, 2019]. (d) Selectivity maps for InAs SAG on GaAs(001) substrate. Depending on the As flux and the substrate temperature the ideal selectivity window is defined [Aseev, 2018]. 13
1.11 Examples of device realization thanks to the SAG technique. (a) False colored SEM micrograph of a Hall Device obtained by selective growth of PbTe. Contacts are colored in yellow and the top gate in orange [Jung, 2022]. (b) Top-view SEM image of a InSb NW loop in which Aharonov-Bohm conductance oscillations are observed. Ohmic contacts are marked in blue, and the top gate in purple [Aseev, 2019]. 14

2.1 Sketch of the different steps for the mask preparation. The SiO_2 is deposited by PECVD. The HF etching reduces its thickness to ~ 10 nm. 19
2.2 Mask opening profiles extracted from AFM scans. (a) displays the shape of a 100 nm-wide opening from five different masks. The two vertical dashed lines in the center are separated by 100 nm. (b) openings with different widths taken from Mask 3. 20
2.3 Examples of patterns designed by EBL for the selective mask. Crosses (a), rings (b) and nanowires (c) are typical shapes. The width varies from 50 to 1000 nm. Several in-plane crystalline directions are studied. In panel (c), the distance between openings, the pitch, is varied to study the diffusion of the adatoms on the hard mask. 21
2.4 Top-view SEM images of HgTe nanostructures grown on a patterned CdTe(001) substrate. (a)-(b) SEM micrographs of two 5 μm-long HgTe NWs grown along, respectively, $\langle\bar{1}10\rangle$ and $\langle 110\rangle$ directions. (c) SEM micrograph of a 10 μm-long $\langle 100\rangle$ type HgTe cross. (d) SEM image of diamond-like structures with junction along $\langle 110\rangle$ ridges. For images (a)-(d) the opening width is 100 nm and the growth temperature is 140°C. (e)-(f) SEM micrographs of 50 nm-wide $\langle 110\rangle/\langle\bar{1}10\rangle$ type grid grown at, respectively, 140°C and 180°C. 22
2.5 AFM scans of nanostructures grown at 170°C and 0.26 ML/s with a 40 nm nominal thickness. Scans of (a) a $\langle 110\rangle/\langle\bar{1}10\rangle$ type and (b) a $\langle 100\rangle$ type NW cross. The darker areas in (a) and (b) correspond to the SiO_2 mask. Both crosses are grown from 100 nm wide slits. (c) AFM scan showing a 100 nm-wide opening before the growth. The darkest area corresponds to the CdTe substrate and the colored sides to the SiO_2 mask. The change in constrast across SiO_2 is caused by the etching process while opening the mask which reduces its thickness to about ten nanometers. (d) AFM profiles extracted from the three AFM images along the respective colored arrows. 24

2.6 (a) Sketch of the HgTe surface reconstruction during the growth. The unit cell shows a (2×1) reconfiguration elongated along the the $\langle 1\bar{1}0\rangle$ direction. (b) The AFM image emphasizes the prensence of diamond shape on HgTe surface. The diamonds are elongated along the $\langle 110\rangle$ direction which allows to determine the in-plane orientation of the substrate. 25
2.7 Analysis of a [110]-oriented nanowire by STEM. (a) High resolution HAADF image of the NW transversal cross-section. We define a frame of reference for each grain with respect to its orientation. The two red 54.7°-tilted dashed lines correspond to grain boundaries of {111}B facets between the center grain G_0 and the two side grains G_1 and G_2. The top red dashed line represents the $(001)_{G_0}$ plane. The dashed green curve highlights the interface between CdTe and HgTe. Numerical g-moiré images are obtained to visualize the respective (b) $(1\bar{1}0)_{G_0}$, (c) $(001)_{G_0}$, (d) $(1\bar{1}1)_{G_0} \Leftrightarrow (\bar{1}11)_{G_1}$ and (e) $(1\bar{1}1)_{G_0} \Leftrightarrow (1\bar{1}1)_{G_2}$ planes. The scale bar in g-moiré maps represents 20 nm. 27
2.8 (a) Zoom on the crystal/mask interface near grains G_0 and G_2 from the HR HAADF-STEM image of figure 2.7(a). The area outlined by a black square is further zoom-in to visualize the atomic columns and clearly shows the {111} twin plane separating grains G_0 and G_2 that are rotated from each other by 70.5° (angle between $[001]_{G_0}$ and $[001]_{G_2}$). (b) Semi-quantitative map of the rotation angle of the filtered area in the FFT of the image (the FFT and the elliptic mask are visible in the inset). The three points with highest intensity in this area correspond to planes $(1\bar{1}1)_{G_1}$, $(001)_{G_0}$ and $(\bar{1}11)_{G_2}$. The reference plane is taken as $(001)_{G_0}$. The rotation between planes $(1\bar{1}1)_{G_1}$, respectively $(\bar{1}11)_{G_2}$, and $(001)_{G_0}$ should be equal to +15.8° (orange area), respectively -15.8° (blue area). 28
2.9 Mapping of different physical properties of 100 nm-wide $\langle 1\bar{1}0\rangle$-oriented NW obtained by NPED in transversal cross-section. In panel (a) the strain is represented along the (left) [110] in-plane direction and (right) the growth direction [001]. Below, in (b), the maps respectively illustrates the rotation and the shear. The scale bar represents 20 nm 30
2.10 Schematics of nanowire cross-section for two crystal orientations (left) [110] and (right) $[\bar{1}10]$. The cross section of a nominal NW is shown in green along with typical overgrowth of experimental NWs in purple for [110] and $[\bar{1}10]$ directions. The parameter ρ is defined as the ratio of the whole NW cross-section (green and purple) over the green area. 31
2.11 Transversal AFM profiles of nanowires from a 20 nm-thick nominal growth. Panels (a) and (b) reveal the morphology of $[1\bar{1}0]$-oriented NWs. (a) Profiles of NWs with three different widths. The nominal thickness is visible in the center of the NWs. The edges displays the {111} facets and the super-elevation on the sides. The $x : y$ scale is 1 : 1. For $W = 50$ nm the merging is almost complete. (b) Morphology of the NWs, up to $W = 500$ nm. The reproducible profile on the edges is emphasized, as well as the characteristic shape of the mask opening. Figures (c) and (d) are focusing on $\langle 110\rangle$-oriented NWs. The overhang can not be revealed by the AFM tip. In (d), the larger thickness due to the change of the crystal orientation is visible. 32

2.12 Evolution of experimental ρ values as a function of $1/W$ for $\langle 1\bar{1}0\rangle$ and $\langle 110\rangle$ orientations types. NWs are grown at 140°C and 0.26 ML/s with a 38 nm nominal thickness and the pitch is above 1000 nm. Dashed lines are linear fit curves. 33
2.13 Influence of growth temperature on the NW morphology. (a) AFM profiles for two $\langle \bar{1}10\rangle$-oriented NWs whose width is 50 nm (top) and 100 nm (bottom). The deposited thickness is 30 nm and the pitch is 1000 nm. (b) Change of ρ versus pitch at different growth temperatures for 30 nm-thick $\langle \bar{1}10\rangle$-oriented NWs and width opening of $W = 100$ nm. 34
2.14 Top-view SEM images of three HgTe ring nanostructures grown at (a) 140°C, (b) 170°C, (c) 185°C. The traces around the outer ring are carbon contamination that have been deposited by the electron beam of the SEM when imaging with a larger magnification. 35
2.15 Thickness influence on the opening filling. (a) AFM scan of 5 a nm-thick growth. The filling of the openings is not uniform but displays a collection of island nucleation sites. Along the $\langle 1\bar{1}0\rangle$ direction the filling of the edges is continuous. In the $\langle 110\rangle$ axis the filling shows discontinuity. (b) Change in the NW cross section morphology for three different nominal thicknesses for two $\langle 1\bar{1}0\rangle$ oriented NWs whose opening width is 50 nm (top) and 100 nm (bottom). The growth temperature is 160°C for the 10 nm-thick growth and 170°C for the 30 and 50 nm-thick growths. 36
2.16 16°-angle birdview SEM image of a selective grid. The nominal thickness is 100 nm. The $\langle 1\bar{1}0\rangle$ axis shows {111} facets on the edges. The overhang can be distinguished for the $\langle 110\rangle$ direction. 37
2.17 Evolution of NWs morphology as the nominal deposited thickness is increased. In panels (a) and (b), respectively (c) and (d), we consider a 50 nm-wide, respectively 100 nm-wide, opening. NWs in (a) and (c), resp. (b) and (d), are oriented along $[1\bar{1}0]$ axis, resp. [110] axis. All growths have been performed at 170°C, but do not come from the same patterned substrate. . 38
2.18 Parasitic growth after cap-layer deposition. (a) SEM micrograph of a 100 nm-wide cross after the growth of 30 nm of HgTe followed by the deposition of a 20 nm-thick CdHgTe cap layer at 180°C. (b) AFM profiles of 50 nm-wide [110]-oriented NWs (red) without cap layer and (blue) from the growth mentioned in (a). The difference of morphology and parasitic growth with and without cap layer are evidenced. 40
2.19 Profile and roughness characterization of different masks. (a) Opening profiles variation between the standard procedure, SiO_2 mask, and the combination with alumina. Both purple and blue lines are extracted from a device mask. (b) Profiles of the top surface masks scanned far from the openings, colors are set accordingly to (a). Their respective roughness, rms, is indicated. Curves are shifted vertically for clarity. 41
2.20 Comparison of growths on Al_2O_3+ SiO_2 masks with (w/) and without (w/o) HF-etching. The growth temperature (GT) is changed during experiments. The nominal thickness of the growth is 20 nm. 42

3.1 Layers arrangement for the device fabrication and device design. (a) Design of a nano-device. The role of the different layers is precised. (b) Zoom-in of the center of (a) to reveal the nanostructure. (c) and (d) are other examples of ring geometry for magneto-transport studies. 46
3.2 Fabrication steps for (a) the gate oxide and (b) the gate electrode. 47
3.3 Steps for the ohmic contacts 48
3.4 (a) Sample on the chip holder. (b) Example of a nanodevice bonded to the connections. The gold wires binding the nanodevice to the chip holder thanks to six ohmic contact and the top gate electrode (at the top of the image) are visible. The grainy part of the ohmic contacts corresponds to the Au/Ti evaporation on the etched HgTe structures. 49
3.5 Schematic representation of the crystal deformation due to in-plane compressive strain in the case of $Cd_xHg_{1-x}Te$ grown on CdZnTe(211). 50

4.1 Top view image of a Hall bar device taken with an optical microscope. The electrical set-up for the magneto-transport measurements is sketched around. 54
4.2 Sketch of the electrical circuit driving and monitoring the superconducting magnet 55
4.3 Sketch of the an ^{3}He insert which can be fitted into a VTI. Taken from [Oxford Instruments, 2013]. 56
4.4 Representation of the Hall effect in a Hall bar of length L and width W. Under a magnetic field B, electrons participating to the current are deflecting towards one side of the sample because of the Lorentz force. Their accumulation creates a charge difference in the transversal direction and so a voltage difference that can be probed through V_{xy}. 57
4.5 (a) Representation of the Quantum Hall effect in a Hall bar. The bulk is insulating and current only flows in counter-propagating channels on the sides. (b) For a standard 2DEG, the energy difference between two LLs is constant. On the edges the confinement potential bend the energy levels that cross the Fermi energy. 60
4.6 Calculated LL spectrum for a thin TI as a function of magnetic field. The hybridization gap Δ is visible at $B = 0$, and the LL splitting increases linearly with B. Dashed arrows indicate the evolution of the filling factor parity (green for odd values and blue for even values) as B increases at fixed Fermi energy. Parameters : $\Delta = 5$ meV, $\hbar e/M = 2.5$ meV/T, $v_F = 5 \times 10^5$ m/s. 62
4.7 SEM image of a HgTe Hall bar grown by selective-area epitaxy. 63
4.8 Panels (a) and (b) respectively display the evolution of the longitudinal resistance R_{xx} and the Hall resistance R_{xy} as a function of the gate voltage in the absence of magnetic field. The response of the Hall resistance under exposition to a magnetic field is plotted in (c) for the electron side and in (d) for the hole side. 65
4.9 Low magnetic field analysis of the Hall bar. All data are displayed as a function of the gate voltage. Panel (a) illustrates the evolution of the Hall resistance at two different magnetic fields. (b) is a zoom-in of the framed area in the hole side from (a). (c) displays the Hall constant of data in (a). (d) represents the carrier density. The yellow dashed line accounts for the slope of electron density, that is the depletion factor. 66

4.10 Analysis of the Hall bar characteristics at 1.5 K extracted from data with magnetic field $B \leq 0.5$ T. All data are displayed as a function of the gate voltage. The purple vertical band highlights the sign inversion of the Hall constant R_H, corresponding to the full depletion of the conduction band electrons. Panel (a) displays the Hall constant R_H. (b) compares the Hall constants from $B = 0.1$ T, $B = 0.2$ T and from the fit. (c) represents the carrier density. The yellow dashed line accounts for the slope of electron and hole densities, which is the depletion factor, common between the two carrier type. (d) shows the mobility of the carriers. The gray color band indicates the voltage range where the single carrier model is not valid. Data within this range should then not be considered. 67
4.11 Band structure of 9 nm-thick HgTe quantum well calculated on the basis of a $H_{4\times4}(\mathbf{k})$ Hamiltonian. Taken from [Krishtopenko, 2018]. 68
4.12 Simulation of carrier densities and Hall response in a two-carrier model. The values are arbitrary and only intended to illustrate the experimental behavior. (a) Simulation of the electrons n and holes p concentrations as a function of the gate voltage. On a finite voltage range $[V_0 - \Delta; V_0 + \Delta]$ electrons and holes co-exist. The related Hall constant expressed from equation 4.18 and its inverse are respectively shown in (b) and (c). The green star in (c) emphasizes the CNP, while the purple band marks the change of sign of the Hall constant. 69
4.13 Shubnikov-de Haas oscillations of R_{xx} and Hall conductance G_{xy} recorded as a function of the magnetic field B and plotted as a function of the filling factor ν. Integer values give the number of filled Landau levels. 71
4.14 2D maps of magneto-transport measurements performed on the Hall bar. (a) Longitudinal resistance $\mathrm{R_{xx}}$ as a function of B and V_{gate}. The black and purple dashed lines respectively represents the even and odd filling factors. (b) Hall resistance R_{xy} as a function of B and V_{gate}. 73
4.15 (a) Longitudinal resistance of the Hall bar as a function of the gate voltage, limited to the electron side. The data is recorded at $B = 3.52$ T and for temperatures ranging from 0.28 to 5 K. Note that the temperatures shown are setpoints. The actual values, corrected for the thermometer magnetoresistance at 3.52 T, are used in panel (b) to extract the activation gaps. R_{xx} minima are labeled with their filling factors. (b) Temperature dependence of these minima for each filling factor. The dashed lines corresponds to the linear fit of the data with an Arrhenius law. (c) Activation gap versus filling factors obtained from the slope of the temperature dependence. 75

5.1 Sketch of a diffusive loop trajectory involved in the weak localization effect. The green and blue arrows indicate time-reversed paths. $*$ denote scattering events. 82
5.2 Sketch of a close loop via boundary scattering resulting in flux cancellation. The two dashed areas must be exactly equal. 83

5.3 Schematic of a loop trajectory leading to destructive interference due to Rashba SOC. The spin is represented by the small thick arrow rotating in opposite directions for the two time-reversed paths. Time invariance is broken as time-reversed partners loops exhibit opposite spin rotations. This yields destructive spin interference in the return probability, thereby increasing the conductance. This effect is at the origin of the WAL conductance peak. 86
5.4 Top view SEM micrograph of the measured HgTe nanowire grown by SAG. It is oriented along $<1\bar{1}0>$ direction on the CdTe substrate. The nanostructure is capped by a 10 nm-thick HgCdTe layer. The presence of parasitic growth on the silicon dioxide mask area is due to the cap layer deposition. The image has been taken before the deposition of the gate oxide and electrode. 90
5.5 Low-field transport properties of the HgTe nanowire. (a) R_{xx} variation versus the gate voltage. (b) R_{xy} variation versus the gate voltage at zero magnetic field (black), $B = 0.1$ T (red) and $B = 0.2$ T (blue). The horizontal dashed line serves as guide for the eye. The measurements are performed under bias voltage $U = 1$mV at 1.5 K. 91
5.6 2D maps of magneto-transport measurements performed on the HgTe nanowire. (a) The longitudinal resistance R_{xx} is plotted as a function of gate voltage and magnetic field. (b) The Hall resistance in units of h/e^2 is displayed with respect to the same parameters. 93
5.7 Traces of (a) R_{xx} and (b) R_{xy} extracted from figure 5.6. The data are plotted as a function of the gate voltage and obtained from three different applied magnetic field : $B = 0.53$ T (black), $B = 2.014$ T (red) and $B = 4.028$ T (red). 93
5.8 Density and mobility in the HgTe nanowire, extracted from the data shown in figure 5.6 on the electron side of the CNP $V_{\text{gate}} \geq -0.6$ V. (a) Hall resistance as a function of the magnetic field for three different gate voltages. (b) Hall constant extracted from a linear fit at each gate voltage. (c) Carrier density with respect to the gate voltage. (d) Electron mobility calculated from the the experimental data together with the mobility $\tilde{\mu}$, calculated from a linearized density with the depletion factor α, and the Hall bar mobility from figure 4.10 for comparison. 95
5.9 UCF measurements in the HgTe nanowire at 0.28 K. (a) Smearing effect due to the bias voltage. Curves are vertically shifted for clarity. (b) Standard deviation of the conductance curves shown in (a). 97
5.10 Auto-correlation function of the UCF shown in figure 5.9(a) for the sweep in gate voltage at $U = 30$ μV at 280 mK. The inset shows a zoom-in to identify ΔV_{corr}. 98
5.11 Band structure of 12.2 nm-thick HgTe quantum well calculated on the basis of a $H_{8\times8}(\mathbf{k})$ Hamiltonian. Taken from [Novik, 2005]. For wave vectors k above 0.25 nm^{-1}, the H1 conduction band has a Dirac-like energy dispersion $E(\mathbf{k}) = \hbar\nu_F k$ with a Fermi velocity $v_F = 8.6 \times 10^5$ m/s. 99

5.12 Universal conductance fluctuations in the HgTE nanowire. (a) Fluctuations in longitudinal resistance as a function of the magnetic field for different applied gate voltages. (b) Resulting conductance difference after subtraction of the mean background. For clarity, the curves are vertically offset. Experiments are performed at 1.5 K with a bias voltage $U = 1000$ μV. . . . 100
5.13 Universal conductance fluctuation in the HgTe nanowire. 2D map of the conductance fluctuations as a function of gate voltage V_{gate} and magnetic field B. The slowly varying background has been subtracted from the raw conductance data to enhance the visibility of mesoscopic conductance fluctuations. Experiments are performed at 1.5 K with a bias voltage $U = 1000$ μV. 102
5.14 Universal conductance fluctuations in the HgTe nanowire at $V_{\text{gate}} = 0$ V. Panel (a) displays the temperature evolution of ΔG_{xx} as a function of the magnetic field under a bias voltage of 30 μV. In panel (b), the standard deviation of ΔG_{xx} is plotted as a function of the temperature. 102
5.15 Conductance variation ΔG_{xx} as a function of the magnetic field under a bias voltage of (a) 30 μV and (b) 1000 μV. Experiments are performed at different temperatures with Vgate $= 0$ V. The figure highlights the influence of the bias voltage. 103
5.16 Dependence of the phase coherence length with temperature extracted from the standard deviation of the UCF acquired at a bias voltage $U = 30$ μV. The figure displays the thermal length l_T and the phase coherence lengths l_ϕ extracted from different expressions corresponding to different regimes. . 104
5.17 Auto-correlation function of the UCF shown in figure 5.14(a) for the sweep in at a bias voltage $U = 30$ μV at 0.28 K. The inset shows a zoom-in to identify ΔB_{corr}. 105
5.18 Dependence of the phase coherence length with the temperature from the magnetic correlation field of the UCF acquired at a bias voltage $U = 30$ μV. The figure displays the thermal length l_T and the phase coherence length l_ϕ extracted from equation 5.25. The phase coherence length obtained from the standard deviation is also plotted for comparison. 106
5.19 The figure summarizes the two different methods used to extract the phase coherence length from the UCF as a function of the temperature. The experiments are performed under the same conditions. Panel (a) shows the standard deviation of UCF measurements, and panel (c) displays the corresponding phase coherence length thanks to the interpolation formula with respect to the thermal length. Panel (b) shows the magnetic correlation field and panel (d) displays the corresponding phase coherence length. . . . 108
5.20 Comparison of the phase coherence length extracted from the standard deviation of the UCF without (w/o) and with (w/) the noise reduction. . . 109

5.21 Weak anti-localization effect in a quasi-1D channel. The black curve is the experimental data for the HgTe nanowire measured at 280 mK with a bias voltage $U = 30$ μV. It corresponds to the variation of the conductance from its value at $B = 0$ T. Colored lines correspond to the theoretical expression 5.27 for different values of the parameters. All curves also represent the conductance change $\Delta G = G - G(B = 0)$ except for the blue and green curves in panel (a) where WL dominates over WAL, here $\Delta G = G - G(B \to \infty)$. When the parameters are not varied, they are respectively set to : $l_{so} = 10$ nm, $l_\phi = 2800$ nm, $l_e = 420$ nm and $W = 100$ nm. 111
5.22 Error map of the fitting mean-squared error σ in the l_ϕ-l_{so} parameter space corresponding to measurements at 280 mK with a bias voltage $U = 30$ μV. The red cross marks the best fit corresponding to the minimum error. The region enclosed by the white dashed line contains the l_ϕ-l_{so} combinations for which the error satisfies $\sigma \leq 1.5 \times \sigma_{\min}$. The extrema of l_ϕ and l_{so} within this region define the error bars of the fit. 112
5.23 Weak anti-localization (WAL) peak in the HgTe nanowire, measured with a bias voltage (a) $U = 30$ μV and (b) $U = 1000$ μV at 280 mK, together with its modeling using equation 5.27. The fitting curves (colored lines) are calculated for the values of l_ϕ and l_{so} indicated in the figure, while $W = 100$ nm and $l_e = 420$ nm are imposed. The red curve fulfills in the requirement $l_m > W$ with $B_{max} = 0.05$ T, while the blue curve is obtained from a wider fitting range with $B_{max} = 0.2$ T, to account for the full height of the WAL peak. 113
5.24 Phase coherence length l_ϕ and spin-orbit length l_{so} as a function of the temperature in the HgTe nanowire. These characteristic lengths are obtained by fitting the experimental data. Different bias voltages and fitting range are considered. In panels (a) and (c), we use a fitting range with $B_{max} = 0.2$ T. In panels (b) and (d), the bias voltage is fixed and the fitting range is varied between $B_{max} = 0.05$ T and $B_{max} = 0.2$ T. 114
5.25 Schematic of the main interference effects arising in a ring geometry. Panel (a) represents the AB effect. Under a magnetic field, partial electronic waves interfere after their propagation along each arm of the loop. The periodicity in enclosed flux is $\Delta\phi = h/e$. Panel (b) displays the AAS effect. Here the interference occurs after the complete revolution around the loop of two time-reversed trajectories. The periodicity in enclosed flux is thus twice smaller $\Delta\phi = h/2e$. 117
5.26 Top view SEM image of the HgTe ring grown by SAG used in the magneto-transport measurements. The indicated dimensions are the lithographic ones. 120
5.27 Four-terminal conductance of the HgTe nanoring. (a) Conductance as a function of the magnetic field at three different temperatures. The oscillating background due to the UCF is computed by application of a Savitzky-Golay filter. (b) Conductance oscillations as a function of the magnetic field in unit of the expected magnetic period $\Delta B_{AB} = 8.45$ mT at 280 mK after removing the background. The red curve shows a combination of h/e and $h/2e$ oscillations extracted around zero magnetic field. The blue curve displays only h/e oscillations extracted a higher field. Curves are vertically offset to enhance clarity. 121

5.28 Temperature dependence of the conductance oscillations in the HgTe nanoring. (a) Evolution of the AB oscillations as the temperature is increased. Curves are vertically shifted to enhance clarity. (b) The corresponding standard deviations as displayed as a function of the temperature. 122
5.29 (a) FFT spectra of the AB oscillations for each temperature. The solid vertical line represent the magnetic frequency calculated from the expected magnetic period. The two vertical dashed lines represent the calculated frequencies considering the inner and outer sides of the ring. The first harmonic peaks h/ne are shown. (b) Corresponding length of the ring side from the maximum amplitude extracted from the FFT spectrum. The red lines respectively represent the minimal and maximum length of the ring sides from the designed pattern. 123
5.30 The change of the FFT area (black squares), the FFT amplitude (blue triangle) and the rms of the AB oscillations (red dots) as a function of the temperature. Each curve is fitted to the diffusive (solid line) and ballistic (dashed line) models. 124

A.1 Schematic of an AFM tool operating in tapping mode 134
A.2 Sketch of an XRD setup with interaction between X-Rays and the crystal lattice. Adapted from [Charpentier, 2012] 135
A.3 (a) TEM column with the convergent electron beam focusing on the sample. Bright Field detector measures the directly transmitted electron beam. High Angle Annular Dark Field detector collects the electrons scattered at high angle. The Energy Dispersive X-rays spectrometer (EDX) collects the photoelectrons. (b) A typical TEM diffraction pattern. The brightest spot in the center corresponds to the direct beam. The others evidence crystallographic axis. Taken from [Thomas, 2016]. 137
A.4 (a) Sketch illustrating the beam precession during nanobeam precession electron diffraction and the collection of obtained diffraction spots. Taken from [Thomas, 2016]. Typical diffraction pattern obtained in CdTe along the $\langle 1\bar{1}0\rangle$ axis The disk in g0 is the central disk. Disks in g1 and g2 correspond to $\langle 111\rangle$ diffraction type. 138

B.1 Mapping of different physical properties of 50 nm-wide $\langle 1\bar{1}0\rangle$-oriented NW obtained by NPED in transversal cross-section. In panel (a) the strain is represented along the (left) [110] in-plande direction and (right) the growth direction [001]. Below, in (b), the maps respectively illustrates the rotation and the shear. The scale bar represents 10 nm. 140
B.2 Surface state and morphology of HgTe nanostructures grown on InSb(001) substrate. (a) AFM image showing the top surface of the HgTe layer in a 2D-like opening. (b) AFM image of a NW grid. (c) Comparison of the morphology between [110]-and $[1\bar{1}0]$-oriented NWs. (d) Comparison of the morphology between 50 nm- and 100 nm-wide NWs. (e) SEM image of a NW grid with a 2 hours exposition to H_2 plasma before growth. 141
B.3 Sketch of layers arrangement for the selective growth of HgTe with a InSb(001) substrate. 142
B.4 Growth of CdTe on patterned CdTe substrate to study the selectivity with respect to a silicon dioxide mask. 143

B.5 Study of selective area epitaxy on CdTe(111) substrate. (a) Al_2O_3 + SiO_2 mask preparation. The substrate top surface in the openings is very rough and of poor quality. (b) Attempt of HgTe SAG. The parasitic growth on the mask is abundant (see Section 5 in main text for explications) and HgTe layers in the openings are far from satisfying. 143

C.1 Panel (a) illustrates the longitudinal resistance R_{xx} of the Hall bar as a function of the gate voltage in the absence of magnetic field. (b) Variation of the transversal resistance R_{xy} at zero magnetic field and at $B = 0.1$ T. Panels (c) and (d) respectively display the carrier density and the mobility as a function of the gate voltage. Data are extracted from measurements at $B = 0.1$ T. In (c) the dashed line represent the depleting factor of the electron side. 145

C.2 Longitudinal resistance R_{xx} and transversal conductance G_{xy} for the samll Hall bar with dimensions $L = 15$ μm/$W = 3$ μm. Data are plotted as a function of the filling factor. Measurements are performed at 1.5 K and at zero gate voltage. 147

C.3 Comparison of the longitudinal resistance R_{xx} of the two Hall bars fabricated during the same SAG process. The two devices have been measured at 1.5 K and zero gate voltage. 147

List of tables

3.1 Presentation of the different devices geometries and their dimensions, length L and width W. For nanorings, r is the inner radius of the circular rings and c is the inner side length of the diamond rings. 45

5.1 Phase coherence lengths in the HgTe nanoring extracted from the different quantities for the diffusive model $l_\phi = pb^{-1}T^{-1/2}$ where $p = 2800$ nm is the ring perimeter. 125

5.2 Determination of the phase coherence length l_ϕ and its temperature law based on different devices and methods. 126

Introduction Générale

L'électronique est au cœur de la société moderne. Elle est présente dans un large éventail d'activités allant de la santé à la communication, en passant par le stockage de données. L'importance de cette technologie a augmenté de manière exponentielle au cours des dernières décennies. Un facteur essentiel pour cette avancée technologique a été la loi de Moore. En 1965, le co-fondateur d'Intel avait en effet prédit que le nombre de transistors sur une puce doublerait tous les deux ans grâce aux progrès technologiques, et ce sans augmentation de prix. De nos jours, des milliards de transistors de taille nanométrique peuvent être intégrés sur une puce, donnant lieu à des dispositifs aux propriétés remarquables. Cependant, cette trajectoire a désormais atteint ses limites fondamentales. A mesure que les dimensions des transistors se rapprochent de l'échelle atomique, la réduction supplémentaire de la longueur de canal est freinée par des effets quantiques, l'effet tunnel, le bruit quantique, mais aussi la dissipation thermique et les contraintes de fabrication. Parallèlement, la demande toujours croissante en ressources de calcul et en fonctionnalités avancées a entraîné une hausse considérable de la consommation énergétique. La société fait désormais face à des défis technologiques et environnementaux. Cette convergence des limites physiques et des coûts énergétiques met en évidence la nécessité d'un changement de paradigme dans le traitement de l'information.

De nouvelles technologies reposant sur les effets quantiques apparaissent comme des solutions très prometteuses pour révolutionner notre manière de communiquer. Les limites quantiques sont désormais envisagées comme des ressources plutôt que comme des obstacles, ouvrant la voie à des modes totalement nouveaux de traitement de l'information.

La solution la plus connue est celle de l'informatique quantique. D'un côté, les ordinateurs classiques fonctionnent avec des transistors codant l'information à l'aide de chiffres binaires, appelés bits, leur valeur est contrainte à être soit 0 soit 1. De l'autre côté, les processeurs quantiques utilisent des bits quantiques, ou qubits, qui peuvent exister dans des superpositions d'états $|0\rangle$ et $|1\rangle$, et s'intriquer. Alors qu'un système classique à N bits stocke l'information dans N coefficients, un système quantique à N qubits peut exister dans n'importe laquelle des 2^N combinaisons possibles. Cela améliore considérablement la puissance de calcul des systèmes quantiques, qui traitent l'information en parallèle. Ils pourraient donc être la clef pour résoudre des problèmes que les ordinateurs classiques ne peuvent traiter efficacement, comme la simulation de matériaux quantiques complexes, la

recherche d'algorithmes d'optimisation, ou la communication sécurisée. Bien qu'encore à ses débuts, l'informatique quantique promet de révolutionner des domaines variés allant de la science des matériaux et la découverte de médicaments à l'intelligence artificielle et la cryptographie, et constitue ainsi un sujet de premier plan aussi bien pour la recherche académique qu'industrielle.

Plusieurs plateformes matérielles sont actuellement explorées pour réaliser des ordinateurs quantiques. Le concept de temps de cohérence est au cœur de ces plateformes : l'état quantique doit rester cohérent pendant le calcul, sans quoi des erreurs apparaissent. Pour atteindre un temps de cohérence suffisamment long, le dispositif doit être isolé des perturbations environnantes, tout en permettant l'accès et la manipulation de l'information. L'objectif majeur est donc de trouver le meilleur compromis. Parmi les plateformes étudiées, les qubits supraconducteurs, basés sur des jonctions Josephson, sont à l'avant-garde du développement industriel grâce à leurs temps de communication rapide et à leur intégration avec les techniques existantes de microfabrication. Les atomes froids, les ions piégés, les qubits de spin, et les qubits photoniques constituent également des pistes explorées [De Leon, 2021].

Au-delà, les qubits topologiques basés sur les modes zéro de Majorana (MZMs) sont apparus comme un candidat particulièrement attrayant, car leur encodage non local de l'information quantique devrait offrir une protection intrinsèque contre la décohérence. Ils permettraient ainsi de surmonter une des principales difficultés dans la construction de processeurs quantiques fiables, en ouvrant la voie vers des qubits tolérants aux fautes (fault-tolerant) [Aguado, 2020 ; Marra, 2022]. L'intérêt pour les MZMs provient de leurs propriétés uniques : ils sont leurs propres antiparticules et obéissent à une statistique d'échange non-Abélienne, contrairement aux fermions ou bosons conventionnels. La démonstration et le contrôle des MZMs constitueraient donc une étape décisive vers l'informatique quantique topologique évolutive. Les MZMs sont prédits à exister aux extrémités de supraconducteurs topologiques unidimensionnels, tels que les nanofils semiconducteurs/supraconducteurs hybrides, grâce à une combinaison d'effet Zeeman, de couplage spin-orbite et d'un gap supraconducteur dur induit par proximité. Toutefois, malgré des signatures expérimentales prometteuses, comme des pics de conductance à polarisation nulle, l'identification non ambiguë des modes zéro de Majorana reste un défi [Vaitiekėnas, 2018a ; Op het Veld, 2020 ; Zhang, 2023 ; Zhang, 2018]. Distinguer les états topologiques véritables des excitations triviales de basse énergie est un objectif clef, et des progrès continus en qualité des matériaux, conception des dispositifs et techniques de mesure sont essentiels pour établir les MZMs comme base fiable pour les technologies quantiques.

En parallèle, la spin-orbitronique offre une autre voie pour dépasser les limitations fondamentales de l'électronique conventionnelle, en exploitant l'interaction entre charge et spin des électrons via le couplage spin-orbite (SOC) [Wang, 2025]. L'avantage majeur de cette approche réside dans sa capacité à échanger entre les degrés de liberté de charge et de spin, permettant la génération et la manipulation purement électriques de courants

de spin sans nécessiter d'éléments ferromagnétiques. Les plateformes spin-orbitroniques peuvent atteindre un fonctionnement à faible consommation et de nouvelles fonctionnalités en utilisant le SOC pour générer et manipuler directement les courants de spin à partir de courants de charge, permettant des effets tels que l'effet Hall de spin, la conversion Rashba-Edelstein, et la commutation efficace par couple de spin [Hoffmann, 2015]. Le contrôle du spin pourrait ainsi être directement intégré dans les architectures électroniques standards. La réalisation de tels dispositifs nécessite des matériaux combinant un SOC intrinsèque fort, une mobilité électronique élevée, et de grandes longueurs de cohérence de spin, afin que l'information de spin puisse être générée et préservée à l'échelle pertinente des dispositifs. Bien que le potentiel de la spin-orbitronique soit largement reconnu, sa concrétisation dépend de manière critique de la capacité à mettre en œuvre des plateformes matérielles adaptées dans des nanostructures évolutives et à démontrer la préservation de la cohérence quantique à l'échelle nanométrique.

Le développement de plateformes pour les technologies quantiques nécessite donc des matériaux combinant simultanément une forte mobilité, un couplage spin-orbite élevé, et une excellente qualité cristalline. Les semi-conducteurs tels que InAs, InSb et HgTe sont des candidats de premier plan. Parmi eux, HgTe se distingue par son SOC élevé, sa grande mobilité et sa structure de bande ajustable, passant de normale à inversée, permettant une manipulation efficace du spin et la réalisation de phases topologiques. Son caractère topologique, établi par la découverte de l'effet Hall quantique de spin dans les puits quantiques HgTe/CdTe [Konig, 2007a], puis confirmé par l'ARPES [Crauste, 2013] et les études de magnéto-transport dans des structures tridimensionnelles [Thomas, 2017], constitue un atout supplémentaire en protégeant les états de surface contre la rétro-diffusion.

Malgré ces propriétés remarquables, HgTe reste difficile à intégrer à l'échelle nanométrique en raison de sa fragilité aux procédés technologiques et aux contraintes de croissance. Ce défi a longtemps empêché la réalisation de dispositifs quantiques robustes à base de HgTe. Toutefois, sa polyvalence pourrait être encore renforcée par la croissance sélective (selective area growth, SAG), une approche prometteuse pour la fabrication de nanostructures planaires avec une géométrie et une disposition précises. En permettant l'intégration évolutive de dispositifs unidimensionnels, la SAG offre une voie directe vers des circuits quantiques avancés et des architectures spin-orbitroniques.

Dans ce contexte, le projet ANR-INSPIRING (21-CE09-0026-01) vise à explorer l'épitaxie sélective de semi-conducteurs III-V et II-VI présentant un fort couplage spin-orbite, dans le but de fabriquer et caractériser des nanofils planaires servant de base à la manipulation cohérente du spin dans des dispositifs spin-orbitroniques, ainsi qu'à la réalisation de jonctions supraconductrices topologiques. Ce travail repose sur les efforts conjoints du CEA-Leti, de l'Institut d'Électronique, de Microélectronique et de Nanotechnologie (IEMN), et de l'Institut Néel. Cette thèse se concentre sur les nanostructures de HgTe. L'objectif majeur est la réalisation de nanostructures planaires de HgTe grâce à la SAG,

ainsi que la caractérisation du transport électronique dans ces nanodispositifs.

Le premier chapitre de ce manuscrit, Chapitre 1, introduit la structure de bande du HgTe ainsi que les techniques épitaxiales pour la croissance unidimensionnelle de nanofils dans le contexte du transport quantique. Le Chapitre 2 met en évidence la croissance de nanostructures planaires de HgTe obtenues par SAG. Une étude approfondie est présentée, avec l'influence de différents paramètres de croissance : vitesse de croissance, température, épaisseur déposée et orientation cristalline. Différents procédés de fabrication de masques sont analysés. La qualité cristalline des nano-objets est évaluée grâce à des images de microscopie électronique en transmission. Les différents mécanismes de croissance sélective sont identifiés. Enfin, la configuration retenue pour la fabrication des dispositifs est présentée. Au Chapitre 3, nous présentons le procédé de nanofabrication des dispositifs. Le rôle de chaque étape technologique est décrit ainsi que son adaptation pour du HgTe. Ensuite, le Chapitre 4 débute par l'introduction du dispositif expérimental pour les mesures de magnéto-transport à basse température. Une analyse complète des caractéristiques de transport d'une barre de Hall micrométrique. Ce chapitre permet la preuve de concept de la fabrication de dispositifs à partir d'épitaxie sélective de couches de HgTe. Les principales caractéristiques du transport électronique, telles que la densité de porteurs, la mobilité électronique et le libre parcours moyen élastique, sont évaluées. Enfin, le Chapitre 5 explore le transport électronique dans des nanostructures quasi-1D à travers l'étude détaillée d'un nanofil et d'un nano-anneau. Les phénomènes d'interférences quantiques sont précisément étudiés pour évaluer la longueur de cohérence de phase et le régime de transport.

General Introduction

Electronics is at the core of modern society. It plays a central role in a wide range of activities spanning from healthcare to communication and data storage. The importance of this technology has increased at an exponential pace for the last decades. A key driver for this technological breakthrough has been Moore's law. In 1965, the co-founder of Intel indeed predicted that the number of transistors on a chip will double every two years just thanks to technological progress, and so without increasing its price. Nowadays, billions of nanometer-size transistors can be embedded on a chip, yielding devices with outstanding properties and power. However, this trend has now reached its fundamental limits. As transistor dimensions approach the atomic scale, further reduction in channel length is hindered by quantum effects, electron tunneling, quantum noise, but also heat dissipation and fabrication constraints. At the same time, the ever-increasing demand for computational resources and enhanced functionalities has led to a tremendous rise in energy consumption, and society is now facing both technological and environmental challenges. This convergence of physical limits and energy costs highlights the need for a paradigm shift in information processing.

New technologies relying on quantum effects stands as very promising solutions to revolutionize the way we communicate. Quantum limits are now seen as resources rather than obstacles, enabling radically new ways of processing information.

The most widely known solution is quantum computing technology. On the one hand, classical computers operate with transistors coding the information using binary digits, known as bits. Their value is then constrained to be either 0 or 1. On the other hand, quantum processors use quantum bits, qubits, which can exist in superpositions of states $|0\rangle$ and $|1\rangle$, and become entangled. Where an N-bit classical system stores information in N coefficients, a N-qubit quantum system can exist in any of the 2^N possible combinations. This drastically improves the computational power of quantum systems that process information in parallel. Therefore, they could be the key to address problems that classical computers cannot efficiently solve, such as simulating complex quantum materials, finding optimization algorithms, or secure communication. While still in its early age, quantum computing holds the promise of revolutionizing diverse areas ranging from materials science and drug discovery to artificial intelligence and cryptography, and thus stands a hot topic in both academic and industrial research.

Several hardware platforms are currently being pursued to realize scalable quantum computers. The concept of coherence time lies at the core of these fabrication platforms, the quantum state needs to remain coherent during computation otherwise it results in error. To achieve a sufficiently long coherence time, the device must be well isolated from external perturbations. At the same time, however, it needs to remain accessible for information readout and manipulation. A major challenge is therefore to find the optimal compromise between isolation and control. Among the investigated hardware platforms, superconducting qubits, based on Josephson junctions, are at the forefront of industrial development due to their fast gate times and integration with existing microfabrication techniques. Cold atoms, trapped ions, spin qubits, and photonic qubits are also part of the exploratory paths [De Leon, 2021].

Beyond these, topological qubits based on Majorana zero modes (MZMs) have emerged as a particularly appealing candidate, since their non-local encoding of quantum information is expected to provide intrinsic protection against decoherence. Thus, it would overcome one of the major difficulties in building reliable quantum processors, offering a pathway toward fault-tolerant qubits [Aguado, 2020 ; Marra, 2022]. The interest in MZMs arises from their unique properties : they are their own antiparticles and obey non-Abelian exchange statistics, unlike conventional fermions or bosons. Demonstrating and controlling MZMs would thus represent a decisive step toward scalable topological quantum computation. MZMs are predicted to exist at the ends of one-dimensional topological superconductors, such as hybrid semiconductor/superconductor nanowires, due to a combination of Zeeman splitting, spin-orbit coupling, and a proximity-induced hard superconducting gap. However, despite promising experimental signatures, such as zero-bias conductance peaks, the unambiguous identification of Majorana zero modes remains challenging [Vaitiekėnas, 2018a ; Op het Veld, 2020 ; Zhang, 2023 ; Zhang, 2018]. Distinguishing genuine topological states from trivial low-energy excitations is a key objective, and continued progress in material quality, device design, and measurement techniques is essential to establish MZMs as a practical resource for quantum technologies.

In parallel, spin-orbitronics offers another pathway to overcome the fundamental limitations of conventional electronics by taking advantage of the interplay between electron charge and spin through spin-orbit coupling (SOC) [Wang, 2025]. The significant advantage of this approach lies in its ability to swap between charge and spin degrees of freedom, enabling purely electrical generation and manipulation of spin currents without the need for ferromagnetic elements. Spin-orbitronic platforms can achieve low-power operation and new functionalities by using SOC to generate and manipulate spin currents directly from charge currents, enabling effects such as the spin Hall effect, Rashba-Edelstein conversion, and efficient spin-torque switching [Hoffmann, 2015]. Thereby, spin control could directly be embedded into standard electronic architectures. The realization of such devices requires materials combining strong intrinsic SOC, high carrier mobility, and long spin-coherence lengths, so that spin information can be both generated and preserved

over relevant device scales. While the potential of spin-orbitronics is widely recognized, its realization critically depends on the ability to implement suitable material platforms into scalable nanostructures and to demonstrate the preservation of quantum coherence at the nanoscale.

Developing platforms for quantum technologies therefore requires materials that simultaneously combine high mobility, strong spin-orbit coupling, and excellent crystalline quality. Semiconductors such as InAs, InSb, and HgTe are leading candidates. Among them, HgTe stands out thanks to its large SOC, high mobility, and tunable band structure, from normal to inverted, enabling efficient spin manipulation and the realization of topological phases. Its topological character, established by the discovery of the quantum spin Hall effect in HgTe/CdTe quantum wells [Konig, 2007a], and later confirmed by ARPES [Crauste, 2013] and magneto-transport studies in three-dimensional structures [Thomas, 2017], provides an additional advantage by protecting surface states against backscattering. Despite these remarkable properties, HgTe remains difficult to integrate at the nanoscale because of its sensitivity to technological processes and growth constraints. This challenge has long prevented the realization of robust HgTe-based quantum devices. However, its versatility could be further enhanced by selective area growth (SAG), a promising approach for fabricating in-plane nanostructures with precise geometry and layout. By enabling scalable integration of one-dimensional devices, SAG provides a direct route toward advanced quantum circuits and spin-orbitronic architectures.

In this context, the ANR-INSPIRING project (21-CE09-0026-01) aims at exploring selective area epitaxy of III-V and II-VI semiconductors manifesting strong spin-orbit coupling, with the goal of fabricating and characterizing in-plane nanowires as basis for coherent spin manipulation in scalable spin-orbitronic devices, and for the realization of topological superconducting junction. This work relies on the joint efforts of CEA-Leti, the Institut d'Electronique de Microélectronique et de Nanotechnologie (IEMN), and the Néel Institute. This PhD work focuses on HgTe nanostructures. The major objective is the realization of in-plane HgTe nanostructure thanks to SAG and the characterization of the electronic transport in these nanodevices.

The first chapter of this dissertation, Chapter 1, introduces the HgTe band structure as well as the epitaxial techniques for one-dimensional growth of nanowires in the context of quantum transport. Chapter 2 evidences the growth of in-plane HgTe nanostructures obtained by SAG. A comprehensive study is presented, with the influence of different growth parameters, growth rate, temperature, deposited thickness, and crystal orientation. Different mask fabrication processes are analyzed. The crystal quality of the nano-objects is assessed by transmission electron microscopy images. The different driving mechanisms of selective growth are identified. Finally, the retained configuration for device fabrication is presented. In Chapter 3, we present the nanofabrication process of the devices. The role of each technological step is presented and how it was adapted to handle the HgTe sensitivity. Then, Chapter 4 starts by introducing the experimental set-up for the

magneto-transport measurements at low temperature. A comprehensive analysis of the transport characteristic of a micro-scale Hall bar is presented. This chapter enables the proof of concept of the device fabrication from selective epitaxy of HgTe layers. The main characteristic of the electronic transport, such as the carrier density, the electron mobility, and the elastic mean free path are assessed. Finally, Chapter 5 explores the electronic transport in quasi-1D nanostructures through the detailed magneto-transport study of a nanowire and a nanoring. The quantum interference phenomena are thoroughly studied to assess the phase coherence length and the transport regime.

Chapter 1

In-plane nanostructures for quantum physics

1 Introduction

The ability to manipulate individual quantum states lies at the heart of revolutionary quantum technologies, ranging from quantum computing and spintronics to ultra-sensitive sensors and secure communication protocols [Nielsen, 2010 ; Awschalom, 2007]. These devices promise advantages way above classical limits, such as exponential speed-up in computation, energy-efficient logic, or fundamentally unbreakable encryption. The cornerstone to all these developments is the requirement to maintain and control quantum coherence : the preservation of phase information in quantum states as they evolve.

To operate those devices efficiently and reliably, one must enter the *phase coherent regime*, where electrons propagate through the system without losing their quantum phase [Imry, 2002 ; Datta, 1997]. In this regime, the transport is not classical, but instead governed by wave-like interference, revealing the quantum behavior of the electrons. The phase coherence length l_ϕ defines the typical scale over which an electron preserves its phase, and so coherent quantum effects dominate. This regime is not only essential for enabling quantum logic operations and coherent transport [Beenakker, 1991], but also of primary interest for probing quantum interference effects and studying the quantum-classical transition in condensed matter systems. Interference phenomena such as weak localization, universal conductance fluctuations, and Aharonov-Bohm oscillations arise in this regime and serve as sensitive diagnostics of decoherence mechanisms, electron interactions, and the topological nature of materials [Altshuler, 2012 ; Washburn, 1986 ; Bergmann, 1984].

The road to achieve controllable phase coherent regime is intrinsically bound to one dimensional (1D) objects as they offer remarkable perspectives of study and manipulation of quantum interference effects. The main reason is the natural longer phase coherence lengths exhibited by 1D systems compared to their 2D or 3D counterparts. In (quasi-)1D systems such as nanowires, reduced dimensionality limits the phase space available for inelastic scattering processes like electron-electron or electron-phonon interactions. As a

consequence, the dephasing rate is greatly reduced compared to higher-dimensional systems. This manifests particularly in the temperature dependence of the phase coherence time : in 1D diffusive conductors, the dominant dephasing mechanism leads to a scaling of the form $\tau_\phi^{-1} \propto T^{2/3}$, slower than in 2D or 3D systems where $\tau_\phi^{-1} \propto T$ or $\tau_\phi^{-1} \propto T^{3/2}$, respectively. As temperature decreases, this slower divergence allows the phase coherence length $l_\phi = \sqrt{D\tau_\phi}$ to become significantly longer, thereby enhancing the manifestation of quantum corrections to conductance [Altshuler, 2012 ; Altshuler, 1982]. In addition, the simple geometry of quasi-1D conductors reduces the number of available interference paths, yielding more reproducible and analyzable signatures of quantum coherence. Furthermore, nanostructures are easy to incorporate for device fabrication. This provides efficient gate tunability of the carrier density and crucial experimental control [Doh, 2005]. Finally, in the context of the ongoing and intense pursuit of Majorana zero modes for topologically protected qubits, one-dimensional geometries offer a key advantage : their compatibility with hybrid architectures that integrate superconductors and magnetic materials. This makes them particularly suitable for engineering topological superconducting phases [Lutchyn, 2018]. These combined advantages have set 1D semiconductor platforms as a cornerstone of modern quantum transport and quantum information research. This unique geometry allowing for cleaner signatures of quantum coherence.

The central role of phase coherence and the advantages of one-dimensional systems have now been presented. A particularly promising direction for innovative solutions lies in the development of spin-manipulation-based devices. These devices aim to harness the electron spin degree of freedom as a quantum resource for information processing, storage, or sensing. Achieving precise and robust spin control requires not only materials with strong spin-orbit coupling (SOC), but also the preservation of quantum phase coherence throughout the device. Without phase coherence, spin states rapidly degrade due to scattering and decoherence, undermining the reliability of quantum operations.

One-dimensional systems offer a unique platform in which these two key ingredients reunite. In such systems, the SOC often manifests through the *Rashba effect*, which couples the electron's momentum and spin. This coupling opens the possibility of all-electrical spin control : a gate voltage can tune the electron momentum, thereby manipulating its spin orientation in a coherent and deterministic way. As a result, 1D phase-coherent conductors with strong SOC are ideal not only for exploring fundamental spin-dependent quantum interference but also key materials for future spintronic and quantum computing technologies. This approach is at the origin of many recent innovations, including electrically gated spin field-effect transistors (spinFETs) [Koo, 2009], the potential to protect spin currents via the quantum spin Hall effect (QSHE) [Konig, 2007b], and the ongoing quest for Majorana zero modes and robust topological qubits [Zhang, 2021].

A material of particular interest for the realization of such nano-devices is the mercury-telluride, HgTe, semiconductor compound with large SOC. Notably, HgTe can be grown on CdTe substrates, forming a highly attractive quasi-lattice-matched system. The lite-

rature has extensively demonstrated the remarkable properties of HgTe : it is a textbook example of a topological insulator (TI), exhibiting well-defined surface states in three dimensions [Thomas, 2017 ; Brüne, 2011 ; Kozlov, 2016], as well as quantum spin Hall states in two dimensions [Konig, 2007b]. However, a major challenge remains : developing a technological solution that enables the fabrication of complex 1D architectures based on HgTe. This material is highly sensitive and can be easily degraded by standard nanofabrication processes [Liu, 2018 ; Daumer, 2005]. To address this issue, this dissertation introduces an original technological approach, selective area growth (SAG) of HgTe nanostructures, as a way to overcome the limitations associated with 1D HgTe-based devices.

We first discuss the remarkable properties of HgTe that make it a strong candidate for 1D device applications. We then present the SAG technique, which is investigated in this work as a method for the controlled growth of HgTe-based nanostructures.

2 Physics of the HgTe/CdTe system

In the following, we present the band structure of the HgTe/CdTe system and explain how it gives rise to a topological insulator (TI), characterized by an insulating bulk and conducting surface states. HgTe and CdTe are II-VI compounds that crystallize in the zinc blende structure as represented in figure 1.1. Here, Hg and Cd atoms (displayed in blue) are organized in a face-centered cubic unit cell. Te atoms (in red) follow the same crystal organization but their unit cell is here shifted from (1/4, 1/4, 1/4)a_0, a_0 being the lattice parameter. Among semiconductors, HgTe exhibits one the largest lattice parameter, $a_{\mathrm{HgTe}} = 6.4615$ Å, while CdTe has the largest, $a_{\mathrm{CdTe}} = 6.4815$ Å. Due to crystal symmetries, their band structure is centered at the center of the Brillouin zone at the Γ point. Their energy bands are a combination of s- and p-states, originating respectively from Hg/Cd atoms and from Te atoms.

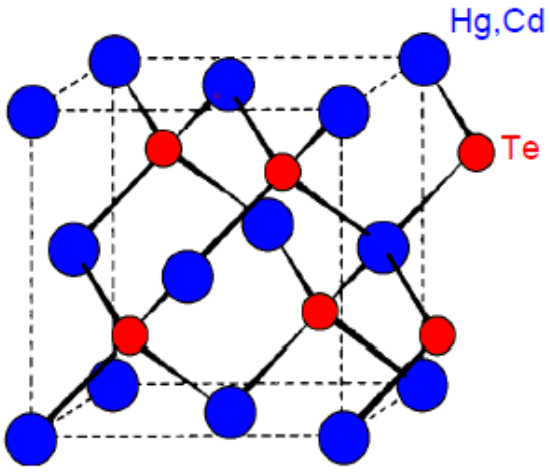

FIGURE 1.1 – Schematic representation of the HgTe and CdTe zinc-blende crystal structure. Taken from [Thomas, 2016].

In addition, these materials are characterized by a strong spin-orbit coupling (SOC) $\Delta_{SO} = 1.08$ eV from [Chu, 2009], that is of particular interest in the context of the project. Besides, large spin orbit interaction is known to alter the band structure of materials. Here, they lead to mixing of the band structure, creating the conditions for exotic physics of the TI.

2.1 Band structure

The derivation of CdTe and HgTe band structures will not be presented here. The reader is invited to refer to [Thomas, 2016] for a precise analysis of the band structure determination. The Kane model, relying on the $k \cdot p$ theory, is used to describe CdTe and HgTe band structures. Bernevig *et al.* have shown that the electronic states in the vicinity of the Γ point are described by a relativistic Dirac equation [Bernevig, 2006]. In this work, we will only describe the main corrections altering the unperturbed Hamiltonian and how

they modify the energy level of the bands. Two relativistic terms are responsible for major alteration of the band structure with respect to an unperturbed Hamiltonian. The first is the mass-velocity correction. The second is the spin-orbit coupling. The total Hamiltonian of the system can therefore be written as :

$$H = H_I + H_{mv} + H_{SO} \tag{1.1}$$

where,

$$\begin{cases} H_I = \frac{p^2}{2m_0} + V(\mathbf{r}) \\ H_{mv} = -\frac{p^4}{8m^3c^2} \\ H_{SO} = \frac{\hbar}{4m_0^2c^2}[\sigma \times \nabla V] \cdot \mathbf{p} \end{cases} \tag{1.2}$$

and $\mathbf{p} = -i\hbar\nabla$ is the electronic momentum, $\hbar k$ is the crystal momentum, $V(\mathbf{r})$ is the periodic crystal potential and σ are the Pauli matrices.

The effect of the mass-velocity term is found to shift the bands toward lower energies [Chu, 2008 ; Franz, 2013]. The effect is not the same for s- and p-type electrons, it is at least five times larger for s-type electron [Cohen-Tannoudji, 1986]. Hg have a higher atomic mass than Cd, $\mathrm{Z_{Hg}} = 80 > \mathrm{Z_{Cd}} = 48$, the mass-velocity term is thus expected to be much more pronounced in HgTe compared to CdTe.

Considering the spin-orbit interaction, one can find that it mainly alters the p-type bands : the Γ_{15} bands are lifted into the four-fold degenerated Γ_8 bands and the two-fold degenerated Γ_7 band. The Γ_8 bands correspond to the light (LH) and heavy (HH) hole bands. Γ_7 accounts for the split-off band. Γ_8 and Γ_7 are separated by the strong spin-orbit coupling induced gap, Δ_{SO}.

The consequences of these two relativistic corrections are presented in figure 1.2. We recall that the Γ_8 band is degenerated at the Γ point with the light holes and heavy holes bands. On one hand, CdTe displays the band structure of a conventional semiconductor, which means a normal band ordering, $\Gamma_7 - \Gamma_8 - \Gamma_6$ as the energy increases, see figure 1.2(a). CdTe thus shows a positive energy gap, $\mathrm{E}_g = 1.6$ eV. On the other hand, HgTe shows an inverted band structure, the Γ_6 band is brought down below the Γ_8 band, see figure 1.2(b). Here, the gap is found to be negative, $\mathrm{E}_g = -0.3$ eV. Therefore, it is the addition of these two relativistic terms that is at the origin of the inverted band structure of HgTe, a peculiar characteristic of this material, that is of major importance for the subband structure of HgTe quantum well.

2.2 Quantum well and band inversion

HgTe and CdTe materials form a highly attractive quasi-lattice-matched system. The lattice mismatch if small enough, $f = -0.3$ %, to authorize the growth of strained HgTe layers on CdTe substrate without misfit dislocation at the interface. The non-trivial band ordering of HgTe is at the core of the stunning properties of HgTe quantum wells. Nevertheless, for quantum well thinner than $d_c \approx 6.3$ nm, the band ordering is that of a

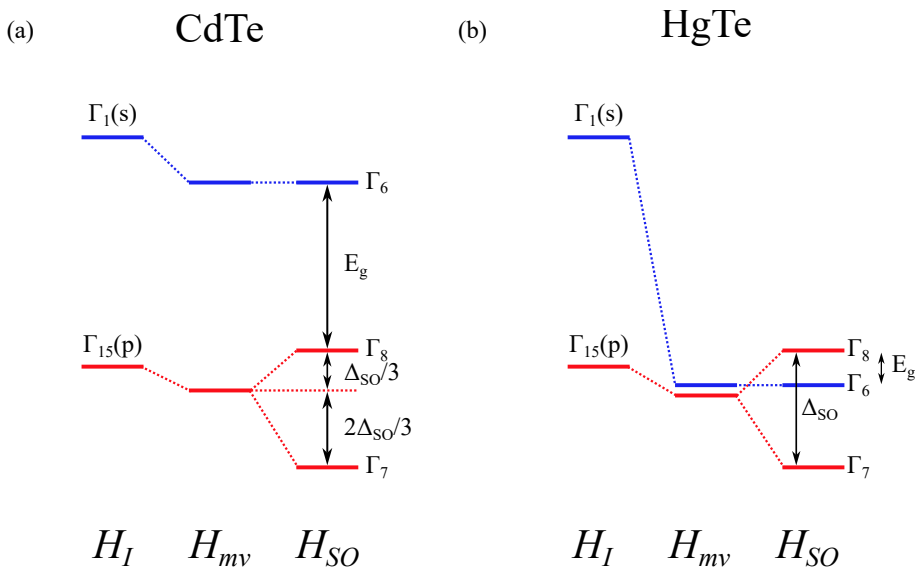

FIGURE 1.2 – Schematic representation of the energy bands at the Γ point of (a) CdTe and (b) HgTe. The alteration of the energy bands from the unperturbed Hamiltonian (H_I) due to relativistic effects : the mass-velocity (H_{mv}) and spin-orbit (H_{SO}) corrections. Adapted from [Chu, 2008].

conventional semiconductor, the lowest electron band lying above the highest hole band. As the HgTe layer thickness increases, the Γ_8-derived subbands, labeled H in the following because they correspond to hole-like subbands in conventional semiconductors, is pushed towards higher energies because of quantum confinement and thus rise above the Γ_6-derived subbands, denoted E. This principle is shown in figure 1.3, where only the thick quantum well, $d > d_c$, shows an inverted band structure.

Büttner *et al.* calculated the dependence of the E_1 subband as a function of the well thickness, as visible in figure 1.4. It was found that the energy of the electron-like subband E_1 decreases with increasing quantum well thickness, whereas the hole-like subbands H_i shift to higher energies. As a result, for a well thickness of $d = 14\,\text{nm}$, E_1 can lie not only below H_1 but also below higher-order hole subbands such as H_4. At the critical thickness $d_c \approx 6.3\,\text{nm}$, the lowest conduction subband E_1 crosses the highest valence subband H_1, resulting in the closure of the band gap. Beyond this point, as the quantum well becomes thicker, the gap reopens with an inverted band ordering, marking the transition to a non-trivial topological phase. This band inversion, a direct consequence of the intrinsically inverted band structure of HgTe, is essential for the emergence of the quantum spin Hall effect.

Gapless metallic edge states are formed at the interface between regions of trivial and non-trivial topology, i.e., at the boundary between CdTe and HgTe. These edge states originate from the band inversion and ensure continuity between the *s*-type conduction band of CdTe and the *p*-type valence band of HgTe, since CdTe has a normal (positive) band gap while HgTe exhibits an inverted (negative) band gap. This phenomenon exemplifies the principle of bulk-boundary correspondence. Figure 1.5 displays the band structure of HgTe and CdTe with the gapless states that allow band continuity. The resulting edge

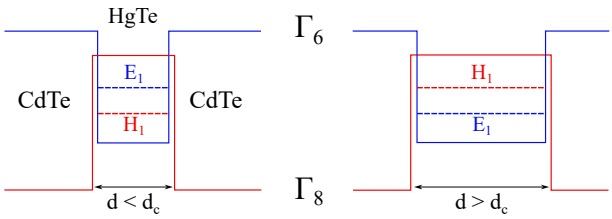

FIGURE 1.3 – Representation of the two main subbands in a CdTe/HgTe/CdTe QW. On the left hand side, $d < d_c$ so the well in the normal regime, $E_1 > H_1$. On the right hand side, we show the inverted regime, $E_1 < H_1$, reached when $d > d_c$. Adapted from [Bernevig, 2006]

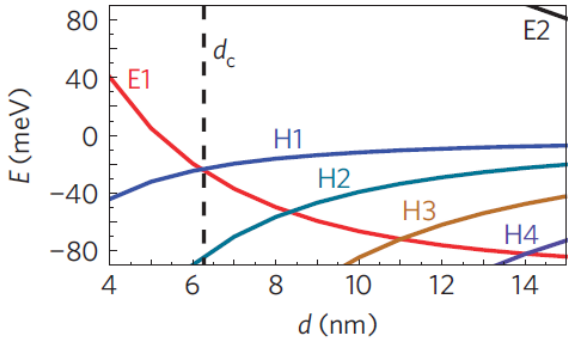

FIGURE 1.4 – Subband energies of $HgTe/Hg_{0.3}Cd_{0.7}Te$ quantum wells as a function of the well thickness, d. Taken from [Büttner, 2011].

states exist across the bulk gap and are helical : they exhibit spin-momentum locking, where two counter-propagating channels exist at each edge, each associated with a specific spin orientation, as experimentally shown [Konig, 2007b].

This section has presented the specificity of the HgTe/CdTe system : because of the inverted band structure of HgTe, one can access a non-trivial topological phase and so realize a 2D topological insulator, also know as the quantum spin Hall insulator [Konig, 2007b ; Bernevig, 2006]. In this regime, the bulk is insulating and the transport occurs thanks to helical edge states. But HgTe/CdTe can also be used to realize a 3D topological insulator [Thomas, 2017 ; Brüne, 2011 ; Kozlov, 2016]. In the 3D regime, the bulk gap originates from the strain of the HgTe lattice grown on a CdTe substrate. This situation lies outside the scope of the present work as we essentially focus on in-plane nanostructures with limited thickness. For such structures, the thickness is too small for strain alone to push the H_1 band above the E_1 band. Although strain is still expected to be present in the thin layers investigated here, it is not sufficient to open the gap ; instead, the dominant mechanism remains the quantum confinement in the well.

2.3 HgTe-based devices

The stunning properties of the HgTe/CdTe system have been widely studied and experimentally demonstrated. Its potential for the development of innovative concepts cannot to be neglected. Nevertheless, the fabrication of HgTe-based nano-devices remains challenging due to the material extreme sensitivity to conventional nanofabrication techniques.

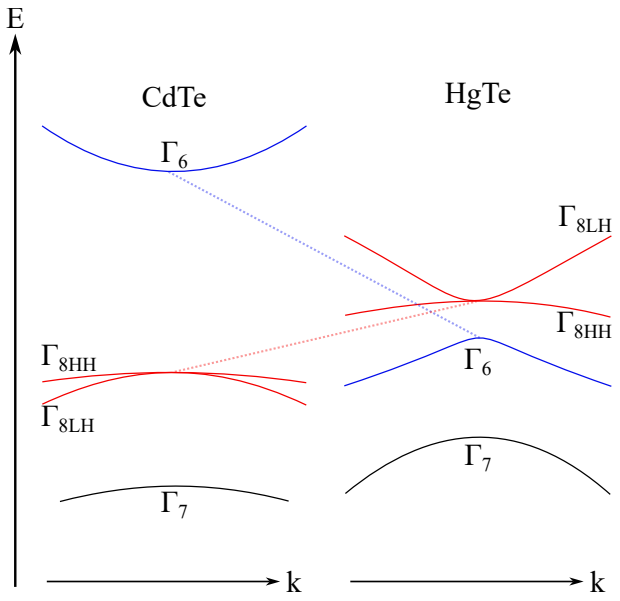

FIGURE 1.5 – Sketch of the CdTe and HgTe band structure in the vicinity of the Γ point. Adapted from [Bernevig, 2006]. When the HgTe layer is thick enough, above d_c, gapless surface state arise at the interface between CdTe and HgTe to ensure band continuity. These states are represented by the dashed lines.

For instance, dry etching introduces electrically active defects, compromising device performance [Liu, 2018 ; Bendias, 2018]. Furthermore, high-resolution electron beam lithography can lead to charge accumulation or even mercury desorption due to local heating effects.

Recent reports have demonstrated the definition of HgTe nano-objects via combination of electron beam lithography and wet etching [Bendias, 2018 ; Ziegler, 2018 ; Shekhar, 2023 ; Daumer, 2005]. These works report promising results but the fabrication technique suffer from limited dimensional control and poor scalability. Other groups have explored the direct growth of one-dimensional HgTe structures. For example, Haakenaasen et al. proposed the growth of HgTe nanowires (NWs) on silicon using gold droplets as catalysts [Selvig, 2006 ; Haakenaasen, 2008b ; Haakenaasen, 2008a]. However, this technique is not suitable for HgTe as the gold particles only function as nucleation sites. So the NWs suffer from poor dimension and orientation control. Moreover, this technique lacks of scalability and geometric flexibility ; it requires NW manipulation for device preparation, and interconnections of only a few NWs are possible. As a result, no convincing data on electronic transport in HgTe-based nano-objects have been reported to date.

In this project, we propose a different strategy : the direct growth of HgTe nanostructures on pre-patterned CdTe substrates. This approach enables the formation of controlled, in-plane, one-dimensional objects at the nanometer scale, thanks to the selective growth of HgTe.

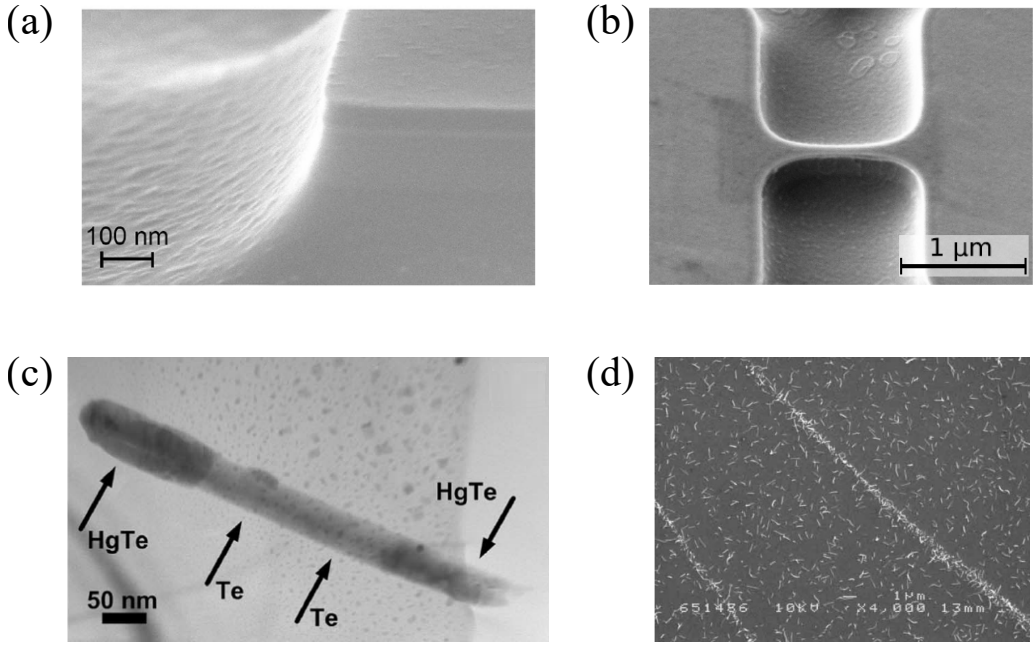

FIGURE 1.6 – Examples of HgTe structures obtained by wet etching techniques or directly as 1D growth. (a) SEM image of a wet-etched mesa. The 7.5 nm HgTe QW is visible as a bright layer [Bendias, 2018]. (b) SEM micrograph of a representative HgTe nanowire. It has a length of 1.3 μm and a median width of 163 nm. (c) TEM image of a HgTe- and Te-based nanowire grown from a Au nucleation site [Haakenaasen, 2008a]. (d) SEM image showing high density of HgTe nanowires grown on Si substrate [Selvig, 2006].

3 Epitaxy of low-dimensional structures

Before focusing on the selective area growth (SAG) technique, we briefly review conventional epitaxial methods and several approaches used to grow low-dimensional structures. Epitaxy refers to the process of growing a crystalline layer in a controlled, layer-by-layer, way on a crystalline substrate. The substrate serves as a structural template : the incoming atoms, later referred to as adatoms, impinge on its surface and form chemical bonds that replicate its crystal lattice. This process enables the fabrication of high-quality semiconductor crystals with precise control over composition and thickness. There are two main classes of epitaxy : homoepitaxy, where the substrate and the grown layer are the same material, and heteroepitaxy, where they differ. In both cases, the crystal structure and lattice parameters of the substrate guide the arrangement of the deposited atoms.

Several methods are commonly used for epitaxial growth. Chemical Vapor Deposition (CVD) technique relies on chemical reactions of gaseous precursors at the substrate surface to deposit material. It is widely used in industry due to its high throughput and compatibility with various materials. Metal-Organic Chemical Vapor Deposition (MOCVD) is a variant of CVD that uses metal-organic precursors. It is particularly suited for III-V semiconductors like GaAs or InP. Finally, Molecular Beam Epitaxy (MBE) is an out-of-equilibrium physical vapor deposition technique where beams of atoms or molecules are directed onto a heated substrate under ultra-high vacuum (UHV) conditions, the pressure inside the chamber is reduced to $\sim 10^{-10}$ mbar. Atomic or molecular fluxes are obtained by thermal evaporation or sublimation when heating the effusion cells. Thanks to the very

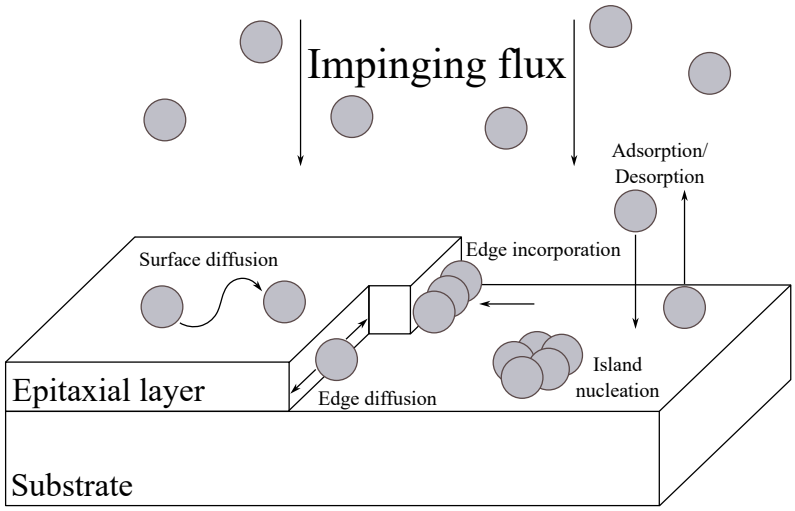

FIGURE 1.7 – Simplified representation of the different behaviors of the adatoms at the substrate surface during epitaxial growth.

low base pressure in MBE chambers, there is no interaction between the fluxes until they reach the substrate where the growth will be initiated. Different scenarios are possible for incoming atoms. The first step is their adsorption on the substrate surface. Then, they can diffuse on the surface and incorporate in energetically favorable sites, it is the nucleation. Different adatoms can create clusters which can be seen as seed for subsequent formation of nucleation sites. Multiple islands can coalesce together and ultimately form an uniform film on the surface [Böer, 2022 ; Ibach, 2013]. The behavior of adatoms is governed by the energy competition between all these possibilities. The different scenarios are illustrated in figure 1.7.

MBE ability to operate at low growth rate, in the range of 1 monolayer per second (ML/s) with high precision, enables exceptional control of the deposited thickness and the layer composition. In addition, the control over effusion cells, that can be closed individually by shutter, favors the control of interfaces and sharpness quality. This extreme work conditions makes of MBE a high precision-driven technique. It offers atomic-level control of growth parameters and is especially suitable for fundamental research and complex heterostructure design. In this work, MBE is thus the technique of choice due to its ability to produce high-purity layers with abrupt interfaces and precise control over thickness and composition. The growth of thin films with well organized atomic layer and sharp interface when growing layers with different materials being indispensable for semiconductor devices and their quantum manifestation.

The conventional epitaxial techniques are mainly optimized for planar structures, such as quantum wells. However, the realization of low-dimensional nanostructures, like quantum wires (1D), are possible. The dimension reduction to obtain nanostructures is indeed one of the key point to develop advanced application such as quantum devices. This approach has driven significant interest in semiconductor nanowires over the past decade, owing to their unique electronic, optical, and quantum transport properties [Thelander,

2006 ; Lu, 2006]. Different methods have been proposed for the bottom-up fabrication of such nanostructures. The main ones use the Vapor-Liquid-Solid (VLS) technique and the Selective Area Growth (SAG), which are detailed below.

3.1 Vapor-Liquid-Solid technique

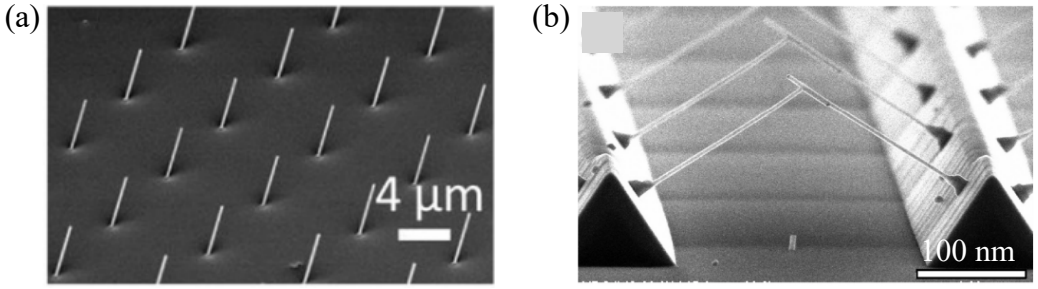

FIGURE 1.8 – Examples of realization performed with the VLS technique. (a) SEM image of GaAs NWs grown on GaAs(110) substrate [Zhang, 2017]. (b) SEM image of a pair of connected InAs nanowires grown on InP ridges. Advanced VLS technique showing high precision control of the NW position to design structures which connect individual nanowires [Dalacu, 2013].

This method consists in the growing of semiconductor crystal from a catalyst previously deposited on the substrate. The vapor-phase precursors are trapped by the liquid catalyst, acting as a nucleation seed for crystal growth. The nanostructure then grows from the liquid-solid interface with the substrate. The VLS technique has been extensively used by Au-catalyzed growth since four decades ago already [Wagner, 1964]. The catalyst droplet promotes the local and unidirectional growth of the nanowire. The size of the catalyst also influences the diameter of the nanowire. The Au nanoparticle becomes an eutectic alloy as it reacts with the substrate and the reactant species. The crystal develops between the substrate and the catalyst, the later thus remains at the top of the nanowire. Growth of Low-Dimensional Structures by the VLS growth technique has originally been able to produce III-V out-of-plane nanowires with appropriate structural quality for transport experiments, see figure 1.8. Extensive efforts have led to fabrication of core-shell nanowires or the realization of connected structures. However, this technique is not suitable for HgTe as the gold particles only function as nucleation sites [Selvig, 2006 ; Haakenaasen, 2008b], as we explained above. So the NWs suffer from poor dimension and orientation control as visible in figure 1.6(c-d). Moreover, this technique lacks scalability and geometric flexibility ; it requires NW manipulation for device preparation, and interconnections of only a few NWs are possible.

3.2 Selective Area Growth

The transport properties of nanowires have primarily been investigated after their transfer to a host substrate, followed by device fabrication steps such as metallic contacts

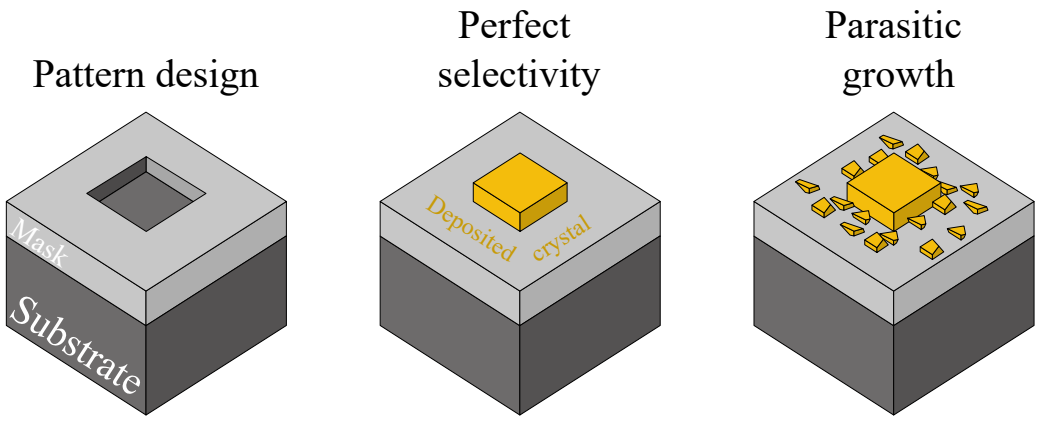

FIGURE 1.9 – Sketch of the SAG principle. The substrate is covered by a hard mask where the desired geometry is patterned. When perfect selectivity is achieved, the grown crystal follows the designed pattern. However, if the selectivity is compromised, parasitic growth may occur on the masked regions.

and gate deposition. These processing steps often introduce surface damage and contamination, which serve as additional scattering centers for charge carriers.

Selective area growth (SAG) for crystal semiconductors has then emerged to overcome this issue and offer scalability in circuit design and integration. Indeed, the precise positioning of the in-plane nanostructures enabled by SAG significantly simplifies device fabrication and experimental implementation compared to those of transferred NWs, while also minimizing surface-related degradation. For the realization of selective area epitaxy, an amorphous mask, typically dielectric SiO_x, SiN_x or Al_2O_3, is deposited on the substrate surface. Nanoscale openings are designed by lithography, thanks to electron beam or optical techniques, in the mask. The pattern is fully determined by the user, reflecting the high flexibility of the technique. The key advantage is that growth only proceeds within the openings while parasitic deposition on the mask is hindered [Pohl, 2013]. Thus, one directly obtains the desired pattern for the semiconductor after the epitaxy step. A schematic of the SAG principle is presented in figure 1.9.

For that reason, SAG appears as a powerful technique for growing low-dimensional structures such as nanowires and nanorings directly during the epitaxial process. It is a versatile and flexible technique that allows the growth of in-plane structure with high crystalline quality preserving the purity advantages of epitaxial techniques.

A condition for the effective growth at nano-scale is the precision of the patterned design which relies on the quality of the nanofabrication process. In particular, the dimension of the opening is highly dependent on the lithographic step. The etching of the mask can also broaden the apertures. Selective area epitaxy (SAE) also requires the optimization of the growth parameters to operate the material deposition within the ideal selectivity window : the growth within the apertures shows appropriate epitaxial quality, there is no lateral overgrowth on the mask and the parasitic growth is hindered.

Governing mechanisms of SAG for III-V materials and PbTe have already been studied by several groups. The main levers are the elevation of the growth temperature and the reduction of the growth rate to avoid nucleation of adatoms on the insulating mask

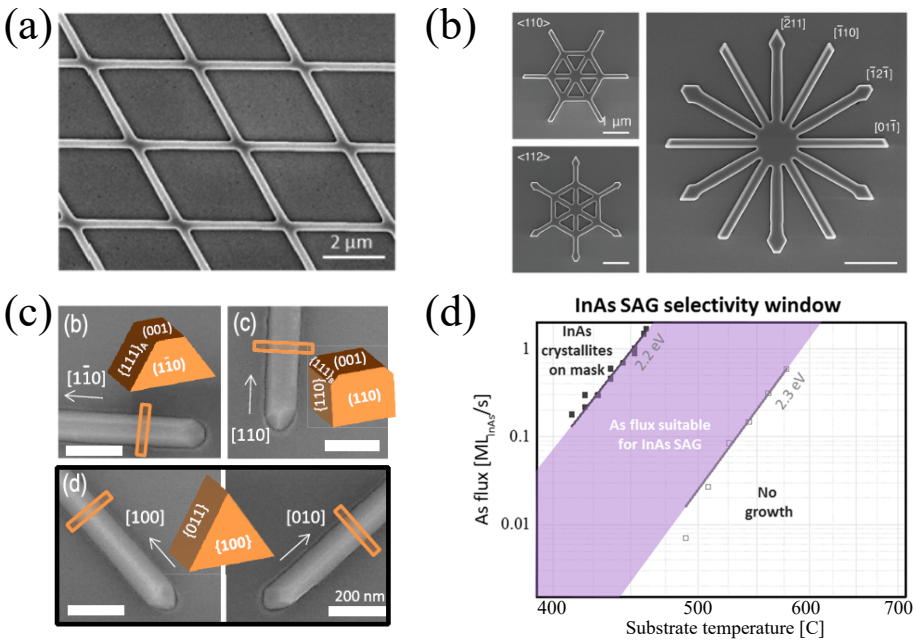

FIGURE 1.10 – Examples of nanostructures obtained by SAE. (a) SEM image of $\langle 11\bar{2}\rangle$-oriented InAs NWs network morphology on InP(111)B substrates [Aseev, 2018] (b) PbTe SAG on InP(111)A substrate. Top left shows all in-plane $\langle 110\rangle$ crysyal directions, while the bottom left, all $\langle 112\rangle$ crystal directions. The pattern on the right hand sign is a combination of both crystal directions families [Jung, 2022]. (c) InAs NWs grown on an InP(001) substrate. Well-defined facets are formed in particular ridge directions : (b) $[1\bar{1}0]$, (c) [110], and (d) [100] [Lee, 2019]. (d) Selectivity maps for InAs SAG on GaAs(001) substrate. Depending on the As flux and the substrate temperature the ideal selectivity window is defined [Aseev, 2018].

[Aseev, 2018]. Different mechanisms are involved such as the surface diffusion of the adatoms, the adsorption and desorption rate. The crystal grown in the openings presents different facets according to the substrate crystalline direction. Under the hypothesis of thermodynamic equilibrium, the Wulff model can be used to determine the morphological shape of the nanostructures [Rottman, 1984]. However, this equilibrium crystal shape can be perturbed by diffusion effects such as the diffusion of adatoms coming from the mask or from the crystal itself, or adatoms diffusing from low energy facets to high energy facets to promote the development of low energy surfaces. The latter could be responsible for the differences predicted by the Wulff model and the growth parameters can be tuned to modulate their impact. Hence, parameters such as adatom diffusion, incorporation or desorption, the mask material, and the pattern geometry, including the opening width, pitch, and orientation relative to the crystal axes, strongly influence the deposited thickness and the resulting nanostructure morphology [Cachaza, 2021 ; Morgan, 2023 ; Dede, 2022 ; Dubrovskii, 2023]. In addition, the use of an atomic hydrogen flux during growth can enhance selectivity [Desplanque, 2018]. Figure 1.10 illustrates some examples of nanostructures obtained by SAG. Panel (a) reflects the scalability of the pattern design with perfect selectivity as no crystal is found on the mask in the vicinity of the nanostructures. Figures (b) and (c) emphasize the influence of the opening direction on the morphology of the in-plane nanowires. According to the crystal orientation, the nanostructures show

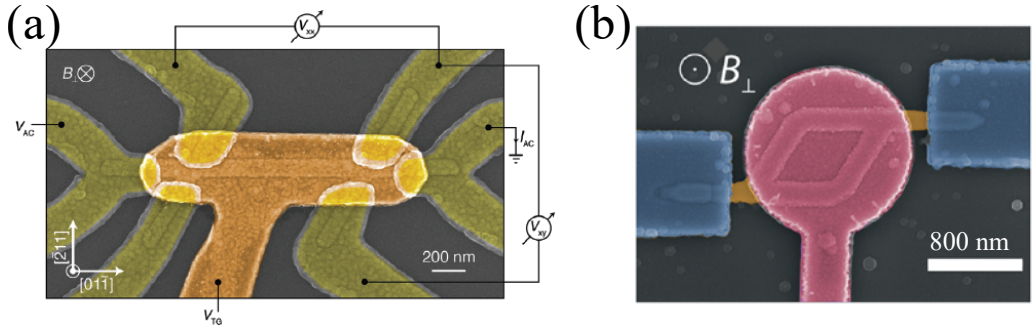

FIGURE 1.11 – Examples of device realization thanks to the SAG technique. (a) False colored SEM micrograph of a Hall Device obtained by selective growth of PbTe. Contacts are colored in yellow and the top gate in orange [Jung, 2022]. (b) Top-view SEM image of a InSb NW loop in which Aharonov-Bohm conductance oscillations are observed. Ohmic contacts are marked in blue, and the top gate in purple [Aseev, 2019].

different preferential crystal facets. It yields different shapes and specific edge terminations. Panel (d) displays a selectivity map of InAs nanowires as a function of the As flux and the substrate temperature. The In flux is kept constant while the As flux and the substrate temperature are varied. Upper bound corresponds to partial coverage by In-element clusters and As desorption (filled points). The lower bound highlights the total absence of growth on both substrate and mask material.

As we have seen, this approach allows the realization of complex in-plane 1D networks, with accurate control of dimensions, geometry and material quality, paving the way toward quantum networks for various materials [Aseev, 2018 ; Lee, 2019 ; Desplanque, 2019 ; Krizek, 2018 ; Desplanque, 2018 ; Jiang, 2022 ; Jung, 2022 ; Vaitiekėnas, 2018b]. The etching steps for the definition of the device geometry are no longer necessary, avoiding damage on the semiconductor crystal. Furthermore, the growth of in-plane nanostructures facilitates device fabrication, as no nanowire manipulation is required. Essential device elements, such as gates or electrical contacts, can be directly aligned with the patterned growth. Figure 1.11 shows two examples of devices fabricated from a SAG template. Panel (a) displays a PbTe-based Hall bar with ohmic contact and a top gate. The Hall bar geometry of the PbTe growth with side-contact leads facilitates contact alignment and deposition. Figure (b) illustrates a device based on a ring geometry. Similarly, the device integration follows naturally from the material deposition.

The scalability of the SAG technique, from the pattern definition in the mask down to the nanometer scale, then the epitaxial growth and the device fabrication, has thus be widely demonstrated. This growth method offers a high control over the geometry of the structures, their morphology and their structural characteristics. The final shape of the structure relies on the mask patterns and on the growth conditions. Importantly, SAG avoids the damage and contamination often associated with top-down etching methods. In conclusion, SAE appears as a promising technique for the growth of 1D HgTe-based nanostructures. The absence of etching steps makes it highly suitable for sensitive materials such as HgTe, which is known to degrade during standard fabrication steps. The material

quality is thus preserved. More importantly, it enables the fabrication of low dimension objects, a crucial point for the exploration of phase-coherent transport and spin-related phenomena in HgTe-based devices. No observation has been conducted regarding the SAG of HgTe and its driving mechanisms so far.

In this dissertation, we propose to explore SAG technique in combination with MBE to grow HgTe-based one-dimensional nanostructures, enabling the exploration of coherent quantum transport and spin-orbit phenomena in topological materials.

Chapter 2

Selective area epitaxy of HgTe-based nanostructures

1 Introduction

The controlled growth of nanostructures with desired geometry and crystallinity is a requirement for the development of quantum devices that exploit low-dimensional quantum phenomena. Among the available fabrication strategies, selective area growth (SAG) or selective area epitaxy (SAE), has emerged as a promising technique for the realization of in-plane nanostructures, offering superior flexibility in design, alignment, and integration compared to conventional top-down or transfer-based techniques. SAE of III-V materials have been extensively studied in the literature as we have presented in the previous Chapter. Selectivity maps, typical shapes of nanowire and model predicting the growth behavior have already been presented [Aseev, 2018 ; Lee, 2019 ; Morgan, 2023]. This chapter presents a systematic study of the SAG behavior of HgTe-based nanostructures that has not been studied so far.

All samples were prepared on CdTe(100) substrates covered with a dielectric hard mask patterned by electron beam lithography to define nanoscale openings. We assess the influence of the fabrication process on the mask openings and explain how the design of the mask can be used to study the growth behavior of HgTe-based SAE. Growths were performed by MBE under various conditions and the resulting nanostructures were systematically characterized. Our study investigates the influence of key parameters on the morphology and crystalline quality of the grown structures : the nominal HgTe thickness, the growth temperature, the design of the mask and the substrate orientation. Therefore, we can detail the growth behavior of the HgTe crystal and describe the evolution of its structural properties. The results provide design guidelines for the fabrication of low-dimensional in-plane HgTe devices tailored for quantum transport experiments.

In this Chapter, several material characterization techniques are used. We employed scanning electron microscopy (SEM) and atomic force microscopy (AFM) to assess the sur-

face morphology and uniformity, while scanning transmission electron microscopy (STEM), including cross-sectional imaging, was used to analyze the crystalline structure, interface quality, and strain relaxation mechanisms. Particular attention was paid to the facet development and interface abruptness of the HgTe nanostructures with respect to the CdTe substrate and the hard mask. To facilitate the reading of this Chapter, the principles of these techniques are reported in Appendix A.

2 MBE growth of HgCdTe material

In this PhD thesis, we focus on the MBE growth of the HgTe/CdTe system. The growth of such Hg-based materials is not common and is performed only by a few laboratories around the world. Our growth process mainly relies on 40 years of accumulated knowledge from CEA in the MBE growth of HgCdTe for InfraRed detection applications. Some details of the molecular beam epitaxy process are thus provided.

HgTe-based nanostructures were grown in a Riber 32P chamber equipped with individual effusion cells for Hg, Cd and Te. The epitaxy of HgTe is performed under a constant Hg overpressure, as the stability of the mercury flux is a critical parameter to ensure reproducible growth. The Hg/Te ratio was in excess of ∼1000/1, following the general requirements for the growth of HgCdTe layers for infrared applications [Ballet, 2013]. The growth conditions are defined by the equilibrium between the substrate surface temperature and the incident Hg flux. In these conditions, the growth is only governed by the behavior of the Te atoms. They are first adsorbed to the surface and then create bounds with the highly volatile mercury element. The lattice mismatch between HgTe and CdTe, $f = -0.3$ %, is small enough to prevent the formation of misfit dislocations at the interface and so avoid disorder [Ballet, 2014 ; Haas, 2017], which is believed to be detrimental for quantum applications [Sarma, 2021 ; Ahn, 2021]. In addition, HgTe exhibits a broad growth window, which permits growth temperature variations of several tens of degrees, compared to only a few degrees in the case of HgCdTe for instance, and greatly simplifies the epitaxial process. In particular, this large growth window increases the chance of encompassing the selective area growth window.

Before the deposition of the mask material, a 200 nm-thick CdTe buffer layer is grown on the bare substrate at 300°C under excess pressure of cadmium. A dedicated CdTe cell is used for the growth of the buffer layer. The steps for the mask fabrication and patterning are described in the following section. Once the substrate is masked, two last steps are necessary before the start of the SAE HgTe growth itself. The sample is first deoxidized under an H_2 plasma for 40 minutes before entering the growth chamber. Thermal annealing up to 350°C is performed under cadmium flux to desorb the residual surface oxide. It enhances the roughness of the top surface for better quality of the HgTe epitaxy. Finally, at the end of the growth process, the sample is cooled down under Hg flux to keep the surface roughness within the monolayer range, a critical condition to achieve high quality 2D layers [Ballet, 2014]. These last steps follow the requirements for standard growths of II-VI materials for InfraRed detection devices.

3 Mask definition and characterization

The nanofabrication processes of the mask deposition and patterning are realized at IEMN, benefiting from their strong experience in mask design. In this study, a silicon

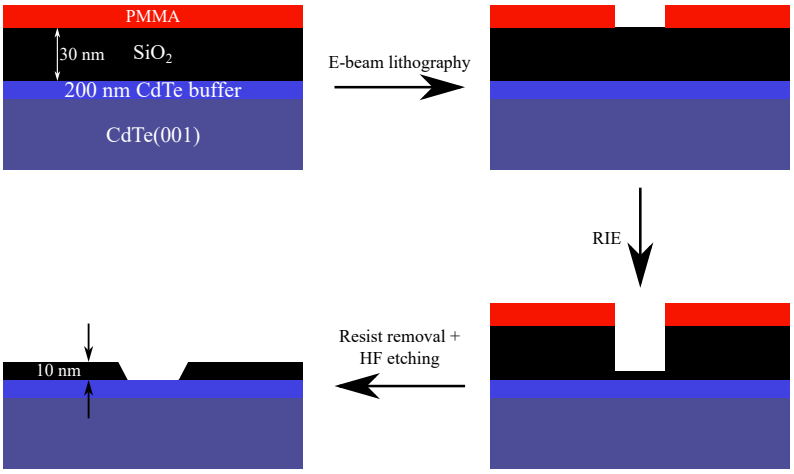

FIGURE 2.1 – Sketch of the different steps for the mask preparation. The SiO_2 is deposited by PECVD. The HF etching reduces its thickness to $\sim$ 10 nm.

dioxide SiO_2 mask is used. It is directly deposited on the substrate by Plasma-Enhanced Chemical Vapor Deposition (PECVD) aiming for a nominal thickness of 30 nm. Then, a 100 nm-thick PMMA photo-resist is deposited on top. The openings are designed by electron-beam lithography (EBL). Their opening includes two steps. First, reactive ion etching (RIE) is used as it can etch with a high-aspect ratio. However, the SiO_2 layer is not fully etched. Indeed, exposure of the CdTe substrate to ions would be detrimental to the quality of the top surface and so to the growth quality. The opening of the remaining nanometers of the mask is achieved by hydrofluoric (HF) wet etching. We note that HF is totally inefficient on CdTe. The detailed process of the mask fabrication can be found in [Fahed, 2016]. Figure 2.1 summarizes the different steps.

In figure 2.2(a), we show the shapes of 100 nm-wide openings from different masks used in this study. Despite following the same technological process, some variability is observed in the aperture profiles. In particular, the edges of the silicon dioxide mask tend to form a V-shape like geometry, most likely due to the isotropic etching of SiO_2 by HF. The roughness of the SiO_2 mask determined from AFM scans is around 0.7 nm, while it is about 0.3 nm for the CdTe top surface in the openings. We also note that the nominal width is respected at the substrate interface as visible from the Y = 0 nm line in figure 2.2(a) where the mask profiles matches the gap between the two vertical dashed lines. However, we note that the V-shape geometry quickly broadens the openings. Therefore, we expect nanostructures wider than the nominal width. Finally, we see that the residual thickness of the mask is reduced to $\sim$10 nm after etching by HF.

Figure figure 2.2(b) displays the morphology of three different openings with varying widths : W = 50, 100 and 200 nm. We note that the wider the opening, the more the edges broaden due to lateral etching. This behavior might be related to the volume of HF solution contained within an opening, which is larger in wide openings. For the different studies detailed below, we will compare the nanostructure morphology of growth originating from the same mask to be consistent with the opening morphology.

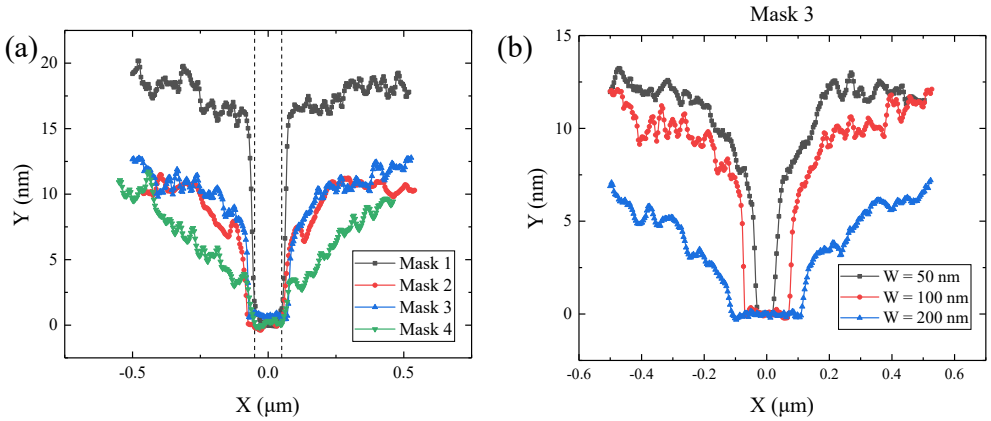

FIGURE 2.2 – Mask opening profiles extracted from AFM scans. (a) displays the shape of a 100 nm-wide opening from five different masks. The two vertical dashed lines in the center are separated by 100 nm. (b) openings with different widths taken from Mask 3.

Figure 2.3 shows patterns designed for the study of the selective area epitaxy of HgTe. In panel (a), 10 μm-long crosses are represented along the main in-plane directions of a CdTe(001) substrate : $\langle 1\bar{1}0 \rangle$ and $\langle 110 \rangle$ in the first row, and the $\langle 100 \rangle$ family in the second row. The influence of the substrate crystal orientation can be revealed with this type of pattern. The width of the opening varies from 50 to 500 nm. The ring pattern, for subsequent study of the Aharonov-Bohm effect, are also represented in panel (b). Different width are considered. Ranges of parallel nanowire with varying distances between them, this distance is referred to as the pitch P, are also designed to study the influence of the mask geometry on the nanowire growth. This is visible in (c), where groups of ten 100 nm-wide openings are separated by 200, 300, 500 and 1000 nm. The mask also includes grid patterns to study interconnection between nanowires, and large openings where the growth is governed by the 2D-like behavior.

The patterned substrate is now presented. In the following sections, we detail the MBE growths for the realization of in-plane HgTe nanostructures.

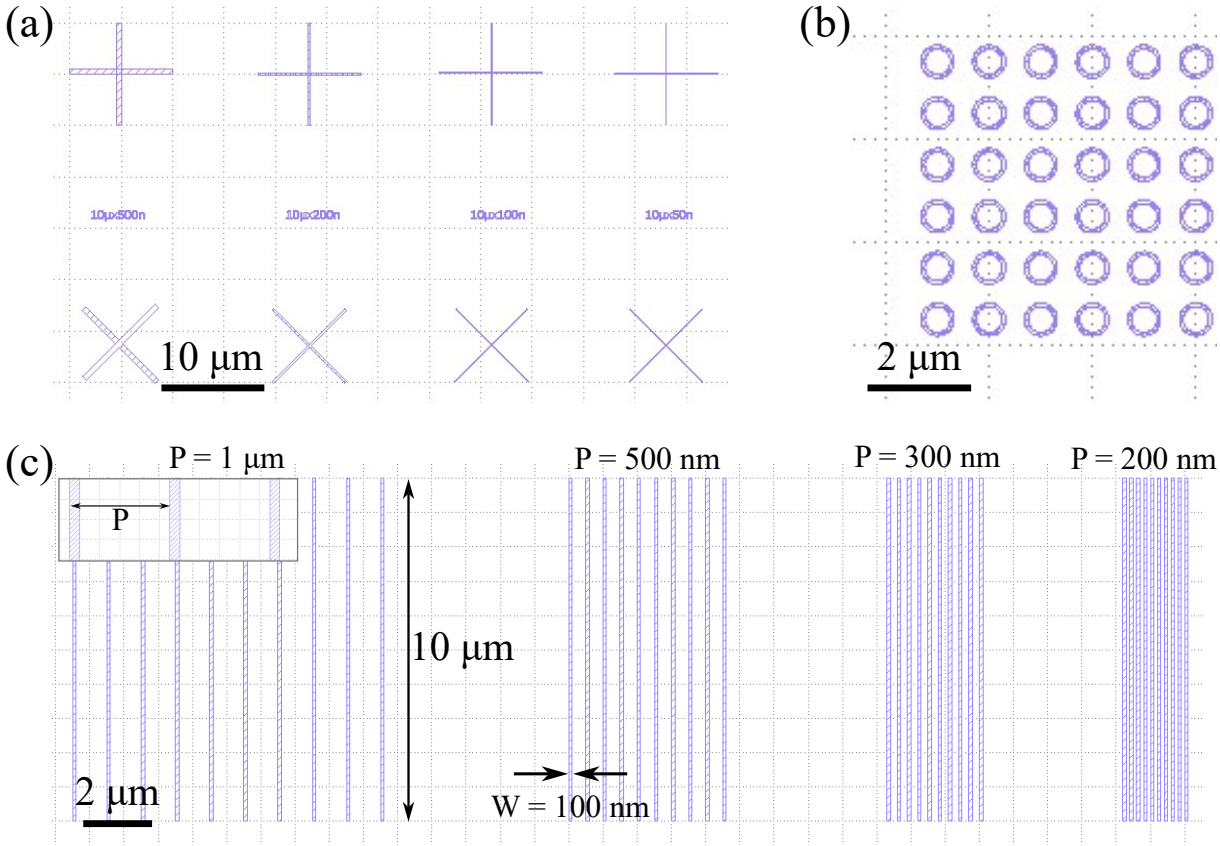

FIGURE 2.3 – Examples of patterns designed by EBL for the selective mask. Crosses (a), rings (b) and nanowires (c) are typical shapes. The width varies from 50 to 1000 nm. Several in-plane crystalline directions are studied. In panel (c), the distance between openings, the pitch, is varied to study the diffusion of the adatoms on the hard mask.

4 Selective epitaxy of HgTe-based nanostructures

In this section, we evidence the growth of in-plane HgTe nanostructures following the patterns designed in a silicon dioxide mask. A systematic study of the influence of the growth parameters is presented. Following the requirements reported by other groups and discussed in Chapter 1, the growth rate (GR) was limited to 1 ML/s. The lowest GR achieved in our experiments was 0.26 ML/s. Within this range, the selectivity was found to be independent of the growth rate. The growth temperature has been varied from 140 to 185°C. The nominal thickness deposition is changed from 5 to 110 nm.

4.1 Demonstration and morphological study

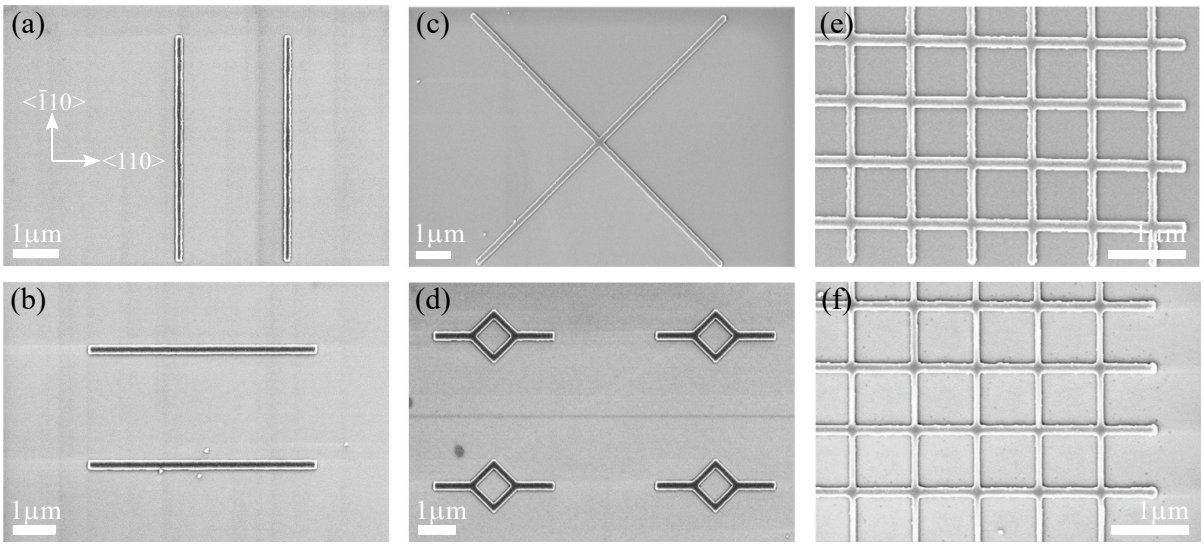

FIGURE 2.4 – Top-view SEM images of HgTe nanostructures grown on a patterned CdTe(001) substrate. (a)-(b) SEM micrographs of two 5 μm-long HgTe NWs grown along, respectively, $\langle\bar{1}10\rangle$ and $\langle 110\rangle$ directions. (c) SEM micrograph of a 10 μm-long $\langle 100\rangle$ type HgTe cross. (d) SEM image of diamond-like structures with junction along $\langle 110\rangle$ ridges. For images (a)-(d) the opening width is 100 nm and the growth temperature is 140°C. (e)-(f) SEM micrographs of 50 nm-wide $\langle 110\rangle/\langle\bar{1}10\rangle$ type grid grown at, respectively, 140°C and 180°C.

The SAG of HgTe nanostructures is investigated thanks to Scanning Electron Microscopy (SEM) observations along the high-symmetry in-plane crystal directions of the CdTe(001) substrate : $\langle 110\rangle$, $\langle\bar{1}10\rangle$, and $\langle 100\rangle$. Figures 2.4(a)-(e) display the morphologies of a 40 nm-thick growth at 140°C and 0.26 ML/s along the these three crystal directions. Figure 2.4(f), shows a 30 nm-thick growth at 180°C with a 0.34 ML/s growth rate. The mask openings are 100 nm-wide for figure 2.4(a)-(d) and 50 nm-wide for figure 2.4(e)-(f). The parasitic growth of HgTe grains on the silicon dioxide mask is almost non-existent and highlights the very good selectivity of HgTe with respect to the SiO_2 mask during the growth even at such low growth temperatures. The filling of the mask slits appears complete in every direction and the NWs have therefore a uniform shape along the entire length, up to several microns. We found that the morphology strongly depends on the

crystalline direction. While the nanostructures appear wider than the nominal opening width, revealing lateral overgrowth on the mask area, the NWs grown along ⟨110⟩ direction in figure 2.4(b) appear wider than the ones in figure 2.4(a), oriented along ⟨$\bar{1}$10⟩. They also seem to have more defined edges as the white rim is smoother than that observed in figure 2.4(a). The cross along ⟨100⟩ directions in figure 2.4(c) shows good filling of the aperture and a well defined junction with no evidence of faceting between the branches. The two branches are alike and this pattern thus exhibits a fourfold-symmetric morphology. In figure 2.4(d), the diamond shape displays good reproducibility of the complex pattern and demonstrates the good junction between ⟨110⟩ and ⟨100⟩ directions enabling more flexibility in nanocircuit design. Unlike the ⟨100⟩ type cross from figure 2.4(c), the networks consisting of perpendicular ⟨$\bar{1}$10⟩ and ⟨110⟩ directions visible in figure 2.4(e) and (f) shows a twofold-symmetric junction due to the different growth behaviors with respect to the orientation. For 50 nm-wide NW networks in figure 2.4(f), ⟨$\bar{1}$10⟩ oriented branches appear thinner. This effect is due to an increase in the growth temperature as we will explain later on.

A more precise description of the nanostructures morphology is visible in figure 2.5, where three cross sectional profiles of ⟨100⟩, ⟨$\bar{1}$10⟩ and ⟨110⟩ oriented HgTe NWs obtained from AFM scans are displayed with respect to a mask opening profile.

Nanostructures have been grown from a 100 nm-wide nominal opening at 170°C, 0.26 ML/s and a 40 nm nominal thickness. The profiles are extracted far enough from the interconnection point or from the branches tip to avoid boundary effects and so highlight the influence of the in-plane crystalline direction on the HgTe crystal growth. From the AFM profiles, a NW oriented along ⟨$\bar{1}$10⟩, in blue in figure 2.5(a) and (d), shows a ∼56° angle between the side facets and the horizontal direction, that would correspond to {111} facets which theoretically form a 54.7° angle with the surface of a (001)-oriented substrate. It is in good agreement with the study from Iwanaga *et al.* [Iwanaga, 1986], which also showed Hg-terminated {111}A facets for this particular direction. Additionally, from the mask opening profile obtained in figure 2.5(c), the thickness in the center corresponds to the nominal thickness of the 2D planar growth. Therefore, the two humps on the sides, forming what we name super-elevations in the following, are most likely stack of adatoms coming from the {111}A facets and not from the center of the NW. The origin of these super-elevations might originate from a kinetically driven (rather than thermodynamically) growth mode. Indeed, a longer incorporation time on the {111}A facet with respect to the (001) top facet would cause adatoms impinging on the {111}A facets to diffuse towards the top facet. However, due to the limited surface diffusion on the top facets, the diffusing atoms stay on the edges of the top surface [Albani, 2019]. In the case of a sufficiently large surface diffusion, the diffusing adatoms would cover the entire top facet, giving a trapezoid cross section. The growth rate of the nanostructure would then be greater than the nominal one as explained in [Morgan, 2023]. They studied GaAs NWs obtained by selective MOVPE. Diffusion from the side facets toward the top facet is also

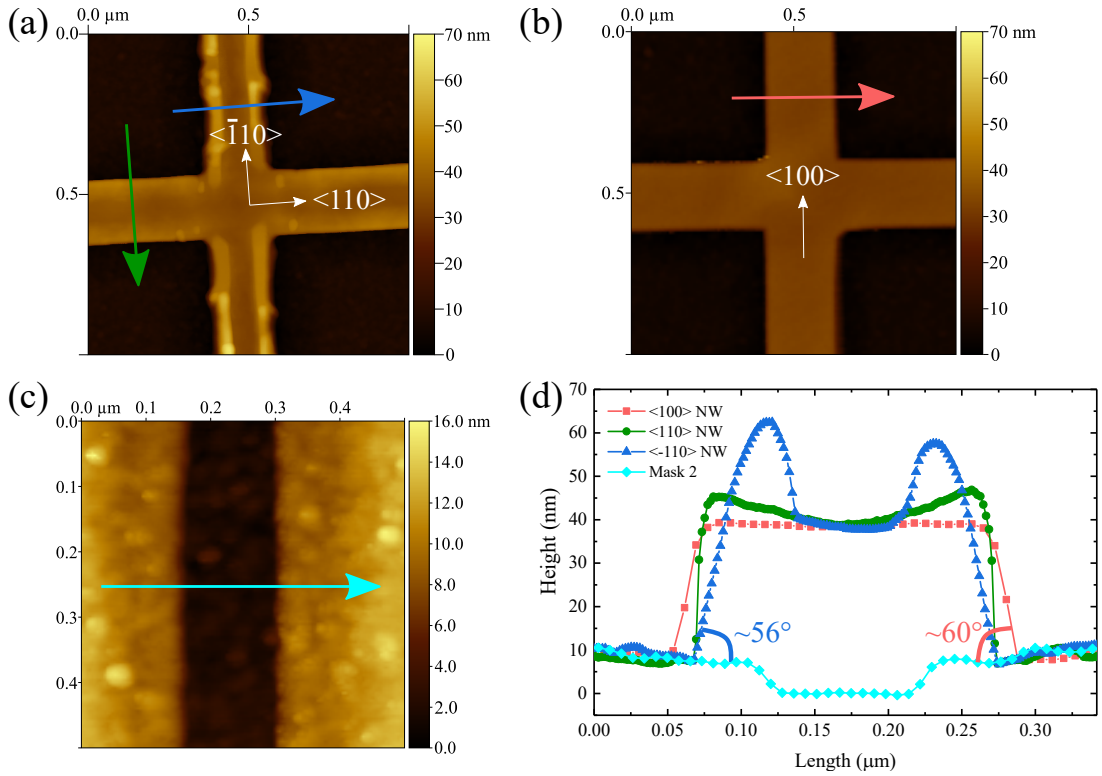

FIGURE 2.5 – AFM scans of nanostructures grown at 170°C and 0.26 ML/s with a 40 nm nominal thickness. Scans of (a) a ⟨110⟩/⟨$\bar{1}$10⟩ type and (b) a ⟨100⟩ type NW cross. The darker areas in (a) and (b) correspond to the SiO_2 mask. Both crosses are grown from 100 nm wide slits. (c) AFM scan showing a 100 nm-wide opening before the growth. The darkest area corresponds to the CdTe substrate and the colored sides to the SiO_2 mask. The change in constrast across SiO_2 is caused by the etching process while opening the mask which reduces its thickness to about ten nanometers. (d) AFM profiles extracted from the three AFM images along the respective colored arrows.

noted, but there is no formation of super-elevation. Rather, the atoms diffuse on the entire top surface, increasing the thickness of the nanostructure compared to the nominal one.

In addition, a NW oriented along ⟨110⟩, in green in figure 2.5(a) and (d), shows a more vertical profile suggesting the formation of {110} side facets. The nominal thickness is also obtained in the center. Hence, for both directions, the growth in the center seems to be similar to a 2D planar growth but with particularities on the edges. The different shapes for these two equivalent crystallographic directions could be due to the (2×1) surface reconstruction, elongated along the ⟨$\bar{1}$10⟩ direction, of the top facet [Oehling, 1996 ; Oehling, 1998]. Figure 2.6(a) illustrates the change of the unit cell during growth. For ⟨$\bar{1}$10⟩-oriented NWs, in the kinetically governed growth regime, diffusing adatoms from the side facets would be able to diffuse along a dimer chain over a certain length, forming the super-elevations as stacks of adatoms. On the contrary, the surface reconstruction strongly restricts adatom diffusion on the top surface of ⟨110⟩-oriented nanowires[LaBella, 2000 ; Zhang, 1997]. In figure 2.6(b), elongated shapes similar to diamonds geometry are revealed by the AFM scan. Those repeated patterns are associated with low roughness of the HgTe top surface [Thomas, 2016]. In this study, we find typical values of 0.33 nm which corresponds to half a monolayer. Nevertheless, the AFM technique could not reveal

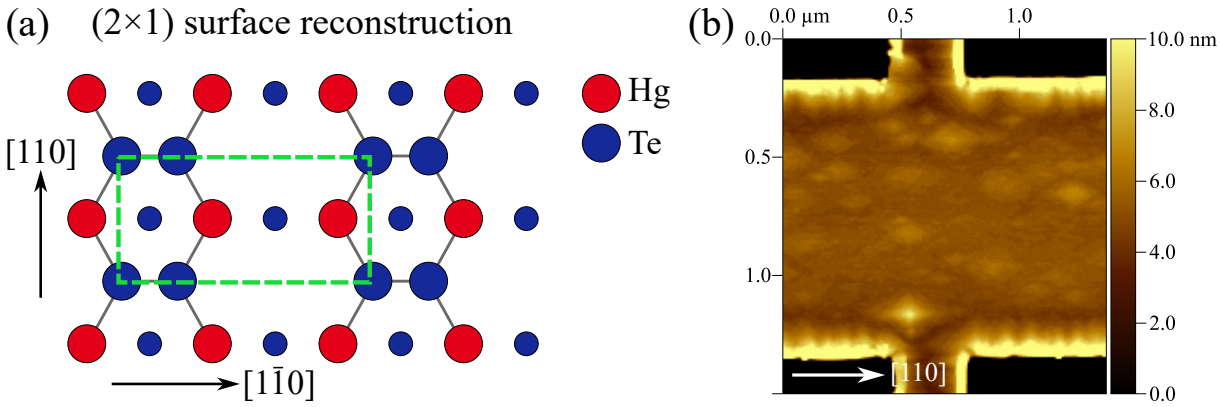

FIGURE 2.6 – (a) Sketch of the HgTe surface reconstruction during the growth. The unit cell shows a (2×1) reconfiguration elongated along the the $\langle 1\bar{1}0\rangle$ direction. (b) The AFM image emphasizes the prensence of diamond shape on HgTe surface. The diamonds are elongated along the $\langle 110\rangle$ direction which allows to determine the in-plane orientation of the substrate.

atomic steps, Scanning Tunneling Microscopy (STM) would be a suitable technique for their observations. Furthermore, the elongated shapes can be used to distinguish the [110] axis from the [1$\bar{1}$0] direction. Their long axis is indeed parallel to the [110] direction. It is consistent with our observations and with the investigations of Oehling *et al.* who found similar patterns also elongated along the same direction [Oehling, 1998]. In essence, this illustrates how these two equivalent directions could be distinguished, a distinction that cannot be made prior to the growth process.

A NW oriented along $\langle 100\rangle$ direction, in red in figure 2.5(b) and (d), shows strongly tilted facets oriented around 60° close to {201} or {302} side facets and a flat top surface with roughness down to 0.3-0.5 nm in good agreement with the monolayer range roughness of HgTe. The height of the NW matches the expected thickness. Comparing the last three NW profiles to the mask profile, in cyan in figure 2.5(c) and (d), one can see that there is a significant lateral overgrowth of the nanostructures on the mask, corroborating the width of the NWs from SEM images in figure 2.4. The lateral overgrowth and the presence of the super-elevations, where the thickness is bigger than the nominal 2D growth, suggest a diffusion of the adatoms from the mask towards the openings during the growth, as discussed later.

This section has evidenced the growth of in-plane HgTe nanostructure. The opening orientation with respect to the crystalline axis of the substrate yield different morphologies. To further investigate their crystal organization and assess their epitaxial quality, it is interesting to perform Scanning Transmission Electron Microscopy (STEM) imaging on the NWs in their transversal cross-section.

4.2 Crystal organization

The modern developments in electron microscopy have set STEM technique as a powerful and reliable tool for the characterization of strain and crystal orientation in semiconductor materials. Many techniques have been developed such as dark field electron holography, nanobeam diffraction or even geometrical phase analysis.

In this section, we present experimental images of a [110]-oriented NW obtained in high-angle annular dark-field (HAADF) mode, and mappings of physical constraints of a $[1\bar{1}0]$-oriented NW realized by Nanobeam Precession Electron Diffraction (NPED). Experiments have been performed and analyzed at the Nanocharacterization Platform of CEA Grenoble using a Thermo Fischer (ex FEI) Titan Themis 200 microscope equipped with spherical aberration corrector on the condenser lens for high resolution STEM imaging. A 200 kV voltage has been used for the experiments. The focused ion beam (FIB) preparation of the TEM lamellas follows a two steps procedure. First, a 50 nm-thick protective carbon layer is deposited by electron beam assisted evaporation as the direct use of ion beam would damage the nanostructure. Then, a 3 μm-thick carbon(10%)-Pt(90%) layer is deposited on top with the ion beam at 12 kV. The lamellas have been prepared using a Thermo Fisher Helios 5 PFIB.

We first present the structural properties of a [110] oriented HgTe NW characterized by High Resolution (HR) STEM. The observed NW is prepared from the same sample as that presented in figure 2.5. The nominal slit width is 100 nm. Figure 2.7(a) shows a HAADF STEM image of the NW transverse cross-section, that is perpendicular to the [110] ridge direction. Due to the $\sim Z^2$ dependence of the HAADF image contrast, Z being the average atomic number of the local material, the "Z-lighter" silicon dioxide mask appears black with respect to the "Z-heavier" CdTe substrate and the HgTe nanostructure. This STEM image reveals the symmetrical shape of the NW with a flat $(001)_{G_0}$ top facet in the center, as suggested from the top-view SEM micrographs in figure 2.4(b) and AFM scans in figure 2.5(a) and (d). The atomic columns of the image are not visible here due to reduced resolution of the figure, but we could identify three grains in the NW crystal structure. We therefore define three frames of reference assigned respectively to these three grains, the G_0 frame corresponds to the substrate orientation while two side grains, G_1 and G_2, are found to extend above the mask with rotated orientation. Thus, the edges of the NW form an overhang above the insulating mask. This geometry could not be revealed by AFM scans, which suggested vertical facets in figure 2.5(d) due to the tip convolution effect. Zooming-in on the HAADF image, see for instance figure 2.8(a), clearly indicates the presence of a {111}B twin boundary between grains G_0, G_1 and G_2. The polarity of the {111}B facet, Te-terminated, is consistent with the work presented by Iwanaga *et al.* [Iwanaga, 1986]. The formation of these grains could be explained by the asymmetric (2×1) surface reconstruction of the top (001) facet during growth [Oehling, 1998 ; Oehling, 1996]. We recall that this asymmetric unit cell is elongated along the $[1\bar{1}0]$ direction, hindering surface diffusion along this direction on the top facet. Therefore,

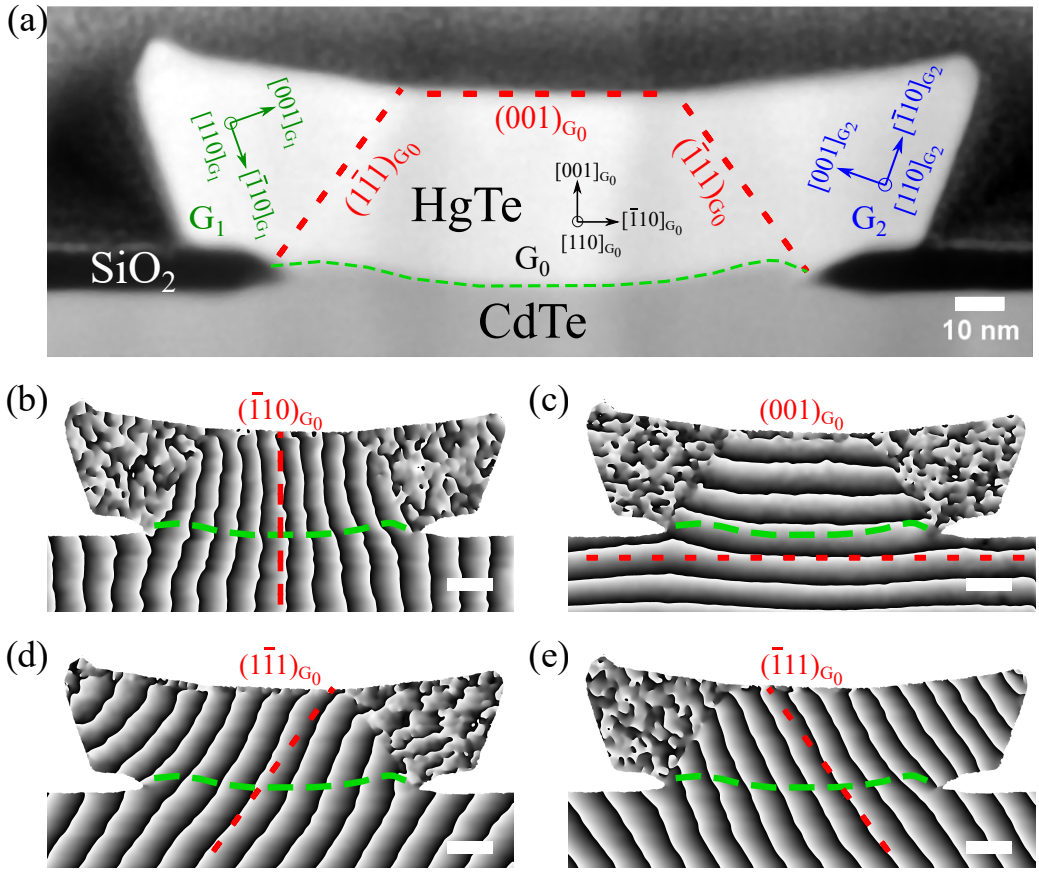

FIGURE 2.7 – Analysis of a [110]-oriented nanowire by STEM. (a) High resolution HAADF image of the NW transversal cross-section. We define a frame of reference for each grain with respect to its orientation. The two red 54.7°-tilted dashed lines correspond to grain boundaries of {111}B facets between the center grain G_0 and the two side grains G_1 and G_2. The top red dashed line represents the $(001)_{G_0}$ plane. The dashed green curve highlights the interface between CdTe and HgTe. Numerical g-moiré images are obtained to visualize the respective (b) $(1\bar{1}0)_{G_0}$, (c) $(001)_{G_0}$, (d) $(1\bar{1}1)_{G_0} \Leftrightarrow (\bar{1}11)_{G_1}$ and (e) $(1\bar{1}1)_{G_0} \Leftrightarrow (1\bar{1}1)_{G_2}$ planes. The scale bar in g-moiré maps represents 20 nm.

spreading adatoms would be forced to form a grain and grow laterally.

To provide a visual representation of these grains particular Geometrical Phase Analysis (GPA) treatments were performed on these images. Either g-moiré images, figure 2.7(b)-(e), or rotation map, figure 2.8(b), were calculated ; here g indicates the reciprocal vector that characterizes a given crystallographic plane. The principle of these treatments is to perform a Fast Fourier Transform (FFT) of the HR STEM image and apply a mask in the Fourier transform in order to select diffraction spots. For the g-moiré images, we select a region around a given g-vector associated to a given family of planes [Wang, 2013 ; Beznasyuk, 2020]. For the rotation map, three diffracted peaks, each of them being associated to one of the three grains G_0, G_1 and G_2, are filtered. The size of the mask is set to preserve a balance between a good spatial resolution and a high signal-to-noise ratio. In figure 2.7, four g-moiré images have been obtained with four different g-planes : (b) $(\bar{1}10)_{G_0}$, (c) $(001)_{G_0}$, (d) $(1\bar{1}1)_{G_0}$ and (e) $(\bar{1}11)_{G_0}$. G-moiré maps reveal the three grains and give a visual representation of the bending and inter-planar distance variations of these crystallographic planes. Vertical $(1\bar{1}0)_{G_0}$, figure 2.7(b), and horizontal $(001)_{G_0}$, fi-

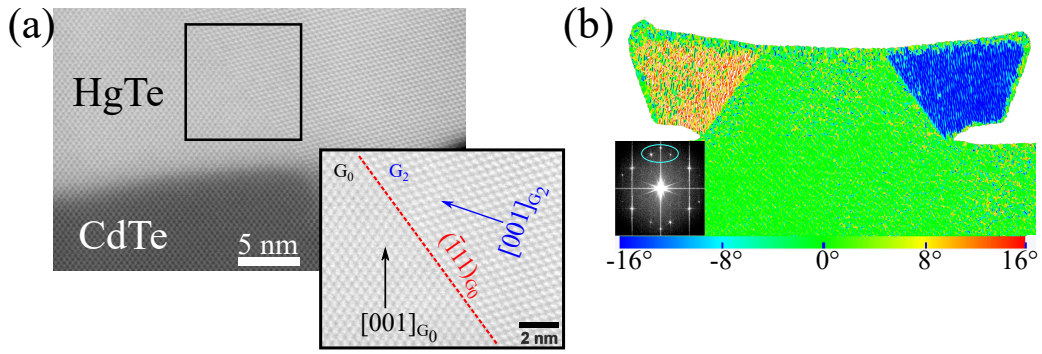

FIGURE 2.8 – (a) Zoom on the crystal/mask interface near grains G_0 and G_2 from the HR HAADF-STEM image of figure 2.7(a). The area outlined by a black square is further zoom-in to visualize the atomic columns and clearly shows the {111} twin plane separating grains G_0 and G_2 that are rotated from each other by 70.5° (angle between $[001]_{G_0}$ and $[001]_{G_2}$). (b) Semi-quantitative map of the rotation angle of the filtered area in the FFT of the image (the FFT and the elliptic mask are visible in the inset). The three points with highest intensity in this area correspond to planes $(1\bar{1}1)_{G_1}$, $(001)_{G_0}$ and $(\bar{1}11)_{G_2}$. The reference plane is taken as $(001)_{G_0}$. The rotation between planes $(1\bar{1}1)_{G_1}$, respectively $(\bar{1}11)_{G_2}$, and $(001)_{G_0}$ should be equal to +15.8° (orange area), respectively -15.8° (blue area).

gure 2.7(c), planes are only present in the substrate and HgTe NW G_0 grain ; so fringes are only present in G_0, while the grains G_1 and G_2 appear noisy. Figure 2.7(b) shows that the vertical lattice fringes in the HgTe NW are smaller than in the substrate, indicating that the NW is partly relaxed and no longer matches the in-plane lattice parameter of the substrate. Very importantly here, there is no fringe discontinuity in the g-moiré map indicating that there is no misfit dislocation in the structure, and so a good epitaxial relation exists between the CdTe substrate and the HgTe nanostructure with a continuous atomic lattice. In the scope of transport experiments, this absence of disorder and defects at the susbtrate/HgTe interface is promising as mentioned in [Sarma, 2021 ; Ahn, 2021]. In figure 2.7(c), there is no clear difference between horizontal fringes of HgTe NW G_0 grain and the substrate. It suggests that the HgTe crystal is relaxed, its out-of-plane lattice paramater is thus very close to that of CdTe. This is consistent with the previous g-moiré maps showing vertical fringes. In addition, inclined $(1\bar{1}1)_{G_0}$ planes are only visible in grains G_0 and G_1 as seen in figure 2.7(d), and inclined $(\bar{1}11)_{G_0}$ planes are only visible in grains G_0 and G_2 as shown in figure 2.7(e). Thus, each grain shares a common {111} plane with the central region G_0 and the substrate. The side grains therefore appear as grain G_0 but tilted by ±70.5°, the ⟨221⟩ direction in the grains is now parallel to the $[001]_{G_0}$ substrate orientation. Here as well, these maps do not show any fringe discontinuity.

In figure 2.8(a), the twin plane boundary between the center grain G_0 and the right grain G_2 is evidenced. The common {111}B plane is marked with a red dashed line. The STEM image evidences the absence of stacking fault in the vicinity of the grain boundary, the substrate/nanowire interface and the nanowire/mask interface. In addition, HgTe has a crystalline structure up to the mask area as the grain atomic lattice is visible until the interface with the black silicon dioxide mask. Intermixing between CdTe and HgTe is limited to a few monolayers around the interface as there is a clear contrast between the CdTe substrate and the HgTe NW. In figure 2.8(b), we show the analysis of lattice plane

orientations obtained by selecting a specific diffraction region in the FFT (highlighted by the blue ellipse in the inset). The selected zone corresponds to the planes with the highest intensity, namely from left to right, $(\bar{1}11)_{G2}$, (001)G0, and $(1\bar{1}1)G_1$, from which the rotation of the planes with respect to the horizontal direction can be determined. While the center area is found free of rotation (consistent with the moiré image of figure 2.7(b)), the G_1 grain, respectively G_2 grain, exhibits a +15°, respectively -15°, rotation. This is consistent with the STEM micrograph from figure 2.8(a), where the tilted $(\bar{1}11)$ plane of the G_2 grain makes a ∼15° angle with the horizontal direction.

The STEM analysis have been of precious help to reveal the real cross sectional morphology of a NW oriented along the [110] axis. Indeed, the formation of two lateral grains leading to overhangs on the sides was not visible in either the AFM scans or the SEM images. The good epitaxial quality of the NW with the substrate has been emphasized. The fringes of the g-moiré maps evidence the relaxation of the HgTe crystal without the formation of dislocations.

Understanding how strain is distributed within the nanowire cross-section would be of great interest to compare a selective growth process involving side facets to a 2D layer growth. Nanobeam precession electron diffraction (NPED) is particularly suited for this purpose, as it combines nanometer-scale spatial resolution with high sensitivity to small lattice parameter variations. This makes it possible to map in-plane and out-of-plane strain, as well as rotation and shear fields, with sufficient precision to capture the local distortions induced by facet formation and selective-area growth geometry.

We performed nanobeam precession electron diffraction (NPED) on a 100 nm-wide $\langle 1\bar{1}0\rangle$-oriented HgTe nanowire to map strain, shear, and lattice rotation. We also present similar results for a 50 nm-wide NW in Appendix B. NPED measurements were carried out in a TEM operated in scanning mode. The precession is achieved by tilting the beam around the optical axis at a constant tilt angle ; the reader is invited to consult Appendix A for details on the technique. This beam movement enables the cutting of more reciprocal nodes in reciprocal space and helps reduce dynamical diffraction effects, which in turn lowers contrast within the diffraction disks. Altogether, this improves both the number and uniformity of accessible reflections [Rouviere, 2013], thereby enhancing measurement accuracy. A reference pattern was first acquired from the underlying CdTe layer. Scanning across the nanowire yields diffraction patterns for each region, which are directly compared to the reference. For a given crystallographic direction, the shift of a diffraction spot position gives the change in lattice parameter, from which the strain is computed. Details of the technique are described in [Rouviere, 2013].

The strain maps in figure 2.9(a) show that the nanowire is essentially fully relaxed in both the in-plane $\langle 110\rangle$ direction ($\epsilon = \frac{\Delta a}{a_s} = \frac{a_{fs}-a_s}{a_s}$) and the out-of-plane $\langle 001\rangle$ growth direction ($\epsilon = \frac{\Delta c}{c_s} = \frac{c_{fs}-c_s}{c_s}$). The central region exhibits a uniform green color corresponding to $f \approx -0.3$ %, matching the relaxed HgTe lattice parameter. This indicates that the lattice mismatch with CdTe is released at the growth interface, most likely through

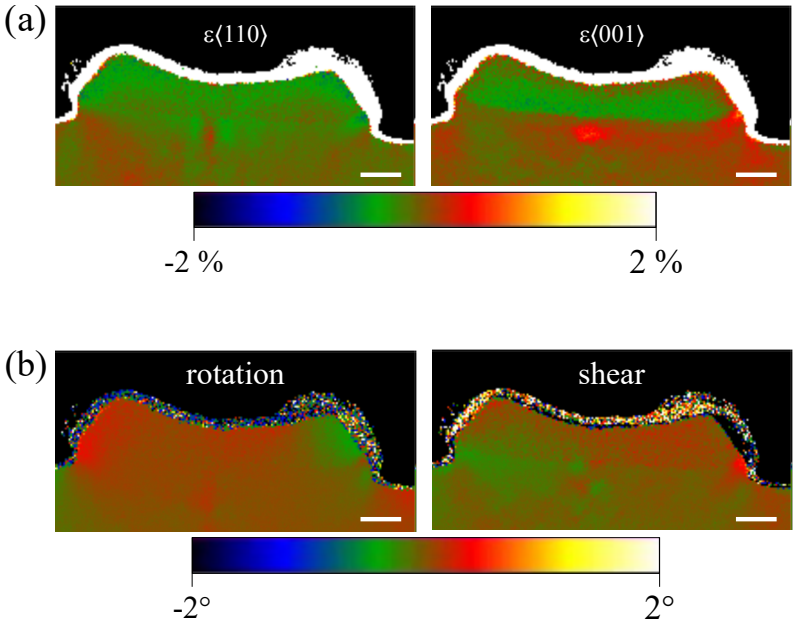

FIGURE 2.9 – Mapping of different physical properties of 100 nm-wide $\langle 1\bar{1}0\rangle$-oriented NW obtained by NPED in transversal cross-section. In panel (a) the strain is represented along the (left) [110] in-plane direction and (right) the growth direction [001]. Below, in (b), the maps respectively illustrates the rotation and the shear. The scale bar represents 20 nm

elastic relaxation enabled by the nanowire reduce contact area with the substrate. If the structure were coherently strained, the out-of-plane lattice parameter c_{fs} would be smaller than that of relaxed HgTe, resulting in a blue-shifted color map, which is not observed here.

Localized compressive strain appears near the sidewalls, possibly arising from facet reconstruction. The rotation map in figure 2.9(b) reveals opposite tilts at the two side facets, consistent with elastic bending of the lattice toward free surfaces to minimize surface energy. The shear map shows localized distortions at the base edges in opposite directions, suggesting a torsional deformation of the nanowire. This torsion may originate from subtle asymmetries in the growth dynamics or facet stability during selective-area growth.

Overall, NPED confirms that SAG-grown HgTe nanowires undergo highly efficient strain relaxation without visible misfit dislocations, while subtle rotation and shear features at the side facets reflect the interplay between surface energy minimization and anisotropic growth kinetics.

The previous sections demonstrated the selective-area epitaxy of in-plane HgTe nanostructures and their characteristic morphologies. Depending on the in-plane orientation, adatom diffusion from the {111}A facets leads to accumulation on the sides of the top surface, as observed for nanowires oriented along $\langle 1\bar{1}0\rangle$. In contrast, $\langle 110\rangle$-aligned slits develop two lateral grains separated by twin planes on {111}B facets, producing side overhangs. The crystal quality remains high, with no misfit dislocations and only rare, localized stacking faults. The $\langle 100\rangle$ orientation appears to promote a square morphology,

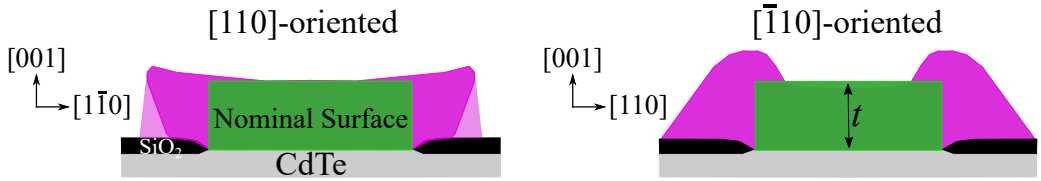

FIGURE 2.10 – Schematics of nanowire cross-section for two crystal orientations (left) [110] and (right) [$\bar{1}$10]. The cross section of a nominal NW is shown in green along with typical overgrowth of experimental NWs in purple for [110] and [$\bar{1}$10] directions. The parameter ρ is defined as the ratio of the whole NW cross-section (green and purple) over the green area.

though this requires confirmation by STEM imaging.

4.3 Influence of the growth parameters and the pattern design

A natural question arises regarding the mechanisms by which the HgTe crystal develops these characteristic shapes. This is the focus of the following sections, in which we assess the influence of the opening width, the deposited thickness, the growth temperature, and the pattern design on nanowire morphology. The growth behavior will be analyzed in detail to identify the set of parameters required for a targeted shape. In the following, we focus on the $\langle 110 \rangle$ and $\langle 1\bar{1}0 \rangle$ orientations.

In figure 2.10 two schematics present the method to compute ρ, the ratio between the NW cross section area (purple plus green areas) and the cross sectional area of a nominal NW (S_{nom} in green). We assume that the nominal NW grows layer-by-layer with vertical sidewalls up to the nominal planar growth thickness t. The lighter purple areas for [110]-oriented slits correspond to extra surface contributions detected in the AFM scans due to the overhang of the side grains. The quantity ρ will be a useful tool for characterizing and analyzing the shape evolution of NWs.

4.3.1 Change with the opening width

In figure 2.11, we display the transversal profiles of 20 nm-thick NWs along the two main in-plane directions [110] and [1$\bar{1}$0] for different opening widths. As we described before, the thickness at the center of the NW corresponds to the nominal deposited thickness, thus the characteristics features of SAG only manifest on the edges. It is exactly what we observe in figure 2.11. In panels (a) and (b), we focus on the [1$\bar{1}$0] axis. Figure (a) shows the morphology with a 1 : 1 aspect ratio. The three profiles are equivalent, but the central part with the (001) top facet, is stretched or compressed depending on the opening width. Indeed, we observe the side {111} facets and the super-elevations. Only the purple profile of the 50 nm-wide opening is slightly different because the super-elevations have started to merge. In panel (b), we detail this morphology and also display the NW from a 500 nm-wide aperture. The top surface in the center is clearly visible, and the super-elevations are alike whatever the opening considered. The same trend can be observed for NWs along the [110] directions in panels (c) and (d). The tilted side grains are visible as

the thickness smoothly reduces from the edges toward the center. In figure 2.11(d), there does not seem to be a correlation between the opening and the width of the flat surface in the center. Indeed, for $W = 200$ nm, the crystal edges seems to originate from the same points as for $W = 50$ or 100 nm, while a larger flat surface would have been expected in the center. This might be due to adatoms deposition on the side grain that blur the boundary between the later and the central grain.

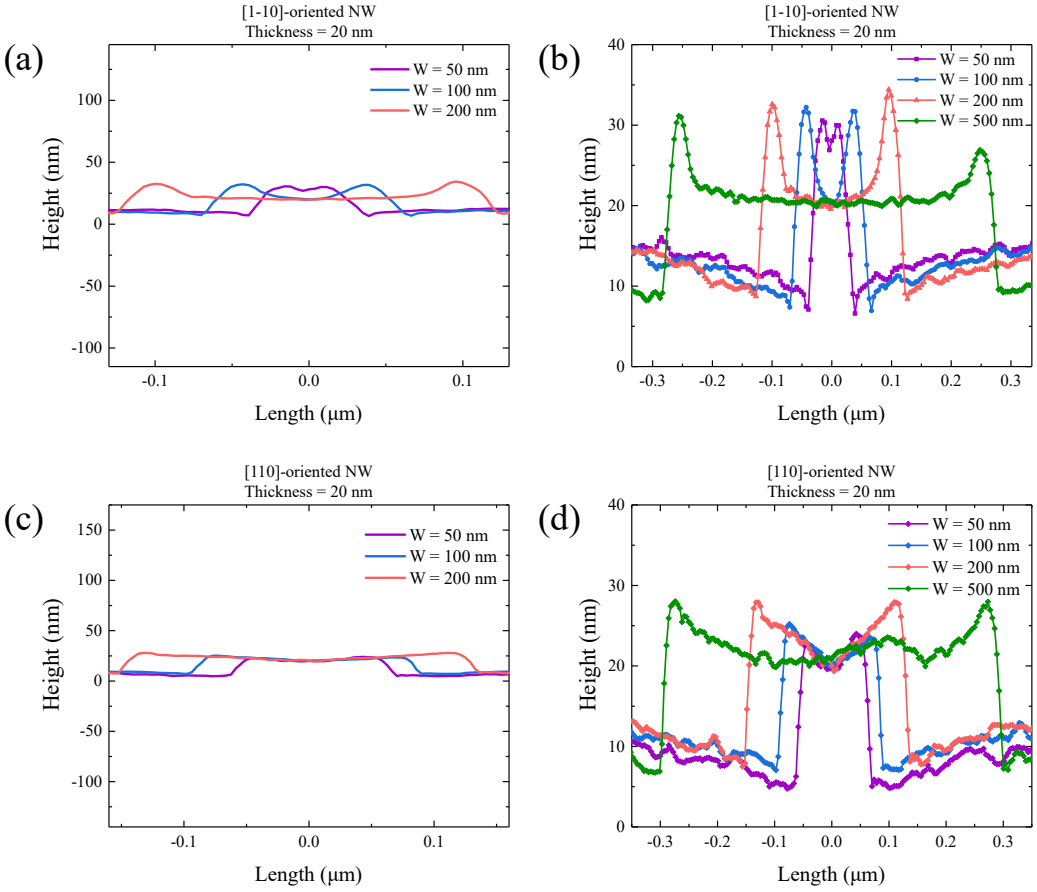

FIGURE 2.11 – Transversal AFM profiles of nanowires from a 20 nm-thick nominal growth. Panels (a) and (b) reveal the morphology of $[1\bar{1}0]$-oriented NWs. (a) Profiles of NWs with three different widths. The nominal thickness is visible in the center of the NWs. The edges displays the {111} facets and the super-elevation on the sides. The $x : y$ scale is 1 : 1. For $W = 50$ nm the merging is almost complete. (b) Morphology of the NWs, up to $W = 500$ nm. The reproducible profile on the edges is emphasized, as well as the characteristic shape of the mask opening. Figures (c) and (d) are focusing on ⟨110⟩-oriented NWs. The overhang can not be revealed by the AFM tip. In (d), the larger thickness due to the change of the crystal orientation is visible.

It is also interesting to characterize the overgrowth with respect to the opening width. In figure 2.12, the evolution of experimental ρ values are plotted as a function of the inverse of the NW width. If the same amount of overgrowth is assumed regardless of the opening width, one gets :

$$S_{\mathrm{nom},i}(\rho_i - 1) = S_{\mathrm{nom},j}(\rho_j - 1) \tag{2.1}$$

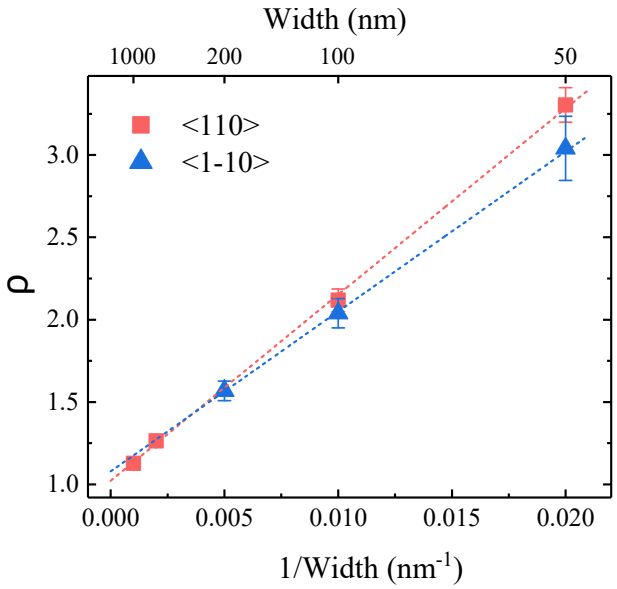

FIGURE 2.12 – Evolution of experimental ρ values as a function of $1/W$ for $\langle 1\bar{1}0\rangle$ and $\langle 110\rangle$ orientations types. NWs are grown at 140°C and 0.26 ML/s with a 38 nm nominal thickness and the pitch is above 1000 nm. Dashed lines are linear fit curves.

And considering that $S_{\mathrm{nom},i} = t \cdot W_i$, ρ_i should be a linear function of $1/W_i$:

$$\rho_i = 1 + (\rho_j - 1)\frac{W_j}{W_i} \tag{2.2}$$

Here we consider a set of NWs whose opening width varies from 50 to 1000 nm. Figure 2.12 shows that the experimental ρ values for NWs in both directions increase linearly with $1/W$ as there is a good alignment between the computed ρ values and the fitting curve. This is fully consistent with the previous assumptions that the characteristics features of SAG only manifest on the edges. The overgrowth is therefore found to be width independent, as long as the super-elevations do not merge as we will explain later. The nanostructures are then relatively more selective the wider they are. One can also notice that the values for $\langle 110\rangle$-oriented slits are larger. This is most likely due to the area below the overhang which is not subtracted in the calculation. This regime is different from most observations with other materials where the effective growth inside an opening depends on its width and where the growth rate is enhanced for wider slits [Dubrovskii, 2023 ; Cachaza, 2021 ; Dede, 2022].

In summary, the opening width has only a minor influence on the overall nanowire morphology. As the characteristic features are confined to the edges, increasing the width mainly extends the central region. Consequently, a 200 nm-wide nanowire can be regarded as a scaled-up version of a 50 nm-wide one.

4.3.2 Growth temperature

In this section, we investigate the influence of the growth temperature (GT) on the morphology of the nanowires, focusing on its impact on lateral overgrowth and thickness.

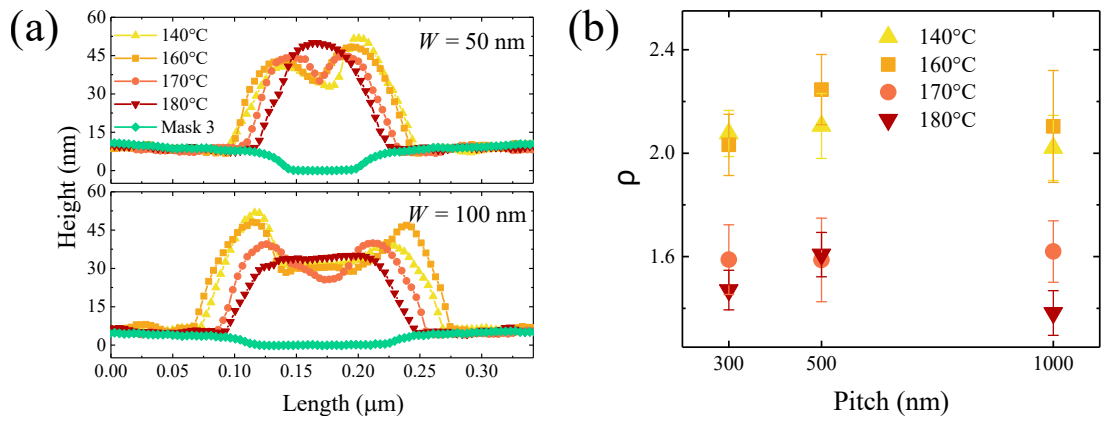

FIGURE 2.13 – Influence of growth temperature on the NW morphology. (a) AFM profiles for two $\langle\bar{1}10\rangle$-oriented NWs whose width is 50 nm (top) and 100 nm (bottom). The deposited thickness is 30 nm and the pitch is 1000 nm. (b) Change of ρ versus pitch at different growth temperatures for 30 nm-thick $\langle\bar{1}10\rangle$-oriented NWs and width opening of $W = 100$ nm.

We restrict our analysis to $\langle 1\bar{1}0\rangle$-oriented NWs as the effect of GT is the most evident for this direction.

The change in the AFM cross section profile of two $\langle\bar{1}10\rangle$-oriented NW widths ($W = 50$ nm top and $W = 100$ nm bottom) with respect to the GT is displayed in figure 2.13(a). The temperature was varied from 140 to 180°C with 10°C steps. For both considered widths, the wider cross sections of NWs grown at 140 and 160°C are visible while the height in the center remains close to the nominal thickness of 30 nm. The growth performed at 180°C shows a different behavior. Indeed, as the lateral overgrowth is reduced with an increasing temperature, super-elevations disappear at 180°C. For $W = 50$ nm, they merge leading to a triangular shape with {111}A facets and a rounded tip. For $W = 100$ nm, a flat (001) top facet is observed. This is due to an enhanced diffusion on the crystal [Albani, 2019] yielding a higher thickness than the nominal one, consistent with the work presented in [Morgan, 2023].

Figure 2.13(b) displays the evolution of ρ as a function of the pitch at four different growth temperatures. Values are calculated from the nanowires shown in panel (a). The evolution of ρ as a function of the pitch yields the diffusion length of Te adatoms on the mask $\lambda_{\mathrm{Te/mask}}$, as Hg adatoms play no role in the growth rate. First, it can be observed that the ρ values are consistently above 1, indicating that material deposition exceeds the nominal growth, thereby preventing a net diffusion from the nanowires to the mask. This regime contrasts with most previous studies, particularly on GaAs, where ρ is below 1 and the net flux occurs from the growing crystal toward the mask area [Dede, 2022 ; Cachaza, 2021]. As no significant change in ρ with the pitch is visible, the slight fluctuations are most likely due to variations in the etching profile of the mask, and $\lambda_{\mathrm{Te/mask}}$ is found to be below $(min(P) - W)/2$. Hence, we get $\lambda_{\mathrm{Te/mask}} < 100$ nm for all studied GTs. For that reason, we conclude that the NWs grow independently from each other and that there is no synergetic growth effect in arrays of NWs. This regime differs from works involving the SAG of III-V materials [Dede, 2022 ; Cachaza, 2021].

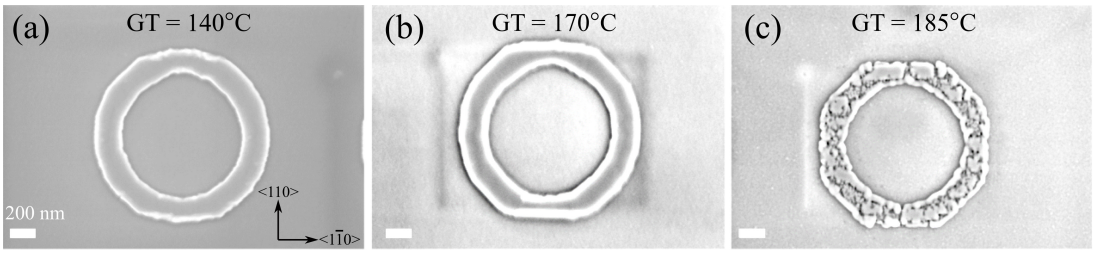

FIGURE 2.14 – Top-view SEM images of three HgTe ring nanostructures grown at (a) 140°C, (b) 170°C, (c) 185°C. The traces around the outer ring are carbon contamination that have been deposited by the electron beam of the SEM when imaging with a larger magnification.

Considering now the change in GT, we can see that NWs grown at 140 and 160°C show significantly higher ρ values than those of growths performed at 170 and 180°C. At GT = 180°C, the overgrowth seems to be the most limited even though there is a bit of overlapping with the NWs grown at 170°C. This change as a function of the temperature can be explained by the competing phenomena at play during the growth. We assume here that there is no adatoms desorption from the surface of the crystalline NW in the studied GT range, the Te sticking coefficient on HgTe or CdTe remaining 1. This assumption is corroborated by the nominal thickness found in the center of the NW for GTs below 180°C in figure 2.13(b). Hence, Te adatoms arriving onto the mask have three different behaviors : i) nucleate on the mask, ii) diffuse toward the HgTe crystal, or iii) undergo desorption. The observed variation in ρ reflects a corresponding change in $\lambda_{\mathrm{Te/mask}}$, which depends on the diffusion coefficient D and the characteristic desorption time τ. As the temperature increases, fewer adatoms contribute to nanowire growth, resulting in a decrease in both ρ and $\lambda_{\mathrm{Te/mask}}$. This reduction limits the number of adatoms available around an opening for nanostructure formation. Moreover, the absence of parasitic clusters on the mask indicates that tellurium adatoms desorb close to their impinging sites.

The effect of temperature is also visible in the shape of ring patterns grown by selective area epitaxy. The three top view SEM images in figure 2.14 illustrate the influence of this parameter on the morphology of a 30 nm-thick ring nanostructure grown at 0.26 ML/s from a 100 nm-wide opening. As the growth temperature increases, the formation of side facets is promoted on the outer rim of the ring which is turned into an octagon. At GT = 140°C, no clear side facet is visible, only accumulation of adatoms at the edges parallel to the $\langle 1\bar{1}0\rangle$ direction (top and bottom part of the ring here) is observable as there is a rougher and wider outline. This effect is weaker in the inner side, at the $\langle 1\bar{1}0\rangle$ edges. Indeed, the collection area of diffusing adatoms for the inner rim is smaller due to its concave shape. At GT = 170°C, the $\{111\}$ facets along the $\langle 1\bar{1}0\rangle$ direction are visible on the external side. Facets along the $\langle 110\rangle$ and $\langle 100\rangle$ directions, are still in the process of formation. Regarding the inner side, there is a slight adatom concentration at the $\langle 1\bar{1}0\rangle$ edges, similarly to the previous image. At GT = 185°C, the facets are formed in every azimuth of the plane for the outer rim. The inner side of the ring, shows no clear faceting and, therefore, keeps a more or less constant shape throughout the different

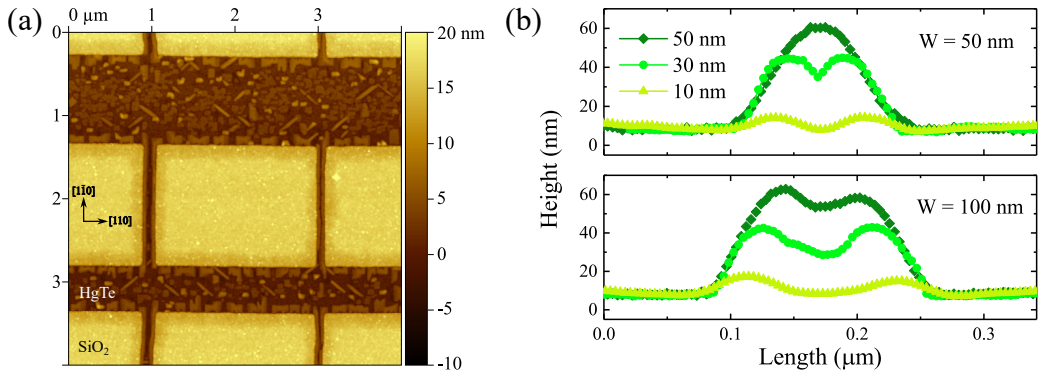

FIGURE 2.15 – Thickness influence on the opening filling. (a) AFM scan of 5 a nm-thick growth. The filling of the openings is not uniform but displays a collection of island nucleation sites. Along the $\langle 1\bar{1}0 \rangle$ direction the filling of the edges is continuous. In the $\langle 110 \rangle$ axis the filling shows discontinuity. (b) Change in the NW cross section morphology for three different nominal thicknesses for two $\langle 1\bar{1}0 \rangle$ oriented NWs whose opening width is 50 nm (top) and 100 nm (bottom). The growth temperature is 160°C for the 10 nm-thick growth and 170°C for the 30 and 50 nm-thick growths.

growth temperatures. This is most likely because the growth is kinetically driven rather than thermodynamically, which would have favored symmetric morphologies between the outer and inner sides, as explained in [De Donno, 2022]. Here, the inner rim would tend to form different side facets than the outer rim but they are likely not stable, yielding to this constant rounded shape of the inner rim for every GT. However, the top surface becomes very rough. This growth temperature is then detrimental in the scope of transport measurements.

In conclusion, the growth temperature is a key parameter governing the morphology of the nanostructures. It affects both the diffusion length of Te adatoms on the HgTe(001) facet and the behavior of adatoms impinging on the SiO_2 mask, providing control on the lateral overgrowth of the nanowires. Higher temperatures promote the formation of side facets, as the crystal reorganizes toward energetically favorable configurations. However, optimizing the morphology must be balanced with maintaining crystal quality, since excessively high growth temperatures can degrade the top surface.

4.3.3 Deposited thickness

This last section focuses on the influence of the deposited thickness on the nanowire morphology. Here, we show the morphological evolution of the NW crystal from the first layers to its typical shape with {111} side facets and side grains.

Figure 2.15(a) displays a 5 nm growth, revealing the first steps of the nanowire formation. We observe that the filling of the opening is not complete and not uniform, and no layers are formed yet, even in large openings. We rather observe the formation of islands. Their geometry change with respect to the opening orientation. For [110]-oriented apertures, the edges display squares ; this shape is not found in the center of the nanowire. For the [1$\bar{1}$0] direction, a continuous deposition along the edges is visible. The 50 nm-wide opening, corresponding to the vertical line on the right hand side, is thus almost

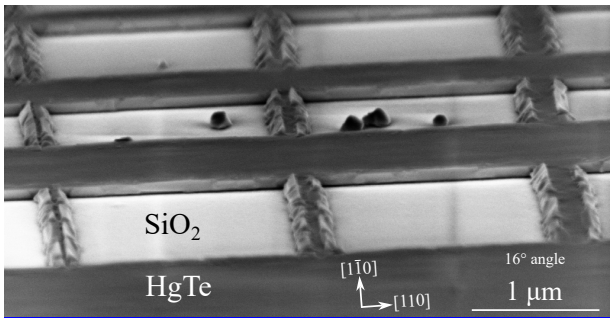

FIGURE 2.16 – 16°-angle birdview SEM image of a selective grid. The nominal thickness is 100 nm. The $\langle 1\bar{1}0 \rangle$ axis shows {111} facets on the edges. The overhang can be distinguished for the $\langle 110 \rangle$ direction.

completely filled in an uniform way.

This also indicates that the morphologies observed in the previous sections do not appear immediately, but evolve progressively with the deposited thickness.

The formation of the side facets depends on the deposited thickness as shown in figure 2.15(b) which displays the morphology evolution of $\langle 1\bar{1}0 \rangle$-oriented NWs for three different nominal thicknesses. AFM cross sections taken from 50 nm- (top) and 100 nm-wide (bottom) openings at for each growth are shown. The upper part of the NW shrinks as the structure grows. Consequently the super-elevations might start to merge. It is the case for the 30 nm-thick growth of the 50 nm-wide NW (bright green top) and the 50 nm-thick growth of the 100 nm-wide NW (dark green bottom). Eventually, they would fully merge as shown by the 50 nm-thick growth of the 50 nm-wide NW (dark green top). Here, the cross section is similar to a triangle with {111}A facets and a rounded tip. Due to the merging, we now have a height in the center exceeding the nominal thickness as described in [Morgan, 2023]. The same trend is expected for the 100 nm wide NW with a greater deposited thickness. Considering a 10 nm deposition (light green), that is just above the mask level, only {115} facets are formed and lateral overgrowth is already present. We suppose that during the growth, the angle of the nanostructure facets will be more pronounced until it reaches 54.7°, the angle of {111} facets. The width at the basis of the NW is constant with the deposited thickness. Nevertheless, after the merging, the lateral overgrowth will be larger as we show below. explained in [Morgan, 2023].

Figure 2.16 presents a grid pattern obtained from the nominal growth of a 100 nm-thick HgTe layer. Thus, we can assess the evolution of the crystal shape after excessively large HgTe deposition. While the selectivity remains good, with only a few parasitic grains on the mask, clear anisotropies appear between the two crystallographic orientations : ridges along [110]-direction show a pronounced overhang, whereas those along [1$\bar{1}$0] exhibit {111} facets. Thus, the typical shapes of these two directions are maintained even for thick growth. However, the side facets and the top surface between the two super-elevations display poor crystalline quality. The increased thickness also results in structures that are significantly larger than the targeted one-dimensional geometry, far from the intended nanometric scale. Consequently, thick depositions of this kind are excluded from further

consideration for device fabrication.

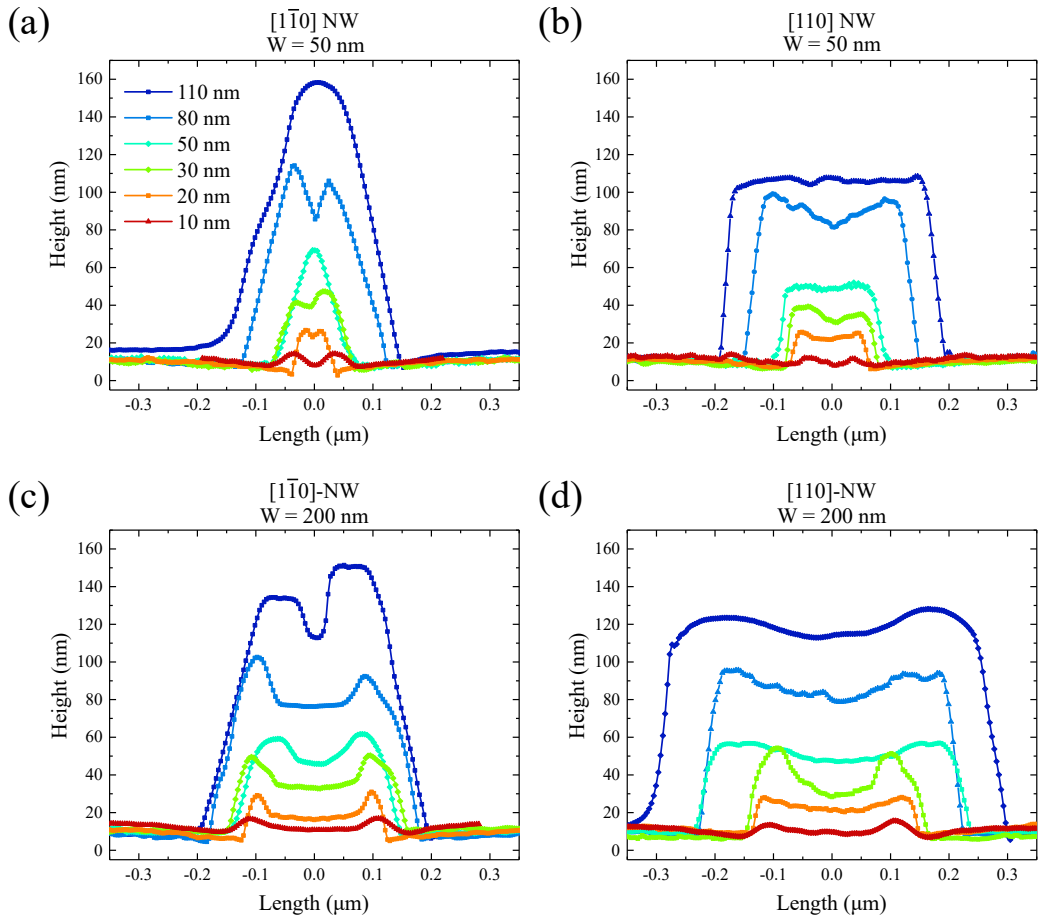

FIGURE 2.17 – Evolution of NWs morphology as the nominal deposited thickness is increased. In panels (a) and (b), respectively (c) and (d), we consider a 50 nm-wide, respectively 100 nm-wide, opening. NWs in (a) and (c), resp. (b) and (d), are oriented along [1$\bar{1}$0] axis, resp. [110] axis. All growths have been performed at 170°C, but do not come from the same patterned substrate.

Figure 2.17 illustrates the morphological evolution of [1$\bar{1}$0]- and [110]-oriented nanowires originating from 50 nm- and 200 nm-wide openings. Considering first the NWs oriented along [1$\bar{1}$0], shown in panels (a) and (c), we observe a striking increase in the NW base width once the super-elevations have merged. For example, the 50 and 80 nm-thick growths from the 50 nm-wide openings, panel (a), are almost as large as their counterparts grown from a 200 nm-wide opening in panel (c). This growth behavior is similar to that reported in [Morgan, 2023], where the incorporation of subsequent adatoms occurs predominantly on the side facets. As a result, the width of the epitaxial structures increases significantly while, the vertical growth rate reduces. Beyond approximately $t = 50$ nm of deposited thickness, the height maxima of nanowires grown from $W = 50$ nm consistently exceed the nominal thickness, indicating an enhanced local growth rate when the super-elevations merge. For NWs with $W = 200$ nm, the formation of a flat surface on top of the super-elevations can postpone the merging of the {111} facets, while the nominal thickness is still reached in the center.

For the [110] in-plane orientation, the AFM profiles are shown in panels (b) and (d).

The characteristic morphology associated with this direction is consistently maintained. The upper part of the structures exhibits either tilted side grains or a flatter region, which may correspond to the progressive filling of the central space. As the deposited thickness increases, this upper region becomes larger. In this orientation, the nominal thickness is rather well preserved. The large apparent increase observed in panel (d) for the 110 nm deposition is likely an artifact of the AFM measurement.

In summary, we have investigated the enhanced selectivity observed for HgTe nanostructures grown in wide openings. The lateral overgrowth of nanowires was found to be independent of the aperture width. Consequently, wider nanowires can be regarded as stretched versions of narrower ones : the central flat region expands while the edge morphology remains essentially unchanged. For $\langle 1\bar{1}0\rangle$-oriented slits, this characteristic is maintained until the super-elevations merge, a process that can be triggered either by increasing the growth temperature or by depositing a thicker HgTe layer. The formation of the characteristic morphologies, $\{111\}$ side facets for $\langle 1\bar{1}0\rangle$-oriented nanowires, side grains for $\langle 110\rangle$-oriented ones, requires a minimum deposition thickness of approximately 20 nm. Finally, the mask design has only a limited impact on nanostructure morphology, as the parameter ρ remains independent of the pitch down to 300 nm, indicating that the nanowires grow independently from each other.

4.4 Cap layer

In the scope of transport measurements, it is mandatory to protect the HgTe top surface electronic states. The in-situ growth of a CdHgTe layer immediately after the SAG has been studied to obtain core-shell structures. This arrangment helps reducing surface states that could trap charge carriers and degrade transport measurements by introducing scattering or instability in the active HgTe layer. In addition, this barrier prevents the desorption of Hg atoms. The CdHgTe cap layer has the advantage of being grown at the same temperature as the HgTe deposition. However, because of the absence of selectivity of CdTe with respect to the SiO_2 extensive parasitic growth is expected, the reader can refer to Appendix B for details.

Figure 2.18 panel (a) shows an SEM image of a 30 nm-thick HgTe layer grown by SAE, followed by the deposition of a 20 nm CdHgTe barrier. The cross-shaped morphology characteristic of the pattern is preserved, although parasitic growth is observed on the mask, in the form of both small and large grains. The larger grains may originate during the HgTe growth, whereas the smaller ones are attributed to the cap layer deposition. Panel (b) displays an AFM profile of a 50 nm-wide and 30 nm-thick nanowire, along with a typical profile of a 50 nm-wide nanowire extracted from the growth shown in (a) for comparison. Parasitic growth is clearly visible, leaving some uncertainty regarding the effective thickness of the cap layer. More importantly, however, the cap layer faithfully reproduces the nanowire profile, confirming complete coverage of the structure and thereby

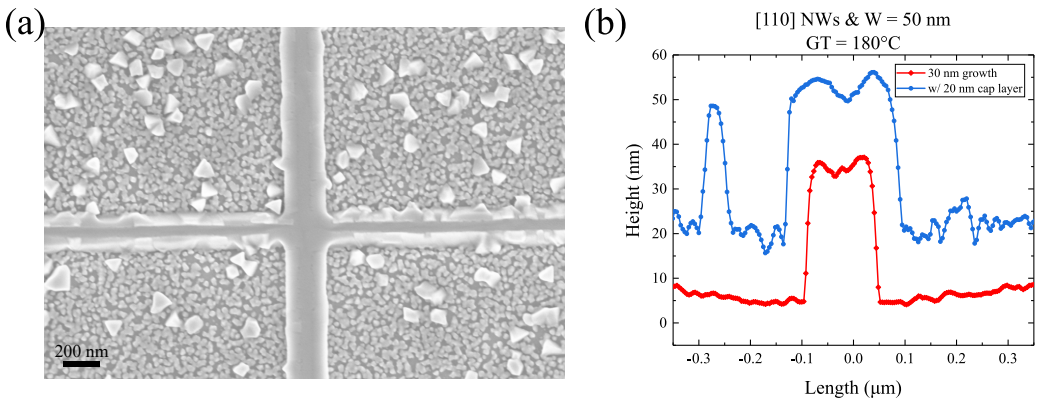

FIGURE 2.18 – Parasitic growth after cap-layer deposition. (a) SEM micrograph of a 100 nm-wide cross after the growth of 30 nm of HgTe followed by the deposition of a 20 nm-thick CdHgTe cap layer at 180°C. (b) AFM profiles of 50 nm-wide [110]-oriented NWs (red) without cap layer and (blue) from the growth mentioned in (a). The difference of morphology and parasitic growth with and without cap layer are evidenced.

ensuring effective protection of the top-surface electronic states.

As we have seen the parasitic growth is non negligible during the cap layer deposition making the nanostructures way larger. In order to limit parasitic growth and the alteration of the nanostructure pattern during the cap layer deposition, the latter has been set to 10 nm. The accurate composition of the cap layer is described in Chapter 3 when computing the capacitance of the gate.

5 Investigation of alternative mask materials

Even though the successful realization of HgTe nanostructures obtained by SAG has been demonstrated, we have studied a different process for the definition of the mask openings. The goal is to design openings with dimensions closer to their nominal value and further reduce the opening width. The process has been engineered by the group at IEMN. For this purpose, the mask consists of two materials. First, a 5 nm-thick alumina layer, Al_2O_3, is deposited on the substrate by atomic layer deposition. Then, 30 nm of silicon dioxide is deposited in the same way as mentioned above. The pattern is also designed similarly as before. The main difference lies in the etching of the openings. Here, the RIE is set until the alumina layer. The final opening through the latter is then completed using a wet chemical etchant selective to Al_2O_3. The wet etch is isotropic and etches beneath the SiO_2. However, they could show that the overhanging SiO_2 disengages and fall on the substrate, preventing lateral widening of the opening. The obtained morphology for the openings are shown as red and purple lines in figure 2.19(a). The mask is therefore much thicker. The openings are very sharp, matching the nominal width from the substrate interface to the mask top surface. A thicker mask would help restrain the nanostructures within the mask openings for thin layers.

An alternative version of this process has also been studied. The silicon dioxide mask

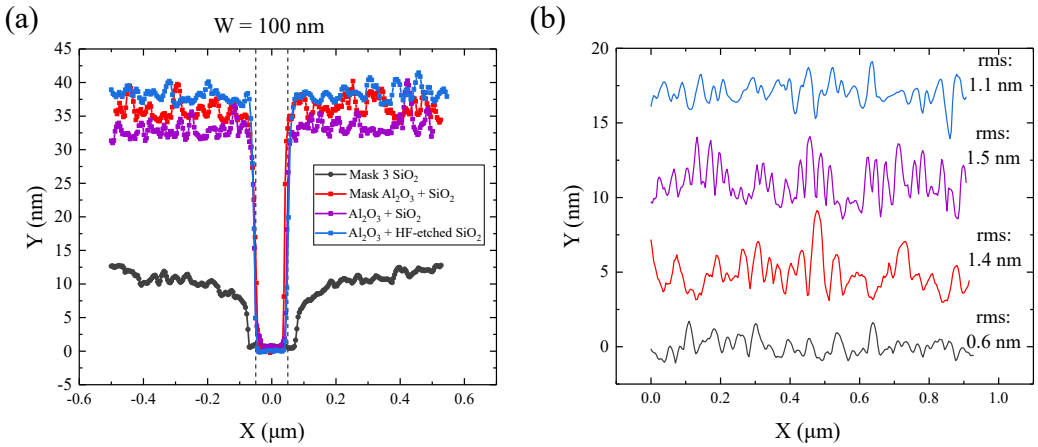

FIGURE 2.19 – Profile and roughness characterization of different masks. (a) Opening profiles variation between the standard procedure, SiO_2 mask, and the combination with alumina. Both purple and blue lines are extracted from a device mask. (b) Profiles of the top surface masks scanned far from the openings, colors are set accordingly to (a). Their respective roughness, rms, is indicated. Curves are shifted vertically for clarity.

is etched with HF at the end of the process. The goal is to reduce the mask top surface roughness. The morphology of the mask is still very precise and matches the wanted dimensions as shown by the blue line figure 2.19(a).

In figure 2.19(b), an AFM-extracted profile of the top-surface mask is shown, where each line corresponds to a different mask, as indicated in the legend of panel (a). The standard process, Mask 3 (SiO_2), exhibits the lowest roughness . In contrast, the Al_2O_3+SiO_2 procedure leads to the highest roughness, with an rms value of up to 1.5 nm, while the variant method including HF etching yields an intermediate roughness of 1.1 nm.

The importance of mask roughness on selectivity is demonstrated in figure 2.20. Four different growths are compared. The HgTe deposited thickness is set to 20 nm, so that the patterned growth remains inside the openings. The growth temperature is changed between 170 and 185°C. The mask is a combination of alumina and silicon dioxide, without (w/o) or with (w/) the final HF-etching step. The effect of the temperature is not visible for the growths on the non HF-etched mask, see first row as both densities of parasitic grains are alike. The deposition on the mask is significant in both cases. However, a slight enhancement is noticed for the HF-etched mask, see second row. Now, considering the impact of the HF-etching, we see that for the two growths at 170°C, see first column, no major difference can be seen. The density of parasitic grain is similar in both cases. If we focus on the second column, at 185°C, the growth with HF-etching is again a bit better. It should be noted that no particular features are visible in the different crystal orientations, thus we can not differentiate between the [110] and [1$\bar{1}$0] axis. Nevertheless, the roughness in the openings is satisfying and does not exceed 0.3 nm.

The low roughness of the mask appears as a parameter of significant importance in achieving SAG.

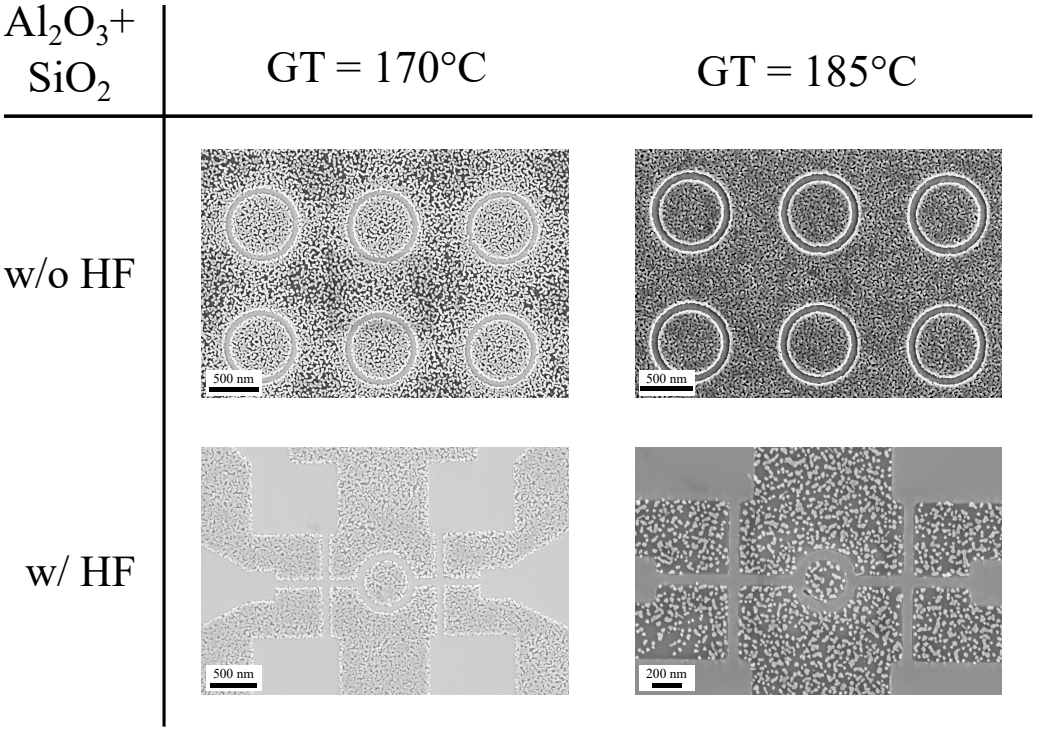

FIGURE 2.20 – Comparison of growths on Al_2O_3+ SiO_2 masks with (w/) and without (w/o) HF-etching. The growth temperature (GT) is changed during experiments. The nominal thickness of the growth is 20 nm.

6 Conclusion

In conclusion, we have demonstrated the SAG of in-plane HgTe nanostructures by MBE. The selectivity is achieved for several growth temperatures and growth rates with almost no parasitic growth on SiO_2 masks, yielding a good reproduction of the designed patterns. The growth temperature has been identified as a preferential parameter for tuning the morphology of the nanostructures. High growth temperatures, typically 170 and 180°C, limit lateral overgrowth on the mask and enhance nanostructure faceting. We have also seen that the design of the mask influences the growth. There is a strong anisotropy of growth morphology with respect to the three in-plane directions : $\langle 100 \rangle$, $\langle 110 \rangle$ and $\langle 1\bar{1}0 \rangle$. While a flat top surface of NW is maintained for the $\langle 100 \rangle$ NW direction, tilted grains appear for the $\langle 110 \rangle$ direction and super elevations for the $\langle 1\bar{1}0 \rangle$ direction. The latter are due to surface diffusion from the $\{111\}$A side facets. The characteristic features of these nanowires remain concentrated at the edges, so that varying the mask opening width essentially results in a stretched or compressed version of the same morphology. For narrow openings, the super-elevations can merge into a single ridge with $\{111\}$A side facets, resulting in a triangular cross section with a rounded top. The deposited thickness can also be used to tune the morphology of the nanowires. Above a certain thickness, for a fixed width, the initially trapezoidal shape progressively suppresses the top surface, and the cross section reverts to a triangular geometry with $\{111\}$ side facets. Once this shape is reached, the top region becomes significantly thicker than the nominal deposition, as

adatom diffusion from the side facets enhances material accumulation at the apex. We further observed that the nanowires expand laterally once the triangular cross section is established. For the [110] orientation, side grains are present throughout the growth process.

In addition, we found that the zinc-blende HgTe NWs exhibit a satisfying epitaxial relation to CdTe(001) substrate. The NWs are found free of misfit dislocation at the interface. Both the g-moiré maps and the NPED technique emphasize the strain relaxation of the NWs above the substrate unlike 2D layers. The tilted grains present along the [110] direction are twin planes of the (111) planes from the central grain. Considering the $[1\bar{1}0]$ direction, the {111}A side facets induce shear at the basis of the NW. The NW is thus compressed towards the center.

So far, the attempts with alternative mask materials, combining Al_2O_3 and SiO_2, are not tailored for the selective growth of HgTe nanostructures. The main limitation identified is the high roughness of the silicon dioxide. In this way, further optimization of the HF-etching process is therefore required to achieve sufficient smoothing of the SiO_2. Nevertheless, the growth within the openings appears satisfactory, revealing a complete and homogeneous filling.

This study have evidenced the growth behavior of HgTe crystal during selective area epitaxy. We demonstrated the homogeneous and complete filling of the openings for growths thicker than 10 nm. In addition, strong parasitic growth was observed during the deposition of the cap layer. These findings motivated the choice of a 10 nm-thick HgTe growth followed by a 10 nm-thick in-situ HgCdTe cap-layer deposition for subsequent device fabrication.

Chapter 3

Nanofabrication

1 Introduction

The patterning of the nanostructures is a key step in obtaining functional and measurable devices, assessing the potential of the SAG technique for HgTe. The central challenge lies in the presence of mercury in the nanostructures. It is a highly sensitive material that can easily desorb during the fabrication process. Therefore, even conventional techniques discussed in this chapter, require a few adaptations to avoid sample degradation. Thus, laser lithography is used instead of electron-beam lithography, to avoid local heating of the sample or introduction of charging defects [Yasuda, 1994]. Furthermore, based on previous HgTe-based work, all steps including thermal processes are limited to below 80°C [Thomas, 2016]. In summary, this section details the various steps required for devices fabrication, emphasizing the modifications introduced to accommodate both the dimensional constraints of the nanostructures and the requirements of subsequent magneto-transport measurements.

2 Definition of the design for the nanodevices

After having successfully demonstrated the capabilities of SAG to obtain HgTe-based nanostructures, the design for nanodevices has been defined. One asset of the SAG is the possibility to define all the layers, from the mask opening to the contacts deposition, directly aligned with each other as visible in figure 3.1(a). The first blue layers define the pattern obtained in the silicon dioxide mask thanks to electron-beam lithography and reactive ion etching, see figure 3.1(b). The selective growth process yields HgTe structures that follow these predefined patterns. They are designed such that the nanostructure is positioned at the center, with large, 2D-like zones expanding outward. These extended areas facilitate laser lithography by accommodating its resolution limits during contact definition. Additionally, fabrication steps are carried out away from the nanostructures to minimize the risk of damage. The top gate contact is divided into two zones : one that covers the central nanostructure, and another that extends laterally without overlapping the HgTe layer. This design reduces the risk of short circuits while providing a larger area to facilitate the bonding step - see figure 3.1(a) and (b).

Considering the epitaxy layer, HgTe layer in figure 3.1, all structures follow the same arrangement that is six ohmic contacts to measure longitudinal and transversal current in a typical Hall bar four-terminal disposition. Only the geometry of interest in the center is changed. Several patterns are designed with different sizes and orientations, as summarized in table 3.1. Figure 3.1 shows the examples of a nanowire (b), a circular ring (c), and a diamond ring (d).

We recall the reader that for the growth of sample tailored for electronic measurements, an in-situ CdHgTe cap layer is deposited on the HgTe layer to obtain core-shell structures, protecting the surface.

TABLE 3.1 – Presentation of the different devices geometries and their dimensions, length L and width W. For nanorings, r is the inner radius of the circular rings and c is the inner side length of the diamond rings.

	Orientation	Dimensions		Radius
Hall bar	[110] & [1$\bar{1}$0]	$L = 120$ μm/$W = 24$ μm $L = 15$ μm/$W = 3$ μm		
Nanowires	[110] & [1$\bar{1}$0]	$L = 2$ μm	$W = 50$ nm $W = 100$ nm $W = 200$ nm	
		$L = 1$ μm $L = 5$ μm	$W = 100$ nm	
	[100]	$L = 2$ μm/$W = 100$ nm		
Nanorings	[110], [1$\bar{1}$0] & [100]	$L = 2$ μm/$W = 100$ nm		$r = 250$ nm $r = 400$ nm $c = 600$ nm

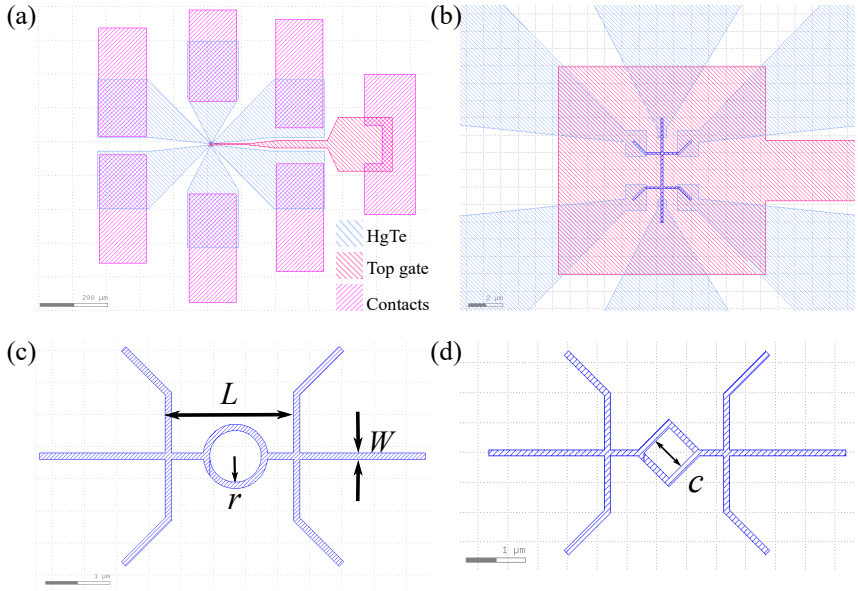

FIGURE 3.1 – Layers arrangement for the device fabrication and device design. (a) Design of a nano-device. The role of the different layers is precised. (b) Zoom-in of the center of (a) to reveal the nanostructure. (c) and (d) are other examples of ring geometry for magneto-transport studies.

3 Process of fabrication

The nanofabrication of the devices took place at the Plateforme Technologique Amont (PTA) in CEA. The following steps have been elaborated thanks to the knowledge and experience of previous works performed at the PTA. It also benefited from the expertise of IEMN and LMP/LITP labs at CEA on device fabrication. The devices are designed to enhance the probability of reliable bonding to the measurement chip while minimizing the risk of damaging the epitaxial HgTe layers

3.1 Gate dielectric

A gate dielectric is a thin insulating layer that isolates the metallic gate from the electron channel while enabling electrostatic control of the transistor. Because of its high dielectric constant, alumina (Al_2O_3) is a relevant material to serve as a gate oxide. The deposition of an alumina layer is performed using atomic layer deposition (ALD) (Fiji, Cambridge Nanotech). A short circuit between the gate contact and the nanostructures resulting from a defective gate dielectric would be highly detrimental. Thus, it was considered advantageous to deposit the passivation layer deposition immediately after the epitaxy, where the surface contamination, for example resist residues, would be minimum. Nevertheless, scanning electron microscopy (SEM) is required after growth to evaluate the quality of the epitaxial nanostructures. As a result, a cleaning step using acetone and ultrasonic agitation is performed before introducing the sample into the ALD chamber. This precaution helps ensure a clean surface while preserving the structural integrity of the nanostructures. The ALD process ensures a complete coverage of the nanostructures by the passivation layer as represented in figure 3.2(a). A conventional planar top-gate

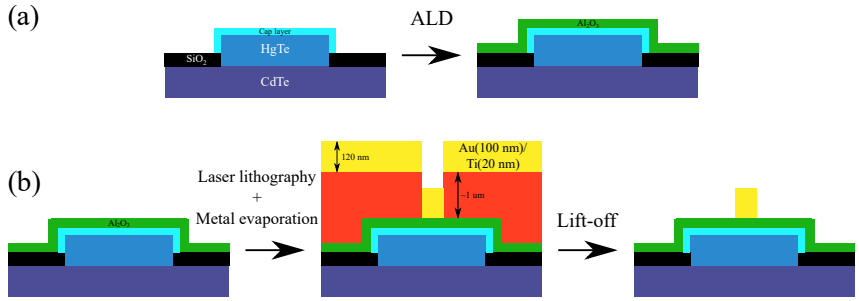

FIGURE 3.2 – Fabrication steps for (a) the gate oxide and (b) the gate electrode.

configuration is expected for the largest Hall bars (width of several micrometers) and a "all-around" gate geometry for the narrowest devices. The deposition has been adapted from an existing process to be performed at 80°C. It is a plasma-free process with trimethylaluminum (TMA) and H_2O as precursors. The deposition of about 15 nm is achieved with a pulse time of 0.06 seconds and a purge time of 60 seconds for each precursor. Here, a reduction in temperature implies a reduction in the growth rate to ≈ 0.80 Å/ cycle.

3.2 Top gate electrode

Following the gate oxide deposition, the gate electrode is immediately fabricated to prevent damage to the alumina layer during subsequent steps and to minimize the risk of current leakage. Here, the sample is cleaned with three successive baths of acetone, isopropanol (IPA), and deionized water, each for one minute. A layer of AZ1512 photoresist is then deposited by spin-coating, using the following parameters : 4000 rpm, 2000 rpm^2 acceleration, for 60 s. The resulting resist thickness is approximately 1 μm. The resist is soft-baked at 80°C for one minute. This lower baking temperature is necessary due to the presence of mercury in the sample ; nonetheless, the resolution achieved remains sufficient for the desired patterning. After exposure to the UV laser beam (Heidelberg μPG101), the development of the exposed zones is performed using a 50% AZ developer and 50% deionized water solution for one minute.

Electrodes are fabricated using metal evaporation of Ti(20 nm) and Au(100 nm) on a Plassys Evaporator tool. An in-situ Ar-etch is performed just before evaporation to remove any resist residues on the Al_2O_3 top surface. Finally, a lift-off with acetone is used to remove the resist anywhere but at the location of the top gate electrodes. A sketch summarizing the above-mentioned steps is visible in figure 3.2(b).

3.3 Ohmic contacts

The last nanofabrication step before is the deposition of the metallic ohmic contacts. The procedure is very similar to the top gate electrode fabrication ; but a 30 seconds BCl_3 plasma etching step is performed before metal evaporation as shown in figure 3.3. The use of plasma etching enables to contact directly the HgTe epitaxial zones, etching at the

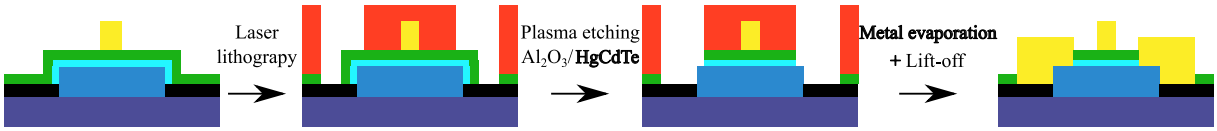

FIGURE 3.3 – Steps for the ohmic contacts

same time the alumina layer and the cap layer. Even though the latter is very thin, it is preferable to remove it for good contacts. There is a high chance for the HgTe layer beneath the cap layer to be also etched as the etching time is short and thus hard to control. However, this is not detrimental as it takes place far from the nanostructure, avoiding any risk of damage. And if the HgTe layer is fully etched, contact can still be made by the sides.

Exposure of the SiO_2 mask to plasma is not detrimental; it is actually beneficial as a rougher surface increases the chance of metal sticking; and therefore bonding. Thus, the contact pads are designed to cover two different zones, the large epitaxial zones of HgTe and the SiO_2 mask, to increase the probability of bonding as shown in figure 3.1(a).

During this step, the area of the metallic gate electrode is also increased. As visible in figure 3.1(a), this second metal evaporation slightly overlaps (far from the device) the first zone. This extension of the contact area enables bonding on a plasma-exposed SiO_2 area that appeared to be more favorable than the gate metal deposited on alumina.

3.4 Bonding

The chip holder for low-temperature measurements has 24 contacts, enabling the simultaneous connection of three devices. The connections are realized with gold threads thanks to a bonding machine. figure 3.4(a) shows a sample connected to the chip. In figure 3.4(b), details of the bonding are shown on the seven contacts (including the gate) of a nanodevice.

4 Gate efficiency

The depletion factor α of this barrier, defined as the ratio between the total capacitance and the electronic charge, characterizes how efficiently the top gate tunes the surface states. Thereby, it is interesting to assess the capacitance of the materials deposited between the metallic gate electrode and the semiconducting nanostructure [Baum, 2014].

In this case, the metallic gate electrode is separated from the HgTe top interface by the CdHgTe cap layer and the Al_2O_3 passivation layer. They will behave as two capacitors in series. Thus, the total capacitance can be expressed as C_{top} :

$$C_{top} = \frac{C_{Al_2O_3} \cdot C_{CdHgTe}}{C_{Al_2O_3} + C_{CdHgTe}} \tag{3.1}$$

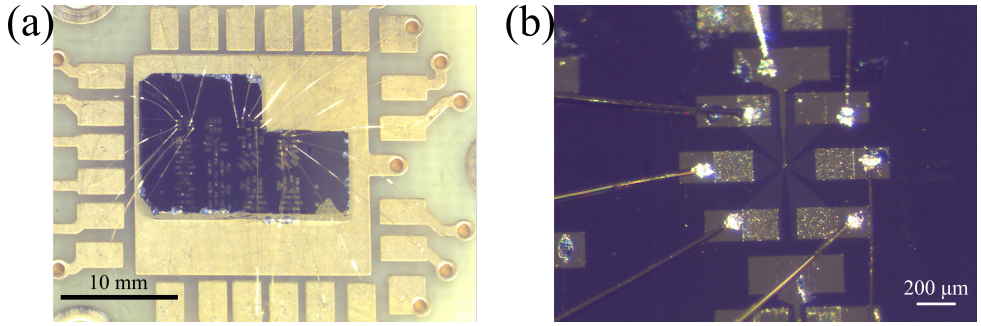

FIGURE 3.4 – (a) Sample on the chip holder. (b) Example of a nanodevice bonded to the connections. The gold wires binding the nanodevice to the chip holder thanks to six ohmic contact and the top gate electrode (at the top of the image) are visible. The grainy part of the ohmic contacts corresponds to the Au/Ti evaporation on the etched HgTe structures.

with surface capacitance calculated as

$$\mathrm{C} = \frac{\epsilon_0 \cdot \epsilon_r}{d} \tag{3.2}$$

where ϵ_0 is the vacuum permittivity, ϵ_r is the material permittivity, and d is the thickness of the considered layer.

The permittivity of the $Cd_x\ Hg_{1-x}Te$ layer is directly related to the amount of cadmium x through the following equation [Rolland, 1994] :

$$\epsilon_r = 20.5 - 15.6x + 5.7x^2 \tag{3.3}$$

The cadmium concentration in the cap layer appears to be essential for the determination of the electrical permittivity of the cap layer, and so, of the devices top capacitance. The evaluation of the cadmium concentration is addressed in the next section.

4.1 Determination of the Cd concentration in the cap layer

The proportion of cadmium in the $Cd_xHg_{1-x}Te$ cap layer is found thanks to its lattice parameter a. Acording to Vegard's law, the latter is indeed directly related to the cadmium concentration through the following expression :

$$a_f(x) = x \cdot a_{\mathrm{CdTe}} + (1 - x) \cdot a_{\mathrm{HgTe}} \tag{3.4}$$

X-ray diffraction (XRD) measurements [1] have been performed on a 1 μm thick growth - under the same conditions as for the cap layer deposition during the selective epitaxial growth - to measure the amount of cadmium. Here, a CdZnTe(211) substrate is used. Its peak is measured at a 2θ-ω angle of 71.405°. While the peak associated with the film is located at 71.276°. Thanks to Bragg's law we find the lattice parameter of the $Cd_xHg_{1-x}Te$

1. The reader can find the principle and operating details of the technique in Appendix A

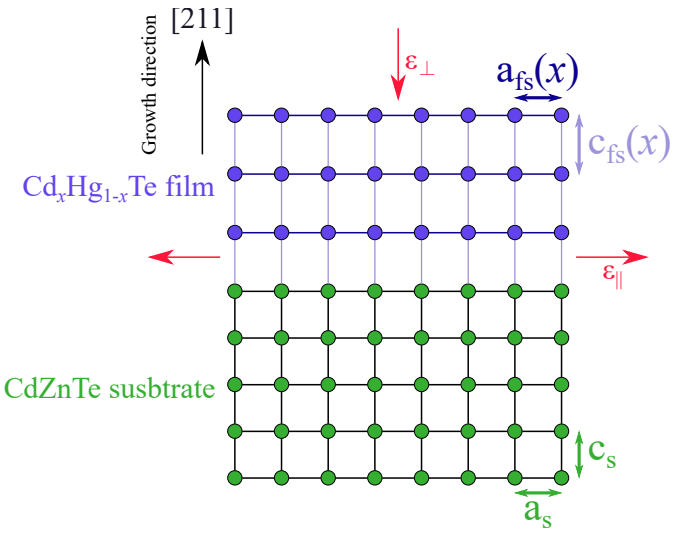

FIGURE 3.5 – Schematic representation of the crystal deformation due to in-plane compressive strain in the case of $Cd_xHg_{1-x}Te$ grown on CdZnTe(211).

layer along the z-direction :

$$c_{sf} = \frac{\lambda}{2\sin\theta}\sqrt{h^2+k^2+l^2} \tag{3.5}$$

Where $(h,k,l) = (4,2,2)$.

If we assume that the film is totally compressed on the substrate, as represented in figure 3.5, we can show that

$$\epsilon_\perp = \frac{c_{sf}-c_f}{c_f} = \frac{-2C_{12}(x)}{C_{11}(x)}\epsilon_\parallel \tag{3.6}$$

where $C_{11}(x)$ and $C_{12}(x)$ GPa are stiffness constants of the CdHgTe alloy following Vegard's law, with $C_{11} = 53.6$ GPa/$C_{12} = 36.6$ GPa for HgTe and $C_{11} = 53.5$ GPa/$C_{12} = 36.5$ GPa for CdTe.

And, as $\epsilon_\parallel = \frac{a_{sf}-a_f}{a_f}$, we find

$$c_{sf} = a_f(x)\left(\frac{2C_{12}(x)}{C_{11}(x)}+1\right) - \frac{2C_{12}(x)}{C_{11}(x)}a_s \tag{3.7}$$

That leads to a cadmium concentration of $x = 45.5\%$. On the other hand, if the film is assumed to be fully relaxed $x = 75\%$. The real concentration lies between this range of values.

4.2 Calculating the depleting factor

The proportion of cadmium being assessed, it makes it trivial to compute the capacitance of the cap layer. We consider the mean value of the Cd concentration, $x = 60.25\%$, and a thickness of 10 nm. For the alumina layer, standard values will be used. The elec-

trical permittivity of Al_2O_3 is taken at 7. Considering its thickness, precisely 180 cycles have been made during alumina deposition, and the thickness of the alumina layer would then be 14.6 nm.

Finally, the depleting factor α is obtained thanks to the following relation :

$$\alpha = \frac{C_{top}}{e} \tag{3.8}$$

where $e = 1.6\ 10^{-19}$ C is the electron charge.

Thus, it yields

$$\alpha = 19.45\ 10^{11}\ \mathrm{cm}^{-2}\mathrm{V}^{-1} \tag{3.9}$$

This value will be compared with the experimental data, obtained as the slope of the carrier density with respect to the gate voltage.

Chapter 4

Hall bars measurements

1 Introduction

After nanofabrication of devices from in-plane patterned structures grown by SAG, electrical measurements are performed to characterize their electronic properties.

This chapter starts by giving an overview of the experimental set up for low temperature magneto-transport measurements. Different aspects of the systems are covered, such as electronics, control of the magnetic field, and cryogeny for low temperature measurements. A comprehensive understanding of the experimental setup is of main importance for accurate measurements of delicate quantum properties.

The aim of this chapter is to demonstrate the proof-of-concept of the SAG technique for device applications. The characterization of the structures grown by SAG starts with two Hall bars with micrometer-scale dimensions to check the properties of the 2D electron gas (2DEG) in the active HgTe layer. Note that this 2D regime has already been studied in the literature [Thomas, 2017; Bendias, 2018]. This approach also provides a global knowledge of the electronic transport properties of HgTe without the complex one-dimensional transport effects. Studying 2D Hall bar geometries is also important to assess the quality of the SAG and device fabrication. These measurements would demonstrate the advantages and possibilities offered by SAG for device applications. In this Chapter only a Hall bar of dimensions $L = 120$ μm/$W = 24$ μm is described. The data referring to the other Hall bar, $L = 15$ μm/$W = 3$ μm, are presented in the Appendix C, as the two devices give similar results.

Several studies have evidenced clear manifestations of the quantum Hall effect in HgTe through magneto-transport measurements [Bendias, 2018; Thomas, 2017; Brüne, 2011]. Thin HgTe quantum wells are indeed characterized by high mobility of the order of magnitude 10^5 cm^{2}V^{-1}s^{-1}, such that one expects to reach the well-defined quantum Hall regime with vanishing longitudinal resistance and plateaus in the transversal conductance.

After a general presentation of this quantum Hall physics in HgTe, we present the experimental results obtained in the Hall bar when performing magneto-transport mea-

surements. Low magnetic field measurements are performed to characterize the electronic properties of the samples. In particular, carrier density, electron mobility, and elastic mean-free-path are extracted from the measurements to assess the quality of the samples. Subsequently, high magnetic field measurements are carried out to probe the band structure of the sample. Consequently, the peculiar properties of thin topological insulators are evidenced.

2 Experimental set up

2.1 Electronics

In this section, we present the organization and the role of the different elements of the setup for the electrical measurements of the nanodevices. A sketch of the setup is shown in figure 4.1. Measurements are performed with voltage bias U using a lock-in amplifier as a voltage source, in combination with a voltage divider composed of 100 Ω and 10 kΩ resistors on electrode n°2. The bias voltage sent to the sample is thus 1% of the lock-in voltage U. Electrode n°5 measures the current I flowing through the nanodevice and a low-noise SR570 current amplifier from Standford Research Systems is used to convert the current intensity to a voltage value, with a gain R_f ranging from 10^6 to 10^7 V/A. The gate voltage V_{gate} on electrode n°1 comes from the applied voltage V_g in series with a 10 MΩ resistor, which limits the current in the event of gate leakage. The voltage V_m across the resistor is monitored to detect any possible leakage current. Due to the 100 MΩ input resistance of the voltmeter, the effective gate voltage, in absence of leakage, is given by

$$V_{gate} = \frac{100}{110} V_g = \frac{V_g}{1.1} \tag{4.1}$$

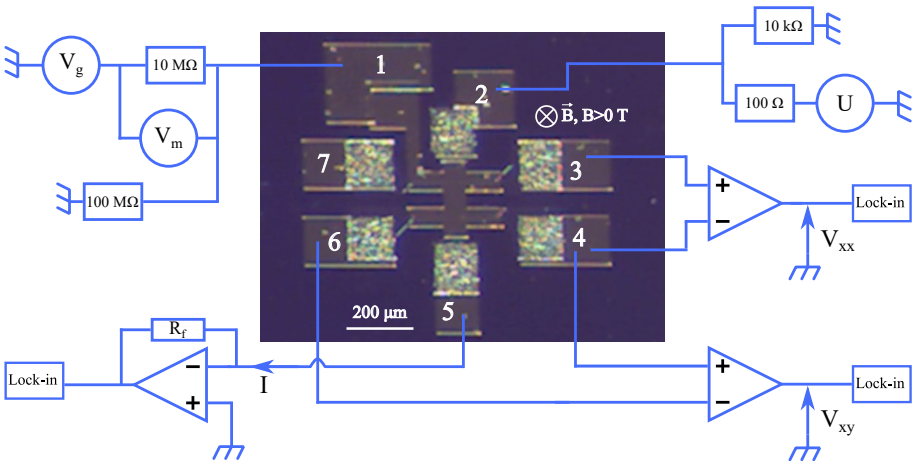

FIGURE 4.1 – Top view image of a Hall bar device taken with an optical microscope. The electrical set-up for the magneto-transport measurements is sketched around.

Both longitudinal and transverse voltages are measured with two lock-in amplifiers, an SR830 from Standford Research Systems and a 7265 from EG&G Instruments. Electrodes 3 and 4 are used to measure V_{xx} ; electrodes 4 and 6 measure the Hall voltage V_{xy}. They give access to longitudinal resistance $R_{xx} = V_{xx}/I$ and the Hall resistance $R_{xy} = V_{xy}/I$.

2.2 Magnetic field control

The magnetic field is applied using a superconducting magnet integrated into the cryostat. When the field is positive, it points upward in the vertical direction and penetrates the sample, which is mounted upside down, as illustrated by the cross in figure 4.1.

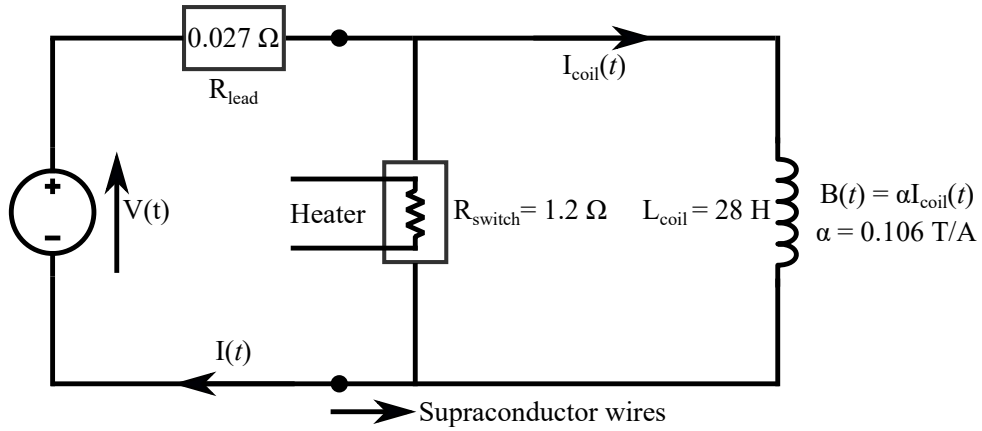

FIGURE 4.2 – Sketch of the electrical circuit driving and monitoring the superconducting magnet

Figure 4.2 reports the electrical circuit of the 28 H inductance magnet. The magnetic field B generated by the coil is proportional to the current flowing through it and is given by $B = \alpha I_{coil}$, where $\alpha = 0.106$ T/A is a calibration factor determined by the geometry of the magnet. The strongest magnetic field used for the measurements is $|B| = 5.3$ T. Since the superconducting magnet can be operated in persistent mode thanks to a superconducting wire placed in parallel with the coil, it is necessary to heat this wire (called switch) with a heater to make it resistive and allow the current source to feed the inductive coil, allowing external control of the current flowing through the coil. The time evolution of I_{coil}, and so B, is given by the following equation :

$$\begin{aligned} V_{coil}(t) = V_{switch}(t) &\iff L_{coil}\frac{dI_{coil}(t)}{dt} = R_{switch}I_{switch}(t) \\ &\iff L_{coil}\frac{dI_{coil}(t)}{dt} = R_{switch}(I(t) - I_{coil}(t)) \\ &\iff I_{coil}(t) + \frac{L_{coil}}{R_{switch}}\frac{dI_{coil}(t)}{dt} = I(t) \end{aligned} \tag{4.2}$$

The time $\tau = \frac{L_{coil}}{R_{switch}}$ is defined as the time constant of the electrical circuit.

The user can choose the setpoint current $I_{set}(t)$ and the sweep rate P_I in A/s. The setpoint current is reached through this ramp and one can express the applied current as a function of time :

$$I_{set}(t) = \begin{cases} I_{start} & \text{if } t < 0 \text{ (i)} \\ P_I t & \text{if } 0 \leq t < T_s \text{ (ii)} \\ I_{set} & \text{if } t \geq T_s \text{ (iii)} \end{cases} \tag{4.3}$$

Here, $T_s = (I_{set} - I_{start})/P_I$ represents the time required for the current to change from its initial value I_{start} to the target value I_{set}, at a rate P_I.

From line (ii) of equation 4.3 and equation 4.2, assuming $T_s \gg \tau$, the coil current is derived as :

$$I_{coil}(t) = I_{start} + P_I(t - \tau) + P_I\tau e^{-\frac{t}{\tau}}, \quad 0 \leq t < T_s \tag{4.4}$$

And

$$\mathrm{I_{coil}}(t) = \mathrm{I_{set}} - P_{\mathrm{I}}\tau e^{-\frac{t-\mathrm{T_s}}{\tau}}, \quad t \geq \mathrm{T_s} \tag{4.5}$$

At each instant of time, we have $\mathrm{B}(t) = \alpha \mathrm{I_{coil}}(t)$. This relationship is used to record the magnetic field during data acquisition, performed continuously during the magnetic field sweep, meaning that measurements are recorded in real time as the field evolves. The accurate determination of the magnetic field intensity relies on the accuracy of the time constant $\tau = \frac{\mathrm{L_{coil}}}{\mathrm{R_{switch}}}$. A comparison between upward and downward magnetic field sweeps reveals a slight offset in the magnetic field values, but it remains below 13 mT and is considered negligible for the analysis.

2.3 Lowering the temperature

The experiments were conducted in a cryogenic environment combining multiple cooling stages to progressively lower the temperature based on the strong dependence of temperature on the helium vapor pressure. The system is based on a liquid helium cryostat from Oxford Instruments which provides a primary cooling at 4.2 K, temperature of liquid ^{4}He at ambient pressure. The cryostat is equipped with a Variable Temperature Insert (VTI) which brings temperature down to 1.5 K when pumping the liquid ^{4}He introduced from the bath into the inner volume of the VTI through a needle valve. The reduction of the pressure evaporates the liquid and cools down the inner volume of the VTI where a ^{3}He insert from ICEoxford can be fitted to enable measurements down to 280 mK.

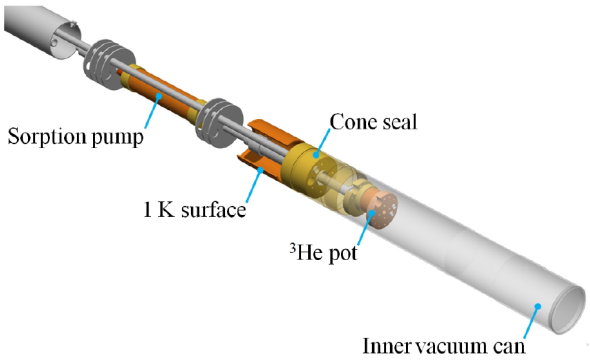

FIGURE 4.3 – Sketch of the an ^{3}He insert which can be fitted into a VTI. Taken from [Oxford Instruments, 2013].

A Variable Temperature Insert (VTI) is thermally linked to the ^{4}He bath via exchange gas. It allows for temperature control above 1.5 K, up to 20 K in this work. The 1.5 K environment provided by the VTI serves as a thermal sink for the ^{3}He condensation process. A sketch presenting the global view of the ^{3}He insert with the main elements is displayed in figure 4.3. The ^{3}He insert operates as a self-contained refrigerator that lowers the temperature to the sub-Kelvin regime. Gaseous ^{3}He is first condensed in a pot by

rising the temperature of the sorption pump with a resistive heater. Then by pumping into this pot, ^{3}He evaporates and cools down the sample to a base temperature around 280 mK. The pressure in the pot is lowered thanks to the sorption pump that cryo-pumps, i.e adsorbs, the gaseous atoms. The sample is mounted below this pot to benefit from the lowest achievable temperature.

For measurements at temperatures above 1.5 K, a heater on the sample holder is used, while the temperature of the sorption pump is kept high to maintain a finite pressure of ^{3}He gas in the stainless-steel tube. This gas serves as thermal link for efficient temperature regulation. Control loops relying on several electrical resistances are used to precisely monitor the temperature from 0.28 to 20 K.

3 Magneto-transport properties of HgTe

The aim of this section is to introduce the expected behavior of the HgTe Hall bars at both low (Hall effect) and high magnetic field (quantum Hall effect) to the reader. By hosting Dirac fermions, the surface states of thin HgTe layers are described by a linear energy dispersion and are thus strongly different from standard 2D parabolic electron gas. It leads to peculiar signatures of the Landau levels at high magnetic field. The description of this theoretical framework will be useful to explain and understand the experimental data.

3.1 Hall effect

One of the main effect when performing magneto-conductance measurements is the Hall effect. In the presence of a perpendicular magnetic field, electrons transported are forced to deviate toward one side of the sample, driven by the Lorentz force, as visible in figure 4.4. This creates a charge difference, that yields a voltage difference V_{xy}, associated with a transversal resistance R_{xy}, also called the Hall resistance.

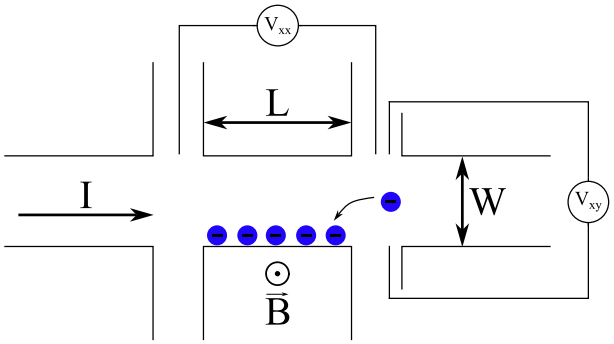

FIGURE 4.4 – Representation of the Hall effect in a Hall bar of length L and width W. Under a magnetic field B, electrons participating to the current are deflecting towards one side of the sample because of the Lorentz force. Their accumulation creates a charge difference in the transversal direction and so a voltage difference that can be probed through V_{xy}.

In a single carrier picture, one can show from the Drude model that the Hall resistance evolves as a linear function of the magnetic field, $R_{xy} \propto B$. The slope coefficient is often denoted as the Hall constant, R_H in Ohm/Tesla. The Hall effect is a useful tool to estimate 2D the carrier density n as

$$R_H = \frac{V_{xy}}{IB} = \frac{1}{ne} \tag{4.6}$$

The sheet resistance is defined as $R_\square = R_{xx}\frac{W}{L}$ and is equivalent to the 2D resistivity ρ_{xx}. The mobility of the carrier can be derived from the Hall constant R_H and the sheet resistance at zero magnetic field, $R_\square(B = 0\ \mathrm{T})$.

$$\mu = \frac{|R_H|}{R_\square(B = 0\ \mathrm{T})} \tag{4.7}$$

This analysis has been presented within the framework of a single-carrier model. However, it is important to emphasize that the expression for the Hall coefficient R_H depends on the number of carrier types contributing to transport. In a two-carrier system, electrons and holes, the Hall voltage is no longer solely determined by carrier densities, n and p for electrons and holes respectively, but also depends explicitly on the mobilities of both carrier types, μ_e and μ_h.

3.2 Quantum Hall effect

When increasing the magnetic force, the Lorentz force compels the electrons to adopt quantized cyclotron trajectories creating insulating states in the bulk, while skipping orbits appear along the edges creating conductive channels. This new state of electronic transport is known as the Quantum Hall effect (QHE). Figure 4.5(a) illustrates the QHE with no transport in the bulk and two counter-propagating conduction channels on the edges. These are chiral edge states propagating uni-directionally along opposite edges of the sample, with forward and backward moving channels spatially separated by the bulk. This absence of accessible backscattering paths renders the transport effectively dissipation-less, resulting in a vanishing longitudinal resistance.

This state of matter transforms a continuous density of state into discrete levels. The 2π-periodicity of the electron wave function results in a quantization of the system energy. These quantized energy levels are known as the Landau Levels (LLs). The number of occupied levels, that is the number of filled LLs, is known as the filling factor ν. Whenever the Fermi level is located between two successive LLs, the Hall conductance is constant with a fixed number of conducting edge channels. As a result, sweeping the Fermi energy through the different Landau levels produces a characteristic plateau-like behavior in the Hall conductance.

In the mean time, the longitudinal resistance R_{xx} experiences quantum oscillations, known as Shubnikov-de Haas (SdH) oscillations. These minima appear when the Fermi energy lies in the gap between two successive LLs with a low conductivity of the bulk, that

is weak backscattering. When the system is fully quantized, these minima reach zero : the bulk is totally insulating and transport only occurs thanks to the chiral edge states. The maxima of R_{xx} evidence the situations where the Fermi level is perfectly aligned with a LL. In addition, the width of the oscillation illustrates the broadening of the LLs, essentially due to the disordered potential of the scattering.

Parabolic electrons

To clarify the principle of the QHE and its applications, we begin with the basic case of electrons with parabolic dispersion in a 2DEG where the Hamiltonian writes $H_{2DEG} = \frac{(\hbar k)^2}{2m^\star}$, even though this does not strictly apply to HgTe crystals. Under a magnetic field, the Hamiltonian of this system yields a mimic of a harmonic oscillator :

$$H_{2DEG} = \hbar\omega_c \left(a^\dagger a + \frac{1}{2}\right) \tag{4.8}$$

where $a^\dagger$ and a are respectively creation and annihilation operators, and $\omega_c = \frac{eB}{m^\star}$ is the cyclotron frequency of the electron.

The energy spectrum can be written :

$$E_N = \hbar\omega_c \left(N + \frac{1}{2}\right) \tag{4.9}$$

where N is the Landau level index. Then, two successive LLs are separated by the constant energy gap $\hbar\omega_c$. This spectrum is illustrated in figure 4.5(b). The confinement potential on the side appears because of the finite dimensions of the sample, in other words, in an infinite 2DEG, LLs are completely flat.

The center of the orbital motion is determined by $x_0 = \frac{\hbar}{\omega_c m^\star} k_y$, where k_y is the wavevector in the y direction. In a sample of finite width W, two adjacent states are separated by $\Delta x_0 = \frac{\hbar \Delta k_y}{eB} = \frac{h}{eBW}$. Since the sample has a finite length L in the x direction, the LL degeneracy is given by $N_{LL} = L/\Delta x_0$. Subsequently, the number of electrons per LL and per unit area is written [1] :

$$g_{LL} = \frac{N_{LL}}{LW} = \frac{eB}{h} \tag{4.10}$$

The number of LLs occupied can now be expressed as the ratio between n and g_{LL}

$$\nu = \frac{n}{g_{LL}} = \frac{nh}{eB} \tag{4.11}$$

ν is an integer when the Fermi level E_F lies between LLs as represented in figure 4.5(b) where $\nu = 2$. This feature is particularly helpful for the determination of the quantized

1. Here we do not consider spin degeneracy, nor valley degeneracy.

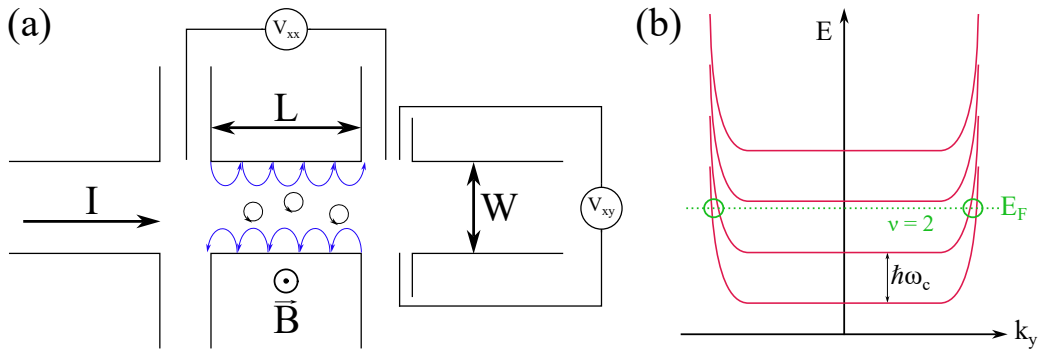

FIGURE 4.5 – (a) Representation of the Quantum Hall effect in a Hall bar. The bulk is insulating and current only flows in counter-propagating channels on the sides. (b) For a standard 2DEG, the energy difference between two LLs is constant. On the edges the confinement potential bend the energy levels that cross the Fermi energy.

Hall conductance proportional to the number of ballistic edge channels :

$$\sigma_{xy} = \nu \frac{e^2}{h} \tag{4.12}$$

Dirac electrons

As mentioned earlier, electrons at the surface of HgTe do not follow a parabolic energy dispersion but rather a Dirac fermion energy dispersion arising from spin-orbit coupling. In fact, states from top and bottom surfaces are represented by a Dirac cone, $E = \hbar v_F k$, where v_F is the Fermi velocity.

If we consider only one single Dirac cone, the Hamiltonian of this system under a magnetic field provides the eigenvalues of a Dirac-like energy spectrum ($\pm$ respectively refers to the electron- and hole-side) :

$$E_N^{\pm} = \pm\sqrt{2e\hbar v_F^2 B|N|} \tag{4.13}$$

Here, the energy separation between the LLs is a function of $\sqrt{N}$, and the zero-th LL is at zero energy, shared between electrons and holes.

In thin HgTe layers, where the thickness t becomes comparable to the spatial extent w of the surface states (typically a few nanometers), the wavefunctions of the top and bottom surfaces exhibit significant spatial overlap. This hybridization lifts the degeneracy between the two Dirac cones and opens an energy gap Δ at the Dirac point, with a mass term M. These modifications fundamentally alter the low-energy band structure and the corresponding Landau level (LL) spectrum in the presence of a perpendicular magnetic field.

The low-energy effective Hamiltonian describing such a system is given by :

$$H = v_F(\tau_z \sigma_x \pi_x + \sigma_y \pi_y) + \Delta \tau_x \tag{4.14}$$

$$H = \nu_F(\sigma_x\pi_y - \sigma_y\pi_x)\tau_z + (\frac{\Delta}{2} - \frac{\boldsymbol{\pi}^2}{2M})\tau_x \tag{4.15}$$

here, v_F is the Fermi velocity, $\boldsymbol{\pi}$ denotes the kinetic momentum including the vector potential, $\sigma_{x,y}$ are Pauli matrices acting on the spin degree of freedom, and $\tau_{x,z}$ operate in the pseudospin space distinguishing the top and bottom surfaces. The hybridization term, with Δ and M, accounts for the tunneling between the two surfaces, introducing a mass term that opens a gap at zero magnetic field.

In the presence of a magnetic field B, the system exhibits a modified LL spectrum that incorporates the hybridization terms Δ and M. The LL energies for electron-like states with $N \geq 0$ are given by :

$$\begin{aligned} E_{N,\pm} &= \sqrt{2e\hbar v_F^2 BN + \left(\frac{\Delta}{2} - N\hbar\omega\right)^2} \pm \frac{\hbar\omega}{2} \\ E_0 &= \frac{\Delta - \hbar\omega}{2} \end{aligned} \tag{4.16}$$

where $\hbar\omega = \frac{\hbar eB}{M}$ characterizes the field-induced orbital splitting, which is linear in B like the usual cyclotron gap of massive electrons with parabolic dispersion.

The calculated LL spectrum shown in figure 4.6 highlights two key features on top of the LL spectrum of Dirac fermions : (i) the hybridization gap Δ at $B = 0$, and (ii) the linear splitting of higher LLs with increasing B. These features break the degeneracy of the Dirac LL and lead to a nontrivial evolution of the quantum Hall effect (QHE) in thin TI systems [Liu, 2010 ; Linder, 2009].

In the decoupled (thick TI) limit, where $\Delta \to 0$ and $M \to +\infty$, each surface contributes independently, and the Hall conductance exhibits odd filling factors, reflecting the half-integer QHE characteristic of Dirac fermions :

$$\sigma_{xy} = 2(N + \frac{1}{2})\frac{e^2}{h} \tag{4.17}$$

However, in the presence of finite hybridization, the LL degeneracy is progressively lifted due to the field-dependent splitting term, enabling the emergence of even filling factors at sufficiently high magnetic fields. This effect is illustrated in figure 4.6, where the alternating green and blue dashed arrows indicate the parity of the filling factors as a function of magnetic field at fixed Fermi energy. The green segments correspond to regions with odd filling factors dominate, characteristic of the Dirac-like spectrum at low magnetic fields. In contrast, the blue segments mark the appearance of even filling factors, which become increasingly prevalent as the magnetic field strength increases, due to a growing energy gap at these filling factors. This effect reflects the enhanced influence of the LL splitting term at high fields. This evolution reflects the crossover from a gapless Dirac system to a gapped with a massive Dirac regime, with the QHE manifesting both

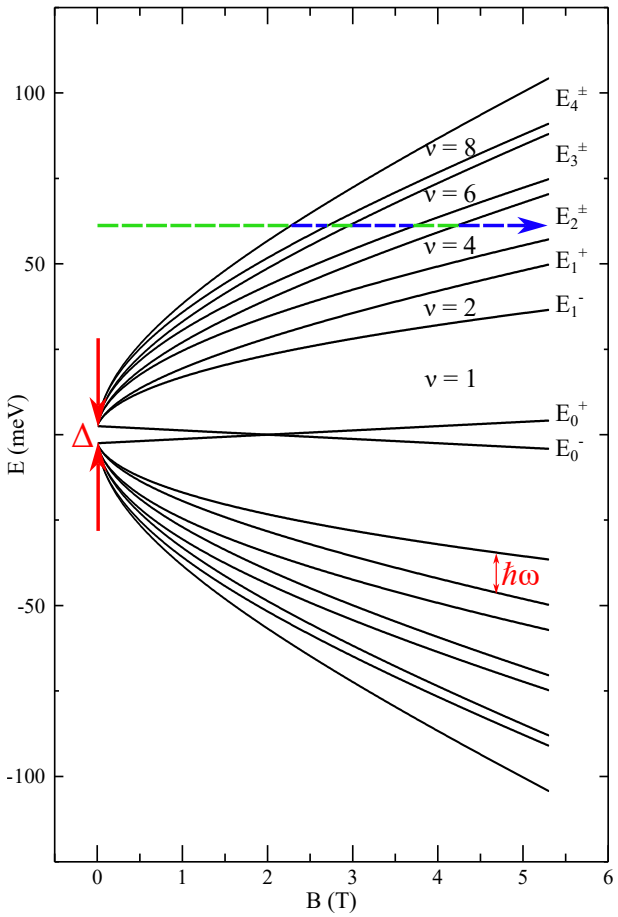

FIGURE 4.6 – Calculated LL spectrum for a thin TI as a function of magnetic field. The hybridization gap Δ is visible at $B = 0$, and the LL splitting increases linearly with B. Dashed arrows indicate the evolution of the filling factor parity (green for odd values and blue for even values) as B increases at fixed Fermi energy. Parameters : $\Delta = 5$ meV, $\hbar e/M = 2.5$ meV/T, $v_F = 5 \times 10^5$ m/s.

odd and even quantized plateaus.

When the Fermi energy resides within the mobility gap between LLs, the bulk becomes insulating, longitudinal resistance R_{xx} vanishes, and transport is mediated exclusively by edge states. The interplay between hybridization-induced mass, and magnetic quantization defines the rich LL structure and Hall conductance phenomenology in thin TI systems. In particular, topologically-protected helical edge states exist, even at zero field, when the Fermi level is in the gap Δ. Figure 4.6 shows the existence of a quantum phase transition from this quantum spin Hall phase at low field to a trivial insulating phase in high field, occurring at the crossing of the LL $E_{0,+}$ and $E_{0,-}$ [Zhang, 2015].

After describing the Landau level spectrum of HgTe in a magnetic field, we now turn to the presentation and interpretation of the experimental data from HgTe Hall bars.

4 Low magnetic field measurements

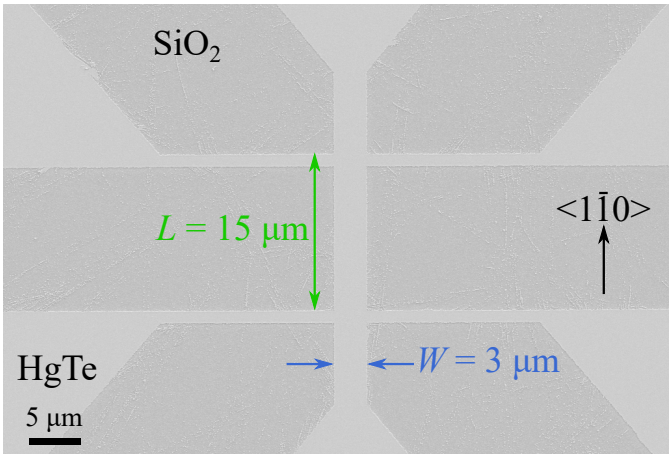

FIGURE 4.7 – SEM image of a HgTe Hall bar grown by selective-area epitaxy.

This section presents the measurements performed at low magnetic field on selective area grown Hall bars. The structures are grown in a HgTe-CdHgTe core-shell geometry of, respectively, 10 nm and 10 nm at 170°C, forming a CdTe/HgTe/CdHgTe quantum well on the CdTe substrate. An example of a Hall bar is shown in figure 4.7. The results obtained on this device with $L = 15$ μm and $W = 3$ μm are reported in Appendix C. Here we focus on the magneto-transport study performed on a larger Hall bar with $L = 120$ μm and $W = 24$ μm. Both longitudinal and Hall resistances are probed as a function of the gate voltage and the magnetic field to extract the carrier density, mobility and elastic mean free path. The measurements are performed at 1.5 K.

4.1 Extraction of the density

We start by characterizing the longitudinal resistance R_{xx}, and the Hall resistance R_{xy} in the absence of magnetic field. Figure 4.8(a) shows the evolution of R_{xx} as a function

of the gate voltage V_{gate}. A pronounced resistance peak is observed at approximately $V_{\text{gate}} = -0.7$ V, reaching a maximum of 43 kΩ, which marks the charge neutrality point (CNP) of the HgTe quantum well. Its 10 nm thickness being above the critical thickness of the topological phase, helical states are expected on the edges, together with a gap in the bulk, which could explain the finite resistance observed at the CNP.

On the electron side, $V_{\text{gate}} > -0.7$ V, the resistance decreases significantly, reaching approximately 300 Ω at zero gate voltage. Considering the dimensions of the Hall bar, we find a sheet resistance $R_{\square} = 300/5 = 60$ Ω. On the hole side, $V_{\text{gate}} < -0.7$ V, the resistance remains comparatively high, with a minimum of approximately 5 kΩ. A shoulder appears on the hole side of the $R_{xx}(V_{\text{gate}})$ curve, indicating the onset of bulk heavy-hole conduction as the Fermi level enters the valence band, increasing V_{gate}. This additional low-mobility conduction channel reduces the resistance increase typically expected in this regime. Similar features have been reported in strained HgTe nanostructures [Brüne, 2016].

Figure 4.8(b) displays the corresponding Hall resistance R_{xy} under identical conditions. Although no external magnetic field is applied, a finite Hall voltage develops around the CNP. This unexpected signal may originate from spatial inhomogeneities in the current distribution at very low density and in the topological gap.

Then, we measured the Hall resistance at low magnetic field $B \leq 0.6$ T at different gate voltages. One expects to observe a linear variation of the Hall resistance with the magnetic field, the quantum Hall plateaus not being formed at this low field.

Figure 4.8(c) displays the R_{xy} variation within the electron side : $-0.46 \leq V_{\text{gate}} \leq 0$ V. In this range of gate voltage, the Hall resistance varies linearly with B. The slope, also referred to as the Hall constant R_H, is positive. It is consistent with electrons governing the transport. We can notice that R_H increases with decreasing gate voltage. Since we approach the CNP, less carriers are available. This behavior is similar to what is observed in graphene away from the Dirac point [Wiedmann, 2011 ; Wehling, 2008]. It is consistent with a single carrier model where the transport is only governed by electrons.

In addition, figure 4.8(d) displays the evolution of R_{xy} on the hole side, for gate voltages in the range $-1.27 \leq V_{\text{gate}} \leq -0.84$ V. For magnetic fields $|B| \geq 0.1$ T, a linear behavior with a negative slope is observed, consistent with hole-dominated transport. However, for $|B| \leq 0.1$ T, R_{xy} shows transitions from negative to positive values, and even exhibits a positive slope at $V_{\text{gate}} = -0.84$ V and -1 V. This change of slope is typical of a two-carrier regime, where a few electrons with higher mobility are added to the dominant hole population with lower mobility.

Even far from the charge neutrality point, for instance at $V_{\text{gate}} = -1.13$, -1.2, and -1.27 V, R_{xy} does not vary linearly with the magnetic field. Slow variations that almost form plateaus are observed between 0.1 and 0.2 T. This non-linearity is attributed to the complex band structure of HgTe on the hole side. Furthermore, at $V_{\text{gate}} = -0.91$ V, R_{xy} at zero magnetic field is not zero, consistent with figure 4.8(b), where a non-zero Hall resistance is observed near the CNP. The linear Hall response is recovered only above a

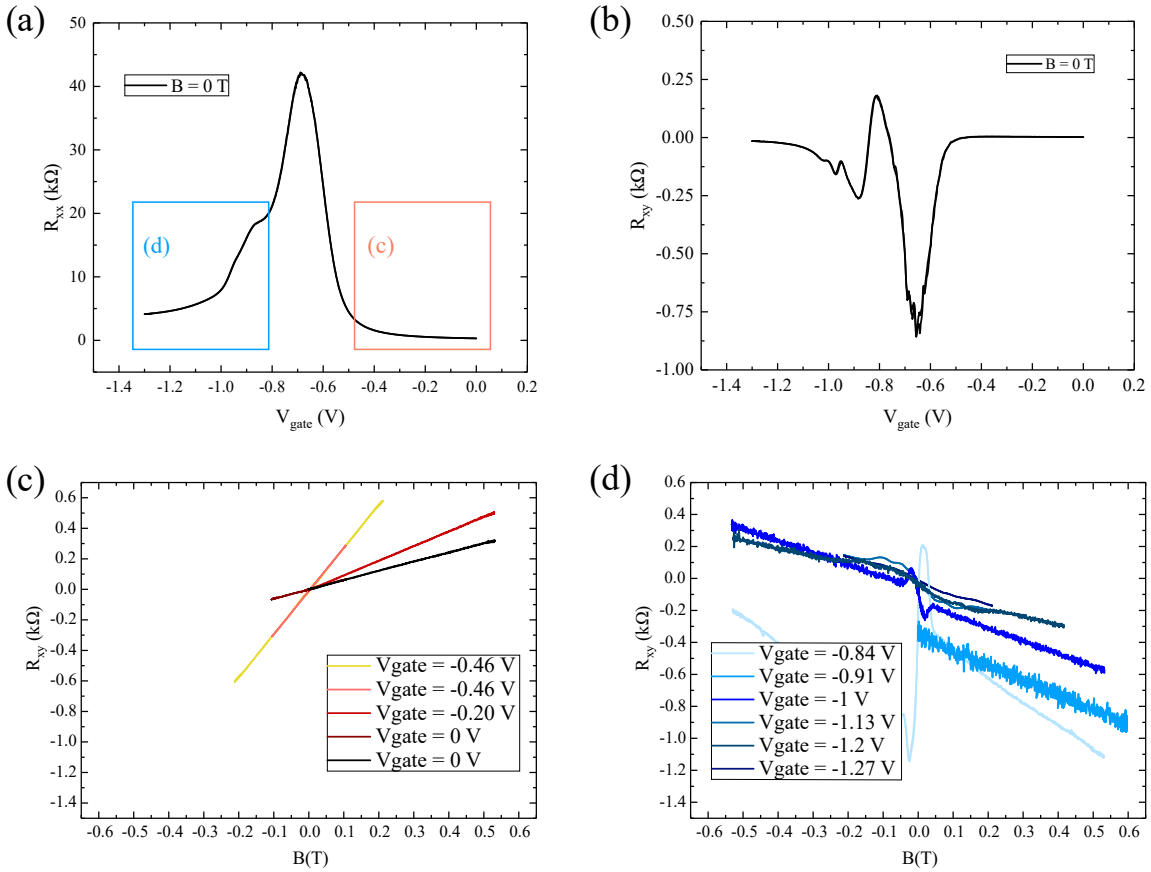

FIGURE 4.8 – Panels (a) and (b) respectively display the evolution of the longitudinal resistance R_{xx} and the Hall resistance R_{xy} as a function of the gate voltage in the absence of magnetic field. The response of the Hall resistance under exposition to a magnetic field is plotted in (c) for the electron side and in (d) for the hole side.

certain magnetic field threshold, rather than immediately at $B = 0$.

In conclusion, the sweeps in low magnetic field highlights the ambipolarity of the structure, composed of electron and hole charge carriers. The electron side, $V_{\text{gate}} \geq -0.7$ V, displays a linear variation of the Hall resistance with the magnetic field. However, the anomalous variation of R_{xy} in the hole side reveals some divergence with a single carrier model. Note that the absolute slope coefficient is larger around the CNP and is reduced when the regime is dominated by one carrier, either holes or electrons.

Despite the divergences from a single carrier model, the Hall constant R_H and the carrier density n have been extracted from measurements of the Hall resistance at $B = 0.1$ and 0.2 T. Figure 4.9(a) shows the variation of the Hall resistance when sweeping the gate voltage. On the electron side from -0.7 to 0 V, we can note that the proportionality between the two curves is respected, that is $R_{xy}(0.2\text{ T}) = 2R_{xy}(0.1\text{ T})$. However, on the hole side, shown also in figure 4.9(b), this ratio is no longer valid. Thus, $R_{xy}(0.2\text{ T})$ have approximately the same value as $R_{xy}(0.1\text{ T})$. This is consistent with the anomalous magnetic field characterization of R_{xy} from figure 4.8(d).

Nevertheless, the Hall constant for each gate voltage is extracted and shown in fi-

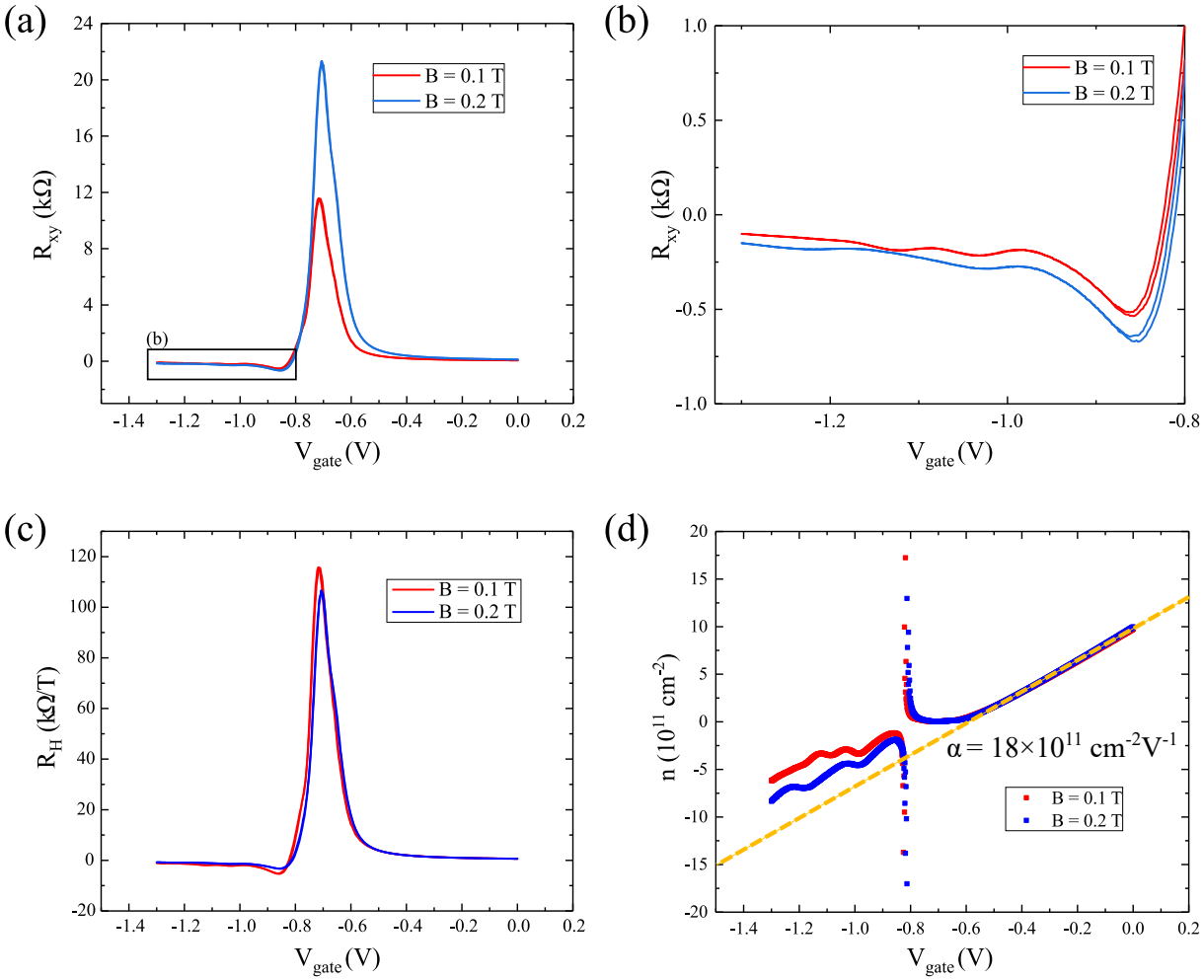

FIGURE 4.9 – Low magnetic field analysis of the Hall bar. All data are displayed as a function of the gate voltage. Panel (a) illustrates the evolution of the Hall resistance at two different magnetic fields. (b) is a zoom-in of the framed area in the hole side from (a). (c) displays the Hall constant of data in (a). (d) represents the carrier density. The yellow dashed line accounts for the slope of electron density, that is the depletion factor.

gure 4.9(c). The Hall constant is determined assuming that the Hall resistance passes through the origin, i.e. $R_{xy} = 0$ kΩ at $B = 0$ T. In a system where R_{xy} varies perfectly linearly with B, the Hall constant extracted at $B = 0.1$ T or $B = 0.2$ T should be identical. This is indeed the case on the electron side, where the two corresponding curves fully overlap. However, as the system approaches the CNP, deviations between the two curves become more pronounced. Although the two curves appear relatively close to each other on the hole side, the carrier density plot in figure 4.9(d) clearly reveals discrepancies. Specifically, two distinct carrier density values are extracted, one for each magnetic field.

The dashed line in figure 4.9(d) represents the gate depletion factor, corresponding to the slope of the electron density with respect to the gate voltage. It emphasizes the linear variation of carrier density on the electron side, where, as expected, the two curves perfectly overlap. Nevertheless, this line does not intersect the zero-density axis at the gate voltage where R_{xy} change sign. This anomalous behavior will be discussed later.

In order to precisely determine the carrier density, a 2D mapping of the Hall resistance in magnetic field and gate voltage has been performed. Thanks to this map, we are able to fit the slope coefficient of $R_{xy}(B)$ at each gate voltage. To avoid quantization effects, we restrict the magnetic field to $B \leq 0.5$ T. The 2D map will be described later on.

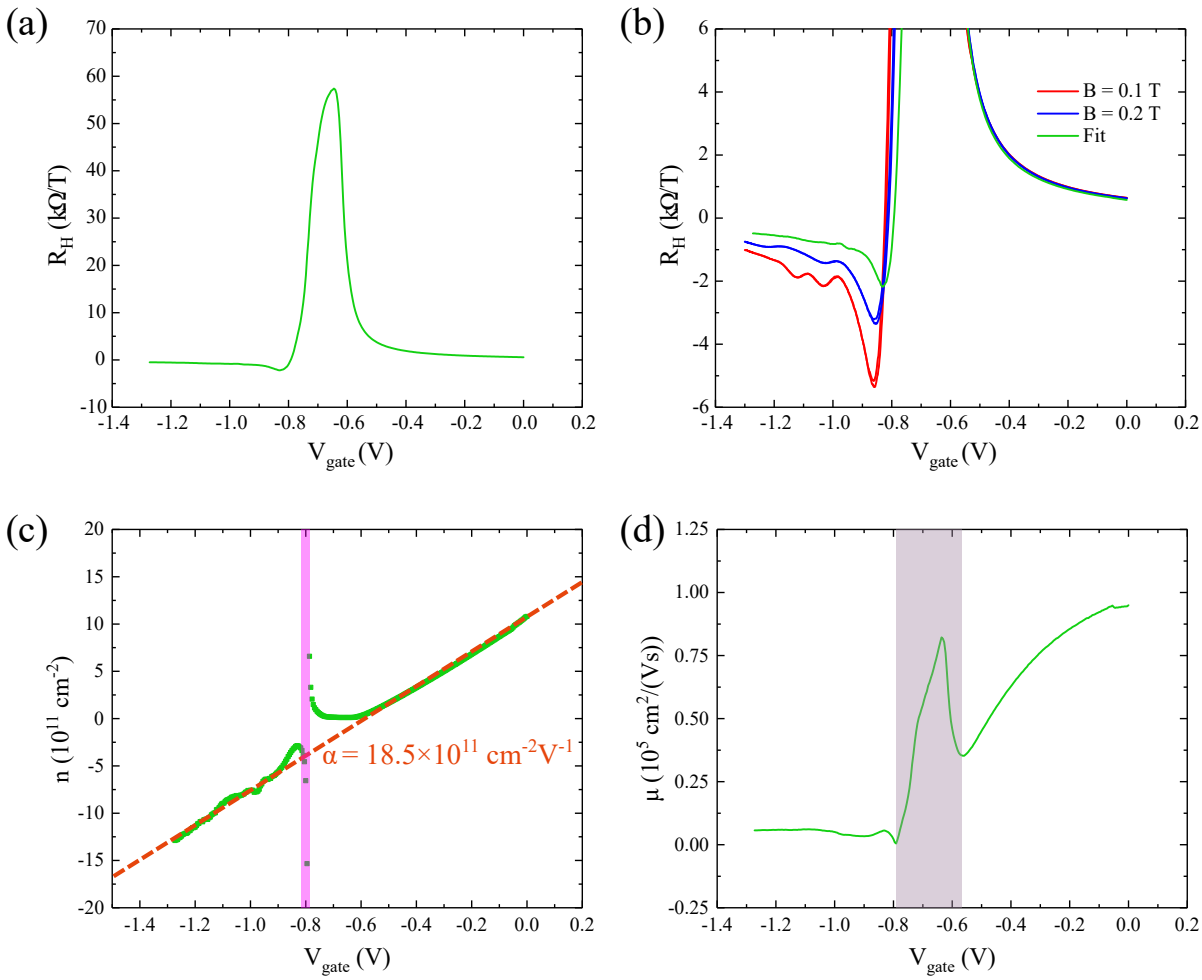

FIGURE 4.10 – Analysis of the Hall bar characteristics at 1.5 K extracted from data with magnetic field $B \leq 0.5$ T. All data are displayed as a function of the gate voltage. The purple vertical band highlights the sign inversion of the Hall constant R_H, corresponding to the full depletion of the conduction band electrons. Panel (a) displays the Hall constant R_H. (b) compares the Hall constants from $B = 0.1$ T, $B = 0.2$ T and from the fit. (c) represents the carrier density. The yellow dashed line accounts for the slope of electron and hole densities, which is the depletion factor, common between the two carrier type. (d) shows the mobility of the carriers. The gray color band indicates the voltage range where the single carrier model is not valid. Data within this range should then not be considered.

Figure 4.10(a) displays the slope coefficient obtained from the linear fit, that is, R_H. Figure 4.10(b) compares the Hall constant extracted from the fit with the previous values obtained at $B = 0.1$ T and $B = 0.2$ T. On the electron side, $V_{\text{gate}} \geq -0.6$ V, the curves clearly overlap due to the purely linear behavior of R_{xy} with the magnetic field. On the hole side, a different behavior is obtained, showing the Hall constant closer to zero, as expected from the presence of the R_{xy} offset at zero field which disturbed the determination of R_H at fixed field. The data for the carrier concentration is shown in figure 4.10(c). The hole and electron densities are now aligned on the same line and the depletion factor is the

same for both carrier types. Here, the depletion factor is $\alpha = 18.5 \times 10^{11}$ cm^{-2}V^{-1}, similar to that of figure 4.9(d). This value is lower than that calculated from the thickness of the layers, where equation 3.9 provided a depletion factor of 19.5×10^{11} cm^{-2}V^{-1}. We also note that the depletion factor line does not cross the zero-density axis at the same gate voltage as that of where the Hall constant R_H changes sign, marked by the purple vertical band, but at a higher gate voltage. In a single carrier model, these two gate voltages should be equal.

This anomalous behavior of the carrier density might result from the co-existence of two carrier types, electrons and holes, on a limited gate voltage range. This odd situation, reflecting an overlap of conduction and valence bands, could arise in HgTe quantum wells due to the peculiar shape of the band structure, as shown in figure 4.11 for a 9 nm-thick quantum well. The valence band displays a Mexican hat shape which could overlap with the conduction band without touching each other.

The Hall constant for two populations of carriers is written as follows

$$R_H = \frac{p\mu_p^2 - n\mu_n^2}{e(p\mu_p + n\mu_n)^2} \tag{4.18}$$

where n and p are the electron and hole densities, while μ_n and μ_p are their respective mobilities. In the case where $\mu_n \gg \mu_p$ (as explained below), the Hall constant changes sign when $n = p\left(\frac{\mu_p}{\mu_n}\right)^2 \sim 0$ and not at the CNP where $n = p$.

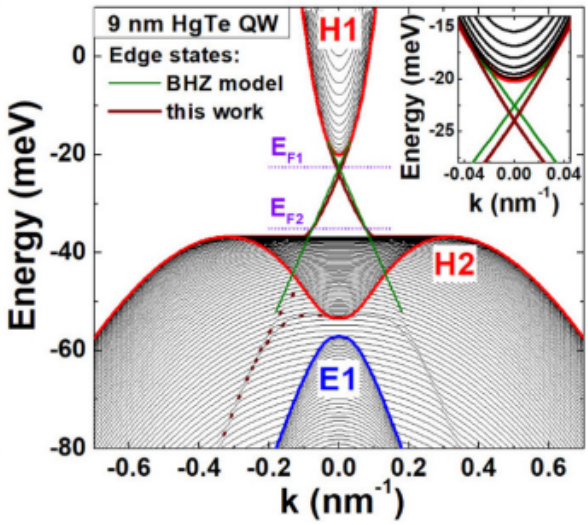

FIGURE 4.11 – Band structure of 9 nm-thick HgTe quantum well calculated on the basis of a $H_{4\times4}(\mathbf{k})$ Hamiltonian. Taken from [Krishtopenko, 2018].

This specificity is found by simulating the overlapping carrier densities of electrons and holes as a quadratic function in a finite range $[V_0 - \Delta; V_0 + \Delta]$, as shown in figure 4.12(a). The subsequent plots of Hall resistance R_H and its inverse $1/R_H$, see figure 4.12(b) and (c), show gate voltage dependencies very similar to the experimental data. In panel (c), the CNP is marked by the green star where the $n - p$ line crosses the zero axis, which is obtained at a gate voltage higher than that of the change of sign of R_H, also marked by

the purple band. We conclude that in our case the CNP is most likely at $V_g \sim -0.6$ V where the line of the depletion factor crosses the zero density axis.

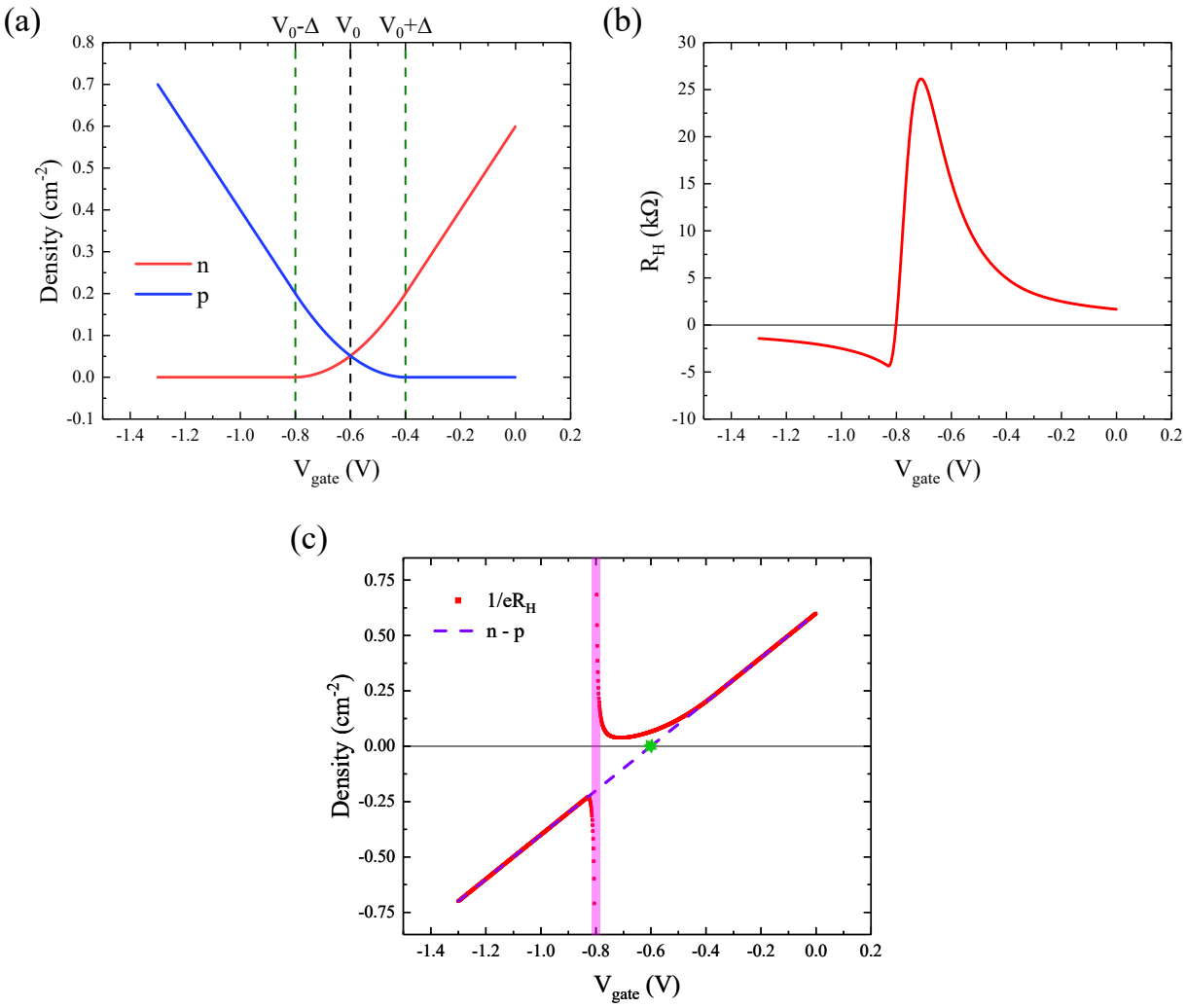

FIGURE 4.12 – Simulation of carrier densities and Hall response in a two-carrier model. The values are arbitrary and only intended to illustrate the experimental behavior. (a) Simulation of the electrons n and holes p concentrations as a function of the gate voltage. On a finite voltage range $[V_0 - \Delta; V_0 + \Delta]$ electrons and holes co-exist. The related Hall constant expressed from equation 4.18 and its inverse are respectively shown in (b) and (c). The green star in (c) emphasizes the CNP, while the purple band marks the change of sign of the Hall constant.

4.2 Extraction of the mobility

The charge carrier mobility within the HgTe quantum well is obtained from equation 4.7 using the Hall constant from figure 4.10(a) and the longitudinal sheet resistance, extracted from R_{xx} at zero magnetic field, visible in figure 4.9(b). The mobility as a function of the gate voltage is shown in figure 4.10(d). The region around the CNP is highlighted in grey where the relation is not applicable because the single carrier model is not valid. On the electron side, the electron mobility increases with gate voltage and reaches 0.94×10^5 cm^{2}V^{-1}s^{-1} at zero gate voltage. This result is comparable, although

slightly lower, than the results reported in previous HgTe Hall bars obtained by wet etching. They authors found an electron mobility up to $\sim 5 \times 10^5$ $m^2V^{-1}s^{-1}$ [Thomas, 2016 ; Bendias, 2018]. The mobility goes to zero at low density since electrons are traveling in a more disordered potential. In particular, reduced screening of charged impurities enhances disorder scattering, which in turn lowers the electron mobility. On the other side, the hole mobility is very low, limited to 0.06×10^5 $cm^2V^{-1}s^{-1}$. The mixing between the surface state and the Γ_{8HH} hole band is suspected to be responsible for this lower mobility.

4.3 Mean free path

From the mobility, we can compute the elastic mean-free path l_e, which is the average distance covered by the electron before it is scattered. This characteristic length is given by the relation :

$$le = \nu_F \tau \tag{4.19}$$

where $\nu_F = \frac{\hbar k_F}{m^*}$, $k_F = \sqrt{2\pi n}$, and $\mu = \frac{e\tau}{m^*}$, which gives :

$$l_e = \mu \frac{h}{e} \sqrt{\frac{n}{2\pi}} \tag{4.20}$$

At zero gate voltage where the electron density is $n = 10.8 \times 10^{11}$ cm^{-2}, we find $l_e = 1.7$ μm. This large value reflects the quality of the CdTe/HgTe/HgCdTe heterostructure grown on a patterned substrate by selective area epitaxy.

Furthermore, we can derive the Fermi wavelength $\lambda_F = 2\pi/k_F$. From the carrier density at zero gate voltage, we find $\lambda_F = 24$ nm. Given that the Fermi wavelength exceeds the thickness of the HgTe layer, electrons are confined to the lowest quantized subband along the growth direction. This strong vertical confinement prevents motion in that direction, effectively reducing the system to two dimensions. As a result, transport takes place within a single subband, with the formation of a two-dimensional electron gas (2DEG) confined within the Hall bar thickness.

5 High magnetic field measurements

The characterization of the topological properties of the Hall bars is carried out at high magnetic field. Hybridization of the surface state leading to a Dirac cone separated by a gap is probed by mapping of the longitudinal and Hall resistance under variation of the gate voltage and magnetic field.

5.1 Parity of dominant filling factors

In this section, we decide to study the Shubnikov-de Haas oscillations (SdHO) at large electron density, $V_{\text{gate}} = 0$ V. Here, the magnetic field is set to 5.3 T while the temperature

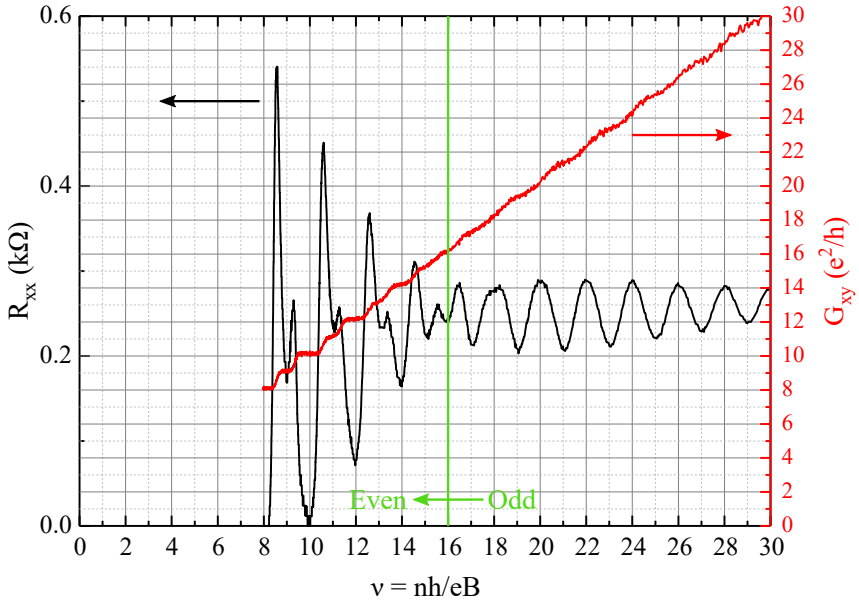

FIGURE 4.13 – Shubnikov-de Haas oscillations of R_{xx} and Hall conductance G_{xy} recorded as a function of the magnetic field B and plotted as a function of the filling factor ν. Integer values give the number of filled Landau levels.

is kept at 1.5 K. Figure 4.13 shows the oscillations of the longitudinal resistance R_{xx} illustrating the filling of the Landau levels for integer values of the filling factor :

$$\nu = \frac{nh}{eB} \tag{4.21}$$

We also observe the quantization of the transverse conductance at sufficiently high magnetic field :

$$G_{xy} = \nu \frac{e^2}{h} \tag{4.22}$$

As the magnetic field increases, we observe a transition from odd to even filling factor. Indeed, at low magnetic field, R_{xx} minima are obtained for odd values of ν, but at high magnetic field, they are associated with even values of ν. The change occurs around $\nu = 16$. As explained in Section 3.2, it originates from the splitting of the Landau Level as a result of the hybridization of the Dirac cones of the two surface states. The longitudinal resistance R_{xx} reaches zero from $\nu = 10$, marking the beginning of the quantum Hall regime, where the bulk is insulating and electrons are only transmitted through chiral edge states. The plateau structure of the transverse conductance is clearly marked for $\nu \leq 14$, with larger steps at even filling factors. While, the plateaus corresponding to odd filling factors are significantly shorter. This behavior is consistent with the Landau level dispersion depicted in figure 4.6, where the segments of the dashed arrow associated with even values of ν become predominant at high magnetic fields. As a result, well-defined quantization is observed exclusively for even filling factors in this regime.

5.2 Fan diagram versus magnetic field and gate voltage

The previous plot was presenting the magneto-resistance oscillations at zero gate voltage only. To gain further insights into the response as a function of the Fermi level, two-dimensional maps of R_{xx} and R_{xy} were recorded and plotted in figure 4.14. These measurements were performed by sweeping both the magnetic field ($|B| \leq 5.3$ T) and the gate voltage ($-1.27 \leq V_{\text{gate}} \leq 0$ V) at a temperature of 1.5 K.

Figure 4.14(a) shows a fan diagram of R_{xx} with zero resistance minima on the electron side. It confirms the occurrence of the Quantum Hall Effect (QHE). The data from figure 4.13 correspond to the farthest vertical line on the right hand side of the plot at $V_{\text{gate}} = 0$ V with B varying from 0 to 5.3 T. The purple area with vanishing resistance in the top right corner is therefore identified as $\nu = 8$. When sweeping down the gate voltage toward the CNP, the filling factor is reduced as the carrier density n reduces. Minima of resistance are observed at both even and odd values of the filling factor, but minima reaching zero are only observed at even values. This rotation of strong and weak minima is consistent with the theoretical Landau level spectrum of HgTe quantum wells, see figure 4.6. The only odd filling factors with vanishing resistance are $\nu = 1$ and $\nu = 3$. Being the closest to the CNP, they indeed have larger energy gaps, which exceed the Landau level broadening. The minima of resistance of an even filling factor corresponds to the splitting of an energy level, $E_N \to E_N^{\pm}$, separated by an energy $\hbar eB/M$. Thus, the larger the magnetic field, the easier it is to observe the resistance minimum between those levels. The separation between the levels E_N^+ and E_{N+1}^- also increases with field, but much slower, which makes these minima less prominent.

In the quantum Hall regime, the voltage difference between two points along a chiral edge channel should be zero, since they are connected by a dissipation-less ballistic edge state. However, in the fully quantized region at $\nu = 1$ in figure 4.14(a), the four-terminal resistance has a very small positive value for positive magnetic field and a very small negative value for negative magnetic field. This discrepancy may originate from a voltage contact of poor quality which does not properly equilibrate its potential with the edge channel. The resulting voltage drop between the two voltage contacts has opposite signs for opposite edge channel chirality.

In contrast, the hole side exhibits no clear signature of the quantum Hall effect : neither vanishing longitudinal resistance nor well-defined low-resistance plateaus are observed. This behavior may arise from the broadening of the Landau levels due to coupling with the bulk $\Gamma_{8,HH}$ band, once again highlighting the complex transport mechanisms and the reduced mobility on the hole side.

At $\nu = 0$, an insulating region of infinite resistance appears above 3.6 T, region in black in figure 4.14(a). It may correspond to the topological phase transition between the conducting quantum spin Hall phase at low field and the trivial insulating phase at high field. This transition takes place at the crossing between the states $E_{0,+}$ and $E_{0,-}$ of the Landau level spectrum shown in figure 4.6. Unfortunately, the $\nu = 0$ helical phase

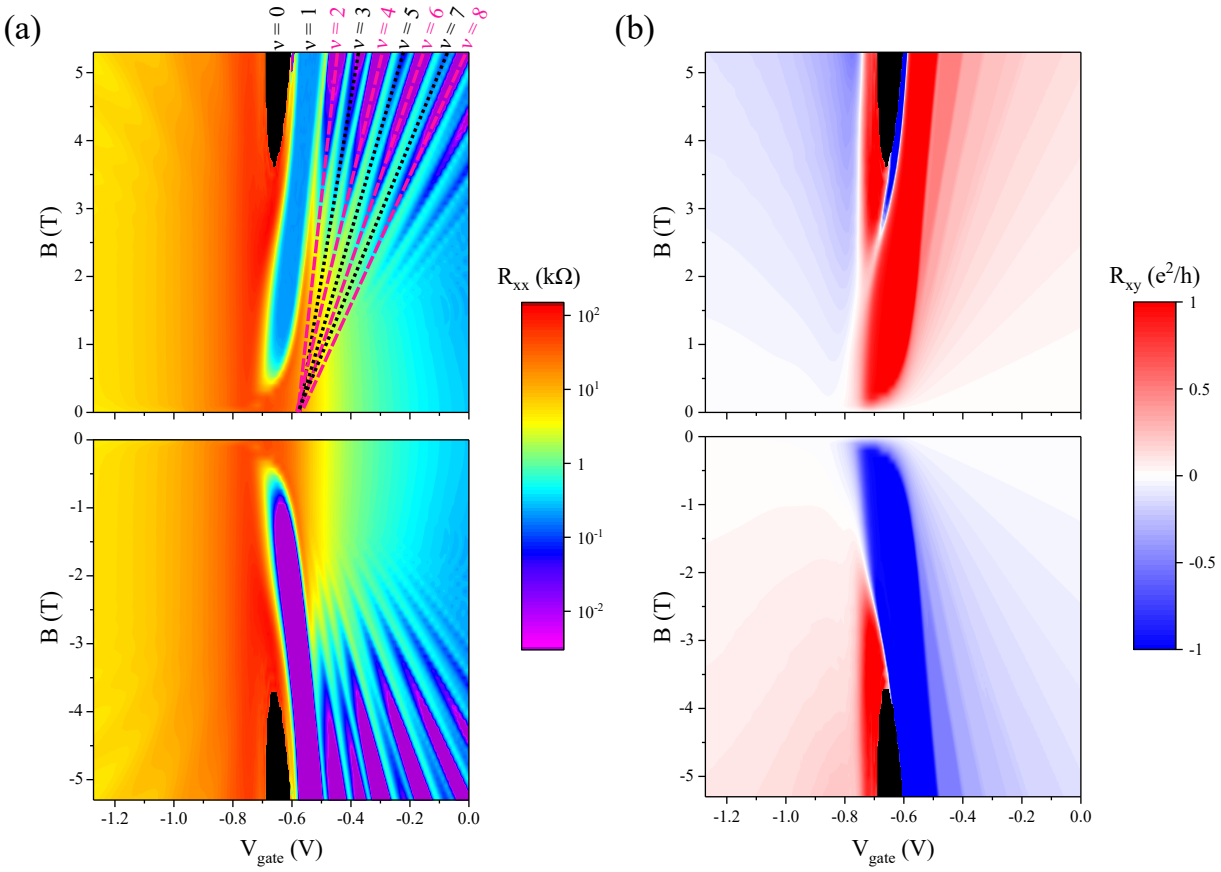

FIGURE 4.14 – 2D maps of magneto-transport measurements performed on the Hall bar. (a) Longitudinal resistance R_{xx} as a function of B and V_{gate}. The black and purple dashed lines respectively represents the even and odd filling factors. (b) Hall resistance R_{xy} as a function of B and V_{gate}.

at low field does not show quantized transport properties. This is possibly due to the parasitic conduction by holes in the valence band, which overlaps with the topological gap, as discussed above in connection with the anomalous shape of the Hall resistance in figure 4.10(a).

Measurements of the Hall resistance R_{xy} have also been performed within the same range of magnetic field and gate voltage. The results are presented in figure 4.14(b). Successive resistances plateaus are visible on the electron side, evidencing good quantization. The plateaus are directly associated with the filling factor lines from figure 4.14(a). However, the hole side does not show any plateau.

In conclusion, the quantum Hall effect signatures observed in our HgTe quantum well nicely fits with the theoretical Landau level spectrum in presence of strong spin-orbit interaction. This result demonstrates the high quality of our heterostructures grown by selective-area epitaxy on a patterned substrate.

6 Temperature dependence of resistance minima

To gain further insight into the Landau level spectrum, we now measure the energy gaps between the Landau levels, using the temperature dependence of the longitudinal resistance R_{xx}. This method has also been used for the study of HgTe devices [Thomas, 2017] and graphene [Jiang, 2007].

It consists in the determination of the minima of R_{xx} oscillations during a gate voltage sweep at fixed magnetic field for different temperatures. Indeed, the R_{xx} minima correspond to integer filling factors for which the Fermi level is in the middle of the cyclotron gap between two Landau levels. The change of this minima value with respect to the temperature highlights a thermal activation of carriers through the gap between the LLs. The activation gap ΔE is determined by fitting the experimental data with an Arrhenius law :

$$R_{xx}^{\min} \propto \exp\left(\frac{-\Delta E}{2k_B T}\right) \tag{4.23}$$

where k_B is the Boltzmann constant and T is the temperature. The determination of the slope between the logarithmic values of the resistance minima and $1/T$ yields the activation gap ΔE between two successive Landau levels.

The measurements have been performed at $B = 3.52$ T with temperature ranging from 0.28 to 5 K. The gate voltage range is limited to the electron side as no quantization has been observed on the hole side. Figure 4.15(a) displays the longitudinal resistance R_{xx} as a function of the gate voltage. The magnetic field value is chosen so that clear identification of the filling factor is possible, but as well, to observe an increase in the R_{xx} minima with the temperature. It is not the case for $\nu = 1$ that remains quantized [2].

2. The resistance does not vanish completely due to the above mentioned problem of poorly coupled

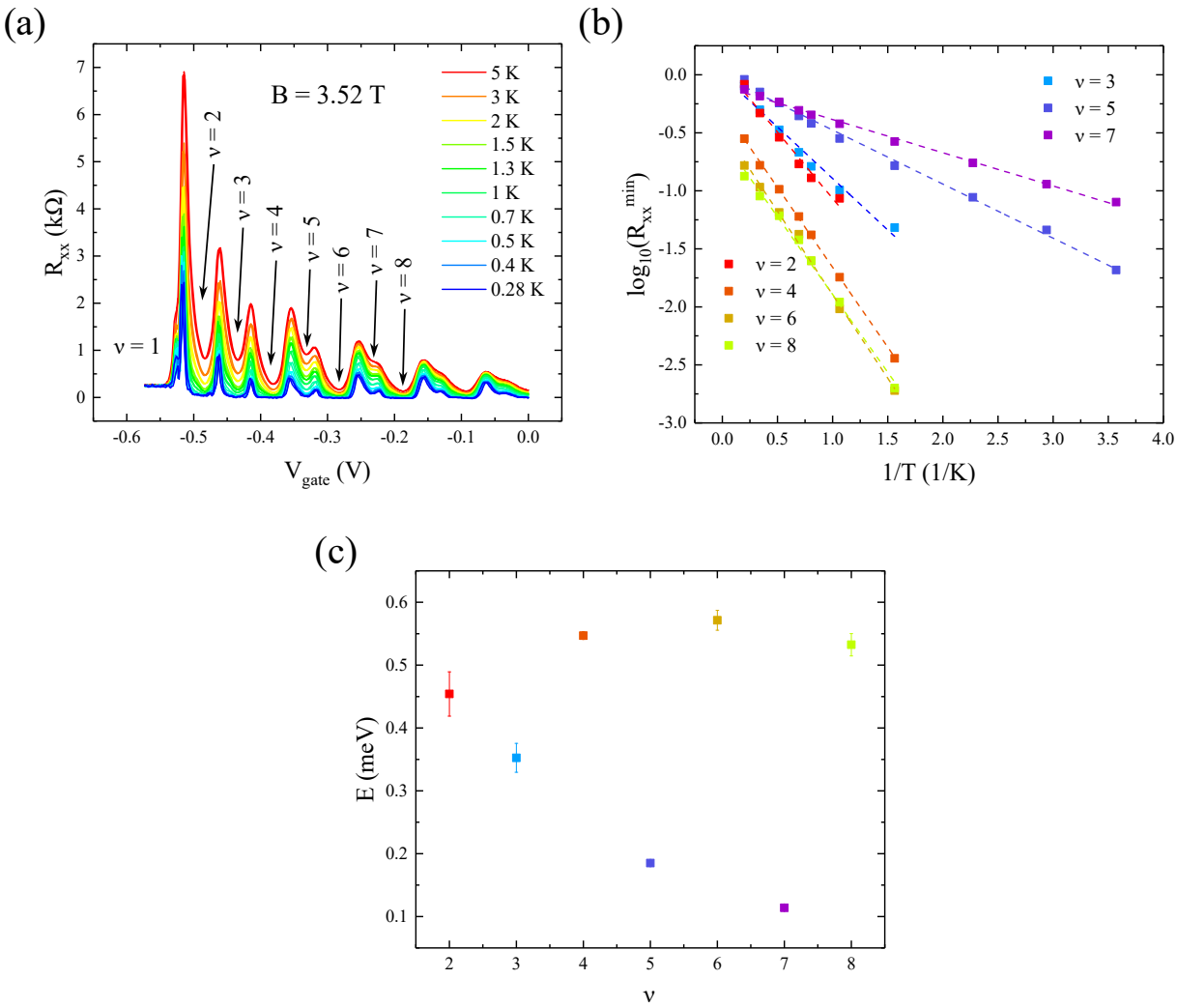

FIGURE 4.15 – (a) Longitudinal resistance of the Hall bar as a function of the gate voltage, limited to the electron side. The data is recorded at $B = 3.52$ T and for temperatures ranging from 0.28 to 5 K. Note that the temperatures shown are setpoints. The actual values, corrected for the thermometer magnetoresistance at 3.52 T, are used in panel (b) to extract the activation gaps. R_{xx} minima are labeled with their filling factors. (b) Temperature dependence of these minima for each filling factor. The dashed lines corresponds to the linear fit of the data with an Arrhenius law. (c) Activation gap versus filling factors obtained from the slope of the temperature dependence.

If the magnetic field is too strong, the resistance would vanish even with the increasing temperature and no fitting to the Arrhenius law from equation 4.23 would be possible.

Figure 4.15(b) presents the evolution of the longitudinal resistance minima as function of $1/T$ for integer values of ν from 2 to 8. The dashed line corresponds to the fits to equation 4.23. Note that for low filling factors, fewer temperature points are available because of the saturation of the resistance in the quantization regime caused by the imperfect coupling of the voltage probe. Their consideration would compromise the slope determination from the fit.

The resulting activation gaps for these filling factors are presented in figure 4.15(c). The values are about a few hundred μeV, which is much smaller than the theoretical gaps

contacts, but what matters here is that the resistance does not change with the temperature, which proves the perfect quantization.

visible in figure 4.6. In a previous work [Thomas, 2016], three regimes of temperature dependence have been identified : a high temperature regime with activation energies of a few meV, and two low temperature regimes with activation energies in the μeV range. Our set of data has been recorded in these low temperature regimes. To understand the difference between the theoretical gaps and the measured activation gaps, we need to consider the role of disorder, which induces Landau level broadening as explained below.

The energy of the Landau levels for $N \geq 1$ follows the relation :

$$E_{N\geq 1,\pm} = \sqrt{2e\hbar v_F^2 NB + \left(\frac{\Delta}{2} - N\frac{\hbar eB}{M}\right)^2} \pm \frac{\hbar eB}{2M} \tag{4.24}$$

First, we consider the activation gaps measured at even filling factor, which result from the presence of the last term of the equation, acting as an effective Zeeman splitting. The activation gap between two LLs for $\nu = 2N$ can be written :

$$\Delta E_{\nu=2N} = E_{N,+} - E_{N,-} - \Gamma = 2\frac{\hbar eB}{M} - \Gamma \tag{4.25}$$

where Γ denotes the Landau level broadening, reflecting the finite energy width of the quantized levels induced by disorder and scattering processes. The activation gap should therefore be identical for all values of even filling factors. This behavior is observed in figure 4.15(c) for the largest even filling factors $\nu = \{4, 6, 8\}$ which share the same activation gap, while the gap for $\nu = 2$ is slightly smaller.

Then, we consider the odd filling factors where two successive LLs come from different orbitals, N and $N + 1$.

$$\Delta E_{\nu=2N+1} = E_{N+1,-} - E_{N,+} - \Gamma \tag{4.26}$$

In this case the expression of the activation gap is more complex, but shows that at fixed magnetic field the energy gap between LLs is decreasing with N. It is indeed what we observe experimentally as $\Delta E_{\nu=3} \geq \Delta E_{\nu=5} \geq \Delta E_{\nu=7}$ in figure 4.15(c).

An experimental determination of Γ would require a detailed investigation of the activation gaps versus magnetic field. A previous study [Thomas, 2016] found Γ of the order of a few meV, comparable with the gaps themselves, such that the measured activation gaps are strongly reduced. In addition, the observation of several activation gaps for the same filling factor could result from the existence of several scattering mechanisms associated with different values of Γ.

7 Conclusion

The results resolve around the characterization of a Hall bar fabricated by selective area growth (SAG), investigated through magneto-transport experiments.

Low-field measurements revealed the coexistence of electron and hole regimes, tunable

via the gate voltage. In the electron regime, carrier density and mobility were reliably extracted from the linear Hall response, confirming the high structural quality of the material. In contrast, the hole regime exhibits an anomalous Hall response at very low field, making B-V_{gate} maps essential for tracking the evolution of hole density as a function of gate voltage.

High-field measurements further confirm the quality of the material and the successful fabrication of in-plane nanostructures by SAG. The quantum Hall regime was unambiguously demonstrated with vanishing longitudinal resistance and well-defined Hall plateaus. The evolution of the Landau levels with increasing magnetic field shows a transition from odd to even filling factors, consistent with Dirac-like transport and lifting of surface-state degeneracy. However, on the hole side, quantum Hall signatures are absent, likely due to the complexity of the band structure in the valence band. Activation gaps in the Landau spectrum were experimentally measured. The results show qualitative agreement with theoretical predictions, with nearly identical gaps for even filling factors and a decreasing gap with increasing Landau indices for odd filling factors. These observations are consistent with the theoretical framework discussed in Section 3.2, highlighting the presence of Dirac fermions and hybridization of top and bottom surface states in thin HgTe layers.

Overall, these results provide a first quantitative assessment of the structural and electronic quality of HgTe heterostructures grown by selective area growth. This work represents an essential step toward understanding the physics of active HgTe quantum wells and opens the way for exploring one-dimensional nanostructures, where quantum confinement is expected to give rise to novel physical phenomena.

Chapter 5

1D nanostructures : nanowire & ring

1 Introduction

The study of magneto-transport in low-dimensional systems reveals quantum phenomena that are absent or masked in higher-dimensional devices. In particular, one-dimensional (1D) devices such as nanowires and nanorings exhibit pronounced interference effects and enhanced sensitivity to spin-orbit coupling. Understanding electron phase coherence is crucial for the development of phase-coherent quantum electronic devices. The loss of phase coherence is not only a limiting factor for such devices but also a valuable probe of the underlying electron-scattering processes. In this chapter, we extend the analysis conducted for 2D HgTe Hall bars to 1D HgTe nanowires and nanorings. Thus, we gain deeper insights into the fundamental role of dimensionality in HgTe quantum transport and validate SAG as a reliable technique for the fabrication of nanoscale devices.

The core objective of this chapter is to characterize electron transport in quasi-one-dimensional quantum nanostructures. In particular, we are interested in the presence of phase coherence. Depending on the size of the mean free path and phase coherence lengths with respect to wire width and length, different regimes of transport are manifesting along with their peculiar mechanisms.

In order to investigate phase coherence and the associated scattering mechanisms, we focus on several well-known quantum interference phenomena observed at low temperature : weak localization (WL), weak anti-localization (WAL), universal conductance fluctuations (UCF), and the Aharonov-Bohm (AB) effect. Each of these effects arises from the coherent properties of the electronic wave functions. We first discuss the theoretical framework and experimental signatures of these phenomena in quasi-1D channels, emphasizing their characteristic magnetic field scales and temperature dependencies.

Next, we present detailed measurements and analysis of HgTe nanostructures. The characterization of the nanowire is systematically compared to that of the Hall bars to emphasize their differences. These basic transport parameters are useful for the subsequent deep analysis of the quantum phenomena : weak anti-localization and universal

conductance fluctuations.

Finally, we study the electronic transport in a ring geometry. The manifestation of the Aharonov-Bohm effect is evidenced. Its analysis as a function of the temperature leads to an estimation of the phase coherence length. We can therefore assess the electronic transport in a loop geometry and compare our experimental results to theoretical predictions and literature results.

2 Quantum transport in nanostructures

The influence of sample dimensions on resistivity has been thoroughly studied for several decades. While classical effects are known to dominate in large samples, the reduction of the achievable dimensions by lithography or etching techniques has enabled the observation of quantum effects. In semiconductor nanostructures, both classical and quantum size effects appear [Beenakker, 1991], and a deep understanding of the former is necessary to distinguish them from the latter. The following sections aim at introducing these concepts to the reader before we dive into the analysis of the experimental results.

2.1 Scattering phenomena

We start by defining the two main natures of scattering. When an electron propagates through a crystal, it will deviate from its trajectory due to impurities, defects, or interface roughness. These scattering events are elastic because the electron is deflected without any loss of energy, affecting only its momentum $\mathbf{k}$, i.e., its direction of motion. In contrast, inelastic scattering involves energy exchange, typically with phonons or other electrons, altering both the direction and energy of the electrons.

Now, we can describe how these scattering events affect the electronic transport of the nanostructures studied at low temperature. The temperature dependence of the Drude resistivity $\rho = m/(ne^2\tau)$ is given by that of the scattering time τ. Lowering the temperature yields larger τ by suppressing inelastic scattering processes, such as electron-phonon interactions, and so a decrease of the resistivity. The residual resistivity, due to elastic scattering, is left temperature independent according to the semi-classical theory. However, experiments with narrow structures have shown that the resistivity increases again below a certain temperature [Van Houten, 1986]. This is a sign of quantum mechanical manifestations leading to long-range correlations in the diffusive motion of the electron. The purpose of this section is to understand the nature of these manifestations and investigate their behavior.

An important aspect to notice is that elastic scatterings are not destroying the phase of the electronic wavefunctions. Subsequently, correlations in the phase are observed, leading to quantum interference correction of the classical Drude model. Thus, the key quantity in this effect is the phase coherence time, τ_ϕ. The latter characterizes the typical time scale over which an electron maintains a well-defined quantum phase during its propagation. Beyond this time, the phase of the electron is randomized, and phase correlations are lost. We also define the coherence length $l_\phi = \sqrt{D\tau_\phi}$ of the electron, where $D = v_F l_e/2$ is the diffusion constant. It is the characteristic length over which phase coherence is sustained. We will now describe the different trajectories that electrons undergo in a diffusive motion to explain these quantum interference effects. We warn the reader that, at this point, the role of the spin-orbit interaction of the material is neglected and will be introduced later.

2.2 Coherent backscattering

Considering all possible paths taken by partial waves through the system, the probability $P(\mathbf{r}, \mathbf{r'}, t)$ for a particle to move from a point $\mathbf{r}$ to $\mathbf{r'}$ in a time t is equal to the absolute value squared of the sum of the probability amplitudes A_i :

$$P(\mathbf{r}, \mathbf{r'}, t) = \left| \sum_i A_i \right|^2 = \sum_i |A_i|^2 + \sum_{i \neq j} A_i A_j^* \tag{5.1}$$

The first term of the right hand side refers to the classical diffusion probability, while the second accounts for quantum interferences. At first glance, one might think that all the different trajectories, carrying uncorrelated phases, are self-averaging. So, the interference term would cancel out. But this is no longer correct for loop trajectories, where $\mathbf{r} = \mathbf{r'}$, traveled in time shorter than τ_ϕ. These are known as back-scattered trajectories. These loops are randomly distributed along the transport path. When electrons scatter around them, their momentum changes direction multiple times while their phase is preserved. So, only paths that can maintain the phase coherence across the loop can contribute to coherent back-scattering. The contributing loops are therefore of size $\sim l_\phi$. In the interference term, we have to consider the time-reversed partner of each loop in the sum of back-scattered trajectories. The loop is the same but traveled in the opposite direction, as illustrated in figure 5.1. This time-reversal symmetry ensures an equal probability amplitude for the two opposite paths : $A^+ = A^- = A$. Therefore, the coherent back-scattering probability can be written as $|A^+ + A^-|^2 = 4|A|^2$. It is twice the classical result. The probability of returning to the crossing point is enhanced, as is the resistivity. It is the core of the *weak localization* concept.

The change in conductivity of the system due to this interference effect can be calculated with the following equation :

$$\frac{\delta\sigma_{loc}}{\sigma} = -\frac{2\hbar}{m} \int_0^\infty C(t) e^{-t/\tau_\phi} dt \tag{5.2}$$

where $C(t) = W^{-1}(4\pi Dt)^{-1/2}(1 - e^{-t/\tau})$ denotes the return probability of an electron to its point of departure after a time t. Its derivation depends on the geometry considered. The factor $\exp(-t/\tau_\phi)$ is inserted to account only for the trajectories within the phase coherence time, excluding trajectories with inelastic scattering events. The weak localization correction to the conductance in the case of a narrow channel of width $W < l_\phi$, also referred to as 1D localization, is of the order of

$$\delta G_{\text{loc}} = \frac{W}{L} \delta\sigma_{loc} \sim -\frac{e^2}{h} \frac{l_\phi}{L} \tag{5.3}$$

It can be seen as the incoherent addition in series of L/l_ϕ coherent sections of conductance change e^2/h. It is worth noticing that the correction is independent of W as one would classically expect. The correction of a coherent section indeed corresponds to the

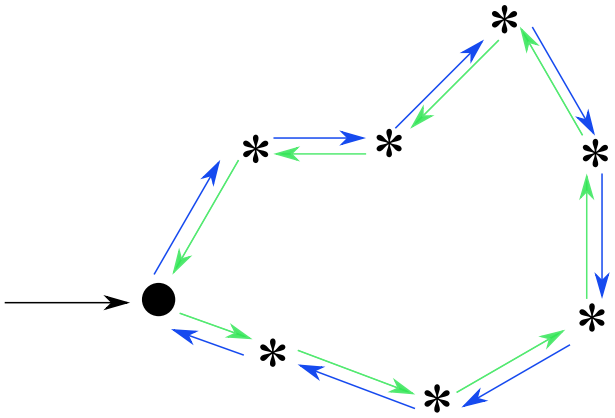

FIGURE 5.1 – Sketch of a diffusive loop trajectory involved in the weak localization effect. The green and blue arrows indicate time-reversed paths. $*$ denote scattering events.

conductance e^2/h of a single quantum channel.

2.3 Dephasing by magnetic field

The weak localization effect highlights the constructive interferences of two time-reversed loop trajectories. Therefore, breaking the time-reversal invariance is breaking this coherent back-scattering effect. If this symmetry is lifted, the probabilities A^+ and A^- are no longer the same and the constructive interferences of coherent back-scattering are suppressed. We can introduce the symmetry breaking thanks to a perpendicular magnetic field. It is not the curvature of the electron trajectories due to the Lorentz force that breaks time-reversal invariance but the phase difference $\Delta\phi$ acquired between the two loops by the application of the vector potential $\mathbf{A}$:

$$\Delta\phi = \frac{2e}{\hbar}\oint \mathbf{A}\cdot d\mathbf{l} = \frac{2e}{\hbar}\iint \mathbf{B}\cdot d\mathbf{S} = \frac{2S}{l_m^2} = 4\pi\frac{\Phi}{\Phi_0} \tag{5.4}$$

where the magnetic length l_m is defined as $l_m = (\hbar/eB)^{1/2}$ and the flux quantum is $\Phi_0 = h/e$.

This phase difference breaks the time-reversal invariance. We see that the stronger the applied magnetic field, the larger the phase difference acquired and so the more efficient the cancellation of the weak localization effect. We also notice that the larger S, the area enclosed by the loop, the most efficient is the symmetry breaking. Those large loops take the most time to complete. Thus, we can view the effect of the magnetic field as the introduction of a time cut-off for the correction of the conductance in equation 5.2. This time limit is known as the magnetic dephasing time $\tau_B \equiv l_m^2/D$ in absence of confinement. The effectiveness of the magnetic field can be represented by a characteristic field B_c occurring when τ_B is as small as τ_ϕ. The significant interest of experimentally measuring the suppression of the weak localization by sweeping a magnetic field relies on the direct possibility of extracting the phase coherence time of the device.

In the following, we discuss how τ_B is expressed in nanostructures depending on ex-

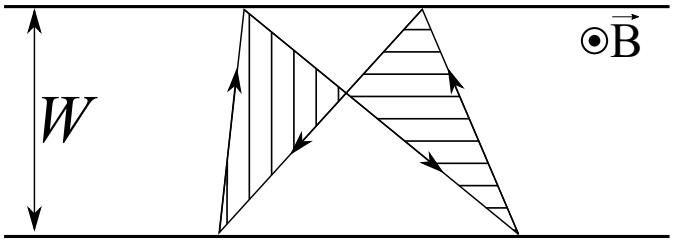

FIGURE 5.2 – Sketch of a close loop via boundary scattering resulting in flux cancellation. The two dashed areas must be exactly equal.

perimental parameters, in particular the channel width W, the phase coherence length l_ϕ and the elastic mean free path l_e. Here we consider relatively narrow nanowires of about 100 nm width, such that the 1D weak localization regime is considered with $W < l_\phi$. The previous Chapter has shown that the mean free path of about 1 μm is also larger than the width of the nanowire, $W < l_e$. This corresponds to the *pure metal* regime. The transport is thus ballistic in the transversal direction but diffusive in the longitudinal direction since $l_e < L$. In this regime the edges play a major role and can reduce the effectiveness of the applied magnetic field in breaking the symmetry [1]. This is known as the flux cancellation effect, which results from back-scattered trajectories involving only wall collisions. Those paths contain smaller loops of equal area but of opposite directions, yielding a net enclosed flux of zero, as illustrated by the dashed areas in figure 5.2. This leads to an enhancement of the characteristic magnetic field B_c (with respect to the *dirty metal* regime $l_e < W$), as impurity collisions are required for the emergence of a phase difference along closed loops.

In the pure metal regime, the ratio Wl_e/l_m^2 corresponds to the maximum phase change acquired on a closed trajectory of length l_e. Depending on the amplitude of this ratio, different regimes are at play. Let us first consider the regime of weak magnetic field : $l_m^2 \gg Wl_e$. Here, the magnetic dephasing time $\tau_B = \frac{C_1 l_m^4}{W^3 \nu_F}$ is independent of l_e [Beenakker, 1988a]. Indeed, because of the flux cancellation effect, increasing l_e will not help to enclose a larger flux. Instead, multiple impurity collisions are required for a loop trajectory to enclose sufficient flux for phase difference accumulation. Then, in the regime of the strong magnetic field, one has $Wl_e \gg l_m^2 \gg W^2$. Here, $\tau_B = \frac{C_2 l_m^2 l_e}{W^2 \nu_F}$ shows a linear dependency with respect to l_e. A single impurity collision can now lead to a loop trajectory enclosing enough flux for phase difference accumulation. It is common to interpolate between the two regimes by considering the analytical formula, $\tau_B = \tau_B^{weak} + \tau_B^{strong}$, for comparison with the experimental data [Beenakker, 1991 ; Kurdak, 1992]. Finally, at very large magnetic fields, when $l_m \ll W$, the cyclotron orbit is smaller than the width of the wire, and quantum Hall physics appears, but it is not the topic here.

Furthermore, the transport being ballistic in the transversal direction, the type of boundary scattering, specular or diffuse, might become meaningful. The type of scattering

1. Contrary to the *dirty metal* regime where the transport is diffusive in both directions. The channel boundaries do not play a role in this case.

considered changes τ_B, mainly by changing specific constants C_i in the expression of τ_B. It appears that the constants C_i are of the same order of magnitude regardless of the type of scattering considered. [2]. The extracted value l_ϕ are then not significantly affected by the choice of the scattering type.

Thanks to the expression of τ_B, we can now write the correction of the conductance in the picture of 1D weak localization when suppressed by a magnetic field. In the integral of equation 5.2, one can add the factor $\exp(-t/\tau_B)$ taking into account the magnetic dephasing time τ_B and using the substituted time :

$$\tau_\phi^{-1} \rightarrow \tau_\phi^{-1} + \tau_B^{-1} \tag{5.5}$$

one obtains :

$$\delta G_{loc}(B) = -g_s g_v \frac{e^2}{h}\frac{1}{L}\left(\left[\frac{1}{D\tau_\phi}+\frac{1}{D\tau_B}\right]^{-1/2} - \left[\frac{1}{D\tau_\phi}+\frac{1}{D\tau_B}+\frac{1}{D\tau}\right]^{-1/2}\right) \tag{5.6}$$

where τ_B is now :

$$\tau_B = \frac{C_1 l_m^4}{W^3 v_F} + \frac{C_2 l_m^2 l_e}{W^2 v_F} \tag{5.7}$$

2.4 Spin-orbit coupling at play

At this point, the spin-orbit interaction can be introduced in the picture. First, we define this concept and then discuss its consequences on the weak localization effect in the frame of transport measurements.

Spin-orbit coupling (SOC) is a relativistic effect arising from the coupling between an electron spin and its motion around the nucleus. As the electron moves through the electric field generated by the positively charged nucleus, it experiences, in its own rest frame, an effective magnetic field due to its motion. This magnetic field interacts with the intrinsic magnetic moment of the electron, which is associated with its spin. For semiconductors with zinc blende crystal structure, the spin-orbit interaction is known to be not canceled by two types of broken symmetry : bulk inversion asymmetry, referred to as the Dresselhaus SOC [Dresselhaus, 1955] and structural inversion asymmetry, known as the Rashba SOC [Bychkov, 1984]. However, the Dresselhaus effect is found to be negligible in low-dimensional structures such as nanowires where the geometry leads to quantum confinement of the electron momentum in the growth direction, which suppresses asymmetry of the crystal structure. On the other hand, the Rashba effect arises from asymmetry in the confining potential that leads to a built-in electric field $\mathbf{E}$ in the structure. It is particularly strong in gated systems and core-shell structures with interfaces. An electric field

2. For specular boundary scattering $C_1 = 9.5$ and $C_2 = 24/5$. For diffuse boundary scattering $C_1 = 4\pi$ and $C_2 = 3$.

perpendicular to the plane creates an effective magnetic field in the electron rest frame, $\mathbf{B}_{so} \propto \mathbf{k} \times \mathbf{E}$ leading to momentum-dependent spin splitting.

In conventional systems, this results in a spin splitting of the electronic bands, yielding two parabolic bands shifted in momentum space, each associated with a distinct spin orientation locked to the electron momentum. This lifts spin degeneracy between states of spin up and down. So instead of a classic parabolic energy distribution where $E_{\uparrow}(\mathbf{k}) = E_{\downarrow}(\mathbf{k})$, two shifted parabolas will be obtained in the momentum space, one for each spin direction, and the two spin states are now bound by the following relation $E_{\uparrow}(\mathbf{k}) = E_{\downarrow}(-\mathbf{k})$:

$$E_{\pm}(\mathbf{k}) = \frac{\hbar^2 k^2}{2m^*} \pm \alpha_R |\mathbf{k}| \tag{5.8}$$

In materials such as HgTe quantum wells, where the electronic dispersion is Dirac-like rather than parabolic, the Rashba spin splitting still occurs but modifies the Dirac cones instead of producing simple shifted parabolas. The resulting spin texture and energy dispersion are therefore more complex, but the essential feature, a momentum-dependent spin splitting due to an electric field perpendicular to the plane, remains present. The Rashba spin-orbit interaction also causes spin precession during electron motion.

In addition, the application of an external electric field through a gate, for instance, allows for the efficient manipulation of the spin-orbit interaction. The strength of the Rashba effect is often described through the coefficient α_R, the Rashba coupling constant, proportional to the electric field [Rashba, 2012]. It ties into an other parameter : l_{so} the spin-orbit length through $l_{so} = \frac{\hbar^2}{m^* \alpha_R}$. The stronger the spin-orbit interaction, the smaller l_{so}. This length characterizes the distance required to rotate the spin during electron motion. Values of l_{so} range from a few microns for weak SO materials like GaAs [Zumbühl, 2002] to a few tens of nanometers for strong SO materials like InSb [Zhang, 2020]. Since the Rashba coupling constant is even higher in HgTe, the spin-orbit length can be as small as 10 nm.

2.5 Weak anti-localization

As the electron travels from impurities to impurities Rashba interaction causes spin precession perpendicular to $\mathbf{k}$. It is of main importance as it modifies quantum interference between time-reversed electron trajectories as illustrated in figure 5.3. Opposite spin rotations suppress the constructive interference of time-reversed paths larger than l_{so} and instead cause destructive interference, which reduces the return probability and so increase the conductance at zero magnetic field. In diffusive transport regimes, such spin rotations suppress the constructive interference responsible for weak localization, leading instead to destructive interference and a positive correction to the conductance near zero magnetic field. Figure 5.3 illustrates spin dephasing between two counter propagating paths, lifting time-reversal invariance. This phenomenon is known as *weak antilocaliza-*

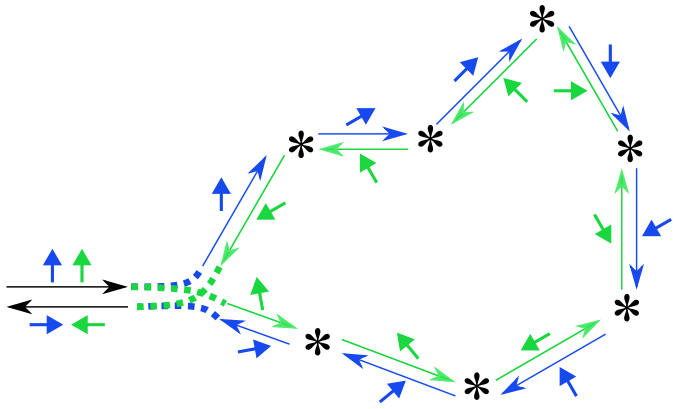

FIGURE 5.3 – Schematic of a loop trajectory leading to destructive interference due to Rashba SOC. The spin is represented by the small thick arrow rotating in opposite directions for the two time-reversed paths. Time invariance is broken as time-reversed partners loops exhibit opposite spin rotations. This yields destructive spin interference in the return probability, thereby increasing the conductance. This effect is at the origin of the WAL conductance peak.

tion (WAL). Exposing the sample to non zero magnetic fields tends this time to lower the conductance by breaking these destructive interferences in loops larger than l_{so}. Beyond a characteristic field B_{so}, these large loops no longer contribute to WAL, and only the shorter loops, where constructive interference dominates, remain. As a result, the conductance correction progressively evolves toward the weak localization regime. The stronger the Rashba coupling α_R, the more pronounced the WAL effect.

After having introduced the effects of spin-orbit interaction in the manifestation of quantum interferences, we can now present its effect in the correction of the conductance ΔG from Kurdak *et al.* [Kurdak, 1992]. They expanded the Al'tshuler-Lee-Stone and Beenakker-van Houten theory [Lee, 1985 ; Beenakker, 1991] to add the SOC in narrow channels of 2D electron gas. An additional term has been added to the return probability integral accounting for spin precession during trajectories :

$$\Delta G(B) = -4\frac{D}{L}\frac{e^2}{h}\int C(t)e^{-t/\tau_\phi}\left[\frac{1}{2}\left(3e^{-4t/3\tau_{so}}-1\right)e^{-t/\tau_B}\right]dt \tag{5.9}$$

where $C(t) = (4\pi Dt)^{-1/2}(1-e^{-t/\tau})$. The $1/2$ factor comes from the standard convention when referring to one spin degree of freedom. The two main features are the addition of -1 for the spin singlet state and $3e^{-4t/3\tau_{so}}$ for the spin triplet state. Here, we assume an isotropic spin-orbit length l_{so} corresponding to a diffusive spin-rotation time $\tau_{so} = l_{so}^2/D$. If the SOC is strong τ_{so} is very small. Therefore, one is left with a $-1/2$ factor in the integral, leading at the end to a plus sign highlighting an increase in the conductance.

The expression obtained in equation 5.6 can therefore be corrected to account for the spin-orbit interaction as :

$$\Delta G(B) = -2\frac{e^2}{h}\frac{1}{L}\Bigg[\frac{3}{2}\left(\frac{1}{D\tau_\phi}+\frac{1}{D\tau_B}+\frac{4}{3D\tau_{so}}\right)^{-1/2} - \frac{3}{2}\left(\frac{1}{D\tau}+\frac{1}{D\tau_\phi}+\frac{1}{D\tau_B}+\frac{4}{3D\tau_{so}}\right)^{-1/2} - \frac{1}{2}\left(\frac{1}{D\tau_\phi}+\frac{1}{D\tau_B}\right)^{-1/2} + \frac{1}{2}\left(\frac{1}{D\tau}+\frac{1}{D\tau_\phi}+\frac{1}{D\tau_B}\right)^{-1/2}\Bigg] \tag{5.10}$$

Finally, fitting the above expression to the experimental data with respect to τ, τ_ϕ, and τ_{so} is an efficient tool to reveal the key characteristics of the nanowire. In the following, we will express these characteristic times in terms of length : $l_e = v_F\tau$, $l_\phi = \sqrt{D\tau_\phi}$, and $l_{so} = \sqrt{D\tau_{so}}$. Note that D is the diffusion constant along the quasi-1D channel in the *pure metal* regime and depends on the type of boundary scattering.

2.6 Universal conductance fluctuations

We now introduce another important manifestation of quantum mechanics in conductance measurements of mesoscopic systems. The measurements manifest fluctuations which are sample specific, random but reproducible deviations from the average conductance. They are a direct consequence of the sensitivity of the quantum phase to external parameters such as magnetic field B, Fermi energy or gate voltage. Importantly, the conductance varies in a non-monotonic but reproducible pattern as these parameters are tuned. Their universal character, as we will explain, naturally gave them the name of *universal conductance fluctuations* (UCF), attributed by Al'tshuler, Lee and Stone [Lee, 1985]. UCF is a fundamental quantum interference phenomenon that originates from the interference of electron wavefunctions along multiple scattering paths in a finite-size coherent conductor. These interference effects indeed require that the electrons maintain a well-defined phase over their trajectories. UCF show up as irregular but reproducible, sample-dependent "fingerprints" of the quantum interference pattern. As explained above, quantum mechanical correlations exist over the phase coherence length l_ϕ that can be much larger than the elastic mean free path l_e. In a narrow channel, as long as phase coherence is maintained, the correction to the conductance is of the order of e^2/h, independent of the properties of the sample. This "universality" is the core of the universal conductance fluctuations. Subsequently, the relative correction $\delta G/\langle G\rangle \propto L$ increases with channel length, meaning that fluctuations are not smoothed out, instead their weight in the conductance increases for long channels. This highlights the absence of self-averaging [Beenakker, 1991]. These features make UCF a powerful probe of phase coherence, dephasing mechanisms, and fundamental symmetries in mesoscopic transport.

Their magnitude at zero temperature is of the order of e^2/h (the phase coherence length being infinite) whatever the size of the sample and the location of the impurities. A convincing derivation of this result is discussed by Lee and Stone in [Lee, 1985 ; Lee, 1986]. However, it is hard to study sample to sample fluctuations because of differences

in the fabrication process, impurity configuration, and so on. Rather, one can study the fluctuations of conductance by sweeping a magnetic field. Indeed, varying the magnetic field is equivalent to a change of the interference pattern because the accumulated phase along electron trajectories is modified. Indeed, time-reversal symmetry and spin-orbit coupling strongly influence the fluctuation patterns. Breaking the time-reversal symmetry with a magnetic field modifies phase contributions from time-reversed paths, thereby changing the interference pattern. A magnetic field sweep therefore mimics a modification of the impurity configuration, revealing conductance fluctuations.

However, in practice, one should take into account that the coherence length l_ϕ is always finite at any non-zero temperature. In addition, the amplitude of the fluctuation can be limited by thermal averaging of the interference, symbolized by the thermal length $l_T = (\hbar D/k_B T)^{1/2}$. Note that the temperature itself does not break the coherence. Rather it is the excitations present a finite temperature inducing inelastic scattering that break the coherence.

In the following, we discuss the amplitude of the UCF depending on the ratio l_ϕ/l_T. We focus on the narrow channel case within the 1D regime, where $W \ll l_\phi \ll L$. In the regime $l_\phi \ll l_T$, the effect of thermal averaging can be neglected since the coherence of the trajectories is already broken before any effect of thermal averaging can occur. In this situation, the channel can be thought of as subdivided into uncorrelated segments of length l_ϕ. Each segment shows conductance fluctuations of the order of e^2/h. The segments being in series, one can easily estimate the amplitude of the total conductance through the channel [Lee, 1987]. That yields, in units of e^2/h :

$$\delta g = \frac{g_s g_v}{2} \beta^{-1/2} \sqrt{12} \left(\frac{l_\phi}{L} \right)^{3/2} \tag{5.11}$$

On the other hand, if $l_\phi \gg l_T$, the temperature will lead to thermal smearing of the UCF amplitude by averaging the interference at different energies around the Fermi level within an interval of order $k_B T$. The energy levels available for transport, within this interval, are split in sub-intervals which are uncorrelated. We can show that it leads to a reduction by l_T/l_ϕ of the results from equation 5.11. The corresponding root-mean-square variation of conductance is now written [Altshuler, 1985] :

$$\delta g = \frac{g_s g_v}{2} \beta^{-1/2} \left(\frac{8\pi}{3} \right)^{1/2} \frac{l_T l_\phi^{1/2}}{L^{3/2}} \tag{5.12}$$

The parameter β depends on the magnetic field, $\beta = 1$ at zero magnetic field and $\beta = 2$ at finite field, and $g_s g_v = 2$ because spin degeneracy is not lifted.

The asymptotic expressions we have just mentioned are not really appropriate for comparison with experiments because generally l_ϕ and l_T are not well separated. For that reason, Beenakker and Van Houten [Beenakker, 1988b] have derived an interpolation formula to be used in the intermediate regime where $l_\phi \sim l_T$:

$$\delta g = \frac{g_s g_v}{2}\beta^{-1/2}\sqrt{12}\left(\frac{l_\phi}{L}\right)^{3/2}\frac{1}{\sqrt{1+\frac{9}{2\pi}\left(\frac{l_\phi}{l_T}\right)^2}} \tag{5.13}$$

2.7 Correlation field of conductance fluctuations

The phase coherence length can also be determined by a characteristic magnetic field. When sweeping the magnetic field, fluctuations in conductance are equivalent to those originating from a different impurity pattern, provided that the change is larger than a correlation field ΔB_C. That is, the conductance obtained at B and $B + \Delta B_C$ is not correlated. The correlation function of the magneto-conductance can be defined by the following expression [Lee, 1987] :

$$\begin{aligned} F(\Delta B) &\equiv \langle [G(B) - \langle G(B)\rangle][G(B+\Delta B) - \langle G(B+\Delta B)\rangle]\rangle \\ &\equiv \langle \Delta G_{xx}(B)\Delta G_{xx}(B+\Delta B)\rangle \end{aligned} \tag{5.14}$$

where the angle brackets $\langle\cdot\rangle$ denote here the average over the magnetic field range. One can express the standard deviation of the conductance variation as $\delta G = F(0)^{1/2}$. The correlation field is defined as the half width at half maximum of the auto-correlation function :

$$F(\Delta B_C) = F(\Delta B = 0)/2 \tag{5.15}$$

We can also extract the phase coherence length from the auto-correlation function. The analysis involves complex physics phenomena that are nicely derived by Beenakker *et al.* in [Beenakker, 1991 ; Beenakker, 1988b]. In short, the calculation of the effective dephasing rate can be written :

$$\frac{1}{\tau_{\text{eff}}} = \frac{1}{\tau_\phi} + \frac{1}{\tau_{\Delta B/2}} \tag{5.16}$$

describing the exponential decay of the average phase factor $\langle \exp(i\Delta\phi)\rangle = \exp(-t/\tau_{\text{eff}})$. In the pure metal regime, where $W \ll l_e$, $\tau_{\Delta B/2}$ can be obtained by interchanging $B \to \Delta B/2$ in the interpolation formula of τ_B for the WL effect, see equation 5.7. From the definition 5.15 the correlation field ΔB_C, one then obtains for the pure and dirty metal regimes :

$$\begin{aligned} \Delta B_C W l_\phi &= \frac{h}{e}\frac{0.38}{\gamma}\frac{l_e^2}{l_\phi W}\left(1+\sqrt{1+3.3\gamma\frac{l_\phi^2 W}{l_e^3}}\right) && \text{for } W \ll l_e \\ \Delta B_C W l_\phi &= \frac{h}{e}C && \text{for } W \gg l_e \end{aligned} \tag{5.17}$$

where $\gamma = 1/3$ for $l_\phi \gg l_T$ and $\gamma = 1.7$ for $l_\phi \ll l_T$ in the pure metal regime, while $C = 0.95$ for $l_\phi \gg l_T$ and $C = 0.42$ for $l_\phi \ll l_T$ in the dirty metal regime. It is interesting to note that the characteristic flux $\Phi_C \equiv \Delta B_C W l_\phi$ in the pure metal regime is larger than

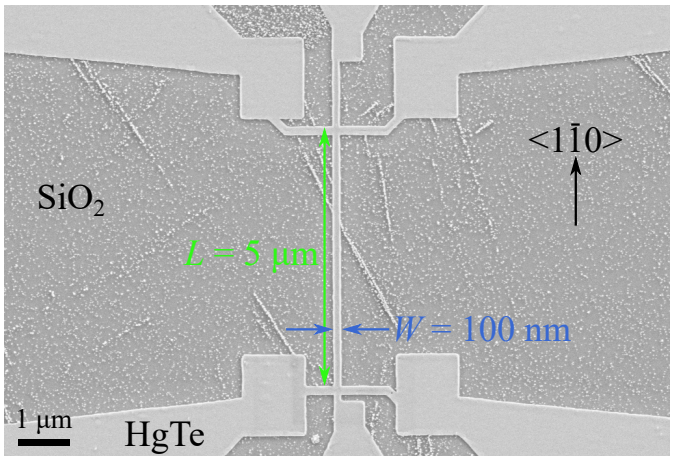

FIGURE 5.4 – Top view SEM micrograph of the measured HgTe nanowire grown by SAG. It is oriented along <1$\bar{1}$0> direction on the CdTe substrate. The nanostructure is capped by a 10 nm-thick HgCdTe layer. The presence of parasitic growth on the silicon dioxide mask area is due to the cap layer deposition. The image has been taken before the deposition of the gate oxide and electrode.

that in the dirty metal regime. This is another consequence of the flux cancellation effect originating from boundary scattering, in which a higher flux is needed to get a noticeable phase shift.

2.8 Summary

In a nutshell, quantum transport phenomena in quasi 1D systems are deeply influenced by phase coherence, which governs the interference effects underlying weak localization and universal conductance fluctuations. Their manifestation depends on the scale of the phase coherence length with respect to the characteristic dimensions of the system, W/L, and temperature. In this section, we described a robust theoretical framework for interpreting conductance variations beyond classical expectations. In the following section, we turn to the experimental results obtained on a nanowire and a nanoring. We assess how these quantum interference signatures manifest in these mesoscopic devices. By confronting the data with the theory presented here, we aim to extract the relevant physical parameters and determine the regime of electronic transport.

3 Nanowire

This section presents magneto-transport measurements performed on a $\langle 1\bar{1}0 \rangle$-oriented nanowire grown by SAG, as shown in figure 5.4. The contacts are arranged in a Hall bar-type configuration with a channel length $L = 5$ μm and a width $W = 100$ nm. The heterostructure is identical to that used for the Hall bar characterization, consisting of a 10 nm HgTe quantum well capped with a 10 nm HgCdTe layer, both grown in-situ at 170°C on a CdTe substrate. The entire structure, including the nanowire and its macroscopic contacts, is covered by an insulating layer of Al_2O_3 and a metallic gate. Given the nanowire

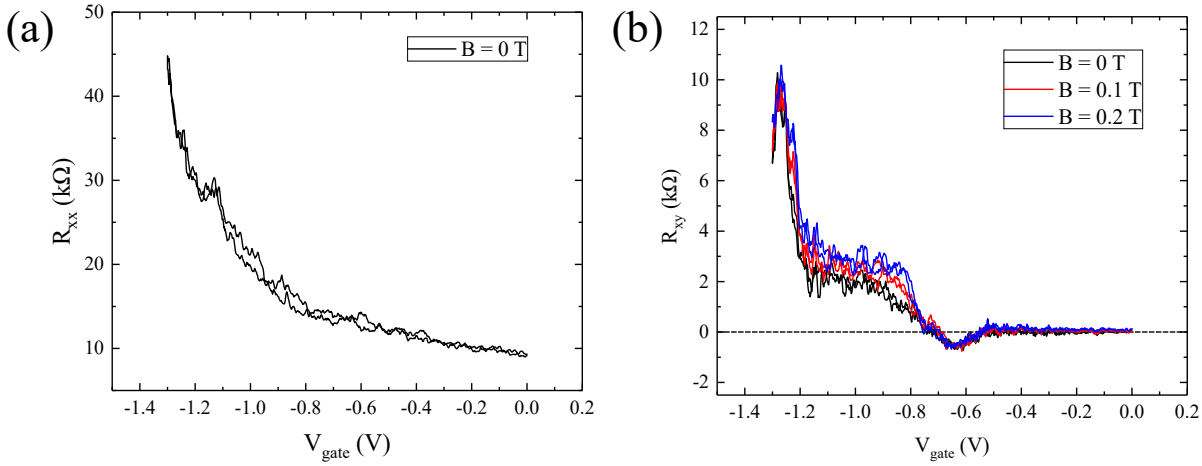

FIGURE 5.5 – Low-field transport properties of the HgTe nanowire. (a) R_{xx} variation versus the gate voltage. (b) R_{xy} variation versus the gate voltage at zero magnetic field (black), $B = 0.1$ T (red) and $B = 0.2$ T (blue). The horizontal dashed line serves as guide for the eye. The measurements are performed under bias voltage $U = 1$mV at 1.5 K.

dimensions and aspect ratio, the gating configuration is most likely of the gate-around type.

We begin by characterizing the basic electronic properties of the device through low-field magneto-transport measurements. To search for signs of Landau levels quantization, we performed gate voltage-magnetic field (V_{gate}-B) mapping and analyzed the resulting magnetoresistance patterns. Then, the study focuses on the analysis of the phase coherence mechanisms at play in the nanowire. We start with universal conductance fluctuations (UCF) measurements, where the magnetic field, temperature, and bias voltage are varied. Finally, we investigate the weak antilocalization (WAL) effect, whose analysis provides additional insights into the coherence length. These experimental observations are discussed in the context of the theoretical framework introduced earlier.

3.1 Density and mobility

3.1.1 Measurements at low magnetic field

Basic characterizations of the nanowire are first performed to get information on the electronic transport properties in such narrow channels. We therefore start at zero and low magnetic field in order to investigate the manifestations of the Hall effect in the structure. The measurements are carried out at 1.5 K.

Figure 5.5(a) displays the longitudinal resistance as a function of the gate voltage in the absence of magnetic field. The resistance at zero gate voltage is around 10 kΩ, much larger than the Hall bar, since the aspect ratio of the nanowire is much larger, 50 squares in series. The corresponding sheet resistance, $R_\square = 10^4/50 = 200\,\Omega$, is about three times larger than that of the Hall bar, indicating a reduction of the effective mean free path because of the collisions on the edges of the narrow wire. This experimental ratio of sheet resistance, or

equivalently of 2D resistivity, between the nanowire and the large Hall can be compared to the predictions by Beenakker and van Houten [Beenakker, 1991]. On one hand, the change in resistivity between the 2D bulk value and a channel of width $W \ll l_e$ due to diffuse boundary scattering only is predicted to scale as $\rho/\rho_{2D} = (\pi/2)(l_e/W)(\ln(l_e/W))^{-1}$. In our case, using the elastic mean free path associated with the large 2D Hall bar $l_e = 1.7\ \mu$m and the width $W = 100$ nm of the nanowire, we obtain $\rho/\rho_{2D} \approx 10$. On the other hand, the ratio would be $\rho/\rho_0 = 1$ in the case of specular boundary scattering. Therefore, the intermediate experimental value suggests that electron reflections at the nanowire boundaries are in a mix regime between specular and diffuse boundary scattering.

In figure 5.5(a), we also observe that the resistance increases when decreasing the gate voltage due to the progressive depletion of the carriers, but do not show a maximum at the CNP contrary to the Hall bar. Discrepancies between the sweep up and down are visible and account for the small changes of the impurity configuration in the nanowire.

Figure 5.5(b) illustrates the Hall resistance variation as a function of the gate voltage under different applied magnetic fields. First, as for the Hall bar presented in Chapter 4, the transversal resistance is not zero at a zero magnetic field. Because the lateral voltage probes have dimensions smaller than the mean free path, electrons can reach them ballistically rather than in the diffusive regime. As a result, the voltage measured at these contacts may not correspond purely to the local transverse potential, leading to a mixing of longitudinal and transverse components in the measured R_{xy}. Furthermore, the Hall resistance crosses several times the zero-resistance line, regardless of the magnetic field strength. Thus, it is hard to identify the charge neutrality point. In addition, and contrary to the Hall bar, there is no linear increase of the Hall resistance with the magnetic field, neither on the electron side nor on the hole side. Therefore, the Hall effect is not well defined in such small structures, and the electronic transport appears to be more complex than in 2D. These preliminary measurements alone are insufficient to characterize the distribution of charge carriers and to understand their mobility and mean free path.

3.1.2 Measurements at high magnetic field

The Landau level quantization observed at high magnetic field produces characteristic features from which the carrier density can be extracted via the filling factor. We therefore perform a two-dimensional mapping of the nanowire transport properties as a function of both magnetic field and gate voltage with the objective to get deeper insights into its electronic properties.

The 2D maps for both the longitudinal resistance R_{xx} and the Hall resistance R_{xy} (in units of h/e^2) are shown in figure 5.6.

Considering first the longitudinal resistance in figure 5.6(a), no clear manifestation of Landau levels is visible. The dark blue area with insulating behavior could be associated with the gap opening between the two $E_0^{\pm}$ energy levels at a finite field, see figure 4.6. As noted in figure 5.5(a), the resistance keeps increasing as the gate voltage is further

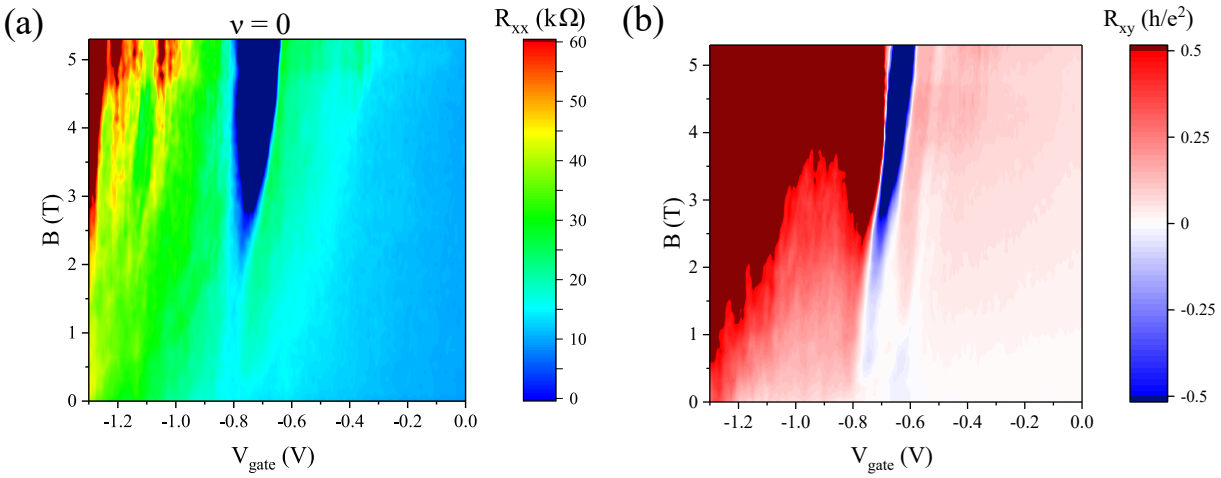

FIGURE 5.6 – 2D maps of magneto-transport measurements performed on the HgTe nanowire. (a) The longitudinal resistance R_{xx} is plotted as a function of gate voltage and magnetic field. (b) The Hall resistance in units of h/e^2 is displayed with respect to the same parameters.

reduced and the system is expected to be on the hole side of the CNP. To analyze this behavior, traces at different magnetic fields of the longitudinal resistance are plotted in figure 5.7(a). No oscillations are visible, confirming the absence of quantum Hall effect. No decrease in resistance is observed as the hole regime is reached at low gate voltage. Rather, the resistance increases continuously. This anomalous variation on the hole side illustrates the complex transport mechanisms with holes as main carriers. The negative resistance data are located at $\nu = 0$ where the system is insulating (the negative sign might be the result of a poor quality voltage contact).

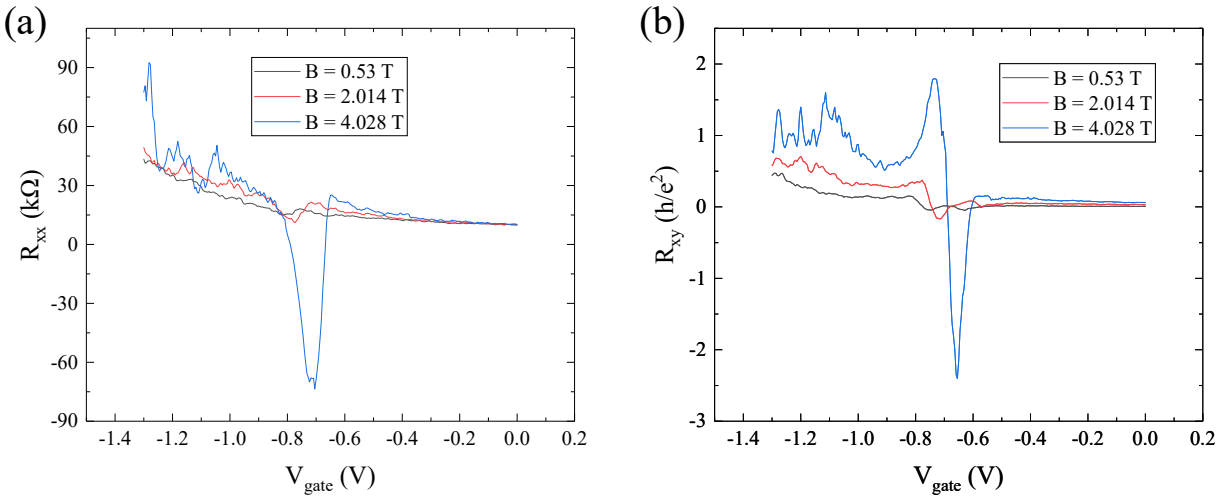

FIGURE 5.7 – Traces of (a) R_{xx} and (b) R_{xy} extracted from figure 5.6. The data are plotted as a function of the gate voltage and obtained from three different applied magnetic field : $B = 0.53$ T (black), $B = 2.014$ T (red) and $B = 4.028$ T (red).

Then, we focus on the Hall resistance shown in figure 5.6(b). No quantized plateau is visible. Similarly to the zero field data from figure 5.5(b), the negative area for $-0.8 \leq V_{\text{gate}} \leq -0.6$ V, persists at all magnetic field so that the Hall resistance is alternatively positive and negative. On the hole side, $V_{\text{gate}} \leq -0.8$ V, the resistance is positive

and higher probably due to a contribution of longitudinal resistance. Traces of the Hall resistance at different magnetic field are displayed in figure 5.7(b). Again no plateau is visible. The similarity of the Hall resistance with the longitudinal resistance confirms the contribution of the latter when measuring the transversal voltage in such a nano-scale Hall cross with dimension smaller than the mean free path.

In a 100 nm-wide nanowire, Hall plateaus are indeed hard to observe because the geometry does not provide the conditions necessary for the quantum Hall effect, which is intrinsically a two-dimensional phenomenon. As we have seen in Chapter 4, a wide 2D electron gas is required to form a bulk region hosting well-defined Landau levels separated by cyclotron gaps. This configuration supports counter-propagating, dissipation-less edge states, which give rise to quantized transport properties. However, in such a narrow channel, there is most likely no distinct bulk : the edges are too close to each other, leading to coupling and back-scattering between counter-propagating edge modes. This overlap prevents the emergence of quantized Hall conductance. As a result, the system behaves more like a quasi-one-dimensional conductor, where mesoscopic effects such as interferences dominate.

3.1.3 Electron side

Despite the complexity of the measurement results in the nanowire, it is possible to estimate its carrier density and mobility on the electron side, as shown below.

Figure 5.8(a) illustrates the magnetic field dependence of the Hall resistance at three different gate voltages. On the electron side, since the Hall resistance evolves linearly with the magnetic field, we compute the Hall constant R_H by linearly fitting the Hall resistance data over the range $0 \leq B \leq 5.3$ T. The variation of the Hall constant as a function of the gate voltage is displayed in figure 5.8(b) and the resulting carrier density is visible in figure 5.8(c). At zero gate voltage, the electron density reaches 18×10^{11} cm^{-2}, which is higher than the value obtained for the Hall bar. The depletion factor $\alpha = 28 \times 10^{11}$ cm^{-2}V^{-1} is also found to be larger. Most likely, the gate around configuration increases the density and the depletion factor by application of an electric field on top but also on the sides of the channel.

The electron mobility extracted from the zero-field longitudinal resistance and the Hall density is shown in figure 5.8(d). The mobility is approximately 0.2×10^5 cm^{2}V^{-1}s^{-1} at zero gate voltage. This value is lower than that found in the Hall bar by a factor about 5. The gate voltage dependence is also very different as here it increases with decreasing the gate voltage, see the green dashed line for comparison with the Hall bar. The lower mobility found in the nanowire is consistent with the literature where one-dimensional geometry systematically exhibits lower mobility than in thin films of corresponding materials [Badawy, 2024]. The reason for that is the enhanced surface-to-volume ratio of nanowires which promotes surface scattering as a dominating mechanism, even in defect-free nanowires. In contrast to the Hall bar, the mobility in the nanowire slightly increases as the

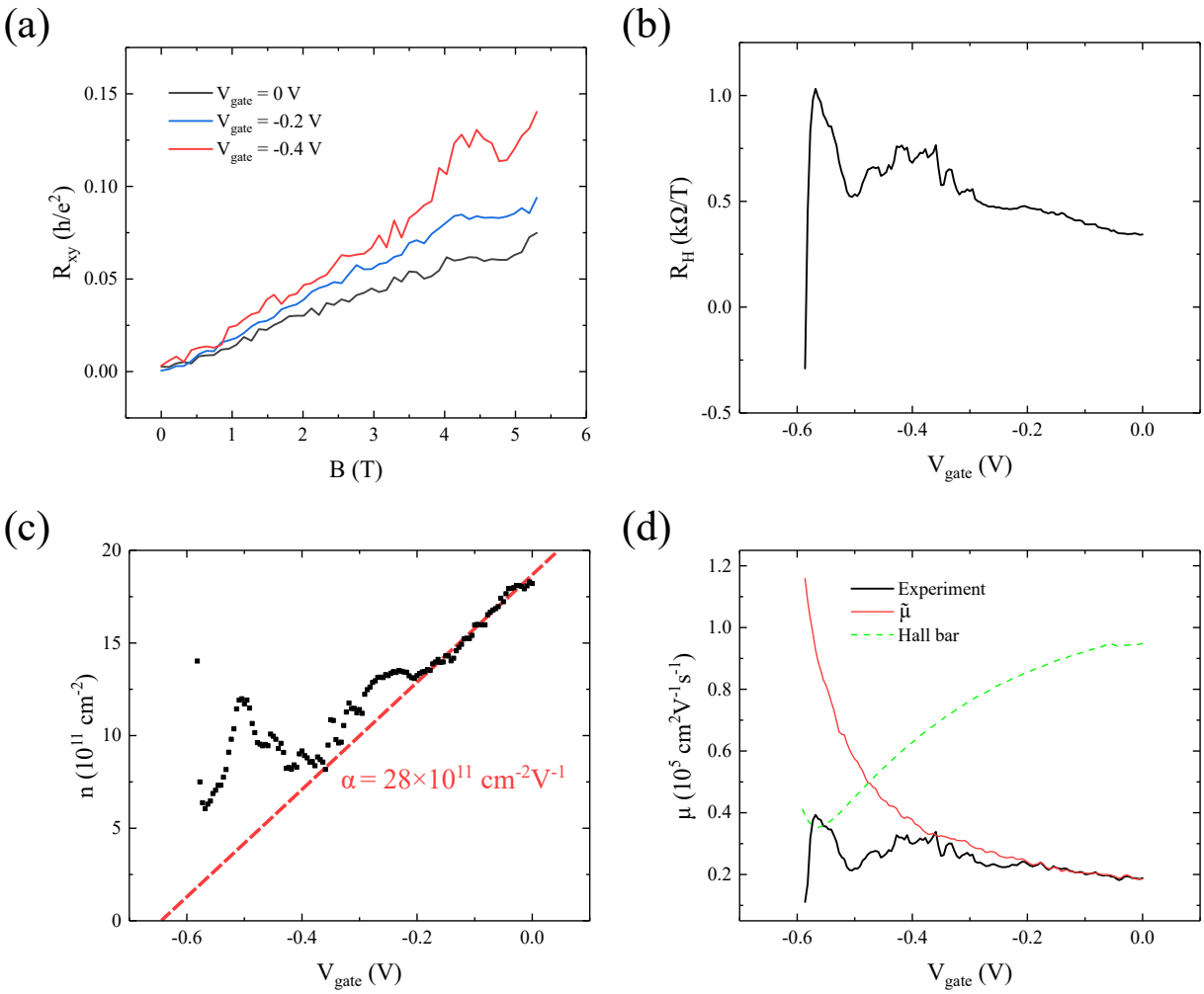

FIGURE 5.8 – Density and mobility in the HgTe nanowire, extracted from the data shown in figure 5.6 on the electron side of the CNP $V_{\text{gate}} \geq -0.6$ V. (a) Hall resistance as a function of the magnetic field for three different gate voltages. (b) Hall constant extracted from a linear fit at each gate voltage. (c) Carrier density with respect to the gate voltage. (d) Electron mobility calculated from the the experimental data together with the mobility $\tilde{\mu}$, calculated from a linearized density with the depletion factor α, and the Hall bar mobility from figure 4.10 for comparison.

gate voltages reduces. This effect has also been observed in InSb nanowires [Aseev, 2019] and is explained as follows. Reducing the gate voltage could push the electron distribution further from the nanowire-gate oxide surface, reducing surface scattering.

We also plot the mobility $\tilde{\mu}$ calculated from the linearized density $\tilde{n} = \alpha(V_{\text{gate}} - V_{g0})$ with $\alpha = 28 \times 10^{11}$ cm^{-2}V^{-1} and $V_{g0} = -0.66$ V, and the zero-field longitudinal resistance. This approach eliminates the density fluctuations induced by the poor quality measurements of the Hall resistance. The resulting mobility $\tilde{\mu}$ is shown in figure 5.8(d) by the red curve. It overlaps with the previously-calculated mobility only in the range -0.2 to 0 V. For $V_{\text{gate}} < -0.4$ V, it shows significantly higher values as the density $\tilde{n}$ goes to zero and no longer reflects the experimental situation. From the Hall bar measurements, we indeed know that the gate starts to accumulate holes in the valence band, and therefore depletes electrons with a lower depletion factor for $V_{\text{gate}} < -0.4$ V.

In the following sections, we will restrict our study to the electron side $V_{\text{gate}} \geq -0.3$

V. The presence of only one carrier type will ease the manifestation and understanding of quantum phenomena.

3.1.4 Mean free path

As explained in section 2, different transport regimes can be considered depending on the elastic mean free path l_e of the electrons, defined as the average length between two scattering events on impurities. It is therefore important to assess its value for an accurate application of the equations describing the quantum interference effects. In the 2D diffusive regime, from the carrier density and mobility at zero gate voltage using the relation 4.20, we can compute an effective mean free path l_e^{eff} in the nanowire

$$l_e^{\text{eff}} = 420 \text{ nm} \tag{5.18}$$

This effective mean free path being larger than the nanowire width $W = 100$ nm, the transport is found to be ballistic in the transversal direction (and diffusive along the nanowire axis). This is the *pure metal* regime where $W < l_e$. We also note that this effective mean free path is significantly smaller than in the large 2D Hall bar where $l_e = 1.7$ μm. The similar width of the channel strongly limits the available space for ballistic transport between impurities and enhances boundary scattering in the transversal direction (assuming a similar impurity configuration in both structures). In these conditions, the effective mean free path can be estimated by the relation :

$$l_e^{\text{eff}} \sim \sqrt{l_e W} = 410 \text{ nm} \tag{5.19}$$

We have seen from the ratio of sheet resistance that boundary scattering is a combination of diffuse and specular scattering, although their relative contributions could not be quantified. Consequently, the intrinsic mean free path, limited solely by impurity scattering, is expected to be larger than the effective one : much larger if diffuse scattering dominates, or slightly larger if specular scattering prevails. In the following, we will therefore use the effective mean free path $l_e^{\text{eff}} = 420$ nm as a practical value, acknowledging that it likely includes boundary-scattering effects.

3.2 Universal conductance fluctuations

The attentive reader would have noticed the small fluctuations of the longitudinal resistance with respect to the gate voltage in figure 5.5(a). These fluctuations reveal the coherent transport of electrons in the nanowire. They arise from quantum interferences and are called universal conductance fluctuations (UCF). They reflect the distribution of impurities in the system, they are like fingerprints of the disorder. Their pattern change as a function of the external parameters such as gate voltage and magnetic field.

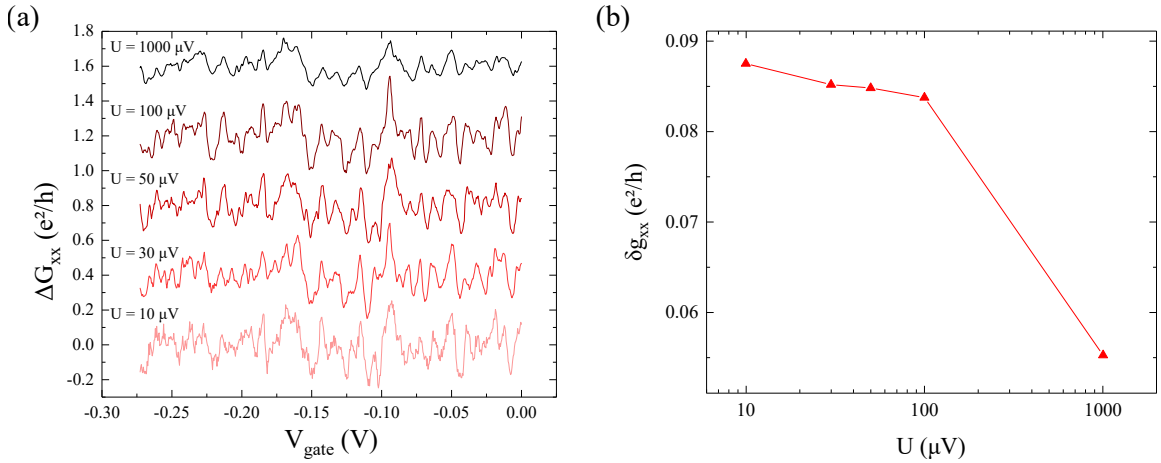

FIGURE 5.9 – UCF measurements in the HgTe nanowire at 0.28 K. (a) Smearing effect due to the bias voltage. Curves are vertically shifted for clarity. (b) Standard deviation of the conductance curves shown in (a).

The ability of the magnetic field to manifest UCF in mesoscopic devices is a well-established topic and is widely used in the community. But, their manifestation is also possible by sweeping the gate voltage. The following section illustrates this method and emphasizes the importance of using a low excitation signal. The subsequent sections will focus on the magnetic field sweeps and the temperature dependence analysis of the UCF.

3.2.1 About measuring accurately

We here present the optimization of the experimental set-up parameters for measuring accurately quantum effects involving interference of electronic waves. If the applied bias voltage is too large, multiple occupied energy levels contribute simultaneously to the transport. As a result, the signatures of individual quantum states are smeared out, leading to a loss of resolution in the observation of fine quantum phenomena. This effect is highlighted in figure 5.9(a).

The longitudinal resistance $R_{xx} = V_{xx}/\mathrm{I}$ is measured for different bias voltages U from 1 mV down to 10 μV. The resistance is then converted into conductance $G_{xx} = 1/R_{xx}$. The figure displays the amplitude of the UCF defined as the difference ΔG_{xx} between the conductance and its slow varying background. The fluctuations of the conductance as we sweep the gate voltage are clearly evidenced. However, at the highest bias voltage, the amplitude of the oscillation is significantly reduced. Figure 5.9(b) shows the standard deviation of the conductance oscillation with respect to the bias voltage. The standard deviation is maximum at the lowest bias U = 10 μV, and so is the UCF amplitude. But in the corresponding curve in figure 5.9(a), noise is also present, artificially increasing the standard deviation. Note that the measurement noise has been minimized by setting the lock-in amplifiers to *autogain* mode. Since the goal is to have the highest amplitude possible and the least noise at the same time the least noise, the optimum bias voltage seems to be 30 μV.

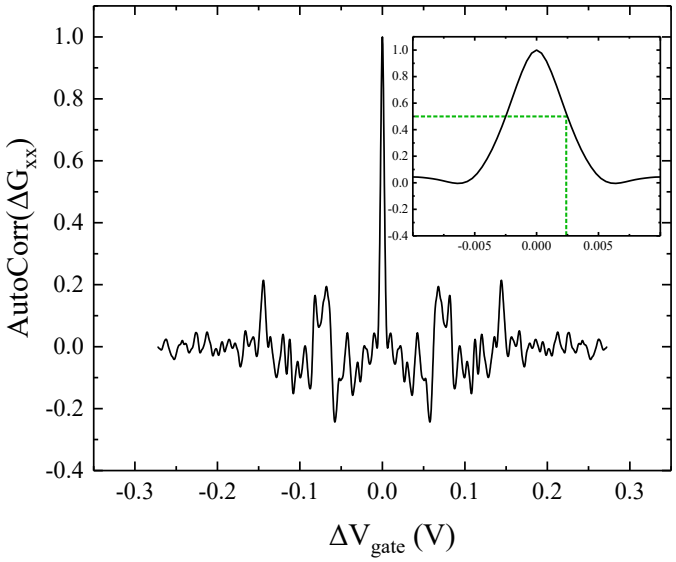

FIGURE 5.10 – Auto-correlation function of the UCF shown in figure 5.9(a) for the sweep in gate voltage at $U = 30$ μV at 280 mK. The inset shows a zoom-in to identify ΔV_{corr}.

Even though the measurement parameters are optimized, the resolution of the measurement is still limited by thermal fluctuations, which introduce an energy spreading of the order of $k_B T$.

3.2.2 Correlation energy from gate voltage sweeps

Similarly to what has been presented in Section 2.6 for the determination of a characteristic magnetic field, we can extract a characteristic gate voltage for the pattern of aperiodic fluctuations and then derive a characteristic energy. This energy reflects the typical energy scale over which the disorder configuration remains effectively unchanged, or equivalently, the energy required to induce significant modifications in the electronic interference pattern. Physically, this correlation in energy reflects the energy resolution of the quantum interference spectrum and is comparable to the Thouless energy $E_{\text{Th}} = \hbar D/L^2$, where D is the diffusion constant and and L is the size of the coherent region, being limited either by the device boundaries or by the phase coherence length l_ϕ.

The correlation voltage is defined in the same way as the correlation magnetic field, so :

$$F(\Delta V_{\text{corr}}) = F(0)/2 \tag{5.20}$$

where F denotes the auto-correlation function. If we consider the curve at $U = 30$ μV from figure 5.9, we can plot the normalized auto-correlation function of the data F, as visible in figure 5.10. We find $\Delta V_{\text{corr}} = 2.5$ mV. Similar results have been found from other data sets with $U = 30$ μV and $T = 0.28$ K.

We now have to relate this change in gate voltage to a corresponding change in energy. To achieve this, we first convert the gate voltage to density thanks to the following rela-

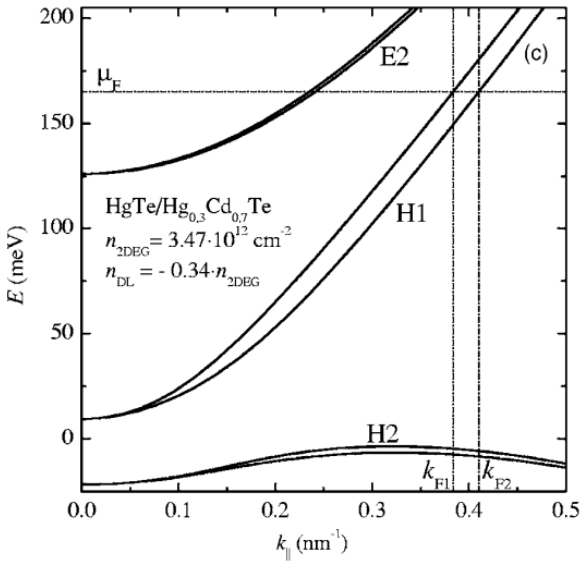

FIGURE 5.11 – Band structure of 12.2 nm-thick HgTe quantum well calculated on the basis of a $H_{8\times8}(\mathbf{k})$ Hamiltonian. Taken from [Novik, 2005]. For wave vectors k above 0.25 nm^{-1}, the H1 conduction band has a Dirac-like energy dispersion $E(\mathbf{k}) = \hbar\nu_F k$ with a Fermi velocity $v_F = 8.6 \times 10^5$ m/s.

tion :

$$\Delta n = \alpha \cdot \Delta V_{\text{corr}} \tag{5.21}$$

where α is the depletion factor estimated from the carrier density variation as a function of the gate voltage in figure 5.8(c).

Then, the conversion from density to energy relies on an accurate description of the band structure in the HgTe quantum well. Since its energy dispersion is closed to that of a Dirac cone, we can write :

$$E = \hbar v_F \sqrt{2\pi n} \tag{5.22}$$

This relation gives the change in energy as a function of the change in density, and thus provides the correlation energy from the gate voltage correlation of the UCF :

$$\Delta E_c = \frac{\hbar v_F \sqrt{2\pi}}{2} \frac{\Delta n}{\sqrt{n}} = \hbar v_F \sqrt{\frac{\pi}{2}} \frac{\alpha \Delta V_{\text{corr}}}{\sqrt{n}} \tag{5.23}$$

The band structure calculations reported by Krishtopenko *et al.* visible in figure 4.11 focuses mainly on the gap region dominated by the mass term at the origin of a locally parabolic dispersion around $k = 0$. Therefore, the linear dispersion is not really visible in this graph and it is necessary to use another band structure calculation performed on a larger range of wave vectors and energies. For this reason, we now consider the band structure calculated by Novik *et al.* [Novik, 2005] for a 12 nm-thick HgTe QW which is shown in figure 5.11. The Fermi velocity of the linear dispersion for k above 0.25 nm^{-1} is $v_F = 8.6 \times 10^5$ m/s. In the gate voltage range from -0.3 to 0 V where the UCF have been measured in figure 5.9(a), the electron density varies from 10 to 18 $\times 10^{11}$ cm^2 according

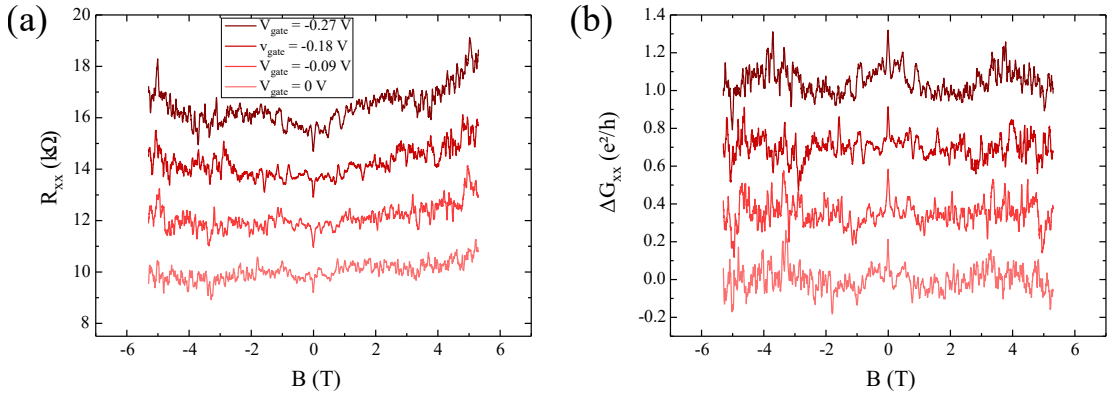

FIGURE 5.12 – Universal conductance fluctuations in the HgTE nanowire. (a) Fluctuations in longitudinal resistance as a function of the magnetic field for different applied gate voltages. (b) Resulting conductance difference after subtraction of the mean background. For clarity, the curves are vertically offset. Experiments are performed at 1.5 K with a bias voltage $U = 1000$ μV.

to figure 5.8(c) and the wave vector $k = \sqrt{2\pi n}$ varies from 0.25 to 0.34 nm^{-1}. In this range, the dispersion relation shown in figure 5.11 is linear with the last value of the Fermi velocity.

Finally, considering the depletion factor $\alpha = 28 \times 10^{11}$ cm^{-2}V^{-1} extracted from the slope of the carrier density and the density at zero gate voltage $n = 18 \times 10^{11}$ cm^{-2}, we can compute the correlation energy ΔE_c associated with ΔV_{corr} :

$$\Delta E_c \sim 0.37 \text{ meV} \tag{5.24}$$

This quantity characterizes the sensitivity of the UCF to the position of the Fermi level.

3.2.3 Magnetic field sweeps

The usual way to investigate UCF is by sweeping the magnetic field which breaks the time-invariance symmetry by introducing phase difference between electron trajectories. Examples of UCF pattern versus magnetic field are shown in figure 5.12(a) for four different gate voltages restricted to the electron side. For each curve, we calculate the average resistance background thanks to a quadratic fit and subtract this background from the raw data to plot the variations of the conductance ΔG_{xx} in figure 5.12(b). The UCF amplitudes are relatively similar on the four curves, around 0.2 e^2/h, and increase progressively from the low field regime to the high field regime. As we change the gate voltage, the oscillating pattern changes. This is a sign that the perception of the disorder by the electronic waves has changed. Looking at each curve separately in figure 5.12(a), one can see that the UCF pattern is not symmetric in B, that is $R_{xx}(B) \neq R_{xx}(-B)$. It is indeed predicted from theory that the four-terminal resistance of a coherent conductor is not symmetric with respect to field inversion (except if the current and voltage leads are consistently exchanged).

A full representation of the UCF as a function of the two parameters can be obtained from a two-dimensional map of the longitudinal resistance. Figure 5.13 displays the variation of conductance ΔG_{xx} as a function of gate voltage V_{gate} and perpendicular magnetic field B. Note that in this case, the fluctuations of conductance are measured while sweeping the gate voltage rather than the magnetic field, as was done previously, since the gate voltage corresponds to the fast scan direction of the 2D map. The measurements reveal pronounced fluctuations throughout the magnetic field range and gate voltage range, with typical amplitudes of $\pm 12\ e^2/h$. The higher amplitude of the oscillations at high magnetic field is also noticeable here. The continuous blue or red areas reflect the range of the parameter range over which the oscillations remain correlated.

These reproducible aperiodic fluctuations are characteristic of universal conductance fluctuations (UCF), resulting from coherent interference of electron trajectories in the quasi-one-dimensional nanowire geometry. The observed sensitivity of the fluctuation pattern to both V_{gate} and B reflects the combined influence of Fermi level tuning and magnetic flux threading the nanowire.

While the UCF pattern is modified by the gate voltage, there is one feature which remains almost unaffected : the conductance peak at zero magnetic field visible in figure 5.12(b). This peak is the signature of the WAL effect explained in Section 2.5. The WAL results from an always-destructive interference of the back-scattered trajectories, in contrast to UCF which arise from random alternation of constructive and destructive interference among multiple electron trajectories. The resulting peak in the conductance disappears rapidly with field, since the magnetic field breaks the time-reversal symmetry required for the spin-orbit-induced destructive interference of time-reversed loops. A quantitative analysis of the WAL peak will be presented in Section 3.4.

This experiment confirms that transport in the nanowire is in the phase-coherent regime, where quantum interference contributes to the conductance response. The evolution of the fluctuation pattern with V_{gate} further indicates efficient electrostatic control of the carrier density in the HgTe channel. The data are also consistent with diffusive transport along the longitudinal axis, in line with expectations for narrow HgTe nanowires where quantum confinement and disorder coexist .

3.2.4 Temperature dependence

The temperature dependence of the UCF amplitudes reflects the level of quantum coherence in the nanowire. The underlying objective is the extraction of the phase coherence length l_ϕ that we present in the subsequent section.

Figure 5.14(a) displays the evolution of conductance variation ΔG_{xx} as the temperature increases from 280 mK to 20 K. Both the UCF amplitude and the height of the WAL peak decrease with temperature. In figure 5.14(b), we plot the corresponding standard deviation as a function of temperature showing a strong reduction at high temperature. The amplitude of UCF is strongly sensitive to temperature as a result of either the ther-

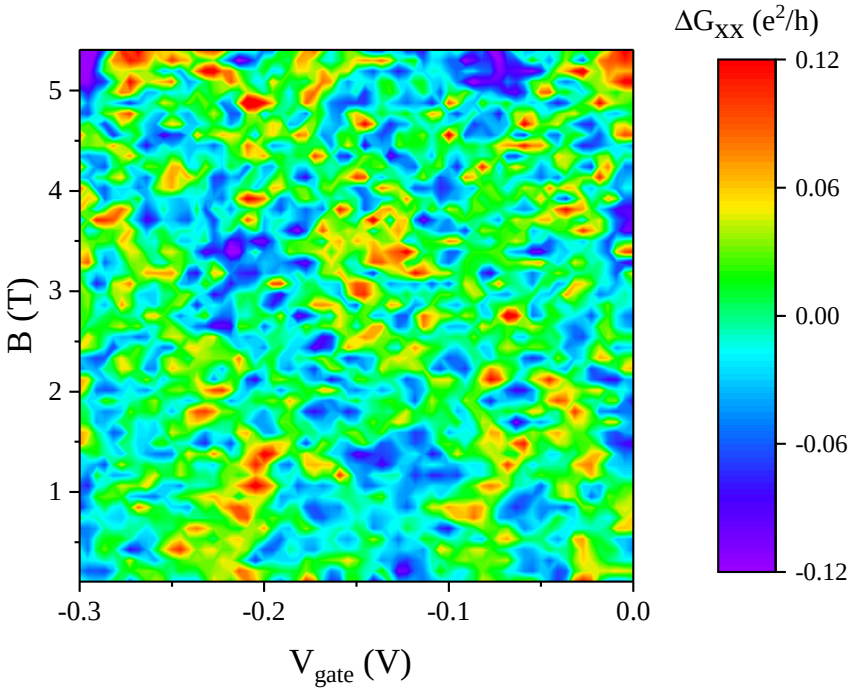

FIGURE 5.13 – Universal conductance fluctuation in the HgTe nanowire. 2D map of the conductance fluctuations as a function of gate voltage V_{gate} and magnetic field B. The slowly varying background has been subtracted from the raw conductance data to enhance the visibility of mesoscopic conductance fluctuations. Experiments are performed at 1.5 K with a bias voltage $U = 1000$ μV.

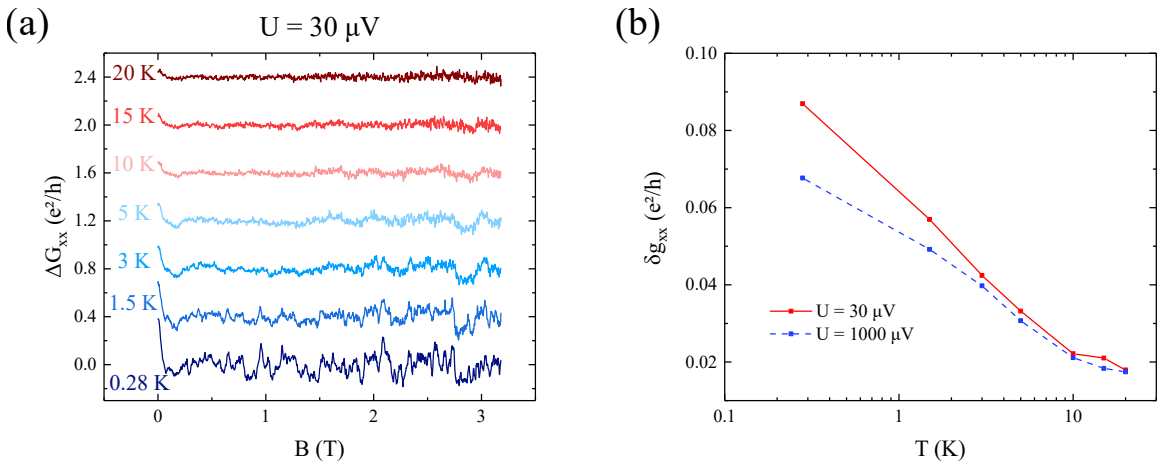

FIGURE 5.14 – Universal conductance fluctuations in the HgTe nanowire at $V_{\text{gate}} = 0$ V. Panel (a) displays the temperature evolution of ΔG_{xx} as a function of the magnetic field under a bias voltage of 30 μV. In panel (b), the standard deviation of ΔG_{xx} is plotted as a function of the temperature.

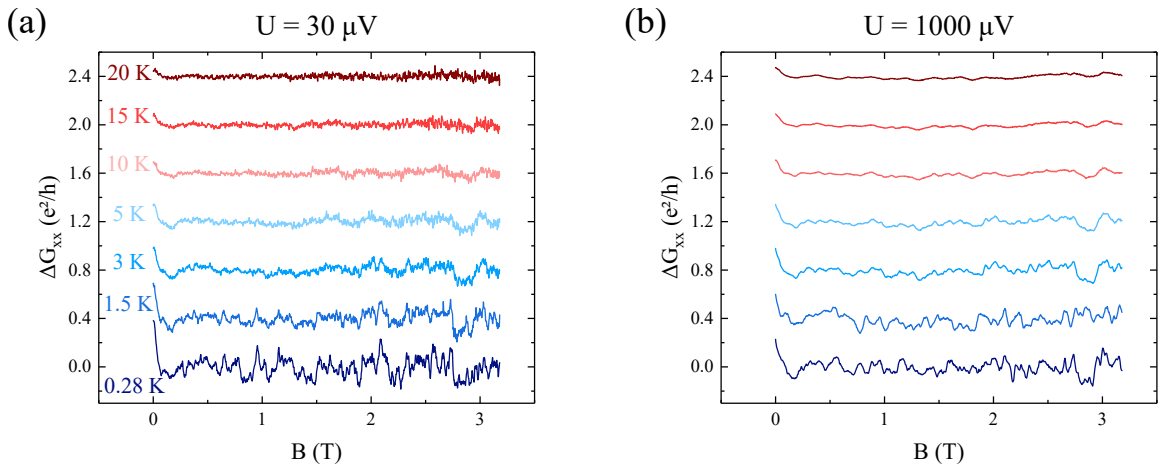

FIGURE 5.15 – Conductance variation ΔG_{xx} as a function of the magnetic field under a bias voltage of (a) 30 μV and (b) 1000 μV. Experiments are performed at different temperatures with Vgate = 0 V. The figure highlights the influence of the bias voltage.

mal averaging of the interference or the loss of electron phase coherence. The UCF indeed originate from quantum interference between different electron trajectories in the disordered conductor, requiring the electrons to maintain phase coherence over their paths. As the temperature increases, inelastic scattering processes, such as electron-phonon and electron-electron interactions, become more significant, thereby reducing the phase coherence time τ_ϕ and the corresponding coherence length $l_\phi = \sqrt{D\tau_\phi}$. Once l_ϕ becomes comparable to or smaller than the characteristic dimensions of the system, quantum interference effects are progressively suppressed, leading to a reduction of the UCF amplitude. Additionally, thermal broadening of the electronic energy distribution introduces averaging over slightly different interference patterns, which further diminishes the amplitude of the fluctuations. As a result, UCF are the most pronounced at the lowest temperatures, where phase coherence is preserved and thermal averaging remains negligible.

Finally, we comment on the standard deviation of the amplitude δg_{xx} for UCF obtained at 280 mK when sweeping the magnetic field, see figure 5.14(b), and the gate voltage, see figure 5.9(b) for the same bias voltage of 30 μV. The measured deviations are both around 0.09 e^2/h, a striking consequence of the universal nature of these oscillations.

Figure 5.15 compares the temperature dependence of the conductance oscillations for two different bias voltages. At each temperature, both the UCF pattern and the WAL peak appear more pronounced for $U = 30$ μV. This highlights the importance of measuring quantum effects with an applied bias as small as possible, as already discussed in Section 3.2.1. A compromise should however be found to limit the signal fluctuations coming from measurement noise. The standard deviation of the conductance fluctuations obtained for $U = 1000$ μV is also shown in figure figure 5.14(b) as a dashed line. The curve is below that obtained for $U = 30$ μV, due to the reduction of the UCF and/or the reduction of the noise at higher bias.

We note that the interference pattern between the two panels are different, peak and valleys of the UCF are not found at the same magnetic field. The reason is that,

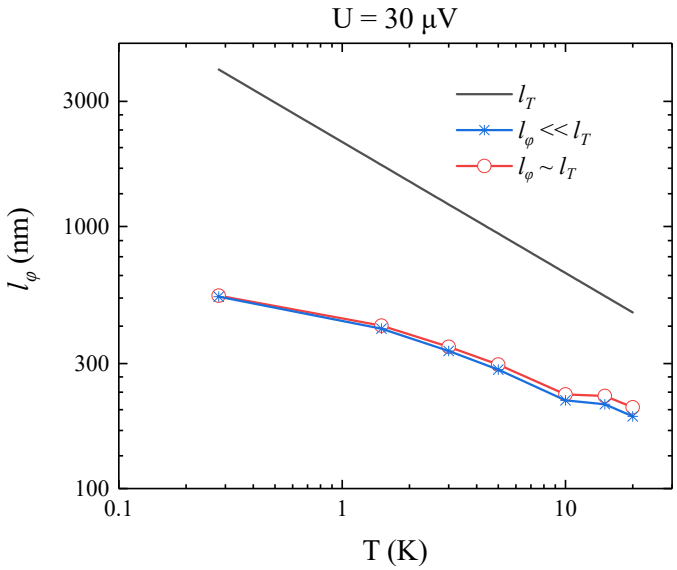

FIGURE 5.16 – Dependence of the phase coherence length with temperature extracted from the standard deviation of the UCF acquired at a bias voltage $U = 30\ \mu$V. The figure displays the thermal length l_T and the phase coherence lengths l_ϕ extracted from different expressions corresponding to different regimes.

between the two measurement campaigns, the sample impurity configuration has been modified, and so is its interference pattern. This change can be attributed to to the gate voltage sweeps which modify the charge configuration in the gate oxide. It highlights the "fingerprint" characteristic of the UCF.

3.3 Phase coherence length

The presence of UCF in the longitudinal resistance of the NW is a sign of coherent electronic transport. One way to characterize this regime is to estimate the phase coherence length, the typical length over which the initial phase of the electron is lost. According to Section 2.6, the standard deviation of the UCF and the magnetic correlation field are two useful tools for estimating l_ϕ.

3.3.1 Extraction from the standard deviation

We start by extracting l_ϕ from the amplitude of the UCF, represented by their standard deviation, δg_{xx} in units of e^2/h. We recall that the appropriate expression, 5.11 or 5.12, depends on the ratio l_ϕ/l_T. The thermal length, $l_T \equiv (\hbar D/k_B T)^{1/2}$, is calculated under the assumption of a temperature-independent diffusion constant expressed as $D = l_e \nu_F/2$ with $l_e = 1.7\ \mu$m and $\nu_F = 8.6 \times 10^5$ m/s. Figure 5.16 presents the phase coherence length extracted from the standard deviation δg_{xx} of the conductance variation versus magnetic field acquired at a bias voltage $U = 30\ \mu$V at different temperatures. It displays the two values of l_ϕ obtained from equation 5.11 in the regime $l_\phi \ll l_T$, and from the equation 5.13 in the intermediate regime $l_\phi \sim l_T$. The two formulas give similar results, both indicating a regime $l_\phi \ll l_T$. Since at high temperature $l_\phi \lesssim l_T$, we chose to keep the interpolation

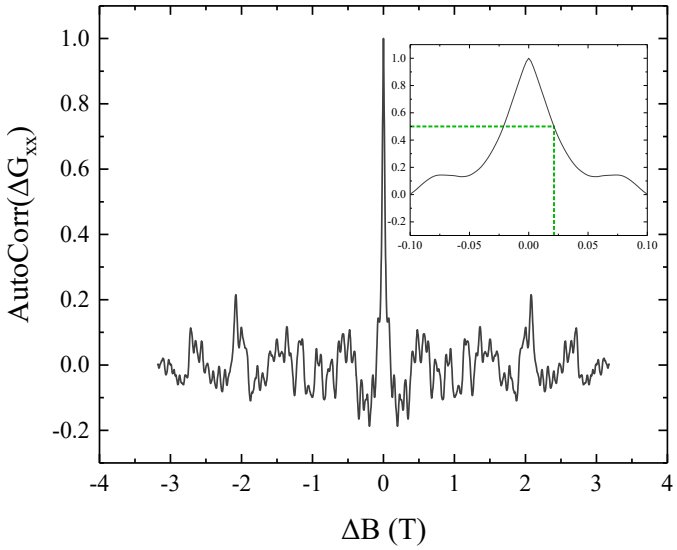

FIGURE 5.17 – Auto-correlation function of the UCF shown in figure 5.14(a) for the sweep in at a bias voltage $U = 30$ μV at 0.28 K. The inset shows a zoom-in to identify ΔB_{corr}.

formula as the estimator of the phase coherence length for the subsequent analysis. Note that the coherence length obtained from the assumption $l_\phi \gg l_T$ is not presented here because it would be lower than 100 nm, such that the inequality would not hold at all. Similar results are found in other measurements at different bias voltages, $U = 50$ and 100 μV. Interestingly, the determination of l_ϕ is independent of the regime of transverse motion of the electron in the nanowire, dirty metal regime with $l_e < W$, or pure metal regime with $l_e > W$, since what matters here is only the coherence of transport, and we have $l_\phi > W$.

3.3.2 Extraction from the correlation field

Furthermore, the phase coherence length can be extracted from the correlation field ΔB_{corr} experimentally measured from the normalized autocorrelation function of the conductance variation ΔG_{xx} as displayed in figure 5.17 for data acquired at 280 mk with a bias voltage $U = 30$ μV at $V_{\text{gate}} = 0$ V. In this example, we get $\Delta B_{\text{corr}} = 0.022$ T, and the subsequent phase coherence length can be extracted using the formalism presented in Section 2.6.

In this case, the ratio l_e/W matters and since we are in the pure metal regime $W \ll l_e$, we should work with :

$$\Delta B_{\text{corr}} = \frac{h}{e}\frac{0.38}{\gamma}\left(\frac{l_e}{l_\phi W}\right)^2\left(1+\sqrt{1+3.3\gamma\frac{l_\phi^2 W}{l_e^3}}\right) \tag{5.25}$$

where $\gamma = 1/3$ if $l_\phi \gg l_T$, and $\gamma = \left(4^{1/3}-1\right)^{-1} \approx 1.7$ if $l_\phi \ll l_T$. Based on the previously determined phase coherence length, we chose to work in the regime where $l_\phi \ll l_T$. Figure 5.18 shows the extraction of l_ϕ from the magnetic correlation field and from

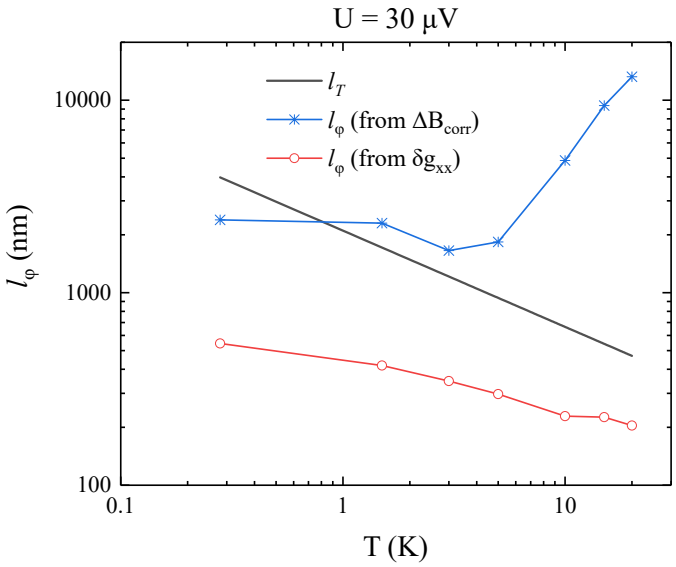

FIGURE 5.18 – Dependence of the phase coherence length with the temperature from the magnetic correlation field of the UCF acquired at a bias voltage $U = 30$ μV. The figure displays the thermal length l_T and the phase coherence length l_ϕ extracted from equation 5.25. The phase coherence length obtained from the standard deviation is also plotted for comparison.

the amplitude of the fluctuations. It appears that l_ϕ is significantly larger when extracted from the correlation field and falls in the intermediate regime $l_\phi \sim l_T$. In order to check the relevance of these higher values, one can calculate l_ϕ from the qualitative relationship $\Delta B_{corr} l_\phi W \approx h/e$ in which the characteristic area of coherent orbits would be calculated as the product of l_ϕ by the small width $W < l_\phi$. This relation would give $l_\phi \sim 1900$ nm in agreement with the value extracted from equation 5.25. This large difference between l_ϕ values extracted from the fluctuation amplitude and from the correlation field is not understood.

Moreover,after a small decrease with temperature, l_ϕ increases again at higher temperature, which is nonphysical. We attribute this inconsistency to the artificial reduction of the correlation field at higher temperatures where conductance fluctuations become barely visible, and the autocorrelation function is dominated by noise.

3.3.3 Influence of the bias voltage

Figure 5.19 gathers the different results obtained with each method at different bias voltages U. Panels (a) and (c) correspond to the standard deviation method while panels (b) and (d) to the correlation field approach. In figure 5.19(a), we see that the higher the bias voltage, the lower the standard deviation, which is consistent with the smearing of the oscillation that we explained before. The largest phase coherence lengths are therefore obtained for $U = 30$ μV as visible in figure 5.19(c). At low temperature, $l_\phi \approx 550$ nm, and at higher temperature, l_ϕ decreases to 250 nm. As the amplitude of the UCF is reduced with temperature, the influence of the bias voltage is also less pronounced, and the three curves give equivalent values. We recall that those values are obtained for $l_\phi \lesssim l_T$.

In5.19(b), we show the magnetic correlation field ΔB_{corr} obtained from the auto-correlation function of the conductance amplitude $\Delta G_{xx}(B)$. We observe a decrease in the correlation field at high temperature for $U = 30\ \mu$V. To guarantee a reliable analysis of measurements performed at this bias voltage, we only consider data acquired at temperatures $T \leq 5\,$K. However, for $U = 1000\ \mu$V, the correlation field increases with temperature. The associated phase coherence lengths are plotted in figure 5.19(d). As before, the longest phase coherence lengths are obtained for $U = 30\ \mu$V and at the lowest temperature. Unfortunately, at this bias voltage we cannot estimate the phase coherence length at high temperature. Compared to the values from the standard deviation method, the phase coherence lengths estimated through the correlation field are much larger. This difference between the two methods has already been noticed by Beenakker in [Beenakker, 1988b]. Indeed, as for their experiment, it seems that $l_\phi \sim l_e$ while the theory derived here works better for $l_\phi \gg l_e$. In this regime, the behavior is different and could explain the discrepancies.

3.3.4 Discussion of the uncertainties

We propose to discuss the calculation of the phase coherence length obtained from the standard deviation of the amplitude. This method relies on the accurate determination of the amplitude of the longitudinal conductance. We have seen that the bias voltage can induce smearing on the oscillation amplitude and so on their dispersion δg_{xx}. But, the intrinsic noise of the experimental set-up can also be detrimental for accurate measurement of the UCF. The residual noise of the experimental setup have therefore been measured, and we propose to define the new standard deviation of the UCF as [3]

$$\delta g_{xx} = \sqrt{\delta g^2_{\text{measure}} - \delta g^2_{\text{noise}}} \tag{5.26}$$

This correction yields new phase coherence lengths visible in figure 5.20. We see that at low temperature, there is no significant change, meaning that the contribution of the UCF amplitude to the standard deviation was clearly dominating. Nevertheless, as the temperature increases, the relative weight of the noise increases, resulting in larger corrections to both standard deviation and l_ϕ. These new values remain, though, on the same order of magnitude. We note that for higher bias voltage, the noise contribution δg_{noise} is reduced. For that reason, the change in l_ϕ is negligible.

A second source of uncertainty lies in the determination of the phase coherence length from the standard deviation of the UCF. The amplitude of the fluctuations seems to depend on the strength of the applied magnetic field. We have already mentioned this aspect on the 2D mapping of the conductance variation in figure 5.13; at high magnetic field the amplitude of the UCF is larger. Thus, the standard deviation is also increased

3. The subtraction of variances assumes that the setup noise and the intrinsic UCF fluctuations are statistically independent and uncorrelated. This assumption seems valid since the instrumental noise is of electromagnetic origin.

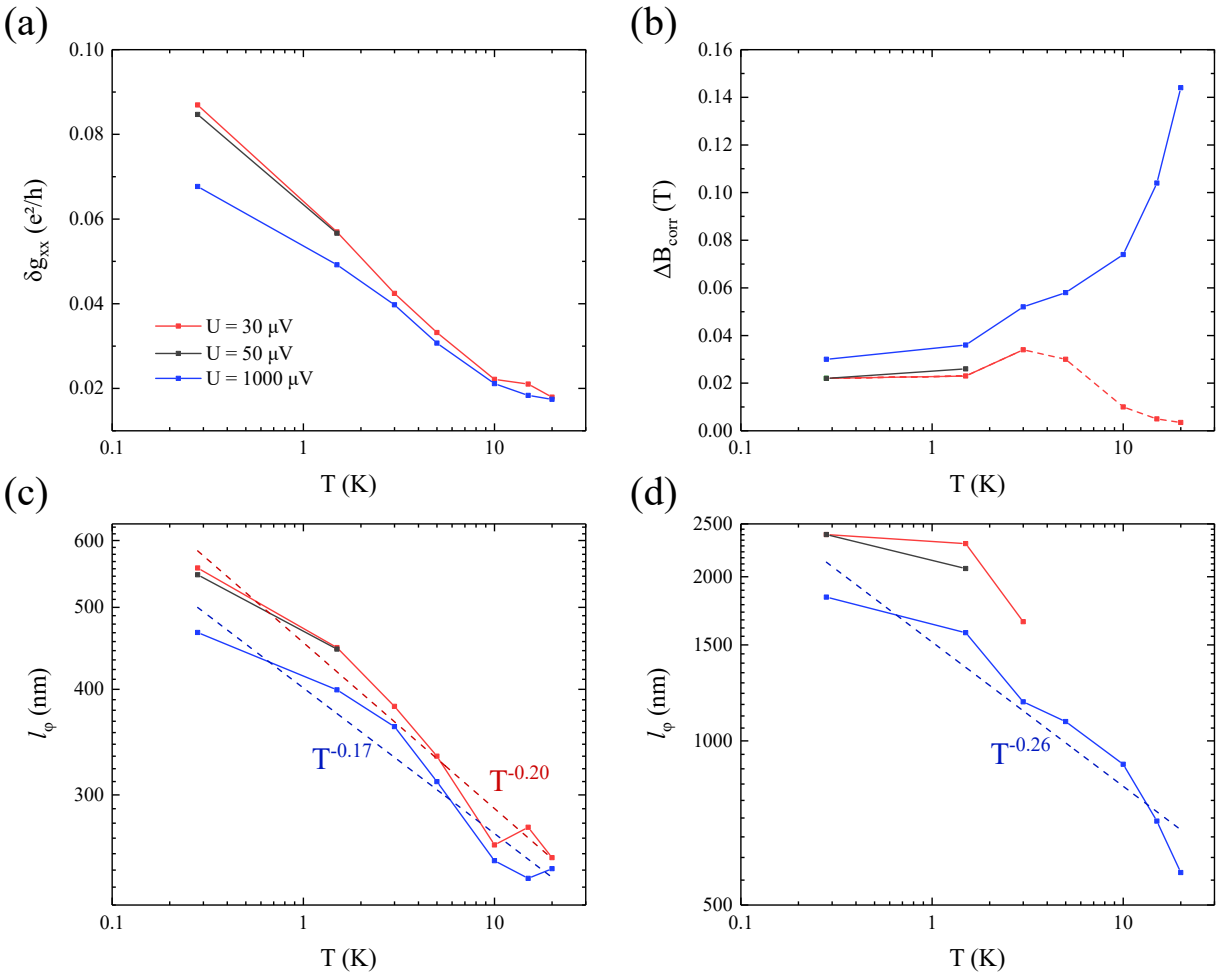

FIGURE 5.19 – The figure summarizes the two different methods used to extract the phase coherence length from the UCF as a function of the temperature. The experiments are performed under the same conditions. Panel (a) shows the standard deviation of UCF measurements, and panel (c) displays the corresponding phase coherence length thanks to the interpolation formula with respect to the thermal length. Panel (b) shows the magnetic correlation field and panel (d) displays the corresponding phase coherence length.

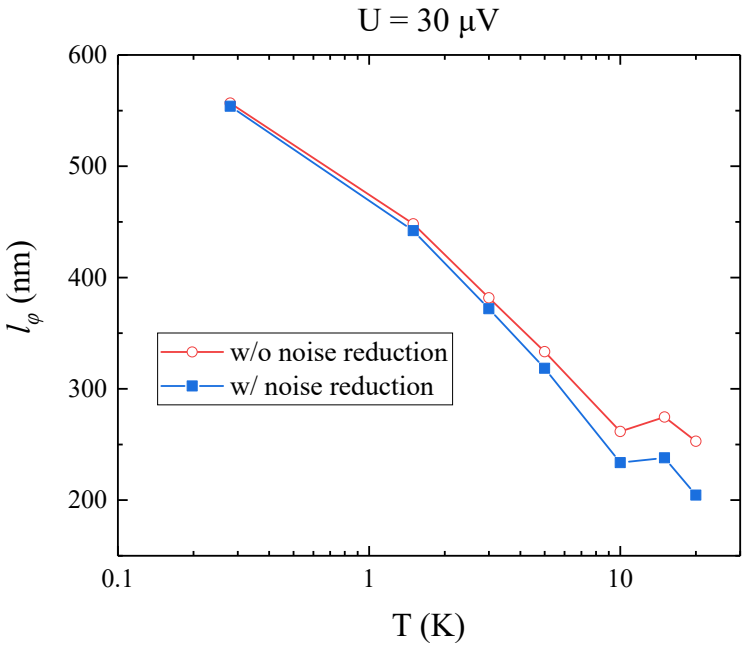

FIGURE 5.20 – Comparison of the phase coherence length extracted from the standard deviation of the UCF without (w/o) and with (w/) the noise reduction.

and so is the extracted phase coherence length. For instance, if we consider the standard deviation of the variation of conductance measured at 0.28 K at a bias voltage $U = 30$ μV in the range $3.18 \leq B \leq 5.3$ T, we obtain $l_\phi = 540$ nm, slightly larger than in the range $0 \leq B \leq 3.18$ T, where $l_\phi = 510$ nm. Therefore, the results obtained using this method should be interpreted with caution.

3.4 Weak anti-localization

3.4.1 Fitting method

The manifestation of the WAL effect is evidenced by the enhanced conductance of the device around $B = 0$ T. The shape and amplitude of the WAL peak are governed by different parameters, among them the mean free path l_e, the channel width W, the spin orbit length l_{so}, and the phase coherence length l_ϕ. As we have shown in Section 2.5, an analytical expression enables to reproduce the WAL peak. Consequently, by fitting our data with this theoretical function, we can estimate the phase coherence and spin orbit lengths of our device, making the WAL an interesting tool for studying quantum coherence. We recall the expression of the change in conductance due to the WAL from

equation 5.10 :

$$\Delta G(B) = -\frac{2e^2}{hL}\left[\frac{3}{2}\left(\frac{1}{l_\phi^2}+\frac{1}{D\tau_B}+\frac{4}{3l_{so}^2}\right)^{-1/2} - \frac{3}{2}\left(\frac{2}{l_e^2}+\frac{1}{l_\phi^2}+\frac{1}{D\tau_B}+\frac{4}{3l_{so}^2}\right)^{-1/2} - \frac{1}{2}\left(\frac{1}{l_\phi^2}+\frac{1}{D\tau_B}\right)^{-1/2} + \frac{1}{2}\left(\frac{2}{l_e^2}+\frac{1}{l_\phi^2}+\frac{1}{D\tau_B}\right)^{-1/2}\right] \tag{5.27}$$

where τ_B is given in equation 5.7 and the characteristic lengths are expressed as : $l_e = v_F\tau$, $D = v_F l_e/2$, $l_\phi = \sqrt{D\tau_\phi}$, and $l_{so} = \sqrt{D\tau_{so}}$.

In figure 5.21, we plot the expression of the model equation with a set of different values for each parameter. For each panel, one of the four parameters, l_{so}, l_ϕ, l_e and W (that appears in τ_B), is varied. In panel (a), the effect of the SOC is emphasized. As the SOC increases, the SO length reduces, corresponding to faster spin rotations and more pronounced destructive interference in the backscattering process and resulting in a higher conductance peak. The conductance curve therefore evolves from a WL dip to a WAL peak. The influence of the nanowire width is shown in panel (b). Increasing the width of the wire narrows the WAL peak. Wider wires are more likely to contain larger loop trajectories with, thus, a larger enclosed area. So, the phase accumulated by a circulating electron is more sensitive to a change in magnetic flux. Also, the flux cancellation effect, that would increase the typical dephasing magnetic field, is less likely in wide nanowire. Consequently, an even smaller magnetic field is required to dephase the time-reversed paths and suppress WL and WAL effects. In panel (c), we display the role of the phase coherence length. As expected, the longer the electronic wave is kept coherent, the larger the magnetic flux required to suppress the WAL effect. A large phase coherence length also increases the height of the conductance peak as there are fewer coherent sections in series, see equation 5.3. Finally, in panel (d), the role of the mean free path l_e is evidenced. The flux cancellation effect is enhanced when l_e is larger, thus the field required to suppress the WAL is larger. Increasing the mean free path also increases the time between two scattering events τ_e, thereby decreasing the return probability $C(t) \propto (1 - e^{-t/\tau_e}) \approx t/\tau_e$ which is inversely proportional to this short-time cutoff. Subsequently, the return probability is reduced, and so is the amplitude of the WAL peak.

In our case, we already know the width $W = 100$ nm and the elastic mean free path $l_e = 420$ nm, and two parameters remain unknown : the phase coherence length l_ϕ and the spin-orbit length l_{so}. The determination of these two parameters will be obtained by fitting the function 5.27 to the experimental data in the $(l_\phi - l_{so})$ parameter space. The fit consists in minimizing the mean-squared error $\sigma = \langle (G_{exp} - G_{fit})^2 \rangle$ between the experimental data and the theoretical model for each pair of parameters (l_ϕ, l_{so}). The error map shown in figure 5.22 provides a quantitative visualization of how sensitive the fit is to variations in both parameters. The global minimum of this map, indicated by the red

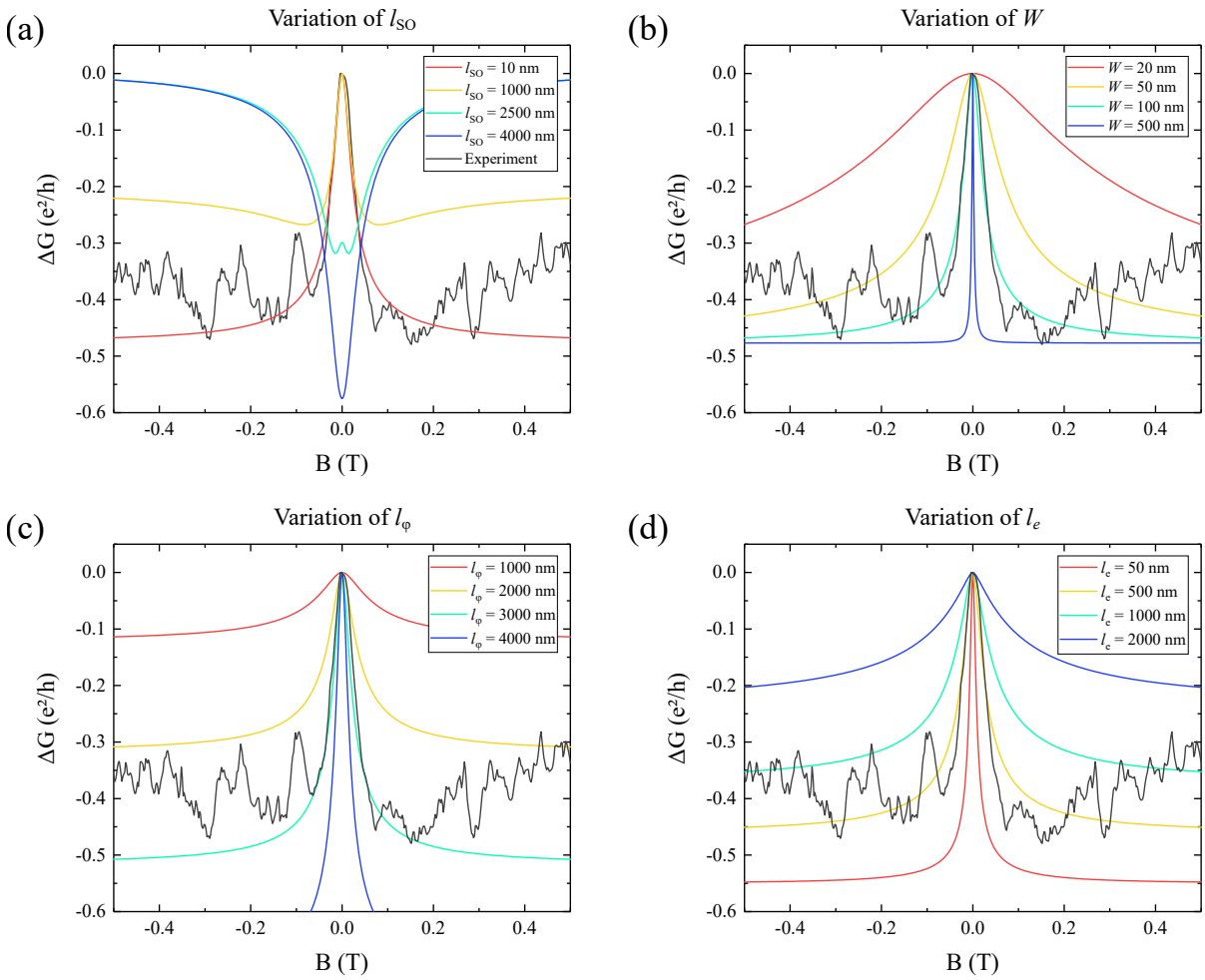

FIGURE 5.21 – Weak anti-localization effect in a quasi-1D channel. The black curve is the experimental data for the HgTe nanowire measured at 280 mK with a bias voltage $U = 30$ μV. It corresponds to the variation of the conductance from its value at $B = 0$ T. Colored lines correspond to the theoretical expression 5.27 for different values of the parameters. All curves also represent the conductance change $\Delta G = G - G(B = 0)$ except for the blue and green curves in panel (a) where WL dominates over WAL, here $\Delta G = G - G(B \to \infty)$. When the parameters are not varied, they are respectively set to : $l_{so} = 10$ nm, $l_\phi = 2800$ nm, $l_e = 420$ nm and $W = 100$ nm.

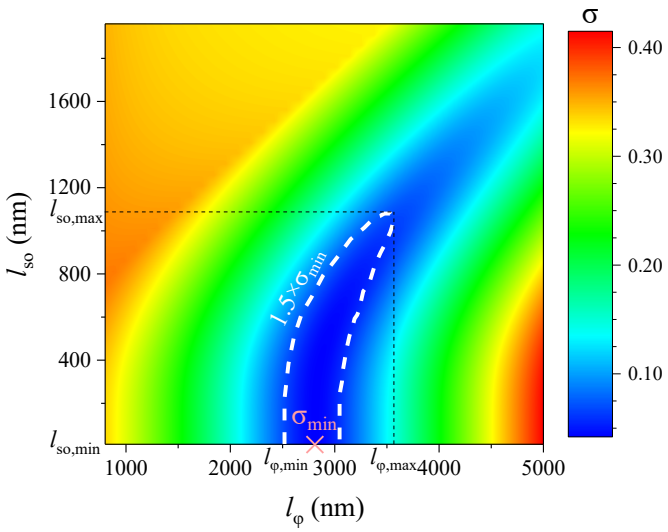

FIGURE 5.22 – Error map of the fitting mean-squared error σ in the l_ϕ-l_{so} parameter space corresponding to measurements at 280 mK with a bias voltage $U = 30$ μV. The red cross marks the best fit corresponding to the minimum error. The region enclosed by the white dashed line contains the l_ϕ-l_{so} combinations for which the error satisfies $\sigma \leq 1.5 \times \sigma_{\min}$. The extrema of l_ϕ and l_{so} within this region define the error bars of the fit.

cross, corresponds to the optimal parameter set that best reproduces the data. To estimate the uncertainties associated with the fit, we define a confidence region based on a tolerance criterion : all (l_ϕ, l_{so}) pairs for which the error remains within $1.5 \times \sigma_{\min}$ are considered statistically relevant fits. This region, outlined by the white dashed contour, therefore reflects the parameter space compatible with the data within the chosen tolerance. The maximum and minimum values of l_ϕ and l_{so} within this region are then taken as the error bars on the fitted parameters. This approach naturally incorporates the correlation between l_ϕ and l_{so}. In our case, the tolerance region is globally elongated in the vertical direction, which means that for a given value of l_ϕ, a wide range of values of l_{so} leads to fits of comparable quality. This indicates that the phase coherence length l_ϕ plays the dominant role in determining the quality of the fit, while l_{so} is less tightly constrained. The slight bending of the contour further shows that an increase in l_ϕ can be compensated for an increase in l_{so}, reflecting the fact that these two parameters are not independent in their influence on the fit. In this way, the error map provides both visual and quantitative means of assessing not only the uncertainties on each parameter but also their mutual correlation.

The theoretical model used to derive equation 5.27 assumes a magnetic field small enough to fulfill the requirement $l_m \gg W$ [Beenakker, 1991]. Here, the condition $l_m \gg 100$ nm corresponds to $B \ll 0.05$ T. In this context, the modeling curve of the WAL peak of conductance based on the best set of parameters for the measurements performed at a bias voltage $U = 30$ μV at 280 mK, displayed in figure 5.21, is determined. The resulting curve is plotted in figure 5.23(a). However, in the example of WAL peak shown in figure figure 5.23(b), the magnetic field range with $B_{max} = 0.05$ T is not large enough to cover the entire WAL peak. For that reason, we also consider a larger fit range with $B_{max} = 0.2$

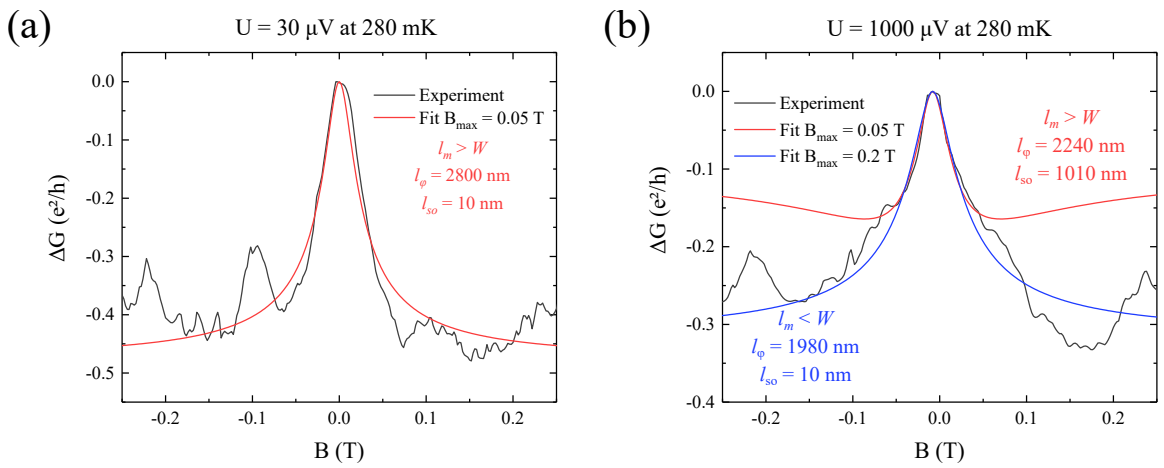

FIGURE 5.23 – Weak anti-localization (WAL) peak in the HgTe nanowire, measured with a bias voltage (a) $U = 30$ μV and (b) $U = 1000$ μV at 280 mK, together with its modeling using equation 5.27. The fitting curves (colored lines) are calculated for the values of l_ϕ and l_{so} indicated in the figure, while $W = 100$ nm and $l_e = 420$ nm are imposed. The red curve fulfills in the requirement $l_m > W$ with $B_{max} = 0.05$ T, while the blue curve is obtained from a wider fitting range with $B_{max} = 0.2$ T, to account for the full height of the WAL peak.

T. From the figure, we see that the upper half of the WAL peak is correctly reproduced for the two fit ranges. This yields phase coherence lengths $l_\phi \approx 200$ nm. On the other hand, the determination of the spin-orbit length has a larger uncertainty as values vary from 10 nm to 1000 nm depending on the fitting range. Since a too large spin-orbit length excessively reduces the height of the WAL peak, as observed for the red curve which is in poor agreement with the experimental data for $|B| > 0.05$ T, it is necessary to increase the fitting range. Therefore, it will be systematically extended to $B_{max} = 0.2$ T to observe the full height of the peak. This larger range is also particularly needed for data acquired only for positive B field, since the peak width is not well defined in this case.

3.4.2 Temperature dependence

Now that the fitting procedure has been presented, we can discuss the results obtained for different temperatures and bias voltages, presented in figure 5.24. In panel (a), we display the extracted phase coherence length as a function of temperature from the measurements performed at bias voltage 30, 50 and 1000 μV, with the fitting range $B_{max} = 0.2$ T. The fit of the data with a power law in temperature $\propto T^{-m}$ is shown as a solid line with the corresponding exponent. The red curve is fitted to the data throughout the temperature range for U = 30 μV. Regarding the blue curve, the points used for the fit at U = 1000 μV are restricted to temperatures above 1.5 K because of the much weaker increase of the phase coherence length from 1.5 to 0.28 K. Even though more measurements at lower temperature would be necessary to confirm the following assumption, it is possible that the phase coherence has reached a plateau. This behavior has already been observed by Milliken *et al.* [Milliken, 1987]. The change as a function of temperature is found here to be between $T^{-0.28}$ and $T^{-0.2}$. This is slightly less than the predictions from

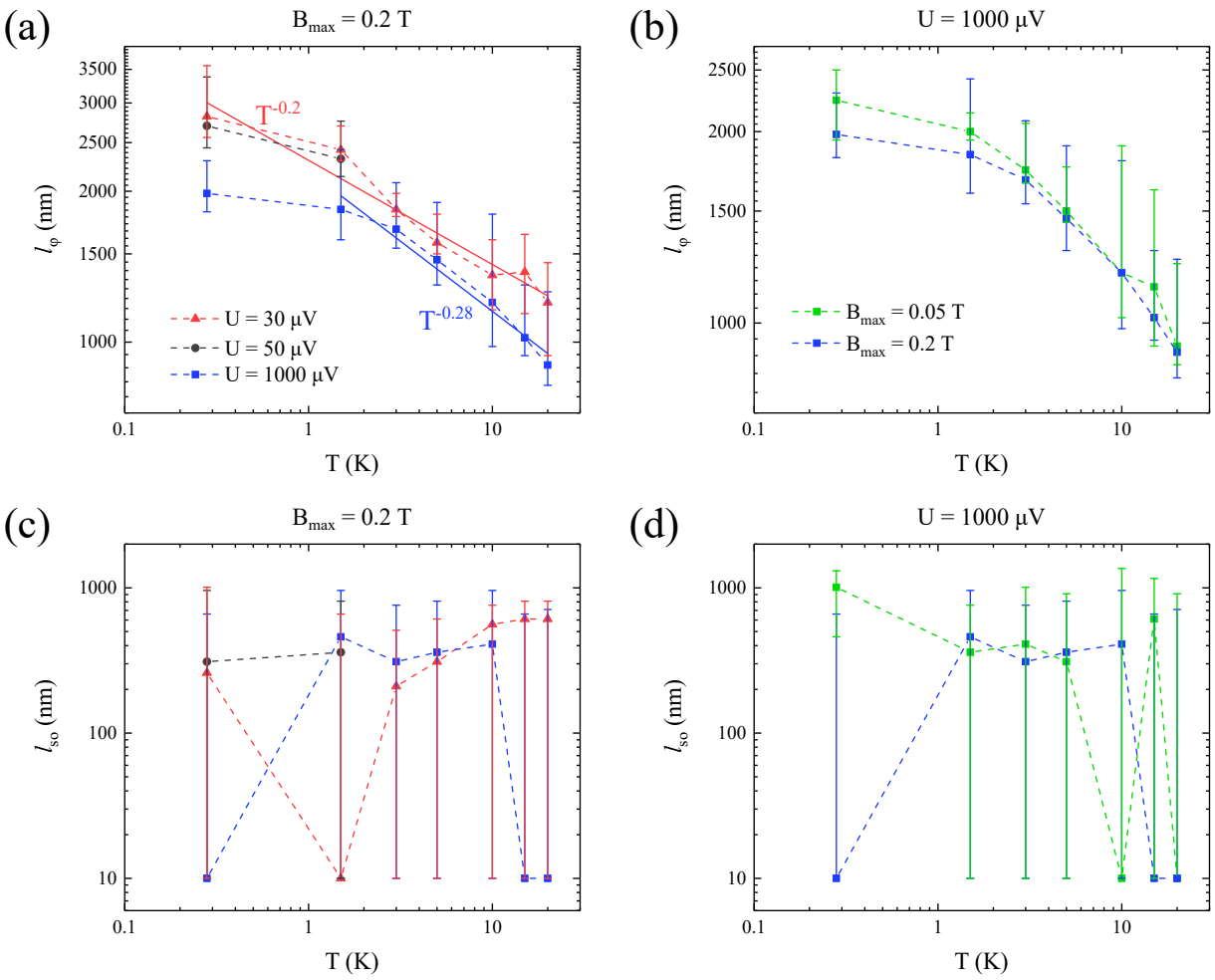

FIGURE 5.24 – Phase coherence length l_ϕ and spin-orbit length l_{so} as a function of the temperature in the HgTe nanowire. These characteristic lengths are obtained by fitting the experimental data. Different bias voltages and fitting range are considered. In panels (a) and (c), we use a fitting range with $B_{max} = 0.2$ T. In panels (b) and (d), the bias voltage is fixed and the fitting range is varied between $B_{max} = 0.05$ T and $B_{max} = 0.2$ T.

[Altshuler, 1982], which foresaw a decrease in $T^{-1/3}$ due to electron-electron interactions in one dimension..

In panel (b), we compare the extracted phase coherence length considering the two fitting windows : $B_{max} = 0.05$ T or $B_{max} = 0.2$ T. The values of l_ϕ obtained from the short fitting range are slightly larger ; but considering the error bars, they are equivalent. The fitting window therefore has very limited influence on l_ϕ.

In panels (c) and (d), the values of the spin orbit lengths are strongly scattered with large error bars. Most of the values are however located between 200 and 600 nm, such that one can write $l_{so} \sim 400 \pm 200$ nm. Interestingly, neither the bias voltage, the fitting window, nor the temperature seems to have an influence. In conclusion, we can say that the SOC is present by the presence of the WAL peak, but its accurate determination is difficult from these data.

Finally, it is interesting to compare the phase coherence lengths obtained from the WAL peak to their counterparts obtained from UCF in figure 5.19. The values extracted

from the WAL peak and the magnetic correlation field of the UCF are in good agreement. Indeed, at 280 mK, $l_\phi = 2200 - 2800$ nm are found with both methods and their temperature dependence are very close with $T^{-0.26}$ for the UCF and $T^{-0.28,-0.2}$ for the WAL peak. Furthermore, the method based on the standard deviation of the UCF systematically gives a lower value of the phase coherence length, below 600 nm. At high temperature, it also seems limited by the noise. A problem with the prefactors could lead to such lower values. The exponent of the temperature dependence $T^{-0.20,-0.17}$ is however similar to the exponent obtained with the other methods.

3.5 Conclusion

In this section, we have studied the electronic transport in a 100 nm-wide and 5 µm-long nanowire. The reduced dimensions hindered a clear manifestation of the Hall and quantum Hall effect. Nonetheless, we extracted a mean free path $l_e = 420$ nm and a depletion factor $\alpha = 28 \times 10^{11}$ cm^{-2}V^{-1} on the electron side. These values are consistent with those previously obtained in large Hall bars.

In addition, we identified the presence of two quantum phenomena that rely on phase coherence of the electronic waves : universal conductance fluctuations (UCF) and weak anti-localization (WAL). We investigated their strength as a function of temperature and bias voltage, as both represent complementary tools to characterize phase coherence in transport. This gave us three approaches to quantify l_ϕ : two from UCF (standard deviation and magnetic correlation field) and one from fitting the WAL peak. The results obtained are globally consistent, except for the standard deviation method, which yields systematically smaller values. A phase coherence length around 2500 nm at 280 mK is obtained. This value is comparable to those reported in the literature for PbTe- or InSb-based devices [Jung, 2022 ; Aseev, 2019] also grown by selective epitaxy, demonstrating the suitability of SAG for the realization of HgTe-based nanodevices.

4 Nanoring

In this section, we focus on the electronic transport through a HgTe nanostructure patterned in a ring geometry. When a perpendicular magnetic flux is threaded through the ring, and if the inelastic scattering length is long enough, the electronic waves traveling along the two branches can interfere at the exit, and the conductance of the device exhibits periodic oscillations as a function of the magnetic flux. It is a manifestation of the Aharonov-Bohm (AB) effect. This effect is a fundamental manifestation of quantum coherence, where a charged particle acquires a measurable phase shift due to the presence of a vector potential, even in regions where the magnetic field is strictly zero. It was predicted by Aharonov and Bohm in 1959 [Aharonov, 1959].

The aim of this section is to evidence the periodic oscillation of the conductance through a HgTe nanoring. The amplitude of these oscillations will be studied as a function of the temperature. The objective is also to compare the determination of the phase coherence length measured in the NW geometry, involving UCF and WAL, to the values obtained in this ring geometry through the AB effect.

4.1 Theoretical background

4.1.1 Origin of the oscillations

The Aharonov-Bohm effect is one of the most striking demonstrations of phase coherence in mesoscopic systems. It reveals that in quantum mechanics, the electromagnetic vector potential $\mathbf{A}$ plays a direct physical role : even in regions where the magnetic field $\mathbf{B} = \nabla \times \mathbf{A}$ vanishes, an electronic wave can still acquire a measurable phase shift [Aharonov, 1959].

When an electron propagates through a mesoscopic ring, its wave splits into partial waves that travel along the two arms of the ring. Each partial wave accumulates a distinct phase before recombining at the exit of the ring. Their relative phase difference governs the interference pattern. The latter gives rise to oscillations in the conductance. Since the relative phase shift is determined by the magnetic flux enclosed by the trajectories, the conductance is periodic in flux, with the fundamental period corresponding to the *flux quantum*

$$\Phi_0 = \frac{h}{e} \tag{5.28}$$

Indeed, an electron encircling a confined magnetic flux Φ, in this context the perpendicular flux passing through the loop, accumulates a quantum mechanical phase difference given by :

$$\Delta\phi = \frac{e}{\hbar} \oint \mathbf{A} \cdot d\mathbf{l} = \frac{2\pi\Phi}{\Phi_0} \tag{5.29}$$

Thus, each increase in magnetic flux Φ of one quantum flux Φ_0 changes the phase difference between the interfering paths by an integer multiple of 2π. This is the funda-

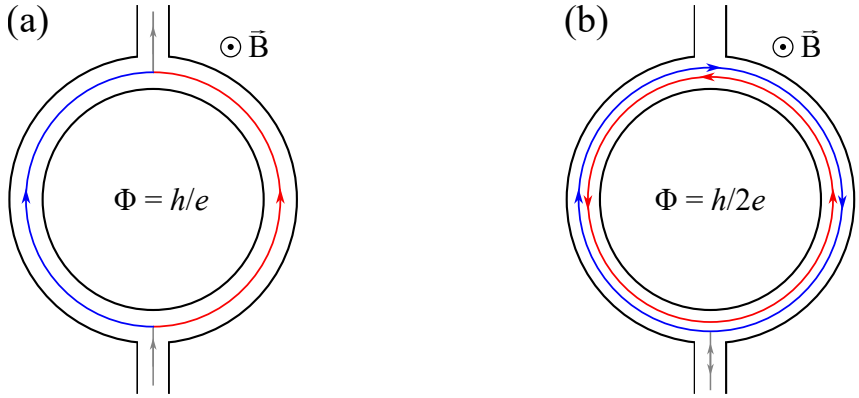

FIGURE 5.25 – Schematic of the main interference effects arising in a ring geometry. Panel (a) represents the AB effect. Under a magnetic field, partial electronic waves interfere after their propagation along each arm of the loop. The periodicity in enclosed flux is $\Delta\phi = h/e$. Panel (b) displays the AAS effect. Here the interference occurs after the complete revolution around the loop of two time-reversed trajectories. The periodicity in enclosed flux is thus twice smaller $\Delta\phi = h/2e$.

mental origin of the periodic oscillations observed in an AB ring. Whenever the enclosed flux increases by one quantum Φ_0, the conductance returns to its original value. For this reason, these oscillations are commonly referred to as h/e oscillations. Figure 5.25(a) represents the AB-type interference, when the enclosed flux is equal to Φ_0. Experimentally, this manifests as magneto-conductance oscillations when sweeping the perpendicular magnetic field, whose period corresponds to one flux quantum threading the enclosed area S of the ring :

$$\Delta B_{AB} = \frac{\Phi_0}{S} \tag{5.30}$$

It is also interesting to note that higher harmonics of the AB oscillation can appear if the partial waves recombine after propagating multiple times the ring. The effective enclosed flux is multiplied, $n\Phi_0$, yielding an effective period h/ne. For these higher harmonics to be observed, the transport has to remain coherent over the whole propagated length.

The observation of these oscillations is a direct signature of phase-coherent transport, requiring the electronic phase-coherence length l_ϕ to exceed the circumference of the ring. In contrast to the original theory of Aharonov and Bohm, the magnetic field is non-zero where the electrons propagate. But it is actually without consequence as only the magnetic flux Φ passing through the loop is important. Similarly to UCF, the root-mean-square (rms) amplitude of the conductance oscillations is expected to be on the order of e^2/h at low temperature [Kurdak, 1992]. The major difference with respect to UCF and other quantum effects lies in the periodicity of the signal. While for UCF, the interfering trajectories enclose a continuous range of flux values, yielding aperiodic oscillations, the flux is here fixed by the ring geometry. We remind the reader that, in practice, UCF are also present in a ring geometry, as a slow varying background of the conductance.

In diffusive rings, additional interference paths give rise to oscillations with half the fundamental period, $\Phi_0/2 = h/2e$, known as the *Altshuler-Aronov-Spivak* (AAS) effect

[AlTshuler, 1981]. In this case, the two partial waves loop around the entire ring and so the total enclosed magnetic flux is twice Φ. The necessary flux increment for constructive interference is therefore $\Phi_0/2$. Hence, these oscillations are usually known as $h/2e$ oscillations. These oscillations are connected to time-reversed trajectories and are closely related to weak (anti-) localization phenomena. Figure 5.25(b) displays a schematic of interfering trajectories yielding the AAS effect.

We would like to attract the reader's attention to the main difference between the two types of interference. The h/e oscillations are sample specific as their phase depends on the impurity configuration of each ring. Therefore, in an array with many rings, this contribution cancels out due to ensemble averaging. In contrast, the $h/2e$ oscillations arise from time-reversed paths and thus have a sample-independent phase. So, they do not cancel out in ensemble averaging. They can be seen as a periodic analog of weak localization imposed by the ring geometry. However, large magnetic fields are detrimental for the observation of the AAS effect, because the different trajectories around the ring have a slightly different magnetic field period for their $h/2e$ oscillations. The maximum field at which the AAS effect survives is given by $B_{max} = \Phi_0/(2\pi RW)$ where W is the width of the ring and $2\pi R$ is the perimeter. It corresponds to having the width of the ring threaded by one flux quantum. Since one usually has $W \ll R$, this maximum field is much larger than the period of the AAS oscillations given by $\Delta B_{AAS} = (\Phi_0/2)/(\pi R^2)$, such that several periods of AAS oscillations can be observed. Interestingly, the AB oscillations do not suffer from this amplitude decay at large field. This difference of behavior between the h/e and $h/2e$ oscillations was initially studied in metal rings [AlTshuler, 1982 ; Chandrasekhar, 1985] but is also observed in semiconductor rings [Geng, 2022]. The same difference exists between UCF which survive at large field and WL which disappears at moderate field. The AB effect is indeed a periodic UCF effect, whereas the AAS effect is a WL effect in a circular quasi-1D wire of width W with l_ϕ replaced by $2\pi R$.

Overall, the AB effect provides a powerful probe of quantum coherence, phase accumulation, and the role of magnetic flux in mesoscopic conductors. Its experimental observation in nanostructures such as quantum rings offers direct evidence of the wave-like nature of electrons and serves as a benchmark for the study of coherent transport. The AB ring geometry is therefore extensively used for the characterization of nanostructures dedicated to quantum sciences and technologies.

4.1.2 Temperature dependence

The temperature dependence of the oscillation amplitude gives access to the phase coherence length of the electrons. For a loop of circumference p, the general evolution of the rms amplitude of the AB oscillations as a function of temperature is given by Kurdac *et al.* [Kurdak, 1992] as :

$$\delta g_{AB} = \gamma \frac{e^2}{h} f\left(\frac{E_c}{k_B T}\right) \exp(-\alpha p/l_\phi(T)) \tag{5.31}$$

where γ is a factor on the order of unity, $f(x)$ is a function equivalent to $\sqrt{x}$ for $x \ll 1$ and saturating to 1 for $x \gg 1$, $E_c = \pi^2\hbar D/p^2$ is the correlation energy (also called Thouless energy), and α is a decay exponent that accounts for the ring geometry. The E_c/k_BT ratio represents the energy averaging due to temperature, that washes out the oscillations at high temperature. The energy averaging should be taken into account when $k_BT > E_c$, or equivalently when the thermal length $l_T < p$. Indeed, depending on their energy, electrons acquire slightly different phase, and the typical energy spread is on the order of k_BT. If k_BT is smaller than the correlation energy E_c, all the transported electrons have about the same energy, and thus interfere the same way, without reducing the amplitude of the AB oscillations. On the other hand, if k_BT is larger than the correlation energy E_c, the thermally activated electrons experience different interference conditions, which reduce the amplitude of the AB oscillations. The same argument can be described in terms of lengths instead of energies. We recall that $l_T = (\hbar D/k_BT)^{1/2}$ is the length over which electrons with an energy difference of order k_BT accumulate a phase difference of order 1. If $p < l_T$, the phase accumulated through the ring by the electrons within the k_BT window is not enough to significantly change its phase, and vice versa. In our case, the ring has a perimeter $p = 2800$ nm and a diffusion constant $D = 0.36$ m^2/s (from the NW analysis) such that $E_c/k_B \approx 3.5$ K. The measurements are mainly performed in the sub-kelvin range ; thus, the thermal energy averaging factor is close to 1.

The explanation for the exponential term $\exp(-\alpha p/l_\phi(T))$ is provided by Milliken *et al.* in [Milliken, 1987]. From the definition of l_ϕ, the fraction of carriers which arrive at the voltage probe retaining phase memory is $\exp(-p/l_\phi)$. Kurdac *et al.* have introduced the prefactor α because the relevant dimension is not necessary the loop perimeter p but rather depends on the geometry of the ring. In their paper, they use $\alpha = 0.63$ for a ring similar to the one presented in this manuscript. Nevertheless to compare more easily with the literature we choose to take $\alpha = 1$ [Aseev, 2019 ; Krizek, 2018 ; Jung, 2022 ; Vaitiekėnas, 2018a] [4]. Kurdak *et al.* also gave the expression δg_{AB} for a material with SOC. In this case, equation 5.31 is scaled with the following factor : $\frac{1}{2}\left(3\exp(-\frac{4}{3}(p/l_{so})^2) - 1\right)$. Thus, a strong-spin orbit coupling will reduce the amplitude of the oscillations.

4.1.3 Coherence length

We now discuss a method to extract the phase coherence length l_ϕ from the temperature dependence of the AB oscillations. If we consider only the influence of l_ϕ, we can write the amplitude of the oscillations as

$$\delta g_{AB}(T) \propto \exp(-p/l_\phi(T)) \tag{5.32}$$

In absence of reliable value of the pre-factor in front of the exponential, the determination of l_ϕ from δg_{AB} requires the knowledge of the scaling law governing the temperature

4. Some authors also use $p/2$, the length of one arm of the ring [Lee, 2019 ; Geng, 2022]. In this case we only overestimate the phase coherence length by a factor two.

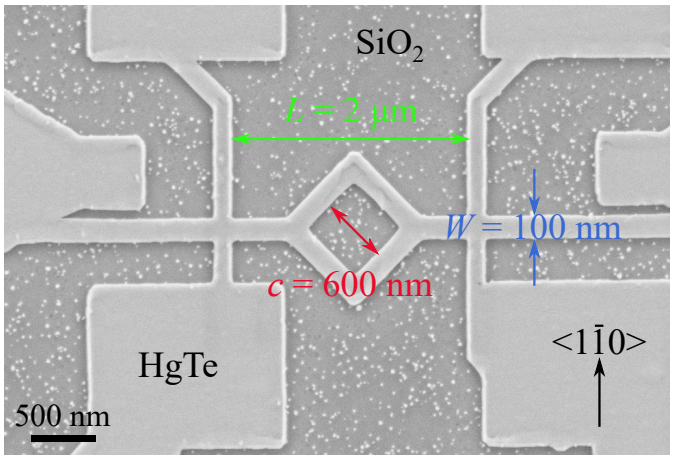

FIGURE 5.26 – Top view SEM image of the HgTe ring grown by SAG used in the magneto-transport measurements. The indicated dimensions are the lithographic ones.

dependence of l_ϕ. It is common to consider the temperature dependence of characteristic lengths as a power law in temperature [Altshuler, 1982]. Here we thus write :

$$l_\phi(T) = \frac{p}{bT^m} \tag{5.33}$$

where b is a proportionality factor that will be determined by fitting. Depending on the type of transport regime, two exponents m can be considered.

— Diffusive regime : $m = 1/2$ and $l_\phi \propto T^{-1/2}$

— Ballistic regime : $m = 1$ and $l_\phi \propto T^{-1}$

The scaling $l_\phi \propto T^{-1/2}$ has been experimentally verified by Washburn *et al.* in gold samples in [Washburn, 1985] and not long after by Milliken *et al.* using Sb rings in [Milliken, 1987]. Since then, the scaling law in $T^{-1/2}$ for the diffusive regime have been extensively used by different groups to characterize the electronic transport in semiconducting materials [Lee, 2019 ; Aseev, 2019 ; Krizek, 2018 ; Jung, 2022 ; Vaitiekėnas, 2018a].

The scaling of the ballistic regime in nanorings has been first experimentally evidenced by Hansen *et al.* in GaAs/$Ga_xAl_{1-x}As$ heterostructures in 2001 [Hansen, 2001]. The theoretical predictions have been led by Seelig and Büttiker [Seelig, 2001] the same year. More recently, Krizek *et al.* have also found a T^{-1} dependence of the phase coherence length for ballistic electronic transport in InAs nanorings grown by selective epitaxy [Krizek, 2018].

Therefore, the experimental data will be fitted with the following expression :

$$\delta g_{AB} \propto A \exp(-bT^m) \tag{5.34}$$

where A and b are the fitting parameters and m is set to 1 for ballistic regime, or 1/2 for the diffusive regime.

The exponent showing the best fit will indicate the transport regime and give the temperature evolution law of the inelastic scattering length.

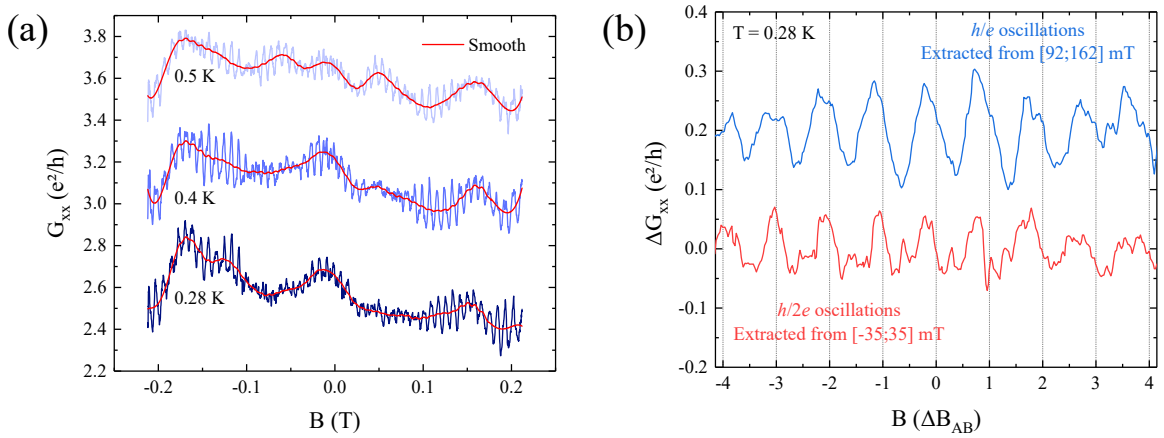

FIGURE 5.27 – Four-terminal conductance of the HgTe nanoring. (a) Conductance as a function of the magnetic field at three different temperatures. The oscillating background due to the UCF is computed by application of a Savitzky-Golay filter. (b) Conductance oscillations as a function of the magnetic field in unit of the expected magnetic period $\Delta B_{AB} = 8.45$ mT at 280 mK after removing the background. The red curve shows a combination of h/e and $h/2e$ oscillations extracted around zero magnetic field. The blue curve displays only h/e oscillations extracted a higher field. Curves are vertically offset to enhance clarity.

4.2 Experimental results

In this section, we investigate the conductance behavior of a HgTe nanoscale ring obtained by SAG and analyze the periodic oscillations. We also report measurements of the phase coherence thanks to the temperature dependence of the AB conductance oscillations.

The measurements at low temperatures are performed on the nanostructure presented in figure 5.26. The gate voltage is fixed at zero throughout the study. The measurements are realized with a bias voltage of 30 μV such that the conductance fluctuations are only limited by temperature. The magnetic field is oriented perpendicular to the substrate. The typical area enclosed by the ring is $S = 700 \times 700$ nm^2. That yields an expected period of the AB oscillation :

$$\Delta B_{AB} = \frac{\Phi_0}{S} = 8.45 \text{ mT} \tag{5.35}$$

This is equivalent to a frequency $f_{AB} = 118$ T^{-1} but considering the inner size $c = 600$ nm and the outer size $c = 800$ nm of the ring, the frequency range is from 87 to 154 T^{-1}. Each arm of the loop measures 1400 nm and the perimenter is $p = 2800$ nm.

4.2.1 Periodic oscillations

The main period of the oscillation is consistent with the expected value of $\Delta B_{AB} = 8.45$ mT. It highlights a phase coherent transport of the electrons through the ring. In addition, we also notice the presence of AAS type oscillations, with a period twice shorter.

As explained in section 4.1.1, these $h/2e$ oscillations originate from counter-propagating time-reversed paths interfering after a complete revolution around the loop, as in the weak

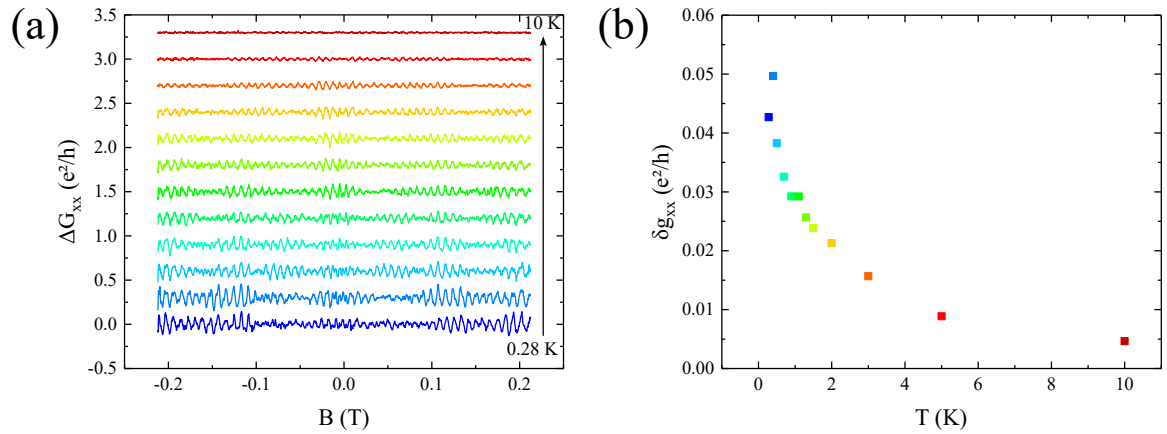

FIGURE 5.28 – Temperature dependence of the conductance oscillations in the HgTe nanoring. (a) Evolution of the AB oscillations as the temperature is increased. Curves are vertically shifted to enhance clarity. (b) The corresponding standard deviations as displayed as a function of the temperature.

localization effect, with a suppression at moderate magnetic field due to the finite width of the wire. This behavior is demonstrated in figure 5.27(b) which shows two traces of conductance oscillations in two different magnetic field ranges : the red curve around 0 mT contains both h/e and $h/2e$ oscillations, whereas the blue curve above 100 mT contains only h/e oscillations.

Figure 5.27(a) presents the four-terminal conductance of the ring. It exhibits periodic oscillations on top of a slowly varying background, due to the presence of UCF, superimposed on the AB oscillation. By filtering out the background usingg a Savitzky-Golay smoothing function, we extract the conductance oscillation ΔG_{xx} resulting from the AB and AAS effects as shown in figure 5.27(b). The rms of the oscillations of the order of 0.1 e^2/h, similar to the UCF in the NW.

4.2.2 Temperature dependence

The presence of h/e and $h/2e$ oscillations reveals the coherent transport of the electron waves through the ring. Their period matches the expected value calculated from the lithographic pattern. We now discuss the thermal dependence of the AB oscillations amplitude. In particular, we focus on the evolution of the root-mean-square (rms) of the amplitude and on the fast Fourier transform (FFT) amplitude of the conductance oscillations.

The AB oscillations ΔG_{xx} are plotted in figure 5.28(a) when changing the temperature. It shows the reduction of their amplitude as the temperature is increased. At 10 K, the oscillations have almost vanished. We observe that the oscillating patterns slightly change as the temperature is varied. This behavior might be explained by a change of the interfering pattern around the loop, induced by the temperature dependence of the inelastic scattering length. This effect was not as pronounced for the UCF patterns. We can also notice a beating effect of the interference pattern, that could indicate the presence of two main trajectories with slightly different perimeter, or the occurence of the Aharonov-

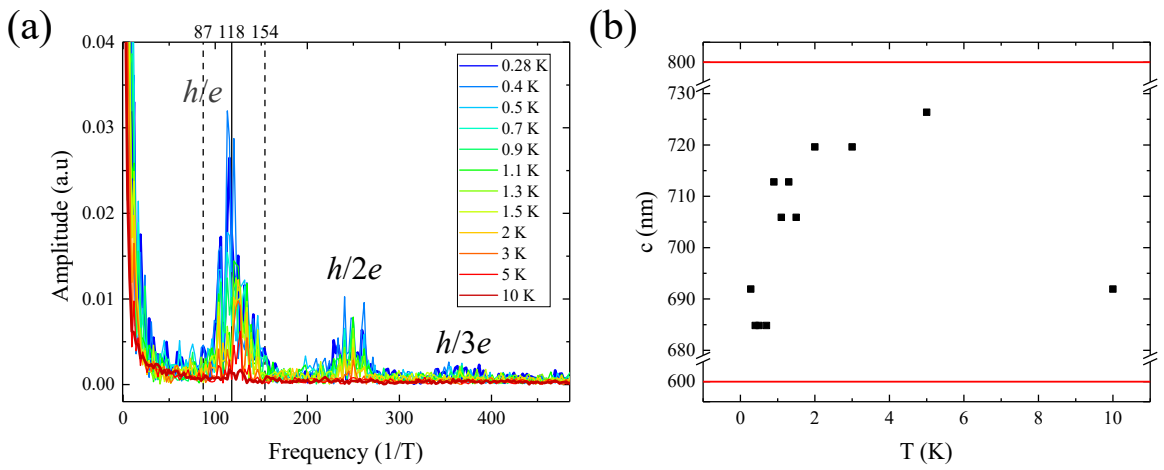

FIGURE 5.29 – (a) FFT spectra of the AB oscillations for each temperature. The solid vertical line represent the magnetic frequency calculated from the expected magnetic period. The two vertical dashed lines represent the calculated frequencies considering the inner and outer sides of the ring. The first harmonic peaks h/ne are shown. (b) Corresponding length of the ring side from the maximum amplitude extracted from the FFT spectrum. The red lines respectively represent the minimal and maximum length of the ring sides from the designed pattern.

Casher effect as previously reported in HgTe quantum rings [König, 2006].

Figure 5.28(b) displays the evolution of the root-mean-square (rms) of the oscillation amplitude as a function of temperature. The drop in amplitude with respect to the temperature is evidenced. The rms value of the amplitude is divided by a factor 10 between 280 mK and 10 K.

The evolution of conductance amplitude can also be studied by plotting the fast Fourier transform (FFT) of the signal for each temperature. Figure 5.29 evidences the significant contribution of the h/e oscillations to the conductance oscillations. The position of the peak stays within the expected window calculated from the lithographic dimensions over the whole temperature range. The maximum amplitude is very close to 118 T^{-1} frequency corresponding to the typical enclosed flux. As the temperature is increased, the amplitude of this first peak is reduced. The FFT spectra also display the presence of the second harmonic, corresponding to the $h/2e$ oscillations. The position of the peak is also consistent with the dimension of the ring as it is centered at 250 T^{-1}, corresponding to a square loop of side 720 nm. As one can expect, they vanish faster than the first peak as the temperature is increased because they result of a twice longer path length. The contribution of the AAS effect disappears completely from 5 K. Finally, we also notice the slight contribution of $h/3e$ oscillations for the lowest temperature measurements, 0.28, 0.4 and 0.5 K. We can not really observe a peak in the FFT, but nonetheless, the amplitude is distinguishable from the noisy background. It evidences the coherent interference of electronic waves after circulating the loop 1.5 times in each direction.

Figure 5.29(b) shows the temperature change of the side length of the square loop c extracted from the frequency position of the dominant peak in the FFT. The data indicate that the electron wave function is on average localized around the center of the ring, with $c \approx 700$ nm. Interestingly, the effective loop size increases slightly with tempe-

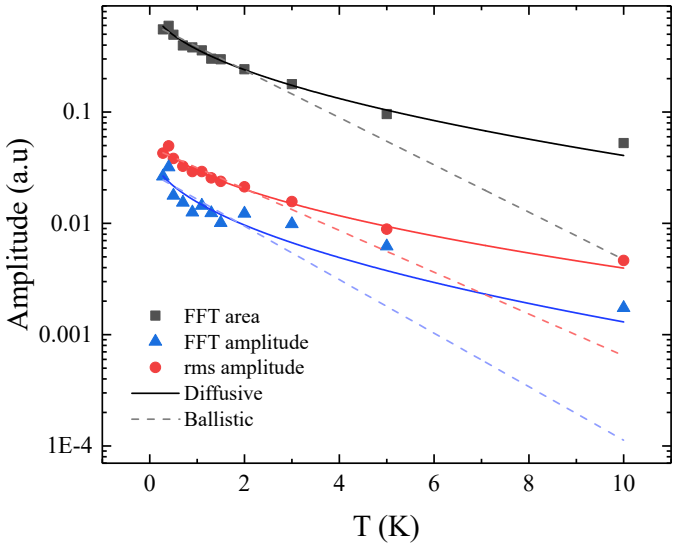

FIGURE 5.30 – The change of the FFT area (black squares), the FFT amplitude (blue triangle) and the rms of the AB oscillations (red dots) as a function of the temperature. Each curve is fitted to the diffusive (solid line) and ballistic (dashed line) models.

rature. This behavior seems counterintuitive : since the phase-coherence length decreases with increasing temperature, one would expect shorter trajectories through the ring to dominate quantum interference. However, shorter trajectories does necessarily imply trajectories closer to the inner edge of the ring but possibly more ballistic trajectories with less reflections on the boundaries.

4.2.3 Determination of the phase coherence length

To effectively quantify the h/e oscillation amplitudes, we plot three quantities in figure 5.30 : the FFT area within the frequency range of the AB effect, the maximum of the FFT within this range, and the rms amplitude of the oscillations. These quantities should be equivalent if the conductance is dominated by the AB oscillations. This is indeed the case when looking at the figure where they exhibit the same temperature dependence. According to the previously derived theory, we use the expression $A\exp(-bT^m)$ to fit the data. The temperature exponent is set alternatively to $m = 1/2$ and $m = 1$, to check if the transport regime is respectively diffusive or ballistic. The coefficient b is essential for the determination of the phase coherence length as

$$l_\phi = \frac{p}{bT^m} \tag{5.36}$$

The fitting results of the three quantities are displayed in figure 5.30 for the diffusive (solid lines) and the ballistic (dashed lines) regimes. We see that the ballistic regime poorly fits the data. In contrast, the diffusive regime smoothly follows the data. In particular, the FFT area and the rms amplitude show a clear dependence in $T^{-1/2}$. Although the 2D mean-free-path l_e is longer than the ring size, the numerous scatterings on the wire boundaries strongly reduce the effective mean free path, explaining the observed diffusive

TABLE 5.1 – Phase coherence lengths in the HgTe nanoring extracted from the different quantities for the diffusive model $l_\phi = pb^{-1}T^{-1/2}$ where $p = 2800$ nm is the ring perimeter.

	FFT area	FFT amplitude	rms amplitude
b ± err ($K^{-1/2}$)	1.01 ± 0.07	1.15 ± 0.24	0.93 ± 0.09
$l_\phi(0.28\ K)$± err (μm)	5.21 ± 0.36	4.62 ± 0.97	5.67 ± 0.55

regime of transport.

The deducted values of the phase coherence length at 280 mK are reported in Table 5.1 together with the proportionality coefficient b. We found $l_\phi(0.28\ K) \sim 5\ \mu$m. It is consistent with the observation of the $h/2e$ oscillations, as $l_\phi > p = 2.8\ \mu$m, and the $h/3e$ contribution obtained for $l_\phi > \frac{3}{2}p = 4.2\ \mu$m. The electronic wave thus remains coherent after circulating the loop 1.5 times.

The inelastic scattering length at 50 mK computed from the diffusive model would be $l_\phi(0.05\ K) \sim 13\ \mu$m. Similar studies on InAs, InSb or PbTe nanoring reported lower to similar values of the phase coherence lengths at 50 mK $l_\phi \sim 2 - 13\ \mu$m [Vaitiekėnas, 2018a ; Lee, 2019 ; Geng, 2022 ; Jung, 2022 ; Aseev, 2019]. The results presented in this thesis are thus of high quality and put the HgTe material as a promising candidate for further experimental manifestation of quantum phenomena.

4.3 Conclusion

This section has evidenced the manifestation of Aharonov-Bohm and Altshuler-Aronov-Spivak oscillations in a HgTe-based nanoring. After subtraction of the slowly varying background, the oscillation period was found to be in excellent agreement with the lithographic dimensions. The FFT analysis of the magneto-transport data revealed the presence of both h/e and $h/2e$ oscillations, confirming coherent transport in the device.

The temperature dependence of the oscillation amplitude allowed us to extract the phase coherence length. The transport is well described by a diffusive regime, with $l_\phi \propto T^{-1/2}$, leading to a maximum phase coherence length of about 5 μm at 280 mK. This value is roughly twice that obtained in the nanowire measurements.

Interestingly, the temperature evolution differs between the two geometries : while the AB oscillations indicate $l_\phi \sim T^{-1/2}$, the nanowire yields $l_\phi \sim T^{-0.24}$. Such discrepancies between ring and wire geometries have already been predicted by Ludwig *et al.*, who showed that the dominant dephasing mechanisms depend on the ring radius [Ludwig, 2004].

5 Conclusion

This Chapter has reported the low temperature magneto-transport measurements of HgTe nanostructures in both nanowire and ring geometries.

Transport in a 100 nm-wide and 5 μm-long nanowire revealed a complex Hall response, particularly on the hole side, and no clear quantum Hall effect due to the reduced dimensionality. Nevertheless, an effective mean free path of approximately 420 nm was extracted. Two phase-coherent phenomena, universal conductance fluctuations (UCF) and weak anti-localization (WAL), were identified and analyzed as a function of temperature and voltage bias. A phase-coherence length of about 2.5 μm at 280 mK was obtained using different analysis methods.

In the ring structure, Aharonov–Bohm (AB) and Altshuler-Aronov-Spivak (AAS) oscillations were observed. Fast Fourier transform analysis revealed both h/e and $h/2e$ periodicities, with oscillation periods consistent with the lithographic dimensions, confirming coherent transport throughout the ring. The temperature dependence followed $l_\phi \propto T^{-1/2}$, reaching approximately 5.6 μm at 280 mK, indicating diffusive transport in this geometry.

Table 5.2 summarizes the main phase-coherent transport parameters extracted for each device. The different temperature scaling laws observed in the two geometries are consistent with previous reports in the literature and support the choice of the selective-are-growth technique for the fabrication of HgTe-based devices.

Taken together, the nanowire and nanoring studies provide complementary insights into phase-coherent transport in HgTe nanostructures. While the nanowire highlights the role of disorder through UCF and WAL effects, the ring directly demonstrates flux-sensitive interference via AB and AAS oscillations. Their comparison emphasizes how geometry governs both the magnitude and temperature dependence of the phase-coherence length, establishing a coherent and unified picture of mesoscopic transport in selectively grown HgTe devices.

TABLE 5.2 – Determination of the phase coherence length l_ϕ and its temperature law based on different devices and methods.

	NW			Ring
	UCF		WAL	AB oscillation
	δg_{xx}	ΔB_{corr}	Fit	FFT area/rms
l_ϕ(0.28 K) (nm)	500	2200	2800	5600
Temperature dependence	$T^{-0.18}$	$T^{-0.26}$	$T^{-0.24}$	$T^{-0.5}$

Conclusions and Perspectives

The objective of this PhD work was to develop and investigate the selective area growth (SAG) of HgTe nanostructures as a novel route toward low-dimensional high-quality in-plane devices. While HgTe quantum wells have been studied for their exceptional electronic properties, their integration into complex nanostructures such as nanowires and rings has remained limited by the difficulty of controlling both their geometry and crystalline quality. The SAG approach introduced in this work offers a new and versatile pathway to pattern epitaxial HgTe directly during epitaxy, enabling the bottom-up fabrication of in-plane quantum devices with controlled dimensions and orientations.

We have first demonstrated the selective area epitaxy of in-plane HgTe nanostructures on CdTe(001) substrates by MBE. The process achieves excellent selectivity for several growth temperatures and growth rates, with almost no parasitic deposition on low-roughness SiO_2 masks, ensuring an accurate reproduction of the lithographically designed patterns. Increasing the growth temperature, up to 180°C, limits the nanostructure lateral expansion on the mask and facilitates the surface diffusion of adatoms on the HgTe crystal. The mask design itself strongly influences the resulting morphology, leading to pronounced anisotropy between the $\langle 100 \rangle$, $\langle 110 \rangle$, and $\langle 1\bar{1}0 \rangle$ crystallographic directions. While $\langle 100 \rangle$ nanowires maintain a flat top surface, $\langle 110 \rangle$ nanowires exhibit tilted grains, and $\langle 1\bar{1}0 \rangle$ wires develop super-elevations associated with diffusion from the {111}A side facets. The opening width and the nominal deposited thickness can be used to tune the morphology of the nanostructures. The triangular cross section bounded by {111} facets is promoted in narrow openings and thick deposition, leading to lateral expansion once the triangular geometry is reached. Structural analyses by STEM reveal that the zinc-blende HgTe nanowires are epitaxial, coherent, and free of misfit dislocations at the HgTe/CdTe interface. We also evidenced strain relaxation in the nanowires, unlike in two-dimensional layers.

This study establishes the growth conditions required for reproducible, defect-free, and morphologically controlled HgTe nanostructures, paving the way for scalable device fabrication. Three basic device geometries were successfully fabricated and measure to demonstrate their potential application in quantum nanoelectronics.

Hall-bar devices made from SAG-grown HgTe were studied through magneto-transport measurements at low temperature, revealing both electron and hole conduction regimes tunable by gate voltage. The electron regime showed a linear Hall response with high mobility, while the hole regime exhibited a nonlinear response likely due to band overlap between conduction and valence bands. At high magnetic fields, the devices displayed clear quantum Hall behavior with transitions from odd to even filling factors, indicating lifted surface-state degeneracy and Dirac-like carriers. These results demonstrate that the SAG approach preserves the topological properties of HgTe quantum wells and establishes a reliable platform for quantum transport studies.

Subsequently, magneto-transport measurements on selectively grown HgTe (quasi-)1D nanowires and rings reveal clear evidence of phase-coherent transport. In 100 nm-wide nanowires, universal conductance fluctuations and weak anti-localization were observed. The conductance measurements lead to an effective mean free path of about 420 nm and a phase-coherence length l_ϕ of about 2.5 μm at 280 mK. In ring structures, Aharonov-Bohm and Altshuler–Aronov–Spivak oscillations with h/e and $h/2e$ periodicities confirm coherent transport through the entire ring, with l_ϕ reaching 5.6 μm and following a $T^{-1/2}$ dependence. The comparison highlights the influence of geometry on phase coherence and demonstrates robust quantum interference in SAG-grown HgTe nanostructures, establishing their potential for topological quantum transport studies.

In the end, this work establishes selective area growth as a powerful technique for engineering high-quality, in-plane HgTe nanostructures. Beyond demonstrating the feasibility of SAG for HgTe, it provides a detailed understanding of the parameters governing morphology, crystallinity, and transport. The demonstration of phase-coherent transport in selectively grown HgTe nanowires constitutes an important milestone toward the realization of hybrid quantum devices based on this material.

Future research may explore several directions. Among them, the optimization of the mask design and interface quality to promote the growth of even narrower devices. This would decrease the bulk to surface ratio hence reducing the bulk contribution during transport and achieve effective 1D topological transport resulting from quantized subbands and the emergence of helical edge modes. Another promising direction is the development of epitaxial semiconductor/superconductor (SM/SC) hybrid nanostructures, exploiting the unique properties of low effective mass and strong spin-orbit coupling of HgTe in combination with a high-quality superconducting proximity effect. Beside the famous quest of Majorana Zero Mode for fault-tolerant quantum computation, such systems are particularly appealing for the implementation of gatemon qubits, in which the Josephson coupling, and thus the qubit frequency, can be tuned electrostatically rather than magnetically. This approach offers enhanced scalability and reduced cross-talk compared to conventional flux-controlled superconducting qubits.

In summary, this thesis demonstrates that selective area growth enables the controlled

fabrication of high-quality HgTe nanostructures and preserves their transport properties across multiple geometries. These results establish HgTe nanostructures as a promising platform for spin-orbitronics and quantum technologies, bridging the gap between material development and device application.

Conclusions et Perspectives

L'objectif de ce travail de thèse était de développer et d'étudier la croissance sélective (Selective Area Growth, SAG) de nanostructures HgTe comme une nouvelle méthode pour des dispositifs planaires de haute qualité et de petite dimension. Bien que les puits quantiques HgTe aient été largement étudiés pour leurs propriétés électroniques exceptionnelles, leur intégration dans des nanostructures complexes telles que des nanofils ou des anneaux est restée limitée par la difficulté de contrôler à la fois leur géométrie et leur qualité cristalline. L'approche SAG introduite dans ce travail offre une alternative nouvelle et polyvalente pour structurer les couches HgTe épitaxiées directement pendant la croissance, permettant la fabrication de dispositifs quantiques plans aux dimensions et orientations contrôlées. Nous avons tout d'abord démontré la croissance sélective de nanostructures planaires de HgTe sur des substrats CdTe(001) par épitaxie par jets moléculaires (EJM). Le procédé présente une excellente sélectivité pour plusieurs températures et vitesses de croissance, avec une absence quasi totale de dépôts parasites sur les masques en SiO_2 à faible rugosité garantisssant une reproduction fidèle des motifs définis par lithographie. L'augmentation de la température de croissance, jusqu'à 180 °C, limite l'expansion latérale des nanostructures sur le masque et favorise la diffusion de surface des adatomes sur le cristal de HgTe. La conception du masque influence fortement la morphologie obtenue, conduisant à une anisotropie marquée entre les directions cristallographiques $\langle 100 \rangle$, $\langle 110 \rangle$ et $\langle 1\bar{1}0 \rangle$. Alors que les nanofils orientés selon $\langle 100 \rangle$ conservent une surface supérieure plane, ceux orientés selon $\langle 110 \rangle$ présentent des grains inclinés, et les fils $\langle 1\bar{1}0 \rangle$ développent des surélévations associées à la diffusion depuis les facettes latérales 111A. La largeur des ouvertures et l'épaisseur nominale déposée permettent d'ajuster la morphologie des nanostructures. Une section transversale triangulaire délimitée par des facettes 111 est favorisée pour des ouvertures étroites et des dépôts épais, conduisant à une expansion latérale une fois cette géométrie atteinte. Les analyses structurales par STEM révèlent que les nanofils HgTe de structure zinc-blende sont épitaxiés, cohérents et exempts de dislocations de désaccord à l'interface HgTe/CdTe. Nous avons également mis en évidence une relaxation de la contrainte dans les nanofils, contrairement aux couches bidimensionnelles.

Cette étude établit les conditions de croissance nécessaires à l'obtention de nanostruc-

tures HgTe reproductibles, sans défauts et à morphologie contrôlée, ouvrant la voie à la fabrication de dispositifs à grande échelle. Trois géométries de dispositifs élémentaires ont été fabriquées et mesurées avec succès afin de démontrer leur potentiel pour des applications en nanoélectronique quantique.

Des dispositifs de type barre de Hall réalisés à partir de HgTe crû par SAG ont été étudiés par des mesures de magnéto-transport à basse température, révélant des régimes de conduction électronique et trou modulables par tension de grille. Le régime électronique présente une réponse de Hall linéaire avec une mobilité élevée, tandis que le régime trou montre une réponse non linéaire probablement due à un recouvrement des bandes de conduction et de valence. À champ magnétique élevé, les dispositifs présentent un comportement clair d'effet Hall quantique avec des transitions entre facteurs de remplissage impairs et pairs, indiquant une levée de la dégénérescence des états de surface et la présence de porteurs de type Dirac. Ces résultats démontrent que l'approche SAG préserve les propriétés topologiques des puits quantiques de HgTe et constitue une plateforme fiable pour l'étude du transport quantique. Par la suite, des mesures de magnéto-transport sur des nanofils et des anneaux HgTe (quasi-)1D obtenus par croissance sélective révèlent des signatures claires de transport cohérent en phase. Dans des nanofils de 100 nm de large, des fluctuations universelles de conductance ainsi qu'une anti-localisation faible ont été observées. Les mesures de conductance conduisent à un libre parcours moyen effectif d'environ 420 nm et à une longueur de cohérence de phase l_ϕ d'environ 2,5 μm à 280 mK. Dans les structures en anneau, des oscillations d'Aharonov–Bohm et d'Altshuler–Aronov–Spivak, de périodicités h/e et $h/2e$, confirment un transport cohérent sur l'ensemble de l'anneau, avec une longueur de cohérence atteignant 5,6 μm et suivant une dépendance en $T^{-1/2}$. La comparaison met en évidence l'influence de la géométrie sur la cohérence de phase et démontre une interférence quantique robuste dans les nanostructures de HgTe obtenues par SAG, confirmant leur potentiel pour les études de transport quantique topologique. En conclusion, ce travail établit la croissance sélective SAG comme une technique fiable pour l'ingénierie de nanostructures planaires de HgTe de haute qualité. Au-delà de la démonstration de la faisabilité de la SAG pour HgTe, cette étude apporte une compréhension détaillée des paramètres gouvernant la morphologie et la cristallinité des nanostructures ainsi que ceux déterminant le régime de transport électronique. La mise en évidence d'un transport maintenant la cohérence de phase dans des nanofils de HgTe obtenus par croissance sélective constitue une étape clé vers la réalisation de dispositifs quantiques hybrides basés sur ce matériau. Les perspectives de recherche futures s'ouvrent sur plusieurs directions. Parmi celles-ci, nous pouvons noter l'optimisation de la conception des masques et de la qualité des interfaces pour favoriser la croissance de dispositifs encore plus étroits. Cela permettrait de réduire le rapport volume/surface, et donc la contribution du volume au transport, pour atteindre un transport topologique effecti-

vement unidimensionnel résultant de la quantification des sous-bandes et de l'émergence de modes de bord hélicoïdaux. Une autre direction prometteuse concerne le développement de nanostructures hybrides semi-conducteur/supraconducteur (SM/SC) épitaxiées, exploitant les propriétés uniques du HgTe — faible masse effective et fort couplage spin-orbite — combinées à un effet de proximité supraconducteur de haute qualité. Au-delà de la célèbre quête des modes de Majorana pour le calcul quantique tolérant aux fautes, ces systèmes sont particulièrement attractifs pour la réalisation de qubits de type gatemon, dans lesquels le couplage de Josephson, et donc la fréquence du qubit, peut être modulé par une tnesion de grille plutôt que magnétiquement. Cette approche offre une meilleure adaptabilité et une réduction des interférences par rapport aux qubits supraconducteurs conventionnels contrôlés par flux.

En résumé, cette thèse démontre que la croissance sélective permet la fabrication de nanostructures HgTe de haute qualité de manière contrôlée tout en préservant leurs propriétés de transport pour différentes géométries. Ces résultats établissent les nanostructures HgTe comme une plateforme prometteuse pour la spin-orbitronique et les technologies quantiques, comblant le fossé entre le développement des matériaux et les applications en dispositifs.

Appendix A

Material characterization techniques

The thorough characterization of the HgTe/CdTe nanostructures relies on a set of experimental technique that we will present here. The methods and setup used are numerous and different, therefore this Appendix provides information about the principle and the experimental setup for each of the characterization techniques used in this report. The data and their analysis have been detailed in Chapter 2. The first part focuses on the principle of atomic force microscopy (AFM), which has been extensively used for the morphological characterization of the HgTe nanowires. Then, characterization thanks to X-rays is introduced. Finally, we provide information on the transmission electron microscopy (TEM) techniques that have been employed here in specific modes of operation.

1 Atomic Force Microscopy

The AFM measurements were performed in air with a Bruker Dimension ICON instrument located at the Nanocharacterization Platform (CEA-Leti). Atomic force microscopy reveals the surface topography of the sample, providing access to its morphology and roughness. Different operating modes are possible with AFM, in this thesis only the tapping mode has been used. In this mode, a tip mounted at the end of a vibrating cantilever is driven close to its resonance frequency and intermittently interacts with the sample surface. Short-range forces such as van der Waals, dipole-dipole, and electrostatic interactions modify the oscillation amplitude and phase of the cantilever. A laser beam reflected from the back of the cantilever is focused onto a photodiode. Changes in the spot position because of interactions of the tip with the sample surface are converted into electrical signals from which the oscillation amplitude is extracted. A feedback loop maintains this amplitude constant by adjusting the vertical position of the cantilever via the z-piezo, thereby reconstructing the surface topography. Figure A.1 illustrates the operation of the AFM tool in the tapping mode. The surface roughness can then be quantified with Ångström precision, typically defined as the root mean square of the height distribution.

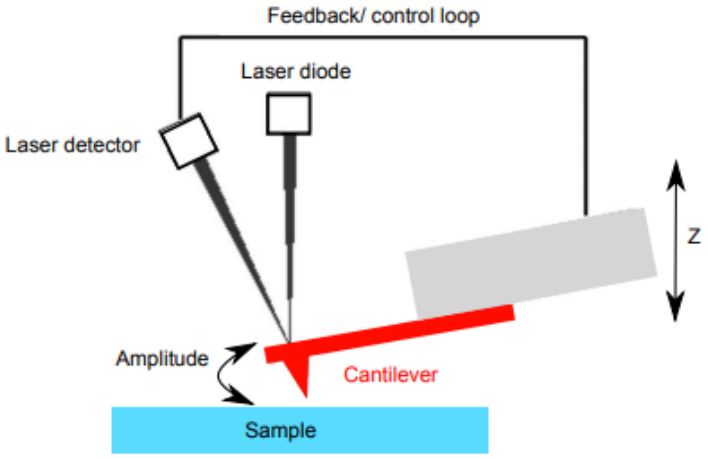

FIGURE A.1 – Schematic of an AFM tool operating in tapping mode

2 X-ray

X-ray-based characterization techniques rely on the interaction between X-ray waves and the material to assess the structural characteristics of a sample. They are non-destructive techniques offering a wide variety of parameters to be probed : crystal quality, roughness, thickness, strain, and more. It makes X-ray techniques an essential tool in semiconductor characterization. X-Rays Diffraction (XRD) is presented in this section. The X-Rays machine used during this study is a Bruker Discover 8.

To produce X-Rays, accelerated electrons, their voltage scales with dozens of kV, are sent on a copper anode where two phenomena lead to X-Rays emissions : the deceleration of the latter electron (K-α energy) and the de-excitation of the anode electrons (K-β energy). Thus, waves at different wavelengths are emitted. To be selective and keep only one specific wavelength, a four-bounds monochromator is added at the end of the source and select the K-α1 wavelength of copper : $\lambda_{K\alpha 1} = 1.54062$ Å. Detection is performed thanks to a triple-axis detector with cancellation of the diffracted beam divergence. Therefore, measurements are realized with a precision of 0.003°. Different optic instruments (slits, collimators, mirrors, etc) are placed before and after the sample to focus and collimate the beam.

2.1 Diffraction

XRD provides information on the crystal quality thanks to interactions of X-Rays waves with the crystal lattice. The diffraction condition occurs when the reflective waves lead to constructive interference at the detector. This situation is governed by Bragg's law which sets a relation between the incident angle of the waves, θ, and the interplanar distance between (hkl) lattice planes (hkl being Miller indexes), $d_{(hkl)}$:

$$2d_{(hkl)} \sin(\theta) = n\lambda$$

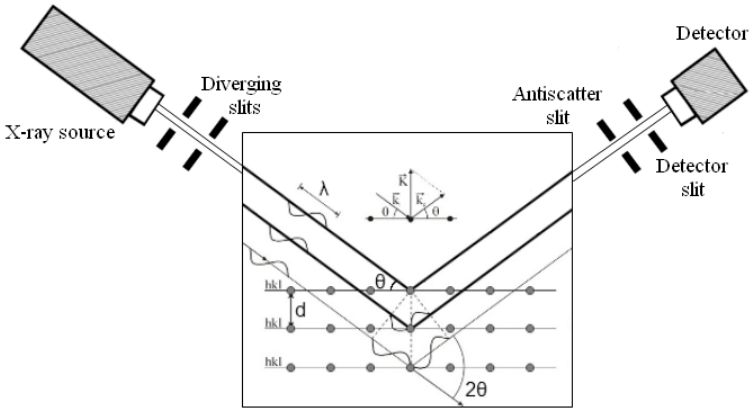

FIGURE A.2 – Sketch of an XRD setup with interaction between X-Rays and the crystal lattice. Adapted from [Charpentier, 2012]

where λ is the wavelength of the incident X-Rays waves and n an integer representing the order of diffraction, set to 1 in this case. figure A.2 displays the interaction of the waves with the sample.

The interplanar distance yields the out-of-plane parameter, c, of the crystal. For cubic systems as HgTe or CdTe, one gets :

$$d_{(hkl)} = \frac{c}{\sqrt{h^2 + k^2 + l^2}}$$

In XRD experiments, the diffracted intensity is proportional to the squared structure factor of the crystal, which describes how the crystal scatters the incoming radiations. Along particular crystal axis directions (hkl), it exhibits extinction conditions, meaning the intensity is zero. Thus, the direction along which the experiment is performed must be carefully selected. For cubic system with zinc-blende structure, the structure factor is expressed as the following :

$$F_{(hkl)} = \sum_i f_i \exp(x_i h + y_i k + z_i l)$$

where i runs on the basis position of the atom in the unit cell and f_i is the form factor of the atom representing the amplitude of the wave when scattered by an isolated atom. In the case of HgTe/CdTe, Hg/Cd atoms form a face centered cubic (fcc) system, and with the conventional simple cubic cell, the basis vectors are (0,0,0), ($\frac{1}{2}$,$\frac{1}{2}$,0), ($\frac{1}{2}$,0,$\frac{1}{2}$) and (0,$\frac{1}{2}$,$\frac{1}{2}$). In the zinc-blende structure, the Te atoms also form a face centered cubic system but shifted of ($\frac{1}{4}$,$\frac{1}{4}$,$\frac{1}{4}$). Hence, the structure factor can be written as :

$$F_{(hkl)} = \left[f_{\mathrm{Hg/Cd}} + f_{\mathrm{Te}} \exp\left(2i\pi \left(\frac{h}{4} + \frac{k}{4} + \frac{l}{4} \right) \right) \right] \times$$
$$[1 + \exp(i\pi(h+k)) + \exp(i\pi(h+l)) + \exp(i\pi(k+l))]$$

The last factor is the one of fcc, which is zero unless h, k, l are all odd or all even. Then, the studied structure having (100) orientation, the XRD measurements will be performed using $(h, k, l) = (2n, 0, 0)$ so that $F_{(hkl)} = 4(f_{\mathrm{Hg/Cd}} + f_{\mathrm{Te}})$.

3 Transmission electron microscopy

TEM has been employed for our HgTe structures to characterize the epitaxial quality at the interface and in the bulk of the nanowires. The chemical composition, the lattice arrangement, and the strain distribution have been investigated. Two different TEM modes have been employed to perform the characterizations : high-resolution Scanning TEM (STEM) and Nanobeam Precession Electron Diffraction (NPED). The aim of this section is to give some keys for understanding the specificity of each of these modes and techniques. One can note that all the TEM characterizations have been performed on the Nanocharacterization Platform of CEA-Leti in collaboration with P.H. Jouneau, E. Gautier, N. Bernier and J.P. Rouvière. The observations have been realized on a Thermo Fischer (ex FEI) Titan Themis 200 microscope equipped with spherical aberration corrector on the condenser lens for high resolution STEM imaging. A 200 kV voltage has been used for the experiments. The focused ion beam (FIB) preparation of the TEM lamellas follows a two steps procedure. First, a 50 nm-thick protective carbon layer is deposited by electron beam assisted evaporation as the direct use of ion beam would damage the nanostructure. Then, a 3 μm-thick carbon(10%)-Pt(90%) layer is deposited on top with the ion beam at 12 kV. The lamellas have been prepared using a Thermo Fisher Helios 5 PFIB.

Scanning transmission electron microscopy is one of the most widely employed imaging modes in TEM instruments. In this configuration, a convergent electron beam is focused on the sample, and rastered across it. The transmitted electrons are detected with respect to the probe position allowing the realization of high-resolution images with nanometric precision. The numerous detectors positioned along the axis of the microscope give access to complementary information on the sample, making STEM a versatile technique. A schematic illustrating the different elements of a TEM is displayed in figure A.3(a).

In this work, the High-Angle Annular Dark Field (HAADF) detector has been particularly used. Consisting of a ring-shaped geometry, it collects electrons scattered to high angles. The intensity in HAADF images scales with approximately the square of the atomic number, $\sim Z^2$. Thus, the contrast is directly sensitive to chemical composition : heavy elements appear brighter than lighter elements.

In contrast, the bright field (BF) detector is aligned with the transmitted beam. This configuration makes it highly sensitive to structural imperfections. BF imaging is thus particularly valuable for assessing crystalline quality and detecting structural defects.

Finally, information on the chemical composition of the sample can be obtained using an Energy-Dispersive X-ray (EDX) detector. Under electron-beam irradiation, characte-

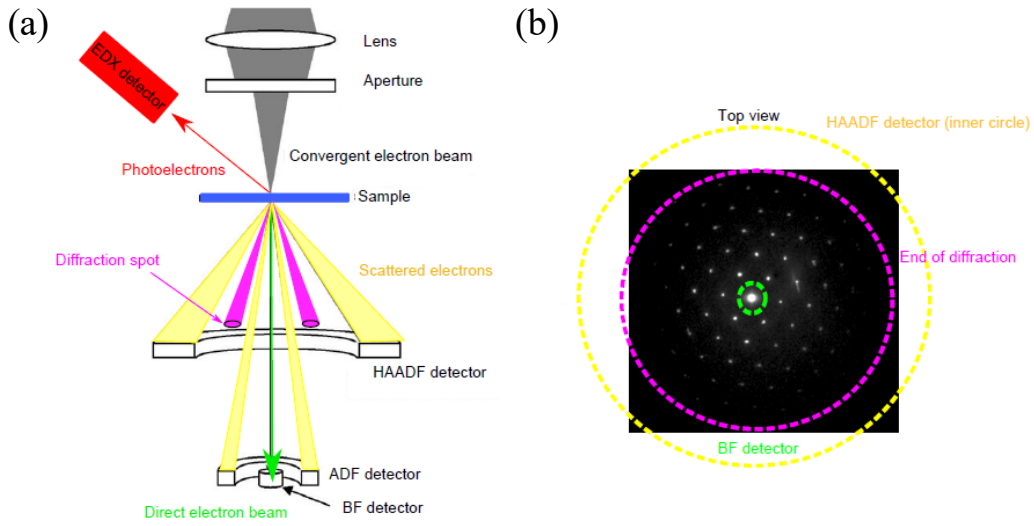

FIGURE A.3 – (a) TEM column with the convergent electron beam focusing on the sample. Bright Field detector measures the directly transmitted electron beam. High Angle Annular Dark Field detector collects the electrons scattered at high angle. The Energy Dispersive X-rays spectrometer (EDX) collects the photoelectrons. (b) A typical TEM diffraction pattern. The brightest spot in the center corresponds to the direct beam. The others evidence crystallographic axis. Taken from [Thomas, 2016].

ristic X-ray photons are emitted from the core electron of the sample. Therefore, measuring the energy of these photons enables an unambiguous identification of the atomic species.

With an electron beam accelerated at an energy of hundreds of kV, TEM enables electron diffraction to be performed. Scattered electrons are focused on a focal plane where a diffraction pattern is formed. This diffraction pattern corresponds to a section of the reciprocal lattice and each spot characterizes a crystallographic plane. The positions of these spots are used to determine the crystallographic axis and their lattice spacing. Thus, the operator can orientate the sample along a particular crystallographic direction to perform a structural study. A typical diffraction pattern is presented in figure A.3(b).

3.1 Nanobeam precession electron diffraction

The NPED technique is applied in TEM under diffraction mode by precessing the electron beam at a constant angle around the optical axis, as illustrated in figure A.4(a). This precession increases the illuminated crystal volume beyond a single unit cell. The resulting diffraction disks are corrected by descan coils and converted into sharp spots. Such features improve the resolution of the diffraction pattern, allowing more accurate determination of lattice parameters and strain. At the same time, the precession introduces a broader spot size, which reflects the reduced spatial resolution inherent to the technique. Nevertheless, precession produces a more homogeneous spot contrast and reveals additional diffraction spots, as shown in figure A.4(b). This figure displays the diffraction pattern obtained from the CdTe substrate in the TEM lamella. The central spot in g0 corresponds to the $\langle 1\bar{1}0 \rangle$ zone axis, while g1 and g2 arise from $\langle 111 \rangle$ scattering. Linear

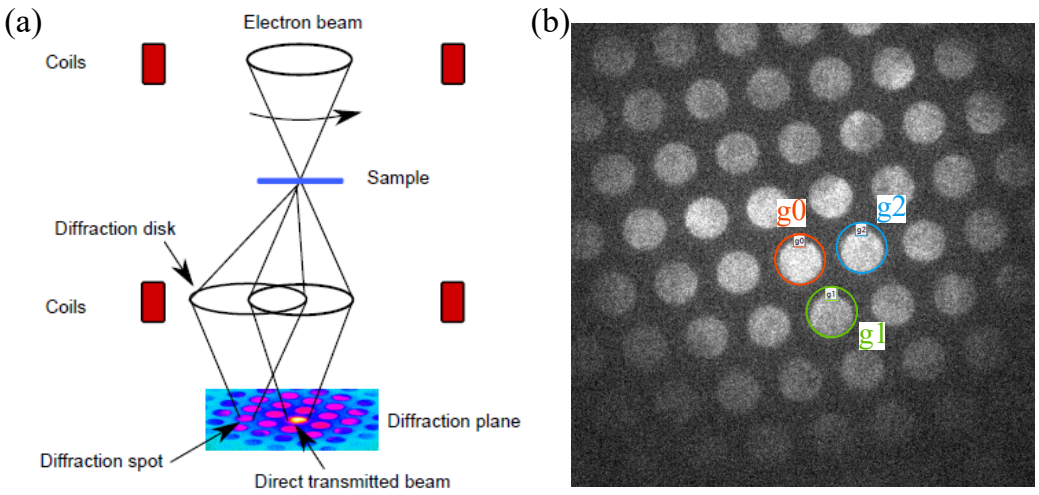

FIGURE A.4 – (a) Sketch illustrating the beam precession during nanobeam precession electron diffraction and the collection of obtained diffraction spots. Taken from [Thomas, 2016]. Typical diffraction pattern obtained in CdTe along the $\langle 1\bar{1}0 \rangle$ axis The disk in g0 is the central disk. Disks in g1 and g2 correspond to $\langle 111 \rangle$ diffraction type.

combinations of the g1 and g2 vectors yield the $\langle 002 \rangle$ vector (the growth direction) and the $\langle 110 \rangle$ vector (an in-plane direction). These vectors are then used to construct precise deformation maps.

Appendix B

Complementary works on selective growth

1 Deformation maps of a 50 nm-wide nanowire

In the main text of this dissertation, we discussed the strain, rotation, and shear properties of a 100 nm-wide nanowire oriented along the $\langle 1\bar{1}0 \rangle$ direction. In addition, we performed NPED measurements on a 50 nm-wide HgTe nanowire with the same orientation, using the same experimental procedure.

The strain maps in figure B.1(a) display a predominantly green contrast at the substrate interface, indicating that the nanowire is fully relaxed in both the in-plane $\langle 110 \rangle$ direction and the out-of-plane $\langle 001 \rangle$ growth direction. This behavior is consistent with the wider nanowire presented in the main text, and can be attributed to the limited contact area with the substrate. However, a blue contrast appears at the upper tip of the nanowire in the $\epsilon\langle 001 \rangle$ map, revealing a reduction of the out-of-plane lattice parameter. This feature is likely related to the geometry of the 50 nm-wide structure : the two side facets merge at the top, forming a tip that compresses the HgTe lattice vertically. Such an effect is absent in wider nanowires where the side facets remain separated. In principle, vertical compression should be accompanied by lateral expansion, yet the red contrast in the $\epsilon\langle 110 \rangle$ map is noticeably weaker than the blue contrast. Considering that NPED provides limited spatial resolution, especially at nanostructure edges, this discrepancy could arise from resolution constraints rather than a true absence of lateral strain.

The rotation map in figure B.1(b) exhibits opposite tilts at the bases of the two side facets, but not along their full extent as observed for the 100 nm-wide nanowire. We attribute this difference to the triangular cross-section of the narrower nanowire, which balances the crystal rotations induced by each side facet and thus results in a globally rotation-free crystal. The shear map shown in figure B.1(b) supports the same conclusion, indicating that the influence of the side facets compensates each other.

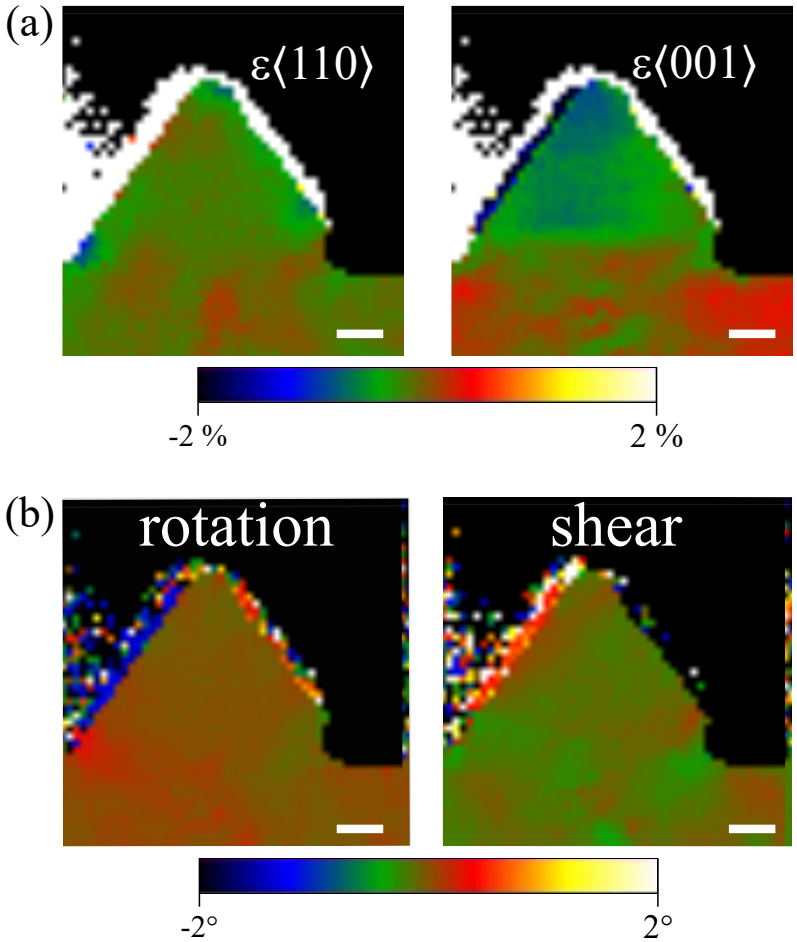

FIGURE B.1 – Mapping of different physical properties of 50 nm-wide $\langle 1\bar{1}0\rangle$-oriented NW obtained by NPED in transversal cross-section. In panel (a) the strain is represented along the (left) [110] in-plande direction and (right) the growth direction [001]. Below, in (b), the maps respectively illustrates the rotation and the shear. The scale bar represents 10 nm.

2 Selective growth of HgTe on InSb(001) substrate

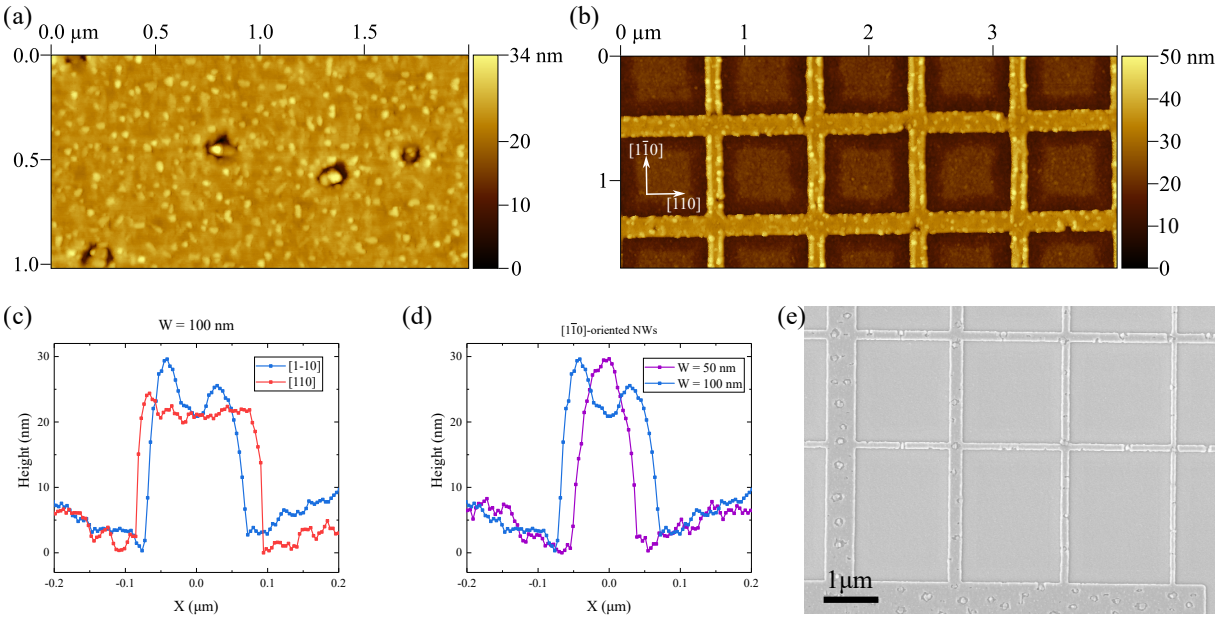

FIGURE B.2 – Surface state and morphology of HgTe nanostructures grown on InSb(001) substrate. (a) AFM image showing the top surface of the HgTe layer in a 2D-like opening. (b) AFM image of a NW grid. (c) Comparison of the morphology between [110]-and [1$\bar{1}$0]-oriented NWs. (d) Comparison of the morphology between 50 nm- and 100 nm-wide NWs. (e) SEM image of a NW grid with a 2 hours exposition to H_2 plasma before growth.

The addition of a global back gate appears as an efficient solution to improve the electrostatic control over the nanodevices. The top gates can be used for local and precise adjustments. However, CdTe substrate can not be used as a gate electrode because it is highly insulating. To overcome this issue, we studied the growth of HgTe patterns on InSb(001) substrate. InSb is a semiconducting crystal of III-V materials showing zinc-belnde crystal structure and with a small lattice mismatch to HgTe, $f \approx -0.27$ %. The hetero-epitaxy of HgTe on top of InSb can therefore be considered. In addition thanks to its electrical properties, InSb can act as a back gate.

The selective growth of HgTe on InSb substrate has been investigated under the same growth conditions as for HgTe/CdTe to ensure selectivity and material quality. The results are presented in figure B.2. Despite the good selectivity with respect to the silicon dioxide mask, the HgTe crystal suffers from poor crystal quality, as we can see in panels (a) and (b). In particular, the feeling is not complete or uniform with the presence of holes where growth does not occur and discontinuities in the growth of nanowires. The top surface roughness is found to be above 2 nm (neglecting holes) on large openings. The in-plane crystal orientation still plays a role as we can see from the AFM image in panel (b) and as confirmed by the profile lines displayed in (c). The typical super-elevations are again present on the sides of the [1$\bar{1}$0]-direction. But here no typical side facets are visible. For NWs oriented along [110], the presence of twisted grains on the side is still possible, the large roughness is visible on the tope surface. In panel (d), we show that the influence of

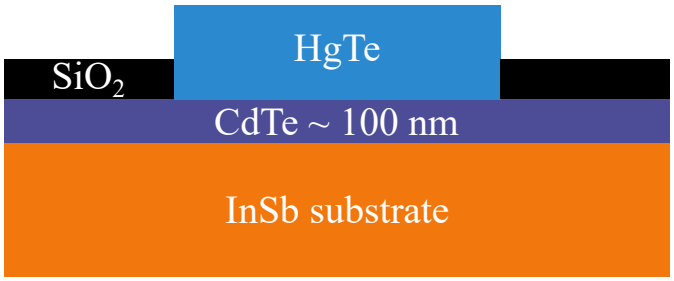

FIGURE B.3 – Sketch of layers arrangement for the selective growth of HgTe with a InSb(001) substrate.

the width is similar to that of the growth on CdTe substrates. However, the absence of clear facets is a sign of poor crystal quality.

The presence of holes and defects in the HgTe nanostructures could be due to the presence of a native oxide at the top surface of the InSb substrate. We therefore tried to remove this potential layer by exposing the sample a longer time to the H_2 plasma before the growth, 2 hours instead of 40 minutes. The subsequent growth has been characterized by SEM as we show in panel (d). The selectivity is still excellent, but no clear improvement has been noticed for HgTe nanostructures. Indeed, holes are again present in large openings while the filling of nanowire is not continuous. The direct use of InSb substrate is therefore detrimental for the fabrication of nanodevices.

An alternative solution that could be explored is a combination of InSb substrate with the growth of a CdTe buffer layer prior to the selective process. Because bulk CdTe is highly insulating and cannot act as a gate electrode, we grow the HgTe structures on a conductive InSb wafer capped with a thin CdTe buffer layer. The CdTe buffer restores the chemical-compatibility required for high-quality HgTe epitaxy (surface morphology, reduced interface defects and suppressed interdiffusion), while the doped InSb substrate serves as the back-gate electrode. This configuration therefore combines the epitaxial benefits of the CdTe/HgTe interface with the electrostatic functionality of a conductive substrate. The thickness of the buffer layer is a crucial point to provide a high-quality template for HgTe growth and at the same time preserve sufficient gate coupling for effective tuning.

A schematic of the alternative configuration to ensure optimal electric control, InSb back gate, and adequate crystal quality, SAG on CdTe buffer layer, is presented in figure B.3.

3 Selective homoepitaxy of CdTe

In this section, we show the absence of selectivity of the CdTe material with respect to the silicon dioxide mask in figure B.4. We tried the SAG of CdTe on CdTe(001) substrate at growth temperature of HgTe SAG, (a) GT = 160°C, and at standard growth temperature of CdTe, (b) GT = 300°C. In both cases, the selectivity is not achieved, resulting in a high density of grains on the mask and poor pattern reproduction.

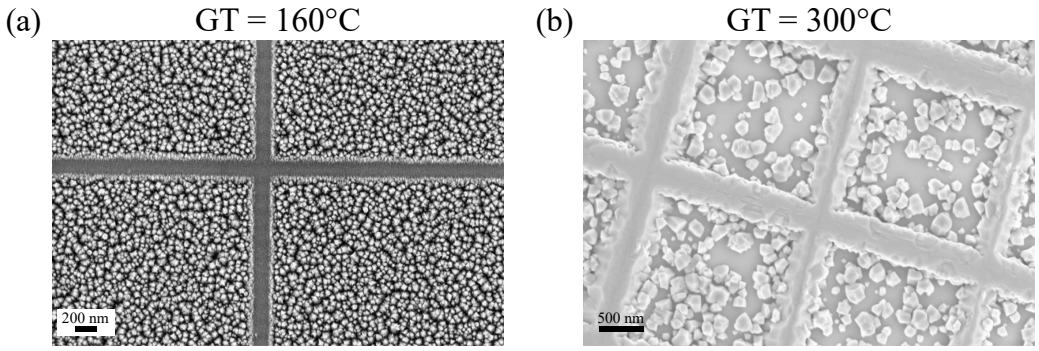

FIGURE B.4 – Growth of CdTe on patterned CdTe substrate to study the selectivity with respect to a silicon dioxide mask.

4 Selective area growth of HgTe/CdTe(111)

The selective area epitaxy of HgTe on (111)-oriented CdTe substrates was investigated using a hard mask composed of a thin alumina layer (5 nm) and a silicon dioxide layer deposited by CVD. In figure B.5(a), the mask openings are clearly visible. While the pattern is well reproduced, the quality of the exposed CdTe surface is poor. Several investigations were carried out to identify the origin of this degradation, including the choice of alumina etchant and the alumina deposition process, but none provided a convincing explanation. When HgTe was subsequently grown, as shown in figure B.5(b), the resulting layer exhibited very poor quality, with significant parasitic growth on the mask area. As discussed in the main text, this issue originates from the excessive roughness of the silicon dioxide layer produced by this fabrication process.

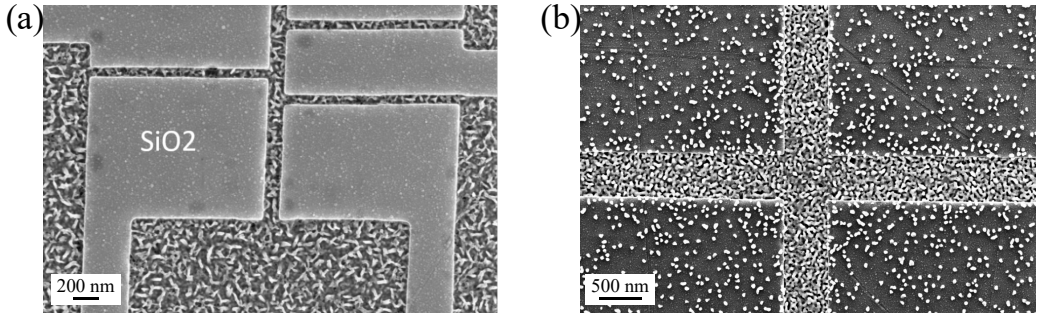

FIGURE B.5 – Study of selective area epitaxy on CdTe(111) substrate. (a) Al_2O_3 + SiO_2 mask preparation. The substrate top surface in the openings is very rough and of poor quality. (b) Attempt of HgTe SAG. The parasitic growth on the mask is abundant (see Section 5 in main text for explications) and HgTe layers in the openings are far from satisfying.

Appendix C

Magneto-transport measurements for a smaller Hall bar

In order to complement the magneto-transport study reported in Chapter 4 on a 10 nm-thick HgTe Hall bar with $L = 120$ μm/$W = 24$ μm, we present here the results obtained for another Hall bar of the same SAG process whose dimensions are $L = 15$ μm/$W = 3$ μm. This Hall bar is thus significantly smaller but can not be assimilated to a nanowire yet. The objective is to compare the transport properties between the two Hall bars.

The measurements are carried out at 1.5 K and at a bias voltage of 100 μV.

1 Low magnetic field measurements

Before applying a magnetic field, we characterize the longitudinal R_{xx} and the transversal R_{xy} resistances at a zero magnetic field. Figure C.1(a) shows the variation of R_{xx} as a function of the gate voltage. The overall shape is very similar, low resistance on the electron side for, $V_{\text{gate}} \geq -0.6$ V, peak of resistance around -0.7 V, and decrease of the resistance on the hole side as we further decrease the gate voltage. Nevertheless, we note that the resistance peak is not that high, and is of the order of h/e^2, that is approximately 26 kΩ. The shoulder visible on the hole side is this time more pronounced and emphasizes a strong contribution of the bulk heavy-hole band in the transport. The sheet resistance on the electron side at zero gate voltage is $R_{\square} = R_{xx}W/L = 325/5 = 65$ Ω, similar with that of the Hall bar of larger dimensions.

In addition, the orange curve from figure C.1(b) displays the variation of R_{xy} as a function of the gate voltage in the absence of magnetic field. Similarly to the other Hall bar, we note the presence of non zero values, highlighting peculiar behavior of the transversal resistance. Therefore, one could expect a non linear behavior of the Hall resistance with respect to the magnetic field around the CNP, as for the previous Hall bar.

The Hall resistance at $B = 0.1$ T is also plotted in figure C.1(b) and the corresponding

variation of the carrier density with respect to the gate voltage is shown in figure C.1(c). The main features from the larger Hall bar are also visible here. The same order of magnitude and the same shape are found. The depletion factor from the electron side is $\alpha = 19 \times 10^{11}$ cm^{-2}V^{-1}, very close to that of the Hall bar and even closer to the one expected from equation 3.9 derived from the layer thicknesses and permittivities.

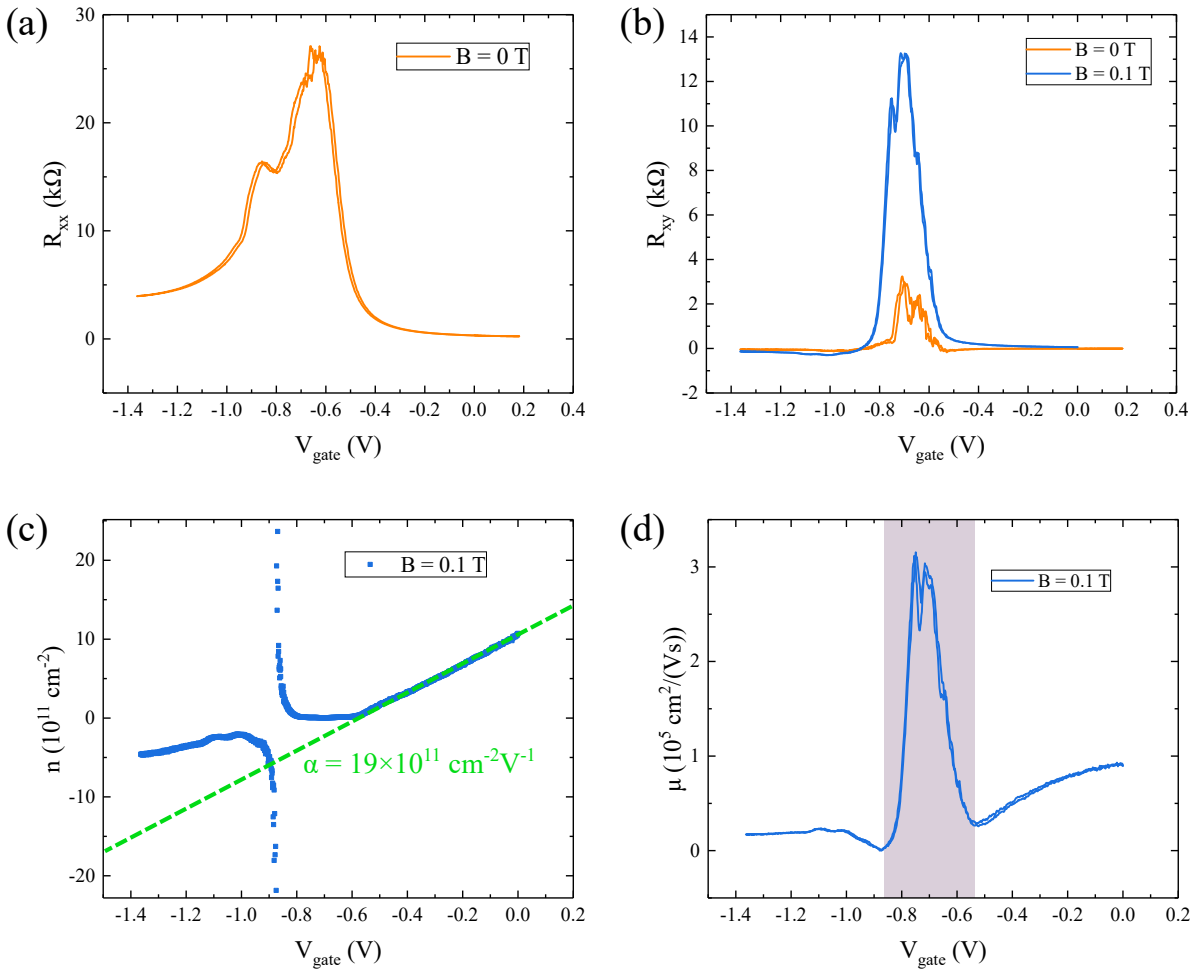

FIGURE C.1 – Panel (a) illustrates the longitudinal resistance R_{xx} of the Hall bar as a function of the gate voltage in the absence of magnetic field. (b) Variation of the transversal resistance R_{xy} at zero magnetic field and at $B = 0.1$ T. Panels (c) and (d) respectively display the carrier density and the mobility as a function of the gate voltage. Data are extracted from measurements at $B = 0.1$ T. In (c) the dashed line represent the depleting factor of the electron side.

Since the Hall resistance is not reliable on the hole side due to its non-linearity with the magnetic field, the plotted hole density should not be considered.

Finally, mobility values are extracted at each gate voltage assuming a single carrier type model, see figure C.1(d) on both sides of the grey band. The order of magnitude is similar to that of the larger Hall bar and the shape is very close : the electron mobility increases as the gate voltage is increased from $V_{\text{gate}} \geq -0.6$ V ; while the hole mobility on the other side should not be considered since the hole density is not reliable.

In conclusion, the low-field magneto-transport results are highly consistent between the two Hall bars. In both devices, an ambipolar behavior is observed as the Fermi level

is tuned via the gate voltage, with comparable resistance, carrier density, and mobility values. On the electron side, the transport characteristics are nearly identical for both structures. On the hole side, the anomalous Hall resistance at low field gives incorrect values of the hole density and mobility. It is anticipated that measurements performed at multiple magnetic field values, as it was done for the larger Hall bar, would allow for a better determination of the hole density with a single depletion factor for both carrier types. Unfortunately, such measurements were not conducted for this device.

2 Shubnikov-de Haas oscillations

By increasing the magnetic field, R_{xx} oscillations appear, also referred to as Shubnikov-de Haas oscillations (SdHO), highlighting the quantization of the energy spectrum into discrete Landau levels. Eventually resistance minima of the oscillations will vanish as the magnetic field is kept increasing, marking the transition into the quantum Hall regime.

Figure C.2 displays the variation of the longitudinal resistance and the transversal conductance as a function of the filling factor $\nu = nh/eB$ for this small Hall bar at 1.5 K and zero gate voltage. Figure C.3 highlights the differences between the two Hall bars at the same temperature and gate voltage.

We first examine the evolution of the longitudinal resistance R_{xx}. At high filling factors, corresponding to low magnetic fields, the amplitude of the Shubnikov-de Haas (SdH) oscillations is smaller than in the large Hall bar due to the reduced topological protection of the ballistic chiral edge states (higher chance of backscattering between the edges). The resistance minima are also aligned with odd filling factors. However, the transition to even filling factors occurs in the small Hall bar. The first resistance minimum associated with even filling is observed at $\nu = 20$, instead of $\nu = 16$ in the large device. As the magnetic field increases, full quantization at even filling factors appears at $\nu = 8$ for both Hall bars. On the other hand, the oscillations corresponding to odd filling factors are more pronounced in the small device, suggesting that the Landau levels associated with odd filling factors are sharper.

We now turn to the transverse conductance G_{xy}. The quantum plateaus expected at $G_{xy} = \nu e^2/h$, are less pronounced in this small Hall bar due to the reduced protection against backscattering for smaller width.

In conclusion, the expected quantum Hall signatures of a thin topological insulator layer are still visible in this small Hall bar. We observe the transition from odd to even filling factors, along with the emergence of complete quantization characterized by vanishing longitudinal resistance and quantized transverse conductance plateaus. Nevertheless, the measurements exhibit larger fluctuations, likely originating from an increased sensitivity to disorder. This could be related to the reduced lateral dimensions of the Hall bar, bringing the system closer to a quasi-one-dimensional wire, where edge effects and confinement play a more significant role, as discussed in Chapter 5.

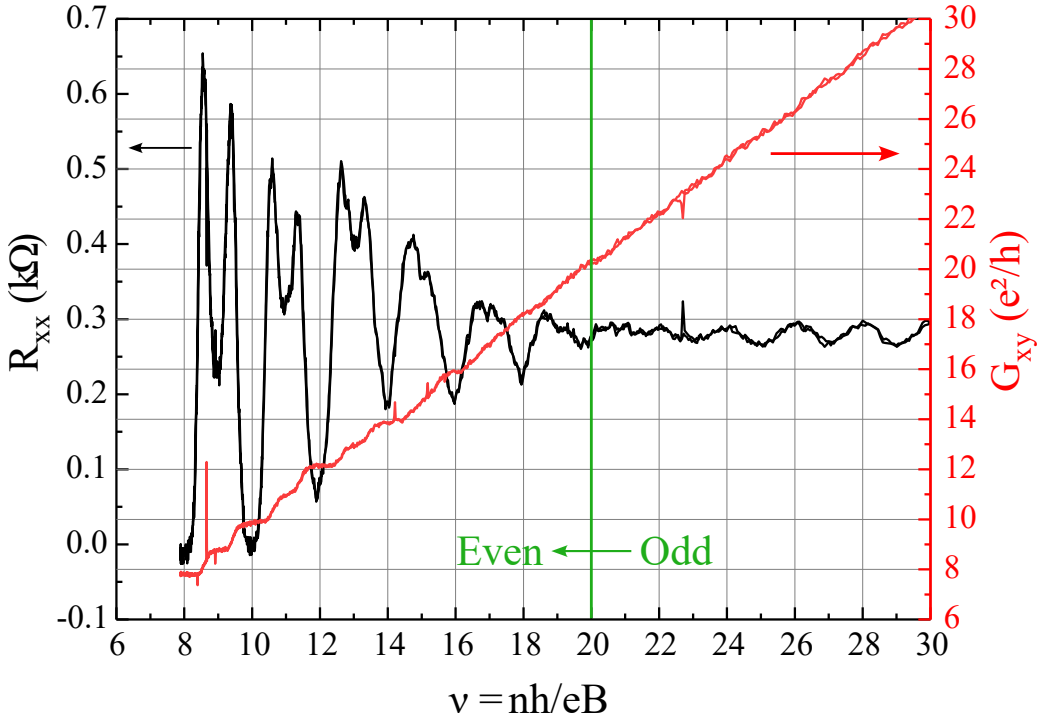

FIGURE C.2 – Longitudinal resistance R_{xx} and transversal conductance G_{xy} for the samll Hall bar with dimensions $L = 15\ \mu m/W = 3\ \mu m$. Data are plotted as a function of the filling factor. Measurements are performed at 1.5 K and at zero gate voltage.

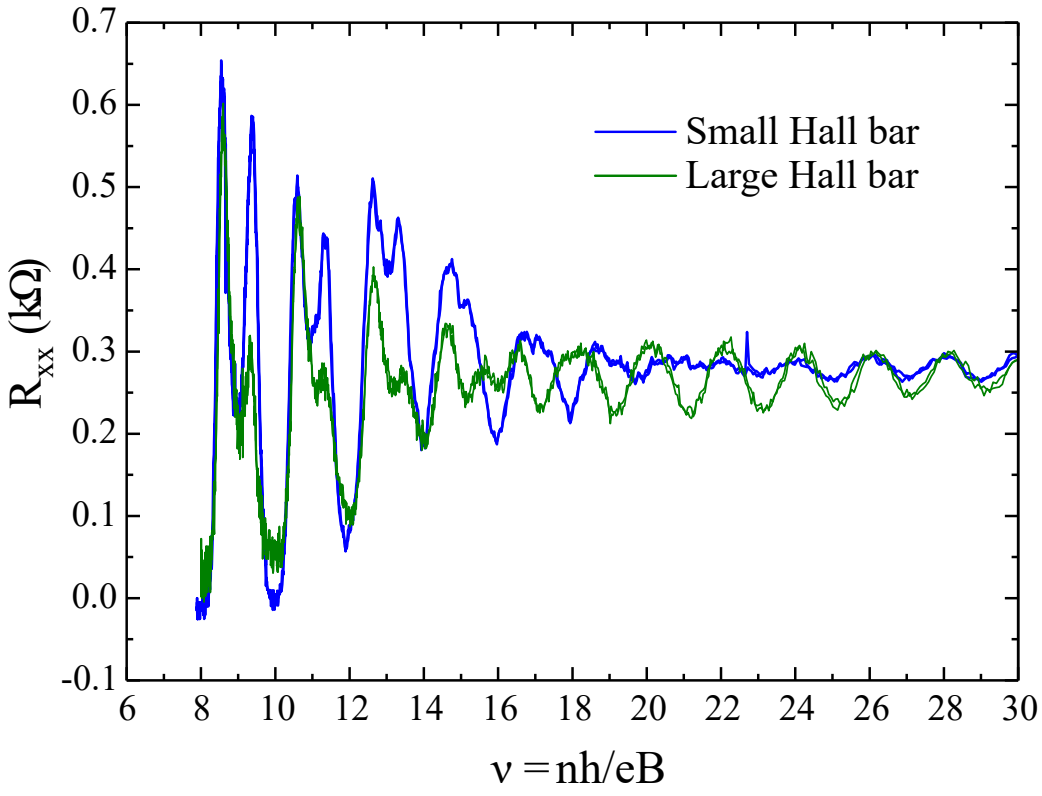

FIGURE C.3 – Comparison of the longitudinal resistance R_{xx} of the two Hall bars fabricated during the same SAG process. The two devices have been measured at 1.5 K and zero gate voltage.

List of publications

Publication

1. **Chaize, N.**, Baudry, X., Jouneau, P-H., Gautier, E., Rouvière, J-L., Deblock, Y., Xu, J., Berthe, M., Barbot, C., Grandidier, B., Desplanque, L., Sellier, H., and Ballet, P., 2024. *Selective area epitaxy of in-plane HgTe nanostructures on CdTe(001) substrate.* Nanotechnology, Volume 35, Number 50.
2. Khelifi, W., Capiod, P., Barbot, C., Coinon, C., Deblock, Y., Santos, C N., **Chaize, N.**, Berthe M., Jouneau, P-H., Amarie, S., Lampin, J-F., Wallart, X., Ballet, P., Grandidier, B. and Desplanque, L., 2025. *Selective area molecular beam epitaxy of InSb on InP(111)B : from thin films to quantum nanostructures.* Nanotechnology, Volume 36, Number 12.

Conferences

1. **Chaize, N.** and Ballet, P., *Selective area epitaxy of HgTe on CdTe(001) substrate.* GDR MatEpi, 2023.
2. **Chaize, N.**, Baudry, X., Jouneau, P-H., Gautier, E., Rouvière, J-L., Deblock, Y., Xu, J., Berthe, M., Barbot, C., Grandidier, B., Desplanque, L., Sellier, H., and Ballet, P., 2024, September. *Selective area epitaxy of in-plane HgTe nanostructures on CdTe(001) substrate.* In 23rd International conference on Molecular Beam Epitaxy (ICMBE 2024).
3. **Chaize, N.**, Baudry, X., Jouneau, P-H., Gautier, E., Rouvière, J-L., Deblock, Y., Xu, J., Berthe, M., Barbot, C., Grandidier, B., Desplanque, L., Sellier, H., and Ballet, P., 2024, October. *Emergign materials for quantum computing : in-plane HgTe nanostructures* In 19th Journées de la Matière Condensée, for the colloquium Emerging materials and Majorana particles : towards topological quantum computing (JMC 2024).

Article in prepration

1. Quantum coherent transport in HgTe nanostructures grown by selective area epitaxy.

Bibliography

[Aguado, 2020] Ramón Aguado et Leo P Kouwenhoven. « Majorana qubits for topological quantum computing ». *Physics today* 73.6 (2020), p. 44-50 (cf. p. xxiii, xxvii).

[Aharonov, 1959] Yakir Aharonov et David Bohm. « Significance of electromagnetic potentials in the quantum theory ». *Physical review* 115.3 (1959), p. 485 (cf. p. 116).

[Ahn, 2021] Seongjin Ahn, Haining Pan, Benjamin Woods, Tudor D Stanescu et Sankar Das Sarma. « Estimating disorder and its adverse effects in semiconductor Majorana nanowires ». *Physical Review Materials* 5.12 (2021), p. 124602 (cf. p. 18, 28).

[AlTshuler, 1981] BL Al'Tshuler, AG Aronov et BZ Spivak. « The Aaronov-Bohm effect in disordered conductors ». *Jetp Lett* 33.2 (1981), p. 94 (cf. p. 118).

[AlTshuler, 1982] BL Al'Tshuler, AG Aronov, BZ Spivak, D Yu Sharvin et Yu V Sharvin. « Observation of the Aaronov-Bohm effect in hollow metal cylinders ». *ZhETF Pisma Redaktsiiu* 35 (1982), p. 476 (cf. p. 118).

[Altshuler, 1985] BL Al'tshuler et DE Khmel'Nitskii. « Fluctuation properties of small conductors ». *Soviet Journal of Experimental and Theoretical Physics Letters* 42 (1985), p. 359 (cf. p. 88).

[Albani, 2019] Marco Albani, Roberto Bergamaschini, Marco Salvalaglio, Axel Voigt, Leo Miglio et Francesco Montalenti. « Competition between kinetics and thermodynamics during the growth of faceted crystal by phase field modeling ». *physica status solidi (b)* 256.7 (2019), p. 1800518 (cf. p. 23, 34).

[Altshuler, 1982] B. L. Altshuler, A. G. Aronov et D. E. Khmelnitsky. « Effects of electron-electron collisions with small energy transfers on quantum localisation ». *Journal of Physics C : Solid State Physics* 15.36 (1982), p. 7367-7386 (cf. p. 2, 114, 120).

[Altshuler, 2012] Boris L'vovich Altshuler, Patrick A Lee et W Richard Webb. *Mesoscopic phenomena in solids*. Elsevier, 2012 (cf. p. 1, 2).

[Aseev, 2018] Pavel Aseev, Alexandra Fursina, Frenk Boekhout, Filip Krizek, Joachim E Sestoft, Francesco Borsoi et al. « Selectivity map for molecular beam epitaxy of advanced III–V quantum nanowire networks ». *Nano letters* 19.1 (2018), p. 218-227 (cf. p. 13, 14, 16).

[Aseev, 2019] Pavel Aseev, Guanzhong Wang, Luca Binci, Amrita Singh, Sara Martí-Sánchez, Marc Botifoll et al. « Ballistic InSb nanowires and networks via metal-sown selective area growth ». *Nano letters* 19.12 (2019), p. 9102-9111 (cf. p. 14, 95, 115, 119, 120, 125).

[Awschalom, 2007] David D Awschalom et Michael E Flatté. « Challenges for semiconductor spintronics ». *Nature physics* 3.3 (2007), p. 153-159 (cf. p. 1).

[Badawy, 2024] Ghada Badawy et Erik PAM Bakkers. « Electronic transport and quantum phenomena in nanowires ». *Chemical reviews* 124.5 (2024), p. 2419-2440 (cf. p. 94).

[Ballet, 2013] P Ballet, X Baudry, B Polge, D Brellier, J Merlin et P Gergaud. « Strain determination in quasi-lattice-matched LWIR HgCdTe/CdZnTe layers ». *Journal of electronic materials* 42 (2013), p. 3133-3137 (cf. p. 18).

[Ballet, 2014] P Ballet, C Thomas, X Baudry, Clément Bouvier, O Crauste, Tristan Meunier et al. « MBE growth of strained HgTe/CdTe topological insulator structures ». *Journal of electronic materials* 43 (2014), p. 2955-2962 (cf. p. 18).

[Baum, 2014] Yuval Baum, Jan Böttcher, Christoph Brüne, Cornelius Thienel, Laurens W Molenkamp, Ady Stern et al. « Self-consistent k · p calculations for gated thin layers of three-dimensional topological insulators ». *Physical Review B* 89.24 (2014), p. 245136 (cf. p. 48).

[Beenakker, 1991] CWJ Beenakker et Henk van Houten. « Quantum transport in semiconductor nanostructures ». *Solid state physics*. T. 44. Elsevier, 1991, p. 1-228 (cf. p. 1, 80, 83, 86, 87, 89, 92, 112).

[Beenakker, 1988a] CWJ Beenakker et H Van Houten. « Boundary scattering and weak localization of electrons in a magnetic field ». *Physical Review B* 38.5 (1988), p. 3232 (cf. p. 83).

[Beenakker, 1988b] CWJ Beenakker et H Van Houten. « Flux-cancellation effect on narrow-channel magnetoresistance fluctuations ». *Physical Review B* 37.11 (1988), p. 6544 (cf. p. 88, 89, 107).

[Bendias, 2018] Kalle Bendias, Saquib Shamim, Oliver Herrmann, Andreas Budewitz, Pragya Shekhar, Philipp Leubner et al. « High mobility HgTe microstructures for quantum spin Hall studies ». *Nano letters* 18.8 (2018), p. 4831-4836 (cf. p. 8, 9, 52, 70).

[Bergmann, 1984] Gerd Bergmann. « Weak localization in thin films : a time-of-flight experiment with conduction electrons ». *Physics Reports* 107.1 (1984), p. 1-58 (cf. p. 1).

[Bernevig, 2006] B Andrei Bernevig, Taylor L Hughes et Shou-Cheng Zhang. « Quantum spin Hall effect and topological phase transition in HgTe quantum wells ». *science* 314.5806 (2006), p. 1757-1761 (cf. p. 4, 7, 8).

[Beznasyuk, 2020] DV Beznasyuk, P Stepanov, Jean-Luc Rouvière, F Glas, M Verheijen, J Claudon et al. « Full characterization and modeling of graded interfaces in a high lattice-mismatch axial nanowire heterostructure ». *Physical Review Materials* 4.7 (2020), p. 074607 (cf. p. 27).

[Böer, 2022] Karl W Böer et Udo W Pohl. « Properties and Growth of Semiconductors ». *Semiconductor Physics*. Springer, 2022, p. 1-32 (cf. p. 10).

[Brüne, 2011] C Brüne, CX Liu, EG Novik, EM Hankiewicz, H Buhmann, YL Chen et al. « Quantum Hall effect from the topological surface states of strained bulk HgTe ». *Physical Review Letters* 106.12 (2011), p. 126803 (cf. p. 3, 7, 52).

[Brüne, 2016] C. Brüne, P. Leubner, O. Raichev, H. Buhmann et L. W. Molenkamp. « Evidence for the ballistic spin Hall effect in HgTe nanostructures ». *Proceedings of the National Academy of Sciences* 113.47 (2016), p. 13222-13227 (cf. p. 64).

[Büttner, 2011] B Büttner, CX Liu, G Tkachov, EG Novik, C Brüne, H Buhmann et al. « Single valley Dirac fermions in zero-gap HgTe quantum wells ». *Nature Physics* 7.5 (2011), p. 418-422 (cf. p. 7).

[Bychkov, 1984] Yua A Bychkov et É I Rashba. « Properties of a 2D electron gas with lifted spectral degeneracy ». *JETP lett* 39.2 (1984), p. 78 (cf. p. 84).

[Cachaza, 2021] Martin Espiñeira Cachaza, Anna Wulff Christensen, Daria Beznasyuk, Tobias Særkjær, Morten Hannibal Madsen, Rawa Tanta et al. « Selective area growth rates of III-V nanowires ». *Physical Review Materials* 5.9 (2021), p. 094601 (cf. p. 13, 33, 34).

[Chandrasekhar, 1985] V Chandrasekhar, MJ Rooks, S Wind et DE Prober. « Observation of Aharonov-Bohm Electron Interference Effects with Periods h e and h 2 e in Individual Micron-Size, Normal-Metal Rings ». *Physical review letters* 55.15 (1985), p. 1610 (cf. p. 118).

[Charpentier, 2012] Coralie Charpentier. « Investigation of deposition conditions and annealing treatments on sputtered ZnO : Al thin films : Material properties and application to microcristalline silicon solar cells ». Thèse de doct. Ecole Polytechnique X, 2012 (cf. p. 135).

[Chu, 2008] Junhao Chu et Arden Sher. *Physics and properties of narrow gap semiconductors*. Springer, 2008 (cf. p. 5, 6).

[Chu, 2009] Junhao Chu et Arden Sher. *Device physics of narrow gap semiconductors*. Springer Science & Business Media, 2009 (cf. p. 4).

[Cohen-Tannoudji, 1986] Claude Cohen-Tannoudji, Bernard Diu et Frank Laloe. « Quantum Mechanics, Volume 2 ». *Quantum Mechanics* 2 (1986), p. 626 (cf. p. 5).

[Crauste, 2013] Olivier Crauste, Yoshiyuki Ohtsubo, Philippe Ballet, Pierre André Louis Delplace, David Carpentier, Clément Bouvier et al. « Topological surface states of strained Mercury-Telluride probed by ARPES ». *arXiv preprint arXiv :1307.2008* (2013) (cf. p. xxiv, xxviii).

[Dalacu, 2013] Dan Dalacu, Alicia Kam, D Guy Austing et Philip J Poole. « Droplet dynamics in controlled InAs nanowire interconnections ». *Nano letters* 13.6 (2013), p. 2676-2681 (cf. p. 11).

[Datta, 1997] Supriyo Datta. *Electronic transport in mesoscopic systems*. Cambridge university press, 1997 (cf. p. 1).

[Daumer, 2005] Volker Daumer. « Phase coherent transport phenomena in HgTe quantum well structrues ». Thèse de doct. Universität Würzburg, 2005 (cf. p. 3, 8).

[De Donno, 2022] Marcello De Donno, Marco Albani, Roberto Bergamaschini et Francesco Montalenti. « Phase-field modeling of the morphological evolution of ringlike structures during growth : Thermodynamics, kinetics, and template effects ». *Physical Review Materials* 6.2 (2022), p. 023401 (cf. p. 36).

[De Leon, 2021] Nathalie P De Leon, Kohei M Itoh, Dohun Kim, Karan K Mehta, Tracy E Northup, Hanhee Paik et al. « Materials challenges and opportunities for quantum computing hardware ». *Science* 372.6539 (2021), eabb2823 (cf. p. xxiii, xxvii).

[Dede, 2022] Didem Dede, Frank Glas, Valerio Piazza, Nicholas Morgan, Martin Friedl, Lucas Güniat et al. « Selective area epitaxy of GaAs : The unintuitive role of feature size and pitch ». *Nanotechnology* 33.48 (2022), p. 485604 (cf. p. 13, 33, 34).

[Desplanque, 2019] L Desplanque, A Bucamp, David Troadec, G Patriarche et X Wallart. « Selective area molecular beam epitaxy of InSb nanostructures on mismatched substrates ». *Journal of Crystal Growth* 512 (2019), p. 6-10 (cf. p. 14).

[Desplanque, 2018] L Desplanque, Alexandre Bucamp, David Troadec, G Patriarche et X Wallart. « In-plane InSb nanowires grown by selective area molecular beam epitaxy on semi-insulating substrate ». *Nanotechnology* 29.30 (2018), p. 305705 (cf. p. 13, 14).

[Doh, 2005] Yong-Joo Doh, Jorden A van Dam, Aarnoud L Roest, Erik PAM Bakkers, Leo P Kouwenhoven et Silvano De Franceschi. « Tunable supercurrent through semiconductor nanowires ». *science* 309.5732 (2005), p. 272-275 (cf. p. 2).

[Dresselhaus, 1955] Gene Dresselhaus. « Spin-orbit coupling effects in zinc blende structures ». *Physical Review* 100.2 (1955), p. 580 (cf. p. 84).

[Dubrovskii, 2023] Vladimir G Dubrovskii. « Theory of diffusion-induced selective area growth of III-V nanostructures ». *Physical Review Materials* 7.2 (2023), p. 026001 (cf. p. 13, 33).

[Fahed, 2016] Maria Fahed. « docteur de l'université ». Thèse de doct. Université de Lille 1, 2016 (cf. p. 19).

[Franz, 2013] Marcel Franz et Laurens Molenkamp. *Topological insulators*. T. 6. Elsevier, 2013 (cf. p. 5).

[Geng, 2022] Zuhan Geng, Zitong Zhang, Fangting Chen, Shuai Yang, Yuying Jiang, Yichun Gao et al. « Observation of Aharonov-Bohm effect in PbTe nanowire networks ». *Physical Review B* 105.24 (2022), p. L241112 (cf. p. 118, 119, 125).

[Haakenaasen, 2008a] R Haakenaasen, E Selvig, S Foss, L Trosdahl-Iversen et J Taftø. « Segmented nanowires of HgTe and Te grown by molecular beam epitaxy ». *Applied Physics Letters* 92.13 (2008) (cf. p. 8, 9).

[Haakenaasen, 2008b] R Haakenaasen, E Selvig, S Hadzialic, T Skauli, V Hansen, JE Tibballs et al. « Nanowires in the CdHgTe material system ». *Journal of electronic materials* 37 (2008), p. 1311-1317 (cf. p. 8, 11).

[Haas, 2017] Benedikt Haas, Candice Thomas, Pierre-Henri Jouneau, Nicolas Bernier, Tristan Meunier, Philippe Ballet et al. « High precision strain mapping of topological insulator HgTe/CdTe ». *Applied Physics Letters* 110.26 (2017), p. 263102 (cf. p. 18).

[Hansen, 2001] AE Hansen, A Kristensen, S Pedersen, CB Sørensen et PE Lindelöf. « Mesoscopic decoherence in Aharonov-Bohm rings ». *Physical Review B* 64.4 (2001), p. 045327 (cf. p. 120).

[Hoffmann, 2015] Axel Hoffmann et Sam D Bader. « Opportunities at the frontiers of spintronics ». *Physical Review Applied* 4.4 (2015), p. 047001 (cf. p. xxiv, xxvii).

[Ibach, 2013] Harald Ibach et Hans Lüth. *Solid-state physics : an introduction to principles of materials science*. Springer Science & Business Media, 2013 (cf. p. 10).

[Imry, 2002] Yoseph Imry. *Introduction to mesoscopic physics*. 2. Oxford university press, 2002 (cf. p. 1).

[Iwanaga, 1986] H Iwanaga, A Tomizuka, N Shibata et K Mochizuki. « Etch pits and polarity identification in CdTe, HgSe and HgTe crystals ». *Journal of crystal growth* 74.1 (1986), p. 113-117 (cf. p. 23, 26).

[Jiang, 2022] Yuying Jiang, Shuai Yang, Lin Li, Wenyu Song, Wentao Miao, Bingbing Tong et al. « Selective area epitaxy of PbTe-Pb hybrid nanowires on a lattice-matched substrate ». *Physical Review Materials* 6.3 (2022), p. 034205 (cf. p. 14).

[Jiang, 2007] Zhigang Jiang, Yuanbo Zhang, HL Stormer et Ph Kim. « Quantum Hall states near the charge-neutral Dirac point in graphene ». *Physical review letters* 99.10 (2007), p. 106802 (cf. p. 74).

[Jung, 2022] Jason Jung, Sander G Schellingerhout, Markus F Ritter, Sofieke C ten Kate, Orson AH van der Molen, Sem de Loijer et al. « Selective Area Growth of PbTe Nanowire Networks on InP ». *Advanced Functional Materials* 32.51 (2022), p. 2208974 (cf. p. 13, 14, 115, 119, 120, 125).

[Konig, 2007a] Markus Konig, Steffen Wiedmann, Christoph Brune, Andreas Roth, Hartmut Buhmann, Laurens W Molenkamp et al. « Quantum spin Hall insulator state in HgTe quantum wells ». *Science* 318.5851 (2007), p. 766-770 (cf. p. xxiv, xxviii).

[Konig, 2007b] Markus Konig, Steffen Wiedmann, Christoph Brune, Andreas Roth, Hartmut Buhmann, Laurens W Molenkamp et al. « Quantum spin Hall insulator state in HgTe quantum wells ». *Science* 318.5851 (2007), p. 766-770 (cf. p. 2, 3, 7).

[König, 2006] M König, A Tschetschetkin, EM Hankiewicz, Jairo Sinova, V Hock, V Daumer et al. « Direct observation of the Aharonov-Casher phase ». *Physical Review Letters* 96.7 (2006), p. 076804 (cf. p. 123).

[Koo, 2009] Hyun Cheol Koo, Jae Hyun Kwon, Jonghwa Eom, Joonyeon Chang, Suk Hee Han et Mark Johnson. « Control of spin precession in a spin-injected field effect transistor ». *Science* 325.5947 (2009), p. 1515-1518 (cf. p. 2).

[Kozlov, 2016] DA Kozlov, Dominik Bauer, Johannes Ziegler, Ralf Fischer, ML Savchenko, ZD Kvon et al. « Probing quantum capacitance in a 3D topological insulator ». *Physical Review Letters* 116.16 (2016), p. 166802 (cf. p. 3, 7).

[Krishtopenko, 2018] Sergey S Krishtopenko et Frederic Teppe. « Realistic picture of helical edge states in HgTe quantum wells ». *Physical Review B* 97.16 (2018), p. 165408 (cf. p. 68).

[Krizek, 2018] Filip Krizek, Joachim E Sestoft, Pavel Aseev, Sara Marti-Sanchez, Saulius Vaitiekėnas, Lucas Casparis et al. « Field effect enhancement in buffered quantum nanowire networks ». *Physical review materials* 2.9 (2018), p. 093401 (cf. p. 14, 119, 120).

[Kurdak, 1992] C Kurdak, AM Chang, Albert Chin et TY Chang. « Quantum interference effects and spin-orbit interaction in quasi-one-dimensional wires and rings ». *Physical Review B* 46.11 (1992), p. 6846 (cf. p. 83, 86, 117, 118).

[LaBella, 2000] V. P. LaBella, D. W. Bullock, Z. Ding, C. Emery, W. G. Harter et P. M. Thibado. « Monte Carlo derived diffusion parameters for Ga on the GaAs(001)- (2×4) surface : A molecular beam epitaxy-scanning tunneling microscopy study ». *Journal of Vacuum Science & Technology A* 18.4 (2000), p. 1526-1531 (cf. p. 24).

[Lee, 2019] Joon Sue Lee, Sukgeun Choi, Mihir Pendharkar, Daniel J Pennachio, Brian Markman, Michael Seas et al. « Selective-area chemical beam epitaxy of in-plane InAs one-dimensional channels grown on InP (001), InP (111) B, and InP (011) surfaces ». *Physical Review Materials* 3.8 (2019), p. 084606 (cf. p. 13, 14, 16, 119, 120, 125).

[Lee, 1987] PA Lee, A Douglas Stone et Hidetoshi Fukuyama. « Universal conductance fluctuations in metals : Effects of finite temperature, interactions, and magnetic field ». *Physical Review B* 35.3 (1987), p. 1039 (cf. p. 88, 89).

[Lee, 1986] Patrick A Lee. « Universal conductance fluctuations in disordered metals ». *Physica A : Statistical Mechanics and its Applications* 140.1-2 (1986), p. 169-174 (cf. p. 87).

[Lee, 1985] Patrick A Lee et A Douglas Stone. « Universal conductance fluctuations in metals ». *Physical review letters* 55.15 (1985), p. 1622 (cf. p. 86, 87).

[Linder, 2009] Jacob Linder, Takehito Yokoyama et Asle Sudbø. « Anomalous finite size effects on surface states in the topological insulator Bi 2 Se 3 ». *Physical Review B—Condensed Matter and Materials Physics* 80.20 (2009), p. 205401 (cf. p. 61).

[Liu, 2010] Chao-Xing Liu, HaiJun Zhang, Binghai Yan, Xiao-Liang Qi, Thomas Frauenheim, Xi Dai et al. « Oscillatory crossover from two-dimensional to three-dimensional topological insulators ». *Physical Review B—Condensed Matter and Materials Physics* 81.4 (2010), p. 041307 (cf. p. 61).

[Liu, 2018] Lingfeng Liu, Yiyu Chen, Zhenhua Ye et Ruijun Ding. « A review on plasma-etch-process induced damage of HgCdTe ». *Infrared Physics & Technology* 90 (2018), p. 175-185 (cf. p. 3, 8).

[Lu, 2006] Wei Lu et Charles M Lieber. « Semiconductor nanowires ». *Journal of Physics D : Applied Physics* 39.21 (2006), R387 (cf. p. 11).

[Ludwig, 2004] T Ludwig et AD Mirlin. « Interaction-induced dephasing of Aharonov-Bohm oscillations ». *Physical Review B* 69.19 (2004), p. 193306 (cf. p. 125).

[Lutchyn, 2018] Roman M Lutchyn, Erik PAM Bakkers, Leo P Kouwenhoven, Peter Krogstrup, Charles M Marcus et Yuval Oreg. « Majorana zero modes in superconductor–semiconductor heterostructures ». *Nature Reviews Materials* 3.5 (2018), p. 52-68 (cf. p. 2).

[Marra, 2022] Pasquale Marra. « Majorana nanowires for topological quantum computation ». *Journal of Applied Physics* 132.23 (2022) (cf. p. xxiii, xxvii).

[Milliken, 1987] FP Milliken, S Washburn, CP Umbach, RB Laibowitz et RA Webb. « Effect of partial phase coherence on Aharonov-Bohm oscillations in metal loops ». *Physical Review B* 36.8 (1987), p. 4465 (cf. p. 113, 119, 120).

[Morgan, 2023] Nicholas Morgan, Vladimir G. Dubrovskii, Ann-Kristin Stief, Didem Dede, Marie Sanglé-Ferrière, Alok Rudra et al. « From Layer-by-Layer Growth to Nanoridge Formation : Selective Area Epitaxy of GaAs by MOVPE ». *Crystal Growth & Design* 23.7 (2023), p. 5083-5092 (cf. p. 13, 16, 23, 34, 37, 38).

[Nielsen, 2010] Michael A Nielsen et Isaac L Chuang. *Quantum computation and quantum information*. Cambridge university press, 2010 (cf. p. 1).

[Novik, 2005] EG Novik, A Pfeuffer-Jeschke, T Jungwirth, V Latussek, CR Becker, G Landwehr et al. « Band structure of semimagnetic Hg 1- y Mn y Te quantum wells ». *Physical Review B—Condensed Matter and Materials Physics* 72.3 (2005), p. 035321 (cf. p. 99).

[Oehling, 1998] S Oehling, M Ehinger, T Gerhard, CR Becker, G Landwehr, M Schneider et al. « Termination, surface structure and morphology of the molecular beam epitaxially grown HgTe (001) surface ». *Applied physics letters* 73.22 (1998), p. 3205-3207 (cf. p. 24-26).

[Oehling, 1996] S Oehling, M Ehinger, W Spahn, A Waag, CR Becker et G Landwehr. « Mechanisms of molecular beam epitaxial growth of (001) HgTe ». *Journal of applied physics* 79.2 (1996), p. 748-751 (cf. p. 24, 26).

[Op het Veld, 2020] Roy LM Op het Veld, Di Xu, Vanessa Schaller, Marcel A Verheijen, Stan ME Peters, Jason Jung et al. « In-plane selective area InSb–Al nanowire quantum networks ». *Communications Physics* 3.1 (2020), p. 59 (cf. p. xxiii, xxvii).

[Oxford Instruments, 2013] Oxford Instruments. *Heliox Sorption Pumped 3He Refrigerator Systems : Principle of Operation and Control*. 2013 (cf. p. 56).

[Pohl, 2013] Udo W Pohl. *Epitaxy of semiconductors*. T. 1. Springer, 2013 (cf. p. 12).

[Rashba, 2012] Emmanuel I Rashba. « Quantum nanostructures in strongly spin-orbit coupled two-dimensional systems ». *Physical Review B—Condensed Matter and Materials Physics* 86.12 (2012), p. 125319 (cf. p. 85).

[Rolland, 1994] S Rolland. « A3. 2 Dielectric constant and refractive index of HgCdTe ». *Properties of Narrow Gap Cadmium-Based Compounds* 10 (1994), p. 80 (cf. p. 49).

[Rottman, 1984] Craig Rottman et Michael Wortis. « Statistical mechanics of equilibrium crystal shapes : Interfacial phase diagrams and phase transitions ». *Physics Reports* 103.1-4 (1984), p. 59-79 (cf. p. 13).

[Rouviere, 2013] Jean-Luc Rouviere, Armand Béché, Yannick Martin, Thibaud Denneulin et David Cooper. « Improved strain precision with high spatial resolution using nanobeam precession electron diffraction ». *Applied Physics Letters* 103.24 (2013) (cf. p. 29).

[Sarma, 2021] Sankar Das Sarma et Haining Pan. « Disorder-induced zero-bias peaks in Majorana nanowires ». *Physical Review B* 103.19 (2021), p. 195158 (cf. p. 18, 28).

[Seelig, 2001] Georg Seelig et Markus Büttiker. « Charge-fluctuation-induced dephasing in a gated mesoscopic interferometer ». *Physical Review B* 64.24 (2001), p. 245313 (cf. p. 120).

[Selvig, 2006] E Selvig, S Hadzialic, T Skauli, H Steen, V Hansen, L Trosdahl-Iversen et al. « Growth of HgTe nanowires ». *Physica Scripta* 2006.T126 (2006), p. 115 (cf. p. 8, 9, 11).

[Shekhar, 2023] Pragya Shekhar, Kalle Bendias, Lena Fürst, Xianhu Liang, Michael K Gbordzoe, Tatiana Borzenko et al. « Realization of smooth side profile using diffusion-controlled wet chemical etching for HgTe/(Hg, Cd) Te heterostructures ». *Nanotechnology* 34.20 (2023), p. 205302 (cf. p. 8).

[Thelander, 2006] Claes Thelander, Prabhat Agarwal, S Brongersma, Joël Eymery, Lou-Fé Feiner, Alfred Forchel et al. « Nanowire-based one-dimensional electronics ». *Materials today* 9.10 (2006), p. 28-35 (cf. p. 10).

[Thomas, 2017] C. Thomas, O. Crauste, B. Haas, P.-H. Jouneau, C. Bäuerle, L. P. Lévy et al. « Revealing topological Dirac fermions at the surface of strained HgTe thin films via quantum Hall transport spectroscopy ». *Physical Review B* 96 (2017), p. 245420 (cf. p. xxiv, xxviii, 3, 7, 52, 74).

[Thomas, 2016] Candice Thomas. « Strained HgTe/CdTe topological insulators, toward spintronic applications ». Thèse de doct. Université Grenoble Alpes, 2016 (cf. p. 4, 24, 44, 70, 76, 137, 138).

[Vaitiekėnas, 2018a] S Vaitiekėnas, Alexander M Whiticar, M-T Deng, Filip Krizek, Joachim E Sestoft, CJ Palmstrøm et al. « Selective-area-grown semiconductor-superconductor hybrids : A basis for topological networks ». *Physical review letters* 121.14 (2018), p. 147701 (cf. p. xxiii, xxvii, 119, 120, 125).

[Vaitiekėnas, 2018b] S Vaitiekėnas, Alexander M Whiticar, M-T Deng, Filip Krizek, Joachim E Sestoft, CJ Palmstrøm et al. « Selective-area-grown semiconductor-superconductor hybrids : A basis for topological networks ». *Physical review letters* 121.14 (2018), p. 147701 (cf. p. 14).

[Van Houten, 1986] H Van Houten, BJ Van Wees, MGJ Heijman et JP Andre. « Submicron conducting channels defined by shallow mesa etch in GaAs-AlGaAs heterojunctions ». *Applied physics letters* 49.26 (1986), p. 1781-1783 (cf. p. 80).

[Wagner, 1964] Rudooh S Wagner et W Chadwick Ellis. « Vapor-liquid-solid mechanism of single crystal growth ». *Applied physics letters* 4.5 (1964), p. 89-90 (cf. p. 11).

[Wang, 2025] Ping Wang, Feng Chen, Yuhe Yang, Shuai Hu, Yue Li, Wenhong Wang et al. « Orbitronics : Mechanisms, materials and devices ». *Advanced Electronic Materials* 11.5 (2025), p. 2400554 (cf. p. xxiii, xxvii).

[Wang, 2013] Y. Y. Wang, J. Bruley, H. van Meer, J. Li, A. Domenicucci, C. E. Murray et al. « Strain mapping of Si devices with stress memorization processing ». *Applied Physics Letters* 103.5 (2013), p. 052104 (cf. p. 27).

[Washburn, 1985] S Washburn, CP Umbach, RB Laibowitz et Richard A Webb. « Temperature dependence of the normal-metal Aharonov-Bohm effect ». *Physical Review B* 32.7 (1985), p. 4789 (cf. p. 120).

[Washburn, 1986] Sean Washburn et Richard A Webb. « Aharonov-Bohm effect in normal metal quantum coherence and transport ». *Advances in Physics* 35.4 (1986), p. 375-422 (cf. p. 1).

[Wehling, 2008] TO Wehling, KS Novoselov, SV Morozov, EE Vdovin, MI Katsnelson, AK Geim et al. « Molecular doping of graphene ». *Nano letters* 8.1 (2008), p. 173-177 (cf. p. 64).

[Wiedmann, 2011] S Wiedmann, HJ Van Elferen, EV Kurganova, MI Katsnelson, AJM Giesbers, A Veligura et al. « Coexistence of electron and hole transport in graphene ». *Physical Review B—Condensed Matter and Materials Physics* 84.11 (2011), p. 115314 (cf. p. 64).

[Yasuda, 1994] M Yasuda, H Kawata, K Murata, K Hashimoto, Y Hirai et N Nomura. « Resist heating effect in electron beam lithography ». *Journal of Vacuum Science & Technology B : Microelectronics and Nanometer Structures Processing, Measurement, and Phenomena* 12.3 (1994), p. 1362-1366 (cf. p. 44).

[Zhang, 2017] Chen Zhang, Xin Miao, Kelson D Chabak et Xiuling Li. « A review of III–V planar nanowire arrays : Selective lateral VLS epitaxy and 3D transistors ». *Journal of Physics D : Applied Physics* 50.39 (2017), p. 393001 (cf. p. 11).

[Zhang, 2018] Hao Zhang, Chun-Xiao Liu, Sasa Gazibegovic, Di Xu, John A Logan, Guanzhong Wang et al. « Retracted article : Quantized majorana conductance ». *Nature* 556.7699 (2018), p. 74-79 (cf. p. xxiii, xxvii).

[Zhang, 2021] Hao Zhang, Michiel WA de Moor, Jouri DS Bommer, Di Xu, Guanzhong Wang, Nick van Loo et al. « Large zero-bias peaks in InSb-Al hybrid semiconductor-superconductor nanowire devices ». *arXiv preprint arXiv :2101.11456* (2021) (cf. p. 2).

[Zhang, 2015] Song-Bo Zhang, Hai-Zhou Lu et Shun-Qing Shen. « Edge states and integer quantum Hall effect in topological insulator thin films ». *Scientific reports* 5.1 (2015), p. 13277 (cf. p. 63).

[Zhang, 2020] Yong Zhang, Fenghua Xue, Chenjia Tang, Jiaming Li, Liyang Liao, Lun Li et al. « Highly efficient electric-field control of giant Rashba spin–orbit coupling in lattice-matched InSb/CdTe heterostructures ». *ACS nano* 14.12 (2020), p. 17396-17404 (cf. p. 85).

[Zhang, 1997] Zhenyu Zhang et Max G. Lagally. « Atomistic Processes in the Early Stages of Thin-Film Growth ». *Science* 276.5311 (1997), p. 377-383 (cf. p. 24).

[Zhang, 2023] Zitong Zhang, Wenyu Song, Yichun Gao, Yuhao Wang, Zehao Yu, Shuai Yang et al. « Proximity effect in PbTe-Pb hybrid nanowire Josephson junctions ». *Phys. Rev. Mater.* 7 (8 2023), p. 086201 (cf. p. xxiii, xxvii).

[Ziegler, 2018] Johannes Ziegler, Raphael Kozlovsky, Cosimo Gorini, M-H Liu, Sabine Weishäupl, Hubert Maier et al. « Probing spin helical surface states in topological HgTe nanowires ». *Physical Review B* 97.3 (2018), p. 035157 (cf. p. 8).

[Zumbühl, 2002] DM Zumbühl, JB Miller, Charles M Marcus, K Campman et AC Gossard. « Spin-orbit coupling, antilocalization, and parallel magnetic fields in quantum dots ». *Physical review letters* 89.27 (2002), p. 276803 (cf. p. 85).